

UC San Diego

UC San Diego Electronic Theses and Dissertations

Title

Seismic Response of Freestanding Structural Systems: Shake Table Tests and Model Validation

Permalink

<https://escholarship.org/uc/item/2q84k59r>

Author

Wittich, Christine Erin

Publication Date

2016

Peer reviewed|Thesis/dissertation

UNIVERSITY OF CALIFORNIA, SAN DIEGO

**Seismic Response of Freestanding Structural Systems: Shake
Table Tests and Model Validation**

A dissertation submitted in partial satisfaction of the
requirements for the degree
Doctor of Philosophy

in

Structural Engineering

by

Christine Erin Wittich

Committee in charge:

Professor Tara C. Hutchinson, Chair
Professor Falko Kuester
Professor Gilberto Mosqueda
Professor David Sandwell
Professor Peter Shearer

2016

©

Christine Erin Wittich, 2016

All rights reserved

The Dissertation of Christine Erin Wittich is approved, and it is acceptable in quality and form for publication on microfilm and electronically:

Chair

University of California, San Diego

2016

DEDICATION

For my mother, Susan.

TABLE OF CONTENTS

Signature Page	iii
Dedication	iv
Table of Contents	vi
List of Figures	x
List of Tables	xviii
Nomenclature	xix
Acknowledgements	xxi
Vita	xxv
Abstract of the Dissertation	vi
Chapter 1 Introduction	1
1.1 Motivation	1
1.2 State of Understanding	5
1.3 Scope of Research	9
1.3.1 Scope of Field Survey	9
1.3.2 Scope of Shake Table Testing	10
1.3.3 Scope of Numerical Modeling	11
1.4 Organization of Dissertation	12
Chapter 2 Research Background and Prior Work	13
2.1 Pioneering Analytical Studies	13
2.1.1 Classical Model	14
2.1.2 Extension of Classical Model for Alternative Modes of Response	16
2.1.3 Extension of Classical Model for Multiple Bodies	17
2.1.4 Extension of Classical Model for Three Dimensions	19
2.1.5 Extension of Classical Model for Flexibility	20
2.2 Previous Experiments on Freestanding Structures	21
2.2.1 Single-Body Systems	22
2.2.2 Multi-Body Systems	28
2.3 State-of-the-Art Numerical Modeling	31
2.4 Summary	36
Chapter 3 Geometric Survey and Characterization of Complex Freestanding Structures	38
3.1 Introduction	38

3.1.1 Brief Review of Past Surveys	39
3.1.2 Scope of Current Survey	42
3.2 Site Survey and Documentation	42
3.2.1 Light Detection and Ranging.....	46
3.2.2 Structure-from-Motion	47
3.2.3 Poisson Reconstruction	50
3.2.4 Mass Properties	51
3.2.5 Survey Results	53
3.3 Effect on Dynamic Response.....	55
3.3.1 Equations of Motion	55
3.3.2 Effect of Point Cloud Resolution on Mass Properties	57
3.3.3 Effect of Point Cloud Resolution on Time History Analysis	60
3.4 Conclusions	62
3.5 Implications on Experimental Program	63
3.6 Acknowledgements.....	64
Chapter 4 Shake Table Tests of Freestanding Structures: Asymmetric Single-Body Tests	66
4.1 Introduction	66
4.2 Shake Table Test Program.....	68
4.2.1 Design and Construction of Model Statue Test Specimens.....	68
4.2.2 Measurement of As-Built Specimen Condition.....	73
4.2.3 Experimental Setup	74
4.2.4 Instrumentation.....	75
4.2.5 Camera Layout	76
4.2.6 Input Motions	79
4.2.7 Test Procedure	83
4.3 Data Processing for High Resolution Videos	85
4.3.1 Raw Data	85
4.3.2 Lens Distortion	86
4.3.3 Motion Tracking Algorithm	87
4.3.4 Time Alignment.....	90
4.4 Results and Interpretation	93
4.4.1 Effect of Horizontal Mass Eccentricity	95
4.4.2 Effect of Height of the Center of Mass.....	99
4.4.3 Effect of the Input Motion Pulse	101

4.5 Comparison with Classical Model.....	104
4.6 Conclusions	107
4.7 Implications on Numerical Modeling	110
4.8 Acknowledgements.....	111
Chapter 5 Shake Table Tests of Freestanding Structures: Dual-Body Systems	112
5.1 Introduction	112
5.1.1 Design and Construction of Experimental Specimens	114
5.1.2 Experimental Setup	118
5.1.3 Instrumentation.....	118
5.1.4 Input Motions	120
5.2 Inter-phase Comparison of Achieved Motions.....	122
5.3 Interface Characterization Tests	125
5.4 Repeatability of Dynamic Tests.....	127
5.4.1 Marble-Marble Interfaces.....	127
5.4.2 Comparison with Low Friction Steel Interfaces.....	135
5.5 Results and Interpretation of Dynamic Tests.....	137
5.5.1 Effect of Pedestal Geometry.....	137
5.5.2 Effect of Tower Geometry.....	140
5.5.3 Effect of Pedestal Friction	142
5.5.4 Combined Effects on Multi-Modal Response	145
5.5.5 Effect of Tower Restraint with Low-Friction Pedestal Interface	147
5.5.6 Effect of Ground Motion	150
5.6 Conclusions	153
5.7 Implications on Numerical Modeling.....	155
5.8 Acknowledgements.....	157
Chapter 6 Numerical Model Development and Validation	158
6.1 Extension of Classical Model for Warped Interfaces	160
6.1.1 Introduction	160
6.1.2 System Description.....	162
6.1.3 Equations of Motion.....	164
6.1.4 Impact and Energy Dissipation.....	168
6.1.5 Experimental Comparison	171
6.1.6 Parametric Study: Effect of Defect Size.....	174
6.1.7 Parametric Study: Effect of Number of Rocking Points	182

6.1.8 Effect of Interface Warps on Overturning Spectra	187
6.1.9 Conclusions	191
6.1.10 Implications of Analytical Study on Numerical Modeling.....	193
6.2 Summary of Implications on Numerical Modeling	194
6.3 Numerical Modeling Methodology	197
6.3.1 Modeling Platform.....	197
6.3.2 Model Geometry and Discretization.....	199
6.3.3 Material Model	201
6.3.4 Contact-Impact Algorithm.....	202
6.3.5 Dynamic Analysis Method.....	206
6.4 Numerical Model Calibration and Sensitivity	209
6.4.1 Contact Damping.....	209
6.4.2 Interface Stiffness.....	213
6.4.3 Interface Discretization	216
6.4.4 Calibration	222
6.5 Numerical Model Validation	230
6.5.1 Multi-Modal Response	230
6.5.2 Multi-Body Interaction.....	233
6.5.3 Fundamental Rocking Dynamics.....	235
6.6 Summary Remarks.....	238
6.7 Acknowledgements.....	240
Chapter 7 Conclusions and Recommendations.....	241
7.1 Motivation and Scope	241
7.2 Key Results.....	243
7.2.1 Field Survey of Culturally Significant Statues	243
7.2.2 Shake Table Tests of Single-Body Systems	245
7.2.3 Shake Table Tests of Dual-Body Systems	247
7.2.4 Numerical Modeling.....	249
7.3 Research Impact.....	252
7.4 Recommendations for Future Work	252
References.....	254
Appendix A.....	260

LIST OF FIGURES

Figure 1.1	Post-earthquake reconnaissance of various freestanding structural systems.	3
Figure 1.2	Post-earthquake freestanding structures emphasizing complex dynamics.	4
Figure 1.3	Schematic of the classical two-dimensional, rigid, rocking block subject to ground acceleration with the classically-derived equation of motion and the coefficient of restitution.....	8
Figure 1.4	Experimental setup for: (a) single-body tests and (b) dual-body tests.....	11
Figure 2.1	Schematic of two-dimensional, arbitrary geometry, rigid, rocking block with two distinct rocking points: (a) nondisplaced and (b) displaced.....	15
Figure 2.2	Response modes of a two-dimensional rigid block.	18
Figure 2.3	Modes of rocking response for a two-dimensional, rectangular rigid dual-body system (from Psycharis 1990).....	19
Figure 2.4	Schematics of the two-dimensional rocking block considering (a) flexibility of the interface (from Chatzis and Smyth 2011) and (b) flexibility of the body (from Acikgoz and DeJong 2012).....	21
Figure 2.5	(a) Experimental setup on the shake table of various precarious stones and slender columns, and (b) resultant overturned configurations atop the shake table. (From Purvance et al. 2009).....	24
Figure 2.6	Granite stone experiment: (a) single block specimens; (b) dual-body specimen; and, (c) trilith frame-like specimen. (From Peña et al. 2008).....	25
Figure 2.7	Experimental setup for the evaluation of interface material, incorporating a slender rigid block fixed from translation through joints at the base with various materials as the foundation material. (From ElGawady et al. 2011).....	26
Figure 2.8	Experimental specimens used in shake table testing of laboratory equipment (from Konstantinidis and Makris 2009).....	27
Figure 2.9	Scaled multi-drum column tested by Mouzakis et al. in (a) image, and (b) schematic including location of string potentiometers (from Mouzakis et al. 2002).....	30
Figure 2.10	Scaled multi-drum column tested by Drosos and Anastasopoulos, shown in a trilith form: (a) as built, and (b) in schematic with instrumentation schedule (from Drosos and Anastasopoulos 2014).....	30
Figure 2.11	The distinct element model as implemented by Winkler et al. for the normal and tangential direction in two dimensions, as well as the flow chart of calculations for this implementation (from Winkler et al. 1995).....	35
Figure 2.12	Three-dimensional discrete element model for the simulation of a multi-body system: (a) discretization of an individual body, and (b) simulated responses of the system showing the separation and interaction of the individual blocks (from Papantonopoulos et al. 2002).....	36

Figure 3.1	Flow chart of implemented methodology for statue documentation including the process of mesh generation in three-dimensional reconstruction.	45
Figure 3.2	Isometric and detail view of <i>Florentine Pieta</i> by Michelangelo: (a) LiDAR point cloud consisting of approximately 3.4 million vertices, and (B) SfM point cloud consisting of approximately 560 thousand vertices.	49
Figure 3.3	Snapshots of statue meshes of high and low resolution LiDAR and SfM.	52
Figure 3.4	Two-dimensional schematic of an arbitrary statue with scatter plot of geometric data for surveyed statues.	54
Figure 3.5	Percent difference between the LiDAR mesh at 1mm and the meshes at 2mm, 10mm, 50mm, and those generated by SfM and envelope shapes for four statues in terms of (a) normalized mass moment of inertia, (b) aspect ratio, and (c) rocking radius.	59
Figure 3.6	The analytical prediction of the rocking response of (a) <i>Abraham and Isaac</i> , and (b) <i>Zuccone</i> subject to (c) the acceleration history of Northridge earthquake at UCLA, scaled to a peak ground acceleration of 0.90g.	61
Figure 4.1	Conceptual design of experimental specimen and the range of the geometrically-variable statue-like structure.	71
Figure 4.2	Key dimensions of the experimental specimen configured symmetrically with a higher center of mass and eccentrically with a lower center of mass, shown in (a) elevation and (b) plan views. (c) Arbitrary two-dimensional block and geometric labels. All units in meters.	71
Figure 4.3	(a) Experimental setup including erect specimen and overturned specimen. (b) Elevation and plan views of the specimen indicating the primary directions and displacements. Note: θ_{xz} and θ_{xy} and Δx are referred to as “rocking”, “twisting”, and “sliding”, respectively.	75
Figure 4.4	Plan view of locations of cameras used.	77
Figure 4.5	Pseudo-spectral elastic acceleration of the target and achieved motions atop the shake table for (a) GM1A-C, (b) GM2A-C, (c) GM3, and (d) GM4 (refer to Table 4.3).	82
Figure 4.6	Acceleration time histories of the input motions as achieved on the shake table.	82
Figure 4.7	Example frames from top-view GOPRO: (a) distorted, color frame, and (b) undistorted, uncolored frame.	87
Figure 4.8	Motion tracking of specimen from top-view GOPRO: (a) original position of targets identified, (b) targets automatically detected in elliptical form for rotation calculations.	89
Figure 4.9	Time synchronization of potentiometer and camera data: (a) Original and down-sampled potentiometer data, (b) down-sampled potentiometer data and horizontal motion tracked by camera, (c) cross-correlation, and (d) synchronized time histories.	92
Figure 4.10	Time history responses of symmetric and in-plane eccentric configurations for (a) smaller, squatter configurations (L11, L31) and (b) larger, taller	

	configurations (U11, U31). The ‘L’ configurations are subject to GM1C and the ‘U’ to GM3-90%.....	94
Figure 4.11	Modal interaction diagrams for (a) slide-rock (M11, GM1A), (b) rock-twist (L12, GM3-225%), and (c) slide-twist (U13, GM3-175%).....	95
Figure 4.12	Bar charts of occurrence of rigid body modes categorized by horizontal eccentricity level for all configurations: (a) primary modes of rock, slide and twist, and (b) interactive modes of slide-rock, slide-twist, and rock-twist.	97
Figure 4.13	Scatter plots of the absolute maximum for (a) rocking, (b) sliding, and (c) twisting for each level of horizontal eccentricity for all configurations.	98
Figure 4.14	Scatter plots of the maximum (a) rocking and (b) sliding by direction of response for each level of horizontal eccentricity including all configurations. Note: A point was plotted only for input motions at the same scale for all configurations for consistency.	98
Figure 4.15	Bar charts of modal occurrences by the height of the center of mass (and frequency parameter p) for all configurations: (a) primary modes; (b) interactive modes. Note: An occurrence was counted only for input motions at the same scale for all configurations for consistency.....	101
Figure 4.16	Scatter plots of the maximum (a) rocking and (b) sliding by direction, for the eccentric (IP3) normalized by the symmetric (IP1) configurations for the same motion. Note: The amplification is limited to ± 5 ; although, larger amplifications are included in the statistics.	101
Figure 4.17	Rocking time history of the (a, c) symmetric ‘U’ and (b, d) symmetric ‘L’ configurations for the two pulse-like input motions.	103
Figure 4.18	Scatter plot of the maximum response of the specimen to GM1A ($T_p = 0.9s$) normalized by that of GM2A ($T_p = 1.8s$) for (a) rocking and (b) sliding. (c) Scatter plot of maximum rocking response of each configuration to total pulse motion, transient, and extracted pulse motions.....	104
Figure 4.19	Experimental free rocking behavior compared to the classical model: (a) decay of peak rocking amplitudes, and (b) rocking time history including simulation with theoretical and modified values of the velocity reduction factor (coefficient of restitution).	107
Figure 5.1	(a) Idealized dual-body system of arbitrary top-block geometry atop symmetric bottom block. Key dimensions shown in (b) elevation and (c) plan views. Notes: all units in meters, orange lines indicate marble interface, hatched lines indicate marble or steel interface.	116
Figure 5.2	Experimental setups: (a) single-body tests, and (b-c) dual-body tests with (b) tall pedestal and marble interface, and (c) squat pedestal on steel plate interface. (d) Low-friction steel plate interface in image and schematic forms. Note orange and hatched lines added for emphasis.	119
Figure 5.3	Nomenclature adopted to characterize the displaced shape of the dual-body system. Note that tower displacements are always taken relative to the pedestal, unless otherwise stated.....	120

Figure 5.4	Achieved acceleration on the shake table for each input motion during the dual-body tests. Note that the x-axis range for GM4 is double that of the other plots.....	121
Figure 5.5	Five percent damped elastic pseudo-spectral acceleration of the achieved input motions for (a) GM1, and (b) GM2-4.....	122
Figure 5.6	Pseudo-spectral acceleration (5% damped) of the target input motions overlaid with that of the mean achieved recording during both the single-body tests (phase-1) and the dual-body tests (phase-2).	124
Figure 5.7	(a) Maximum absolute acceleration, (b) pseudo-spectral acceleration averaged over $T = [0, 0.25]$ s, and (c) pseudo-spectral acceleration averaged over $T = [0.25, 0.50]$ s, against that of the peak target acceleration for each of the input motions for single- and dual-body tests.	125
Figure 5.8	(a) Experimental setup for the interface characterization tests, shown for the squat pedestal. (b) Free body diagram for the extraction of coefficient of friction.....	127
Figure 5.9	(a) Three trials of pull tests for the three interfaces at constant velocity (50 mm/s) after dynamic testing. (b) Comparison of extracted coefficients for each interface before and after dynamic testing.	127
Figure 5.10	Time history comparison of repeatability trials for L11sm configuration to GM1A.	129
Figure 5.11	Time history comparison of repeatability trials for L11tm configuration to GM1A.	129
Figure 5.12	Time history comparison of repeatability trials for L31sm configuration to GM1A.	130
Figure 5.13	Time history comparison of repeatability trials for L31tm configuration to GM1A.	130
Figure 5.14	Time history comparison of repeatability trials for U11sm configuration to GM1A.	133
Figure 5.15	Repeatability of various response quantities for pedestal and tower in which histograms of deviation from the median are presented.	134
Figure 5.16	Specimen U31sm (tall, eccentric tower atop squat pedestal with marble interface) subject to repeated trials of motion GM1A (1999 Duzce Earthquake at Bolu Station).	136
Figure 5.17	Typical repeatability tests for U31ss (tall, eccentric tower atop squat pedestal with steel plate interface) subject to GM2 (1989 Loma Prieta Earthquake at Gavilan College).	136
Figure 5.18	Scatter plot of maximum absolute (normalized) rocking, sliding, and twisting for individual motions and tower configurations atop the taller ('tm') pedestal versus that (top row) as a single-body ('np') and (bottom row) atop the squat ('sm') pedestal on the marble interface.	138
Figure 5.19	Time history of rocking for L31 (squat, eccentric) tower in (a) single-body, and (b) dual-body atop tall ('tm') pedestal with detail view of impact and (c)	

	schematic of impact. Note that the tower rocking is plotted absolutely and is not with respect to the pedestal.	140
Figure 5.20	Rocking, sliding, and twisting time histories for L11tm (squat, symmetric tower on tall marble pedestal) and U11tm (tall, symmetric tower on tall marble pedestal) subject to GM1A overlaid with response of single-body towers. Note that tower responses are absolute.	142
Figure 5.21	Scatter plot of maximum absolute rocking, sliding, and twisting for individual motions and towers atop the squat pedestal on steel plate interface ('ss') versus the marble interface ('sm'). Note: The thick grey line represents the marble-marble interfaces in schematics.	144
Figure 5.22	(top) Acceleration history of the shake table and squat pedestal on the steel plate interface ('ss') as well as (bottom) the tower rocking response, to GM1A and GM3.	144
Figure 5.23	Maximum sliding of a single test against the maximum rocking of the same test. Symbols correspond to a specific tower configuration and the color corresponds to the pedestal configuration.	146
Figure 5.24	Images of L11ss_mod1 configuration highlighting the restraint mechanism. ...	148
Figure 5.25	Time history of L11ss_mod1 configuration with response of L11ss to GM4 in terms of rocking, sliding, and twisting for (a-c) the pedestal and (d-f) the tower, as well as (g) acceleration of table.	149
Figure 5.26	Scatter plots comparing (a) maximum normalized rocking of the tower and (b) acceleration at the top of the tower in shaking direction for L11ss versus L11ss_mod1.	149
Figure 5.27	Maximum rocking and sliding of individual tower configurations for each of the four pedestal configurations versus the characteristic length of the input motion. Note that the trendlines correspond to individual configurations by color.	152
Figure 5.28	(a) Maximum sliding of SS pedestal versus the characteristic length of the input motion. (b) The maximum rocking of the tower on 'ss' pedestal normalized by that of the 'sm' pedestal versus the characteristic length of the input motions.	152
Figure 6.1	Schematics of an arbitrary rigid block overlaid with relevant geometric and mass parameters for (a) level interface and two rocking points, (b) singular interface defect and three rocking points, and (c) highly jagged interface and multiple rocking points.	163
Figure 6.2	Uplifted rigid block subjected to horizontal acceleration at the base.	165
Figure 6.3	Setup for free rocking tests of L11 configuration (see Chapter 4) with (b - c) highlights of the areas of no contact which allow a wobble mode to occur.	173
Figure 6.4	Experimental free rocking in (a) rotation and (b) rotational velocity, overlaid with the results of the classical model and the extended model with three rocking points (shown at right).	174
Figure 6.5	Velocity adjustment factor, r , for each rocking point as a function of aspect ratio for a symmetric, rectangular block with three rocking points, as shown	

	at right, where the height and width of the defect, are: (a) $0.025h$, $0.25B$, (b) $0.025h$, $0.45B$, (c) $0.05h$, $0.25B$, (d) $0.05h$, $0.45B$	176
Figure 6.6	Effective velocity adjustment factor for (a, c) impact at the defect (positive angular velocity) and (b, d) impact away from the defect (negative angular velocity) for the block at right with varying height and width of the defect.	179
Figure 6.7	Time history of free rocking of symmetric, rectangular block with aspect ratio of 2 and $R_I = 1$ m with and without a single interface defect, shown at right: (a) angular displacement, (b) angular velocity, and (c, d) detail inset of first two reversal events.	181
Figure 6.8	Time history of free rocking of symmetric, rectangular block with aspect ratio of 6 and $R_I = 1$ m with and without a single interface defect, shown at right: (a) angular displacement, (b) angular velocity, and (c) close-up of angular velocity for the first two reversals.	181
Figure 6.9	Velocity adjustment factor, r , as a function of the number of rocking points when the block is moving with (a, c) negative angular velocity and (b, d) positive angular velocity for aspect ratios of (a, b) 2 and (c, d) 8. Note that the color is mapped according to schematic at right.	183
Figure 6.10	Effective velocity adjustment factor, r , as a function of the number of rocking points (see schematic at right) for (a) negative angular velocity, and (b) positive angular velocity with detail view inset.	186
Figure 6.11	Time history of free rocking response of symmetric, rectangular block with an interface defect as shown at right with variable number of rocking points for (a, b) angular displacement and (c, d) angular velocity and aspect ratios (a, c) of 2 and (b, d) 6.	186
Figure 6.12	Overtuning spectra for a squat block ($H/B = 2$), where the defect is characterized as $0.25B$ and 0.3α for (a) two rocking points or no defect, (b) three rocking points, and (c) three rocking points with the sinusoidal input in the direction of the defect.	190
Figure 6.13	Overtuning spectra for a tall block ($H/B = 6$), where the defect is characterized as $0.25B$ and 0.3α for (a) two rocking points or no defect, (b) three rocking points, and (c) three rocking points with the sinusoidal input in the direction of the defect.	191
Figure 6.14	Geometry of baseline numerical model showing one part for each freestanding structure with variable discretization at the interface.	201
Figure 6.15	Penalty-based contact algorithm as utilized within LS-DYNA.	205
Figure 6.16	Flow chart of time stepping process in the developed LS-DYNA model: (a) primary steps, and (b) detailed steps.	208
Figure 6.17	Nodal penetration, contact force, and rigid body rocking of a tower with consistent interface stiffness and variable levels of contact damping over two cycles of rotational response.	212
Figure 6.18	Nodal penetration, contact force, and rigid body rocking of a tower with consistent interface stiffness and variable levels of contact damping for a detail view of a single impact event.	212

Figure 6.19	Nodal penetration, contact force, and rigid body rocking of a tower with consistent interface stiffness and variable levels of contact damping for a detail view of two nodal penetration events.	213
Figure 6.20	Nodal penetration, contact force, and rigid body rocking of a tower with consistent contact damping and variable levels of interface stiffness for two rocking cycles.	215
Figure 6.21	Nodal penetration, contact force, and rigid body rocking of a tower with consistent contact damping and variable levels of interface stiffness for a detail view of a single impact event.....	216
Figure 6.22	Rigid body rocking, contact force at the edge, nodal penetration, and the total slave mass in contact for various levels of discretization, where the discretization is listed with respect to the x-direction but is identical in the y-direction.	219
Figure 6.23	Rigid body rocking for a single impact event, contact force at the edge, nodal penetration, and the total slave mass in contact for various levels of discretization, where the discretization is listed with respect to the x-direction but is identical in the y-direction.	220
Figure 6.24	Nodal penetration for a single impact event of rocking at four discrete locations along the base of the rocking tower for variable levels of interface discretization.....	221
Figure 6.25	Detail drawing of the modeled interface of the tower during experimental model calibration.	225
Figure 6.26	Detail drawing of the base of the TM and SM pedestals as modeled during experimental model calibration.	225
Figure 6.27	Detail drawing of the top of the SM pedestal as modeled during experimental model calibration.	226
Figure 6.28	Detail drawing of the top of the TM pedestal as modeled during experimental model calibration.	226
Figure 6.29	Fitting of the friction parameter for the L11 configuration.	227
Figure 6.30	Comparison of experimental response of L11ss configuration (refer to Chapter 5) with numerical predictions utilizing the measured ($\mu_p = 0.15$, $\mu_t = 0.40$) and fitted ($\mu_p = 0.20$, $\mu_t = 0.35$) friction parameters.....	228
Figure 6.31	Modal interaction diagrams for sample test cases overlaid with numerical predictions for all interactive modes: (a) slide-rock, (b) slide-twist, and (c) rock-twist.	232
Figure 6.32	Experimental results versus numerical predictions utilizing average model for (a) peak rocking, (b) peak normalized rocking, (c) peak sliding, and (d) peak twisting.....	233
Figure 6.33	Experimental response versus numerical prediction for rocking and sliding time histories of the pedestal and tower of the U11tm configuration as well as the tower of the U11 configuration.....	236

Figure 6.34	Experimental response versus numerical prediction for rocking and sliding time histories of the pedestal and tower of the L31tm configuration as well as the tower of the L31 configuration.	237
Figure 6.35	Experimental free rocking of the L11 configuration overlaid with that of the classical model and the extended analytical model assuming a 1 mm warp.	237
Figure 6.36	Experimental free rocking of the L11 configuration overlaid with the results of the numerical model incorporating a flat interface as well as a warped interface of 1 mm.	237

LIST OF TABLES

Table 3.1	List of sites and surveyed statues in Florence, Italy.	44
Table 3.2	Summary of survey data and calculated geometric and mass properties for four statues using LiDAR _{1mm} meshes.	54
Table 3.3	Geometric and mass properties of four surveyed statues for rocking time history analysis in the transverse direction calculated using LiDAR _{1mm} meshes.....	57
Table 4.1	Geometric parameters of tested configurations.	72
Table 4.2	Specifications of cameras used and sample viewpoints.....	78
Table 4.3	Specifications of selected input motions.....	81
Table 5.1	Geometric and mass properties of the individual experimental specimens.	117
Table 5.2	List of tested configurations including tower and pedestal combinations.	117
Table 5.3	Input motions and select intensity characteristics, as achieved on the shake table for the dual-body tests.....	121
Table 6.1	Summary conclusions from shake table testing and analytical modeling with the corresponding implications on numerical model development.	196
Table 6.2	Implications of preliminary analyses on numerical modeling and treatment within the proposed numerical model.....	198
Table 6.3	Selected coefficients of static friction for single-body configurations	229
Table 6.4	Selected coefficients of static friction for dual-body configurations.....	229

NOMENCLATURE

The following section provides a list of variables and parameters used in this dissertation, in alphabetical order. Note that the base dimensions include: mass (M), force (F), length (L), and time (T).

<u>Symbol</u>	<u>Description</u>	<u>Base Units</u>
A		
A_p	Acceleration amplitude of sinusoidal pulse	L/T^2
b	Horizontal distance from edge to center of mass	L
b_{defect}	Width of geometric defect	L
B	Total width of the base of a freestanding structure	L
E	Young's modulus of elasticity	F/L^2
F_n	Resultant contact force normal to the master segment	F
F_R	Resultant contact force	F
h	Height to the center of mass from base of freestanding structure	L
h_{defect}	Height of geometric defect	L
H	Total height from the base of a freestanding structure	L
I	Mass moment of inertia	ML^2
K	Contact stiffness	F/L
K_b	Bulk modulus	F/L^2
L_c	Characteristic length of ground motion	L
m	Mass	M
n	Number of rocking points	Dimensionless
p	Frequency parameter for classical rocking model	$1/T$
PGA	Peak ground acceleration	L/T^2
PGD	Peak ground displacement	L
PDV	Peak ground velocity	L/T
PTA	Peak table acceleration	L/T^2
PTD	Peak table displacement	L
PTV	Peak table velocity	L/T
r	Velocity adjustment factor (or coefficient of restitution)	Dimensionless
R	Rocking radius	L
RP	Rocking point	Dimensionless

<u>Symbol</u>	<u>Description</u>	<u>Base Units</u>
T_p	Pulse period	T
V	Volume of a master element	L^3
VDC	Viscous damping coefficient for contact damping	Dimensionless
\ddot{x}_g	Horizontal acceleration of the ground	L/T^2
α	Slenderness (equivalent to θ_c)	Dimensionless
γ	Aspect ratio (height-to-width)	Dimensionless
Δ	Sliding or horizontal displacement	L
Δ_{node}	Penetration of a node into a master segment	L
μ	coefficient of friction	Dimensionless
θ	Angle of rotation of a freestanding structure	Dimensionless
θ_c	Critical angle or slenderness	Dimensionless
$\dot{\theta}$	Angular velocity of a freestanding structure	rad/T
$\ddot{\theta}$	Angular acceleration of a freestanding structure	rad/T^2
ρ	Mass density of a material	M/L^3
Φ	Rocking normalized by slenderness angle	Dimensionless
ω	Natural frequency of vibration	rad/T
ω_p	Angular frequency of pulse	rad/T

ACKNOWLEDGEMENTS

The research and experiments presented in this dissertation were supported by numerous individuals and organizations. First, I would like to express my sincere gratitude to my advisor, Professor Tara C. Hutchinson, for the granting me the opportunity and the freedom to a research an exciting and interdisciplinary topic. In addition, I am also indebted for the countless opportunities to learn from her as a researcher, including earthquake reconnaissance and field testing of statues. Professor Falko Kuester has also been a significant influence in my development as an interdisciplinary researcher and teacher. With his support, I have been able to travel and present my research internationally to diverse audiences, as well as to travel and collaborate during fieldwork in Florence, Italy, and San Francisco, CA. I would also like to thank my committee members, Professors Gilberto Mosqueda, Peter Shearer, and David Sandwell, for their time, dedication, and thoughtful insights throughout the preparation of this dissertation.

Shake table tests presented in this dissertation were conducted at the Charles Lee Powell Laboratory at UC San Diego. The efforts of the laboratory staff were instrumental in the successful completion of these campaigns, including Mr. Paul Greco, Dr. Chris Latham, Mr. Noah Aldrich, and Mr. Timothy McAuliffe. A special note of gratitude to Mr. Darren McKay who worked extensively with me in the implementation of these tests, and whose insights and suggestions were highly valued. Additionally, numerous fellow students assisted including Professor Richard Wood, Ms. Sara Grossi, Mr. Joshua Vallecillos, and Ms. Kay Do.

The fieldwork portions of this dissertation were made possible by the collaboration and dedication of many individuals and organizations including Ms. Alex Hubenko and Ms. Vanessa Pool of UC San Diego, Dr. Maurizio Seracini in Florence, Italy, Mr. Don Clyde and Mr. Paul Segas of EQX Global, Mr. Vincent Avalos of the Asian Art Museum, and Ms. Kim Cobb of the Smithsonian Institute. The distributed computing employed in large-scale parametric studies would

not have been possible without the guidance and assistance of Dr. Dan Crawl of the San Diego Supercomputer Center, Mr. Joe Keefe, Mr. John Graham, and Mr. Chris McFarland of the Qualcomm Institute. Also at UC San Diego, I would like to thank my classmates and fellow research students for their support and camaraderie including Professor Richard Wood, Dr. Weian Liu, Dr. Xiang Wang, Ms. Michelle Chen, Mr. Michael Hess, and Mr. Li Ge.

Finally, I would like to thank all of my family for their unending support, including my brothers Luke and Daniel, my parents, and my grandparents. Particularly, I would like thank my sister, Debbie, for welcoming me to San Diego, taking care of me when I was sick and injured on numerous occasions, always helping me move, and for genuinely being an incredible sister, role model, and friend. This dissertation is ultimately dedicated to my mother, Susan, for being the single-most influential person in my life. Thank you for everything, for raising four kids, and for always putting our education first. I can only hope to be half the woman that you are – thank you for everything.

The research program described in this dissertation was financially supported by the National Science Foundation under IGERT Award #DGE-0966375, “Training, Research, and Education in Engineering for Cultural Heritage Diagnostics.” Additional support for this research included the National Science Foundation under award #CNS-1338192, “MRI: Development of Advanced Visualization Instrumentation for the Collaborative Exploration of Big Data,” the UC San Diego Academic Senate, the Qualcomm Institute at UC San Diego, the Friends of CISA3, and the World Cultural Heritage Society. Additional fellowships which supported me throughout my graduate career include the Achievement Rewards for College Scientists (ARCS) Fellowship, the San Diego Diversity Fellowship, the Frontiers of Innovation Scholars Program Fellowship, and the NSF-IGERT Fellowship. Opinions, findings, and conclusions are those of the author and do not reflect those of the sponsoring agencies.

It is noted that multiple sections and chapters of this dissertation have been published or will be submitted for potential publication in technical journals or technical reports. The dissertation author was the first author and primary investigator for each of these publications. Each is summarized in the following paragraphs.

Chapter 3, in part, is a reprint of the material as it appears in the Journal of Computing in Civil Engineering, a technical journal of the American Society of Civil Engineers. Wittich, C.E., Hutchinson, T.C., Wood, R.L., Seracini, M., and Kuester, F. (2016). “Characterization of full-scale, human-form, culturally important statues: case study.” *J. Comput. Civ. Eng. (ASCE)*, 30(3), 05015001.

Chapter 4, in part, is a reprint of the material as it appears in Earthquake Engineering and Structural Dynamics. Wittich, C.E. and Hutchinson, T.C. (2015). “Shake table tests of stiff, unattached, asymmetric structures.” *Earthquake Eng. Struct. Dyn.*, 44(14), 2425-2443.

§4.2.5, 4.2.7, and 4.3 are based upon a technical report as it appears in the Structural Systems Research Report Series. Wittich, C.E. and Hutchinson, T.C. (2014). *Shake Table Tests of Stiff, Unattached, Asymmetric Structures – Phase 1: Floor-Mounted*. Structural Systems Research Project Report Series, SSRP-2013/18, Department of Structural Engineering, University of California, San Diego, La Jolla, CA.

Chapter 5, in part, has been submitted for publication of the material as it may appear in Earthquake Engineering and Structural Dynamics. Wittich, C.E. and Hutchinson, T.C. (201X). “Shake table tests of unattached, asymmetric dual-body systems.” *Earthquake Eng. Struct. Dyn.*

§5.2, 5.4, and 5.5.5 are based upon a technical report as it appears in the Structural Systems Research Report Series. Wittich, C.E. and Hutchinson, T.C. (2015). *Shake Table Tests of Stiff, Unattached, Asymmetric Structures – Phase 2: Pedestal-Mounted*. Structural Systems Research

Project Report Series, SSRP-2015/05, Department of Structural Engineering, University of California, San Diego, La Jolla, CA.

Chapter 6, in part, has been submitted for publication and is currently being prepared for submission of the material in two separate manuscripts. The first has been submitted for publication of the material as it may appear in *Earthquake Engineering and Structural Dynamics*. Wittich, C.E. and Hutchinson T.C. (201X). “Rocking blocks with geometric interface defects: analytical development and experimental verification.” *Earthquake Eng. Struct. Dyn.* The second is currently being prepared for submission for publication of the material. Wittich, C.E. and Hutchinson T.C. (201X). “Multi-physics model for the seismic response of rigid, freestanding structural systems.”

VITA

EDUCATION

- 2010 B.S., Civil and Environmental Engineering, summa cum laude with honors
Lafayette College, Easton, PA
- 2012 M.S., Structural Engineering
University of California, San Diego, La Jolla, CA
- 2016 Ph.D., Structural Engineering
University of California, San Diego, La Jolla, CA

AWARDS & FELLOWSHIPS

- 2011-2015 San Diego Diversity Fellowship
- 2015 Association for Women in Science San Diego Scholarship
- 2010-2016 NSF-IGERT Fellowship
- 2015-2016 Achievement Rewards for College Scientists Scholar
- 2016 Frontiers of Innovation Scholars Program Fellowship

PUBLICATIONS

Journal Papers (In Print)

- Wittich, C.E.** and Hutchinson, T.C. (2016). “Experimental modal analysis and seismic mitigation of statue-pedestal systems.” *J. Cult. Herit.*, 20(1), 641-648.
- Wittich, C.E.**, Hutchinson, T.C., Wood, R.L., Seracini, M., and Kuester, F. (2016). “Characterization of full-scale human-form culturally important statues: case study.” *J. Comput. Civ. Eng. (ASCE)*, 30(3), 05015001.
- Wittich, C.E.** and Hutchinson, T.C. (2015). “Shake table tests of stiff, unattached, asymmetric structures.” *Earthquake Eng. Struct. Dyn.*, 44(14), 2425-2443.

Journal Papers (In Review and Preparation)

- Wittich, C.E.** and Hutchinson, T.C. (201X). “Shake table tests of unattached, asymmetric dual-body systems.” *Earthquake Eng. Struct. Dyn.* (Submitted 01/2016, Revised 08/16).
- Wittich, C.E.** and Hutchinson, T.C. (201X). “Rocking blocks with geometric interface defects: analytical development and experimental verification.” *Earthquake Eng. Struct. Dyn.* (Submitted 08/16).
- Wittich, C.E.** and Hutchinson, T.C. (201X). “Development and validation of a multi-physics model for freestanding structural systems.” *J. Earthq. Eng.* (In Preparation).

Technical Reports

- Wittich, C.E.** and Hutchinson, T.C. (2015). *Shake Table Tests of Stiff, Unattached, Asymmetric Structures – Phase 2: Pedestal-Mounted*. Structural Systems Research Project Report Series. SSRP 15/05. Department of Structural Engineering, University of California, San Diego, La Jolla, CA.
- Wittich, C.E.**, Hutchinson, T.C., Lo, E., Meyer, D., and Kuester, F. (2014). *The South Napa Earthquake of August 24, 2014: Drone-based Aerial and Ground-based LiDAR Imaging Survey*. Structure Systems Research Project Report Series. SSRP 14/09. Department of Structural Engineering, University of California, San Diego, La Jolla, CA.
- Wittich, C.E.** and Hutchinson, T.C. (2014). *Shake Table Tests of Stiff, Unattached, Asymmetric Structures – Phase 1: Floor-Mounted*. Structural Systems Research Project Report Series. SSRP 13/18. Department of Structural Engineering, University of California, San Diego, La Jolla, CA.
- Wittich, C.E.**, Hutchinson, T.C., Wood, R.L., and Kuester, F. (2012). *Survey and Characterization of Culturally Important Statues in Florence, Italy*. Structural Systems Research Project Report Series. SSRP 12/10. Department of Structural Engineering, University of California, San Diego. La Jolla, CA.

Refereed Conference Proceedings

- Wittich, C.E.** and Hutchinson, T.C. (2017). “Experimental validation of a multi-physics model for the seismic response of freestanding structural systems.” *Proc., 16th World Conference on Earthquake Engineering*, Santiago, Chile, 1-10.
- Meyer, D., Hess, M., Lo, E., **Wittich, C.E.**, Hutchinson, T.C., and Kuester, F. (2015). “UAV-based assessment of cultural heritage sites following the 2014 South Napa Earthquake.” *Proc., International Congress on Digital Heritage*, Granada, Spain, 1-4.
- Wittich, C.E.** and Hutchinson, T.C. (2015). “Dynamic characterization and 3D reconstructions of massive human-form archaeological statues for earthquake loading.” *Proc., 43rd Conference on Computer Applications and Quantitative Methods in Archaeology*, Siena, Italy, 106-106.
- Wittich, C.E.** and Hutchinson, T.C. (2014). “Development of a rocking-period centered protocol for shake table testing of unattached stiff components.” *Proc., 10th National Conference in Earthquake Engineering*, Anchorage, AK, 1-11.
- Wittich, C.E.** and Hutchinson, T.C. (2013). “Computing geometric and mass properties of statues for rigid body rocking analysis.” *Proc., ASCE International Workshop on Computing in Civil Engineering*, Los Angeles, CA, 810-817.
- Wittich, C.E.**, Hutchinson, T.C., Wood, R.L., and Kuester, F. (2012). “A method for an integrative documentation and characterization of culturally important statues for seismic analysis.” *Proc., 4th Euro-Mediterranean Conference on Cultural Heritage*, Lemesos, Cyprus, 825-832.
- Wood, R.L., Hutchinson, T.C., **Wittich, C.E.**, and Kuester, F. (2012). “Characterizing cracks in the frescoes of Sala degli Elementi within Florence’s Palazzo Vecchio.” *Proc., 4th Euro-Mediterranean Conference on Cultural Heritage*, Lemesos, Cyprus, 776-783.

ABSTRACT OF THE DISSERTATION

Seismic Response of Freestanding Structural Systems: Shake Table Tests and Model Validation

by

Christine Erin Wittich

Doctor of Philosophy in Structural Engineering

University of California, San Diego, 2016

Professor Tara C. Hutchinson, Chair

Systems of unattached, or freestanding, structures are highly vulnerable to sliding and/or overturning when subject to seismic excitation. This class of structures includes many rigid and heavy systems such as classical multi-drum columns, statue-pedestal systems, and various building contents. Damage to these structures can result in loss of irreplaceable heritage, limited functionality of critical facilities, and even loss of life. As a result, accurate predictions of their response are essential. However, traditional analytical methods cannot be feasibly extended to account for the multiple modes engaged during the excitation, the three dimensional nature of the body, and (if present) additional blocks in a system. All of which may be necessary to model realistic structures.

In an effort to develop robust predictive tools for freestanding structural systems, three research objectives are addressed in this dissertation. The first is to understand the general geometric and mass characteristics of freestanding structural systems. This was accomplished through a field survey targeting the geometrically complex statue-pedestal system. The geometry of these structures was captured using light detection and ranging scanning and computer vision techniques. The resulting range of geometry guided the design of two phases of shake table testing addressing the second objective, which is to generate a comprehensive database of the experimental response of freestanding structural systems. In these tests, a tower structure, which was adaptable to a variety of geometries and mass configurations, was subject to seismic excitation in unanchored single-body and dual-body arrangements. Test results emphasize the multi-modal and three-dimensional nature of the seismic response of these systems.

The final objective is to develop and validate a numerical model for predicting the seismic response of freestanding structures. This model was developed utilizing the contact-impact capabilities within the multi-physics solver, LS-DYNA. An analytical extension was developed in conjunction with the numerical model accounting for warped interfaces, an aspect that was revealed to have a pronounced effect on the response. The numerical model was validated against the experimental results, with particular attention given to capturing the multi-modal and multi-body behavior. Numerical simulations indicate that this model can be used to predict the dynamic response of freestanding structures with high fidelity.

Chapter 1 Introduction

1.1 Motivation

A freestanding structural system is defined as any component or structure that is unanchored, or unattached, to another component or structure. This general class of structures encompasses a wide variety of everyday, critical, and unique components. Structures of cultural importance are often of this category, the most common including classical multi-drum columns and stone statue-pedestal systems. These culturally, nationally, or religiously significant artifacts have an impact on people and fields of study around the world; and, in many cases, are irreplaceable. Another subset of freestanding structures includes building contents and other components that support a facility's operations, including mechanical and electrical equipment, stacked computer systems, laboratory and office equipment, nuclear radiation shields, and switchboard cabinets. The importance of these structures increases with the criticality of the facility, most notably for schools, hospitals, nuclear power plants, and nuclear storage facilities. A similarly critical subset of freestanding structures includes historic stone buildings and unreinforced masonry walls, which are common throughout the world and typical of residential construction.

Freestanding structural systems represent a very broad classification of structures, which impact cultural heritage, critical facility functionality, and residential construction. However, these structures have been observed to perform quite poorly during even moderate seismic excitation. Figure 1.1 presents four example images taken post-earthquake during reconnaissance, which emphasize the multitude of structural types affected. Specifically, in this figure, an overturned and heavily damaged stone statue is shown following the M_w 6.3 2011 Christchurch earthquake. This example shows the loss of irreplaceable cultural heritage. This is juxtaposed with the collapse of

an unreinforced masonry wall of a residence, in which each of the individual masonry blocks is a freestanding structure. This collapse had the potential to injure occupants or even cause loss of life, in addition to the ‘red-tagging’ and need for demolition. Further examples in Figure 1.1 include the loss of components that support the functionality of a facility, namely overturned transformers at a power plant following the M_w 7.5 2003 Colima earthquake, and overturned office equipment at a high school following the M_w 6.0 2014 South Napa earthquake.

Following a number of recent earthquakes, freestanding structures have overturned resulting in loss of cultural heritage, reduced functionality of a facility, and potential for loss of life and injury. However, these systems have additionally been observed to respond with numerous failure modes and in complex patterns (Wittich et al. 2014). This is highlighted in the post-earthquake reconnaissance images in Figure 1.2. Specifically, the first image in this figure shows an electrical transformer which did not overturn following the M_w 6.0 2014 South Napa earthquake; rather, it translated and twisted during the event. This resulted in the component being ‘red-tagged’ as its internal components were compromised, and the residential apartment complex had reduced functionality following the disaster. In addition to this transformer, a statue was observed to have overturned from its pedestal during the same event. However, upon inspection of the statue’s original orientation as seen in the inset image, the statue twisted 180° about its vertical axis at some point during the earthquake excitation. A final example, Figure 1.2c, shows a number of tombstones in a cemetery following the M_w 5.8 2011 Virginia earthquake. Specifically, the two tombstones in the foreground overturned in opposite directions, and a third tombstone in the background of the image did not overturn at all – highlighting the complexities of a seemingly simple structural system.

In conclusion of the motivation, freestanding structural systems encompass a very broad array of everyday, critical, and culturally significant components and structures. However, these

systems have been observed to perform quite poorly during earthquake excitation, which can lead to loss of irreplaceable heritage, reduced functionality of a critical facility, and even loss of life. Therefore, there is a critical need to accurately predict the seismic response of freestanding structural systems. This critical need motivates the research presented in this dissertation, which aims to develop tools capable of predicting the dynamic response of freestanding systems, such that protective measures can be taken.

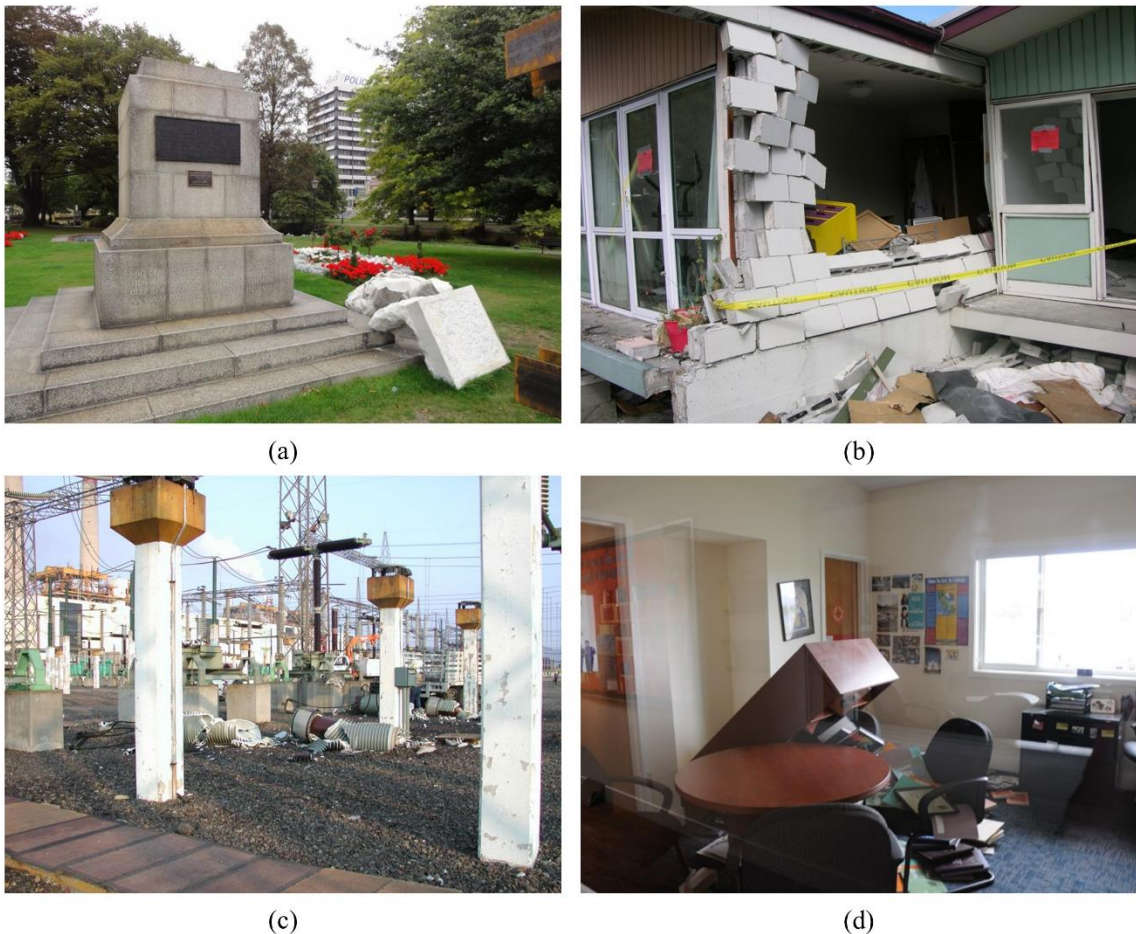


Figure 1.1 Post-earthquake reconnaissance of various freestanding structural systems. (a) Overturned statue following 2011 Christchurch earthquake (Photo courtesy of EERI Photo Galleries (EERI, 2015)); (b) Collapse of unreinforced masonry wall following 2011 Christchurch earthquake (Photo courtesy of EERI Photo Galleries (EERI, 2015)); (c) Overturned transformers at a power plant following 2003 Colima earthquake (Photo courtesy of EERI Photo Galleries (EERI, 2015)); and, (d) Overturned office equipment following 2014 South Napa earthquake (Photo courtesy of Justin Siena High School (Wittich et al, 2014)).



(a)



(b)



(c)

Figure 1.2 Post-earthquake freestanding structures emphasizing complex dynamics. (a) Electrical transformer that translated and twisted during the 2014 South Napa earthquake (Wittich et al. 2014); (b) Statue that overturned and twisted 180° about the vertical, as seen by the original placement in the inset photo (Wittich et al. 2014); and, (c) Tombstones following the 2011 Virginia earthquake, where the two tombstones in the foreground overturned in opposite directions and the tombstone in the background did not overturn (Photo courtesy of the EERI Photo Galleries (EERI, 2015)).

1.2 State of Understanding

While a critical need to accurately predict the seismic response of freestanding systems has been identified, existing analysis methods are quite limited. In an effort to further motivate the research presented herein, the current state of understanding is documented in this section. However, a detailed review of the literature including analytical, experimental, and numerical studies is included in the following chapter.

The earliest research in this area is typically accredited to Housner (1963), in which the equation of motion for a freestanding, two-dimensional, rectangular, rigid block is derived. A schematic of this block, which is frequently referred to as an inverted pendulum, is included in Figure 1.3. The classically derived equation of motion assumes: 1) the block and the foundation are rigid; 2) the block is always in contact with the foundation with instantaneous change of pivot points; 3) the block does not translate horizontally (no sliding); and, 4) energy is lost only at instantaneous, perfectly inelastic impacts modeled through a coefficient of restitution, which is a function solely of geometry. It can be seen in Figure 1.3, that the equation of motion and the coefficient of restitution are both nonlinear with respect to the geometry and orientation of the block. As such, linearization of this model is not recommended if the block is not exceedingly slender. However, in an effort to derive overturning criteria for the block subject to ground acceleration, Housner linearized the equations which revealed that the larger of two blocks (larger R) of equal slenderness (equal θ_c) was inherently more stable.

The classically derived model for two-dimensional rigid body rocking has formed the basis of a number of studies. Notably, Yim et al. numerically integrated the classically derived equations of motion subject to earthquake excitation and observed that the rocking response was very sensitive to small changes in geometry and input motion (Yim et al. 1980). In addition, Yim et al. concluded that the stability of a block does not necessarily increase monotonically with increasing

size or decreasing slenderness due to this high level of sensitivity. Furthermore, it was noted that vertical motion similarly does not have a systematic trend on the overturning and rocking response. Ishiyama (1982) extended the classical derivation to account for sliding and free flight (separation of the block from the foundation), which was followed by Shenton and Jones who derived equations of motion for the simultaneous response of the two-dimensional block in two modes, namely the slide-rocking mode (Shenton and Jones 1991). In further attempts to extend the classical model, Konstantinidis and Makris (2007) as well as Zulli et al. (2012) derived the equations of motion under similar assumptions as Housner for the rocking motion of a three-dimensional rectangular, rigid block. These studies emphasized the inability of the two-dimensional model to holistically capture the dynamics of the problem when in the presence of geometric eccentricity or non-planar base excitation. Furthermore, it was concluded that the numerical integration of the three-dimensional equations of motion is significantly cumbersome and not feasibly extended to additional modes of response or systems of multiple rigid blocks. A similar conclusion was found by Psycharis (1990) who presented the equations of motion for rocking of a two-dimensional, rectangular, symmetric, dual-block system. This system has four possible modes of rocking response, each with two equations of motion depending upon the direction of block rotation. These modes are free to transition throughout a single simulation, where transitions may occur with or without an impact event adding to the complexity of the integration and the solution.

Aforementioned classical derivations have provided a significant understanding of the dynamics and sensitivity of freestanding structures through the examination of the classically derived equations of motion and its extension to additional modes, dimensions, and number of blocks. However, it is not feasible to extend the classical model to account for all of these additional variables simultaneously, which is necessary for the study of realistic structural systems. For this reason, numerical modeling techniques have been recommended for exploration (e.g. Spanos et al. 2001). This is further compounded by the need to relax many of the original assumptions of the

classical model, specifically, that the blocks and foundation are rigid and that energy dissipation is solely a function of geometry. Recent efforts have studied the efficacy of spring elements to represent the contact between the block and its foundation, as well as between multiple blocks in higher-order systems (e.g. Winker et al. 1995; Papantonopoulos et al. 2002; Chatzis and Smyth 2011; DeJong and Vibert 2012). This modeling technique can account for energy dissipation at impacts as well as allowing for sliding and complete separation of the blocks. While certain studies have explicitly incorporated these springs within a classical dynamics approach (e.g. Chatzis and Smyth 2012), many have sought to utilize existing, specialized discrete element method platforms (e.g. Lemos 2007; Peña et al. 2007).

In an effort to develop more robust predictive tools for the seismic response of freestanding structural systems, numerical modeling techniques have been identified to account for realistic structures which require the incorporation of multiple modes, dimensions, and blocks in a system. While a number of numerical techniques can be studied for applicability, all approaches, including the analytical models, must be validated against experimental response data. One of the earliest experimental campaigns focused on the free rocking response of single rigid blocks with various slenderness angles, which highlighted the significance of bouncing and twisting, even for symmetric structures (Lipscombe and Pellegrino 1993). More recently, Konstantinidis and Makris (2009) conducted shake table tests of realistic freestanding structures, including large laboratory equipment, in which the flexibility of the legs and sliding mechanisms were found to be significant. A more recent experimental campaign studied the response of a multi-body system, which observed the heavy presence of multiple modes and three-dimensional effects (Drosos and Anastasopoulos 2014). While these tests have highlighted the multi-modal and three-dimensional behavior of freestanding structures, they have been limited with respect to the geometries tests and a broader experimental investigation is warranted.

The multitude of analytical studies on the classical dynamics of freestanding structures has generated an understanding of the geometrically nonlinear problem and its high sensitivity to small perturbations. Furthermore, even minor extensions of the model to a third dimension, a second response mode, or a second block in the system increase the complexity of the solution exponentially. As such, it is not feasible to combine these extensions in an analytical framework to model realistic structures. Therefore, numerical models must be explored, which require the results of experimentation for calibration and validation. Given the known nonlinearities of freestanding structures with respect to geometry, experimental data must be available across a broad range of geometric configurations. This dissertation aims to complement existing experimental data to address this need, and contribute to the overarching effort to develop predictive numerical tools for freestanding structural systems.

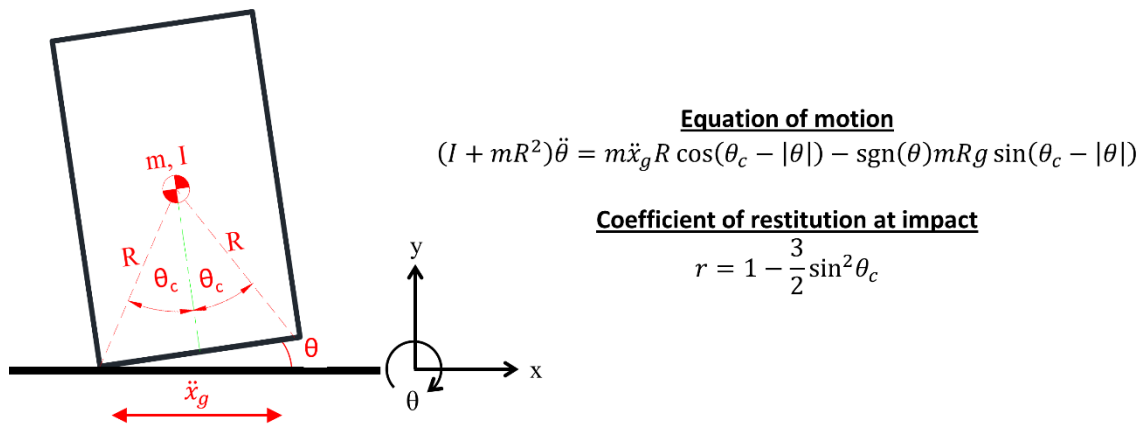


Figure 1.3 Schematic of the classical two-dimensional, rigid, rocking block subject to ground acceleration with the classically-derived equation of motion and the coefficient of restitution as originally presented in Housner (1963). Note all parameters of the classical equation of motion for rocking are defined in the schematic on the left.

1.3 Scope of Research

This dissertation aims to address three primary research objectives in the effort to further understand and develop predictive tools for the study of freestanding structural systems subject to earthquake loads. The first objective is to quantify and bound a range of geometry of freestanding structural systems, including the most extreme cases. The second objective is to generate a comprehensive database of the experimental response of freestanding structural systems subject to seismic excitation, across the range of anticipated geometries and configurations. The results of which are directly used in the development and validation of a numerical model for the prediction of the seismic response of freestanding structural systems with arbitrary geometry, which addresses the third and final objective of this research. To address these objectives, three distinct phases of research are outlined in this dissertation, namely: 1) a field survey, 2) shake table testing, and 3) numerical modeling.

1.3.1 Scope of Field Survey

The first phase of research presented in this dissertation focuses on the characterization of freestanding structural systems and the quantification of a range of geometry. Freestanding structures are known to respond to seismic excitation with a geometrically nonlinear motion. As such, the target of this field survey focused on statue-pedestal systems in Florence, Italy, which have complex and nonsystematic geometries. In addition, these culturally significant structures are irreplaceable and critical to understand and protect. The statues surveyed were limited to monolithic, homogenous, stone construction, as determined in consult with art historians, which yielded a sample size of twenty-four statues.

The survey included observations of geometry, materials, friction, and boundary conditions including pedestals. Geometric data was acquired using two non-contact methods for comparison, namely light detection and ranging (LiDAR) and structure-from-motion (SfM). Both of these

techniques yield a three-dimensional point cloud, which can subsequently be processed into a watertight, triangulated surface mesh for computation of geometric and mass properties. The results of this geometric survey yielded a range of extreme geometries to be anticipated for statues, with significant levels of asymmetry observed.

1.3.2 Scope of Shake Table Testing

Given the results of the aforementioned field survey, a range of geometries was selected in an effort to bound the survey results, which was subsequently incorporated in the design of a freestanding, geometrically-variable test specimen. This stiff, statue-like tower was capable of representing freestanding bodies with rocking radii, R , ranging from 0.7 m – 1.6 m and slenderness, θ_c , ranging from 9° to 35° , where these parameters are shown schematically in Figure 1.3. Furthermore, this tower was outfitted with a bonded marble base resting freely atop a fixed marble slab on a uniaxial shaking table to account for the stone-stone interfaces anticipated for statue-pedestal systems. A total of fifteen unique tower configurations were tested as single-body systems, while a subset of four of these configurations were tested in dual-body systems, as seen in Figure 1.4. A total of two geometric variations of the ‘pedestal’ or bottom body were incorporated into the dual-body systems with heights to the center of mass ranging from 0.38 m – 0.76 m. In addition, the material at the base of this pedestal was varied between marble and a low-friction steel plate. These geometric and material variations yielded a total of twenty-seven unique freestanding structural systems. The test results were intended to validate subsequent numerical modeling tools; and, thus, needed to capture the expected modes of response as well as the demand amplitudes under realistic earthquake motion scenarios. As such, the fully three-dimensional response of the various test configurations subject to recorded earthquake motions was measured in addition to free rocking and sliding motions.

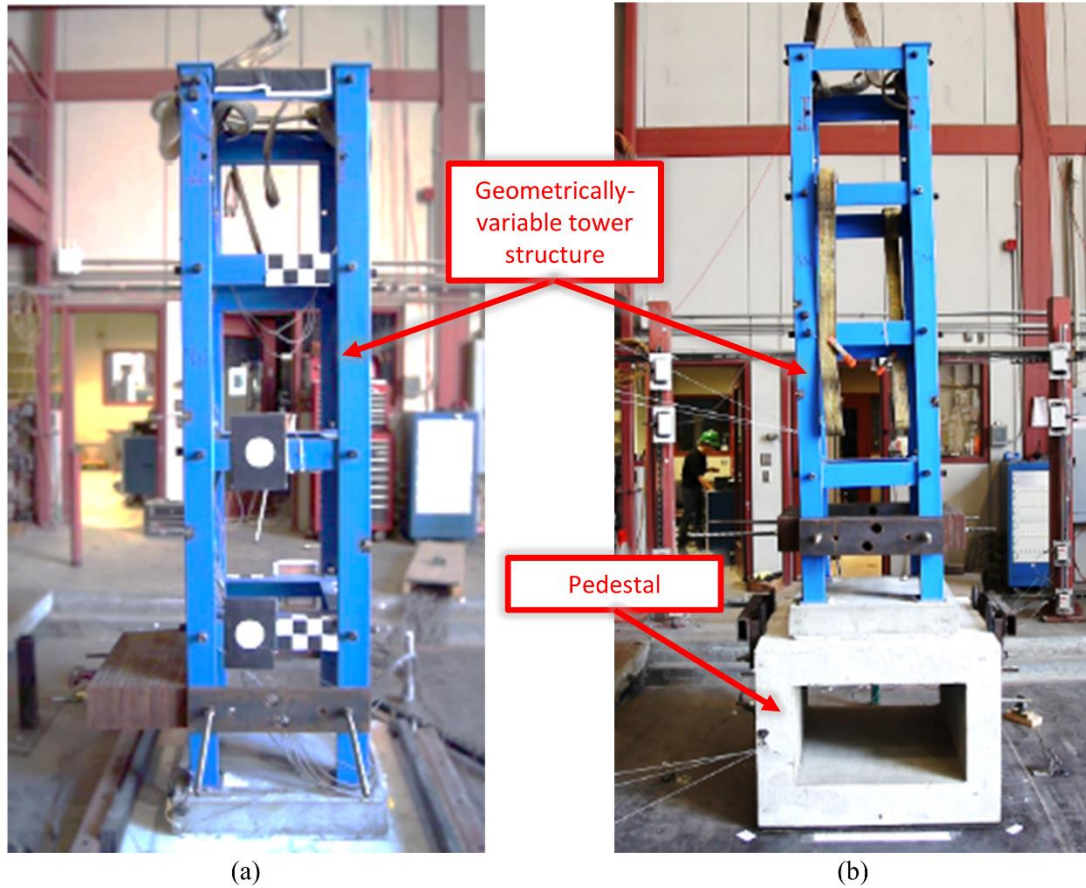


Figure 1.4 Experimental setup for: (a) single-body tests and (b) dual-body tests.

1.3.3 Scope of Numerical Modeling

The numerical model detailed in this dissertation is developed in the widely-utilized, commercially-available, explicit multi-physics solver, LS-DYNA (LSTC 2013). This model is based on similar principles as other recent studies in the literature (e.g. Lemos 2007, and those cited therein). Specifically, rigid body dynamics is utilized to model the large displacement and rotation behavior of the individual bodies in the simulation, and the interaction between these bodies is modeled using a penalty-based contact algorithm. This algorithm generates forces of contact through normal and transverse spring and dashpot elements that exist only at the time and location of detected contact. Therefore, this model is intended to capture rocking, sliding, and complete

separation of the individual bodies of a freestanding system. The proposed numerical model is calibrated using the results of free rocking and sliding tests, and validated with respect to the multi-modal and multi-body dynamic responses captured during shake table testing. Furthermore, this approximate model is validated with respect to the classically-derived rocking dynamics. Since this model is validated across a broad range of geometry, it can be used extensively in further studies for many types of structural systems including, but not limited to, culturally significant statues, precariously balanced rocks, and structural columns.

1.4 Organization of Dissertation

This dissertation consists of seven chapters. This chapter motivates the study of freestanding structural systems, details the current state of understanding of their seismic response, and presents the primary research objectives and scope of the dissertation. Chapter 2 provides a detailed review of the literature with respect to analytical, experimental, and numerical studies of the dynamics of freestanding structural systems. Chapter 3 presents an extensive field survey of culturally significant stone statue-pedestal systems, the most geometrically complex freestanding structural system. Chapter 4 introduces the design of a shake table testing campaign on single-body freestanding structures and analyzes the results in the context of variable geometry and mass eccentricity. Chapter 5 extends the previous shake table tests to incorporate dual-body systems and variable friction interfaces. Chapter 6 presents the development of a numerical model for the seismic response of freestanding structural systems, as well as the calibration and validation of this model utilizing the results of both phases of shake table testing. Chapter 7 concludes this dissertation with a summary of the primary contributions and recommends areas for further research.

Chapter 2 Research Background and Prior Work

The dynamics of freestanding structures has been studied in many contexts, including water towers, tombstones, statues, and bridge piers. The majority of the early studies were purely analytical; and, as such, incorporated a number of idealizations and assumptions that have limited its extensibility to realistic structures. The necessary simplifications for analytical studies, compounded by the cumbersome and complex formulations, warrant the exploration of numerical studies. While a number of recent numerical models have emerged for the study of freestanding structures, calibration and validation of these models require experimentation of realistic systems. To date, a handful of experimental campaigns have been conducted on these systems; however, these tests have focused on specific geometries or structures of interest, which limits the extensibility of the results and provides a significant motivation for this dissertation. As a result, this chapter first focuses on the pioneering analytical studies and lessons learnt, followed by a detailed discussion of the key findings and limitations of recent experimental campaigns, and ultimately this chapter concludes by describing state-of-the-art numerical models for freestanding structural systems.

2.1 Pioneering Analytical Studies

This section details the derivation of the classical equations of motion for a two-dimensional rigid rocking block and the lessons learnt from its study. Further sub-sections aim to detail the many extensions of this model that have been presented in the literature over the course of the past few decades including extensions to additional modes of response other than rocking, additional dimensions, additional bodies, and the relaxation of the rigid-body, rigid-foundation assumption. However, it is emphasized that the extensions to the classical model are not cumulative; rather, each has been investigated independently to study the dynamic implications.

The combined effects of these additional variables are not feasibly studied in an analytical context, and motivate the study of numerical models.

2.1.1 Classical Model

While observations of overturning and studies on rigid body dynamics had been conducted since the 19th century (e.g. Perry 1881; Kirkpatrick 1927), the landmark study of Housner (1963) presents a detailed analysis of the piecewise equation of motion for the two-dimensional rectangular rigid block. In this dissertation, the analytical model presented by Housner is referred to as the classical model. The classical model considers the two-dimensional rigid block in Figure 2.1, which is characterized by mass m , mass moment of inertia about the centroid I , rocking radius R , slenderness θ_c , ground acceleration \ddot{x}_g , and two discrete rocking points. The derivation of the equations of motion assumes the following:

1. the block and foundation are perfectly rigid;
2. the block maintains constant contact with the foundation (no uplift and instantaneous change of pivot points);
3. the block does not translate horizontally (sufficiently high friction to preclude sliding); and,
4. energy is dissipated only at instantaneous, perfectly inelastic impacts.

Under these assumptions, the equation of motion for a rocking mode is derived by summing the moments about either rocking point which yields a piecewise differential equation:

$$\left(\frac{I}{m} + R_i^2\right) \cdot \ddot{\theta} = \ddot{x}_g \cdot R_i \cdot \cos(\theta_{c,i} - |\theta|) - \text{sgn}(\theta) \cdot R_i \cdot g \cdot \sin(\theta_{c,i} - |\theta|) \quad (2.1)$$

where the double-dot represents the second derivative with respect to time, $\text{sgn}(\theta)$ is the Signum function, and $i = 1$ or $i = 2$ corresponds to rocking about RP_1 or RP_2 , respectively.

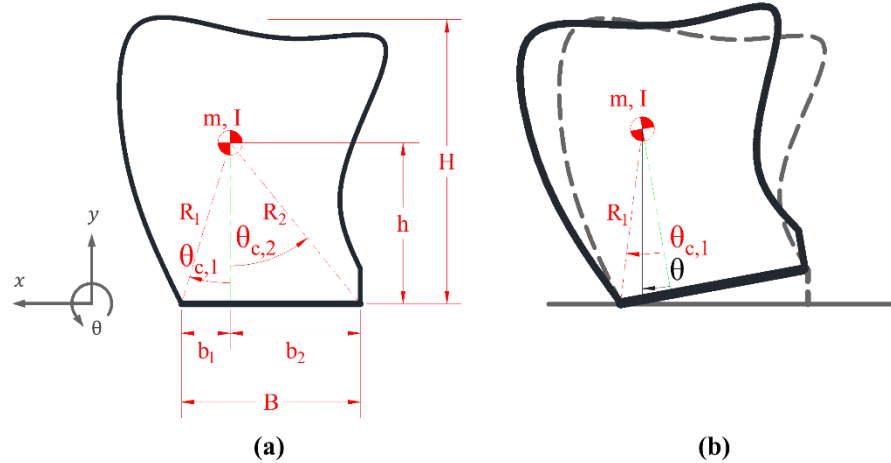


Figure 2.1 Schematic of two-dimensional, arbitrary geometry, rigid, rocking block with two distinct rocking points: (a) nondisplaced and (b) displaced.

Once the block is rotated, the block will either overturn or return to equilibrium position. In the latter case, the block will impact the foundation causing dissipation of the block's kinetic energy. The model assumes that this transition from RP_1 to RP_2 is smooth, experiences no bouncing, and is an instantaneous impact. The reduction of the kinetic energy of the block at impact is derived through conservation of momentum about the rocking point immediately before and after the impact. This yields a velocity ratio, commonly referred to in the analytical literature as a "coefficient of restitution", which for the rigid block of interest is:

$$r_i = \frac{1}{\left(\frac{I}{m} + R_i^2\right)} \cdot \left[\left(\frac{I}{m} + R_j^2\right) - B \cdot R_j \cdot \sin(\theta_{c,j}) \right] \quad (2.2)$$

where $i = 1, j = 2$ for impact about RP_1 and $i = 2, j = 1$ for impact about RP_2 . Note that the energy dissipation modeled in the coefficient of restitution is only a function of geometry and does not account for any material effects.

Given the nonlinearity of the equations of motion and energy dissipation, linearization of the problem is not typically done. However, in the absence of sufficient computational capabilities, Housner studied the linearized equations for very slender blocks. In an effort to derive overturning

criteria for the block subject to ground acceleration, Housner revealed that the larger of two blocks (larger R) of equal slenderness (equal θ_c) was inherently more stable. In addition, the overturning can be correlated with strong velocity pulses.

Analyses of the rocking block subject to earthquake motion, not considering linearization, requires numerical integration at fairly small time steps due to the discontinuity at impact. To this end, the governing differential equation can be cast in a state-space formulation to allow the use of standard solvers for ordinary differential equations. Commonly, the equation is solved using a 4th-5th order Runge-Kutta scheme. During the solution, the velocity reduction is applied using Equation (2.2) at every detected impact or zero-crossing. The first major contribution considering the complete numerical integration of the non-linearized equation of motion was presented by Yim et al. (1980). This study built upon the original conclusions of Housner's work. Notably, it was observed that the rocking response was very sensitive to small changes in geometry and input motion. Additionally, it was concluded that the stability of a block does not necessarily increase monotonically with increasing size or decreasing slenderness due to this high level of sensitivity. Furthermore, it was noted that while vertical motion may have a significant impact on an individual simulation, it does not systematically affect the overturning and rocking response.

2.1.2 Extension of Classical Model for Alternative Modes of Response

The first significant extension to the classical model aimed to incorporate additional modes of response, namely sliding and uplift (jump). This extension specifically relaxed the second and third assumptions of the classical model. Ishiyama (1982) first identified the six possible modes of response for a single, two-dimensional, rigid body: 1) rest, 2) slide, 3) rock, 4) slide-rock, 5) uplift, and 6) rock-uplift. These six modes are shown schematically for the arbitrarily-shaped rigid block in Figure 2.2. Ishiyama further derived the equations of motion for each of these response modes as well as transitions between modes with or without impact. Due to the nature of the multiple

modes, the impact model deviates from that introduced by Housner. Specifically, the impact model incorporates both a normal and a tangential coefficient of restitution as well as coefficients of friction. Shenton and Jones similarly studied the multi-modal response of the two-dimensional rigid block (Shenton and Jones 1991). However, in this derivation, modal transitions and impact considered classical impact theory based on an instantaneous point impact, normal restitution, and tangential Coulomb friction. While Shenton and Jones presented approximate and linearized solutions for rocking and slide-rocking, Ishiyama presented the numerical integration of the equations of motion for harmonic and earthquake excitation. These simulations concluded the significance of the choice of normal and tangential restitution coefficients as well as reiterated Housner's finding of the importance of the base velocity for overturning criteria.

2.1.3 Extension of Classical Model for Multiple Bodies

Relatively few studies have been presented in the literature that examine the analytical treatment of freestanding structural systems of more than a single block (e.g. Allen et al. 1986, Psycharis 1990, Spanos et al. 2001). The majority of these studies have focused on the specific trilith frame-like freestanding structure, while the minority have studied the dual-body or multi-body stacked system. The most fundamental effort in this regard was presented by Psycharis (1990), in which the equations of motion were derived for a purely rocking response of the symmetric, rectangular dual-body system, as shown schematically in Figure 2.3. The derivation is based on the same fundamental assumptions of Housner's classical model, namely rigid bodies, rigid foundation, perfectly inelastic impacts, and sufficient friction to preclude sliding and uplift. Each of the four unique modes shown in the figure has two distinct equations of motion depending upon the direction of rotation. Each of these modes is free to transition to another at any time during its response, with or without an impact event, complicating its solution. As expected, the complexity of the classical model is increased exponentially for this dual-body model and would

increase with any additional degree of freedom, asymmetry, or irregularity of geometry. Subsequently, the conclusions of Yim et al. (1980) are exacerbated, as observed in Psycharis's numerical investigation of the linearized equations of motion. Specifically, minute changes in the geometry or input motion can result in radically different time history responses of the system.

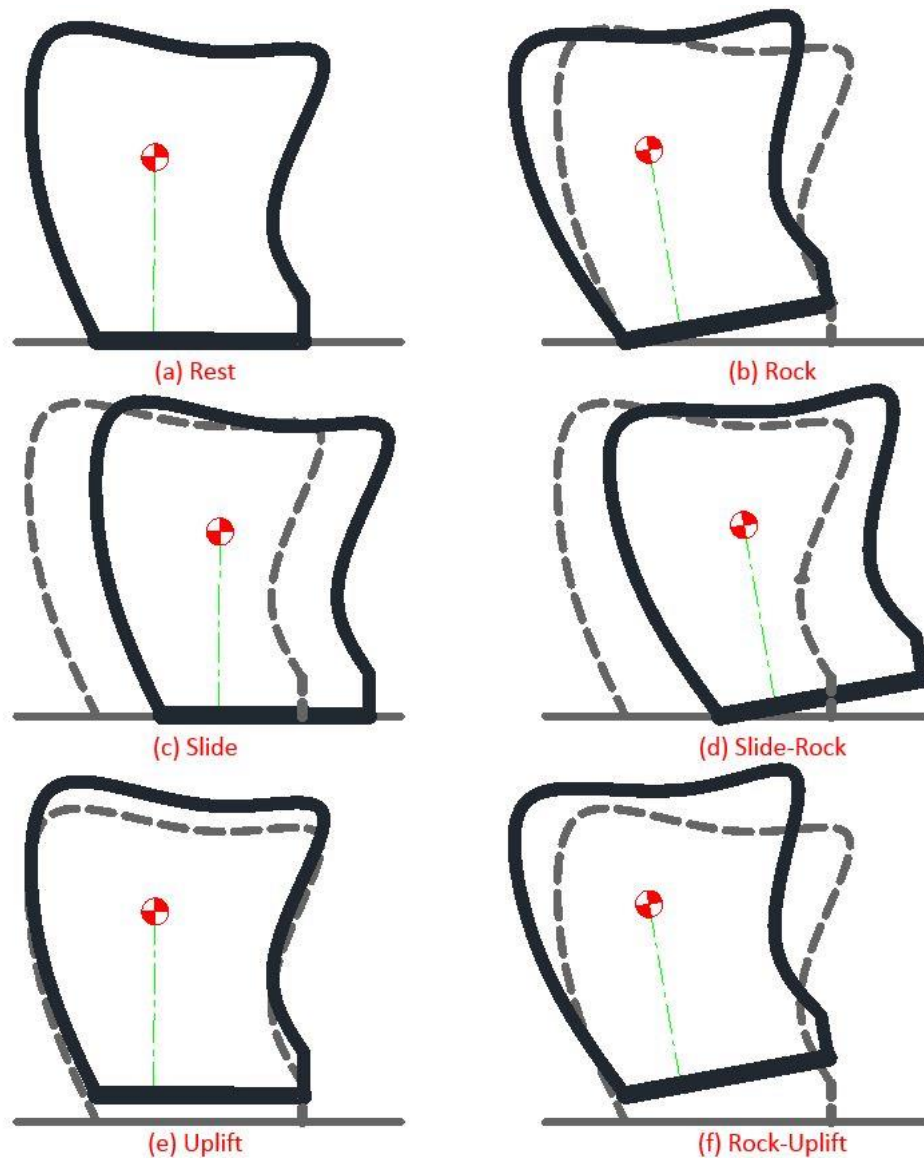


Figure 2.2 Response modes of a two-dimensional rigid block.

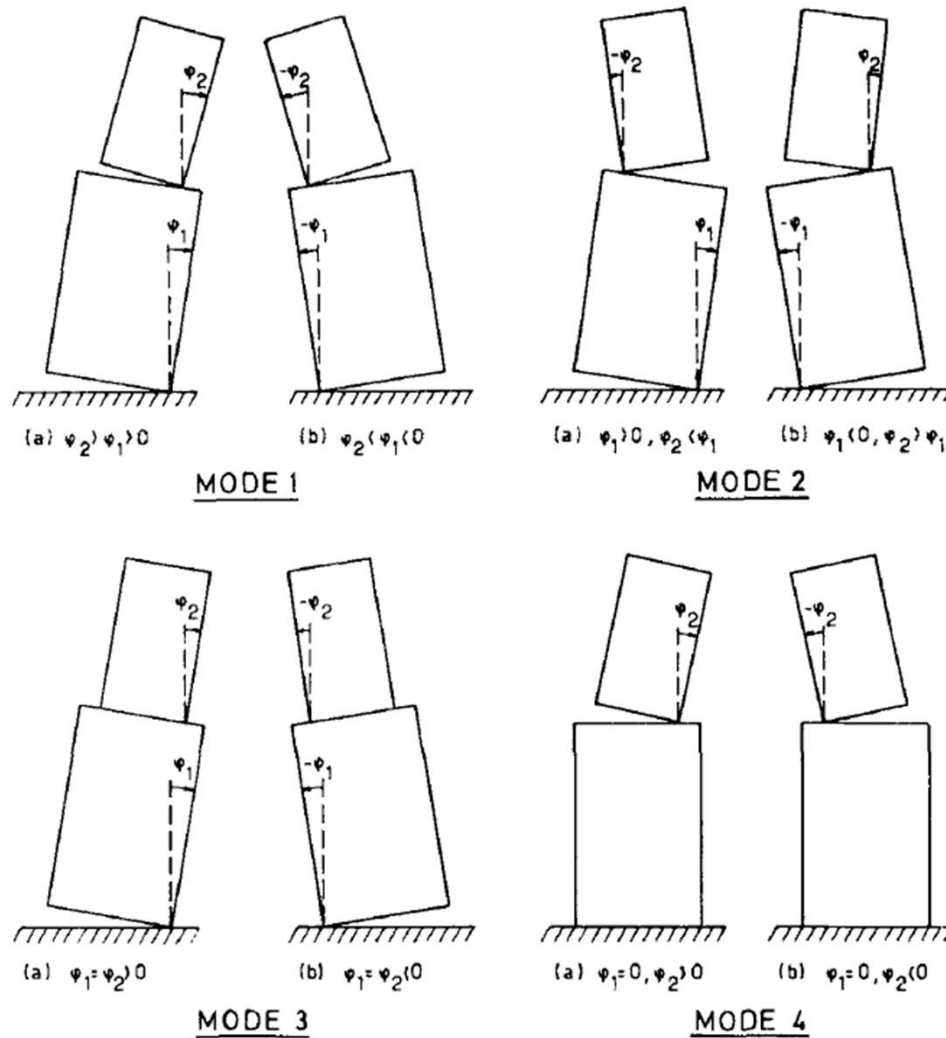


Figure 2.3 Modes of rocking response for a two-dimensional, rectangular rigid dual-body system (from Psycharis 1990).

2.1.4 Extension of Classical Model for Three Dimensions

A natural extension to the classical model is for the three-dimensional block, following all stated assumptions regarding rigidity, instantaneous impacts, and sufficient friction to preclude sliding and uplift. While a preliminary investigation presented a partial derivation for a three-dimensional block neglecting motion after impact (Konstantinidis and Makris 2007), Zulli et al. (2012) derived the equations of motion for a three-dimensional rigid block with a rectangular base

and an arbitrarily located center of mass. Numerical integration of the three-dimensional equations of motion with single sine-pulse excitation emphasize that a two-dimensional analysis may not be conservative in the presence of multi-directional motion, even for symmetric bodies. Therefore, the criticality of three-dimensional simulations is emphasized. However, the solution of the equations of motion is quite cumbersome and difficult to extend to multiple bodies or a non-rectangular base.

2.1.5 Extension of Classical Model for Flexibility

In efforts to extend the classical model to more realistic structures, the assumption of rigidity, both with respect to the interface and with respect to the rocking block, has been relaxed in a number of recent studies. Most notably, Chatzis and Smyth (2011) present an extension of the model that incorporates a bed of springs, or a Winkler foundation, beneath the rigid block that introduces interface flexibility. A schematic of the two-dimensional rocking block with interface compliance is provided in Figure 2.4a. The interface incorporates vertical tensionless springs, horizontal springs for a treatment of Coulomb friction, and dashpots. As the entire block is used for evaluating the contact forces that act upon the block (see Figure 2.4a), the discontinuity and explicit treatment of energy dissipation is not required in this formulation. Another significant extension in the area of flexibility concerned the flexibility of the rocking body upon a rigid foundation (Acikgoz and DeJong 2012). A schematic of the system presented is provided in Figure 2.4b, in which the rocking body is treated as a single-degree-of-freedom, linear elastic oscillator. The base of this lollipop structure is fixed to a rigid base that is free to rotate about a rigid foundation, resulting in rigid-rigid impacts as in the classical model. The equations of motion for this system were derived classically in a Lagrangian formulation, and impact was treated under the classical assumptions of conservation of angular momentum immediately before and after the impact event. While both of these studies revealed a number of insights into the dynamics of

flexible systems, neither has been compared to experimental data for the prediction of realistic structures.

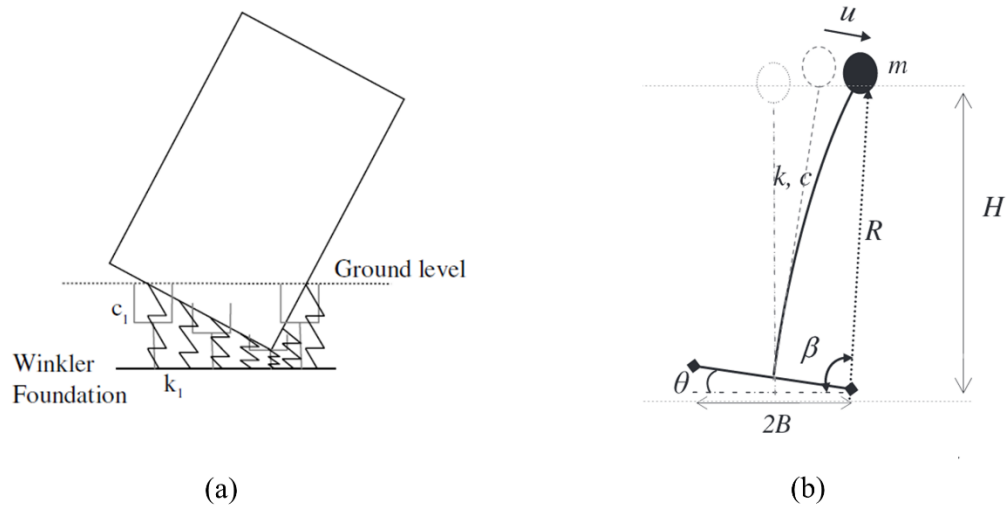


Figure 2.4 Schematics of the two-dimensional rocking block considering (a) flexibility of the interface (from Chatzis and Smyth 2011) and (b) flexibility of the body (from Acikgoz and DeJong 2012).

2.2 Previous Experiments on Freestanding Structures

While there have been extensive studies into the analytical response of freestanding structural systems, as partially detailed in the previous section, there have been relatively few experimental studies into the dynamics of these critical structural systems. Given the multiple assumptions that form the basis of the analytical studies, compounded by the need for calibration and validation of numerical models, there is a very significant need for experimental studies of these systems. In addition, the analytical studies highlighted the nonlinearity of the response with respect to geometry, the sensitivity of the response to small changes, and the exponential increase of these complexities with additional dimensions and degrees of freedom. As a result, experimental campaigns have been designed to account for a number of these expected response variables. This

section aims to detail the key experimental studies presented in the literature and provide the motivation for the two experimental campaigns presented in this dissertation. The section is partitioned into two primary sub-sections, which focus on the dynamics of single-body freestanding structures and the dynamics of multi-body freestanding structural systems.

2.2.1 Single-Body Systems

Single-body systems are the simplest of all freestanding structures; and, as such, have been the focus of many analytical and a number of experimental studies. The first thorough experimental study, in this regard, was presented by Lipscombe and Pellegrino (1993). In this study, a number of manufactured, rectangular blocks of variable slenderness, or aspect ratio, were initiated into a free rocking response. The specific aspect ratios tested included height-to-width ratios from 1.0 to 8.0, and the blocks further incorporated grooved edges on a grooved foundation in an attempt to prevent a sliding mode. The free rocking response of the individual blocks was measured through high-frame rate cameras. The results of these systematic dynamic tests were compared to the classical model to gage the model's robustness. The free rocking response of very slender blocks (height-to-width ratio in excess of 4.0), with two distinct rocking points and symmetric geometry, can be sufficiently modeled with the classical model. However, blocks of squatter aspect ratios evidenced significant three-dimensionality and bouncing (uplift or jump) upon impacts. This type of behavior violates two key assumptions of the classical model, and results in radically inaccurate predictions of the response. In addition, the ability of the classical model to predict the motion after two impacts is quite poor, even for the more slender configurations. This is attributed to the accumulation of the effects of small imperfections, which propagate throughout the time history response.

Around a similar time, Winkler et al. (1995) presented the results of an experimental campaign of rectangular blocks of similar aspect ratios to those of Lipscombe and Pellegrino,

ranging from 3.33 to 10. All of the tested blocks were symmetric, rectangular, and wooden. The experimental setup incorporated abrasive paper at the interface to preclude any sliding effects. In this experimental setup, a number of accelerometers were incorporated to monitor the free rocking response and the response to harmonic base excitation. As a result, a displacement or rotation time history was unable to be adequately obtained for the blocks. Rather, the results were used to capture the moment of overturning for a given block and a given amplitude and frequency of harmonic motion. Furthermore, the primary goal of this experiment was a preliminary investigation into distinct element modeling for the rocking block problem; and, the experimental results were primarily used for calibration and comparison with these preliminary models.

While the first two primary experimental campaigns discussed focused on the general behavior of single blocks, a more recent study focused on the response of precariously balanced rocks, which are a naturally occurring structure of interest. In this study, a number of stones as well as steel and timber columns were tested on a shake table to simulated and recorded ground motions. These blocks were characterized by slenderness values ranging from 0.19 – 0.37 radians, with mild eccentricities present in a handful of these blocks. A representative image of these columns and rocks are included in Figure 2.5. While the range of blocks tested in this experiment addressed the nonlinearity of the rocking problem, the rotational and translational time history responses were not recorded for any of these tests. Rather, these tests were utilized to record the amplitude of a ground motion necessary to overturn these structures. The primary goal of these experiments were to validate a fragility curve, or probabilistic, approach to the overturning of precarious rock structures, which may have seismological implications.

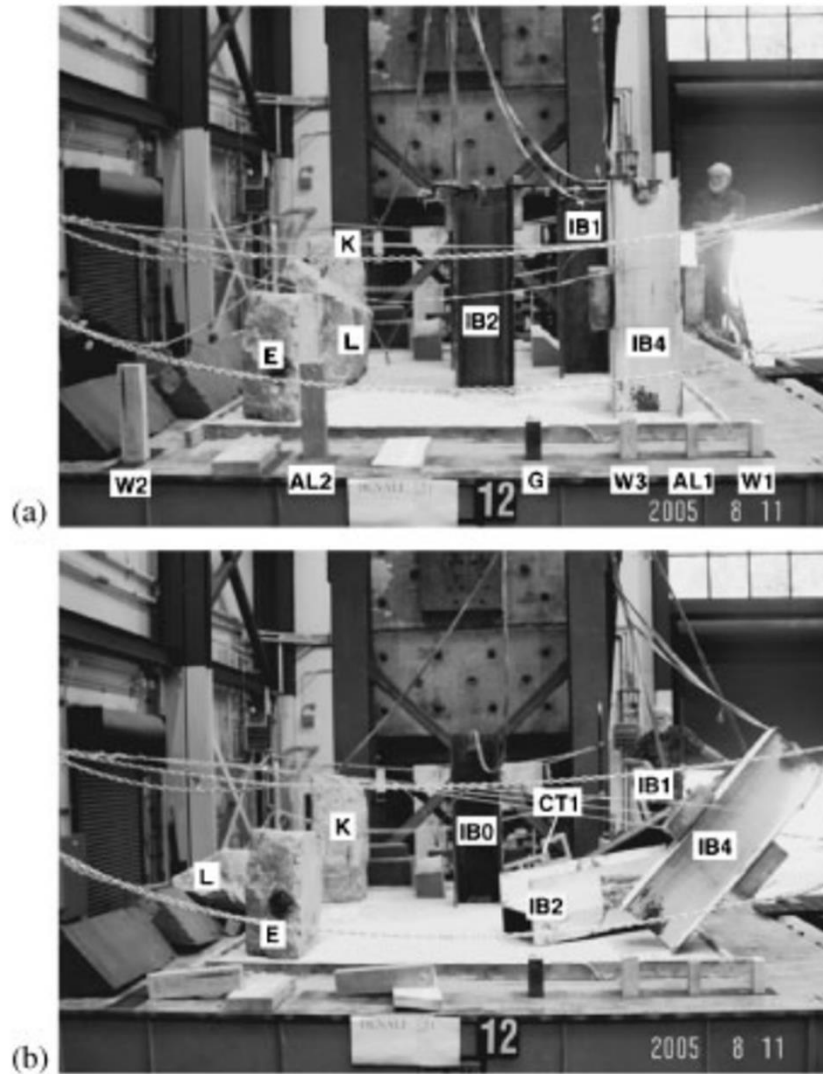


Figure 2.5 (a) Experimental setup on the shake table of various precarious stones and slender columns, and (b) resultant overturned configurations atop the shake table. (From Purvance et al. 2009)

More recently, additional experiments have been conducted in an attempt to monitor the entire time history of rotation and translation for manufactured blocks. The primary goal was to further the understanding of the dynamics of symmetric rocking blocks, in general. Peña et al. (2008) presented the results of shake table tests on stone, blue granite blocks of varying aspect ratios of 4, 6, and 8, as shown in Figure 2.6a. The stone material was chosen as it is a high-strength

material that has a high resistance to crushing and wear, in an effort to maintain consistent interface and boundary conditions throughout the course of testing. The blocks were manufactured to be very long out-of-plane (see Figure 2.6a) to minimize three-dimensional effects. Furthermore, the blocks were modified with small cuts at the edges to reduce impact degradation. A total of 379 tests were conducted during this extensive shake table testing campaign, which included free rocking tests, harmonic motion, and random earthquake motions. While sliding and three-dimensional effects were observed, they were fairly minimal. However, the blocks were also outfitted with accelerometers, which evidenced impulsive accelerations in three orthogonal directions upon impact. These impulses act to increase the likelihood of three-dimensional responses, and emphasize the necessity of accounting for three-dimensional motion of symmetric blocks.

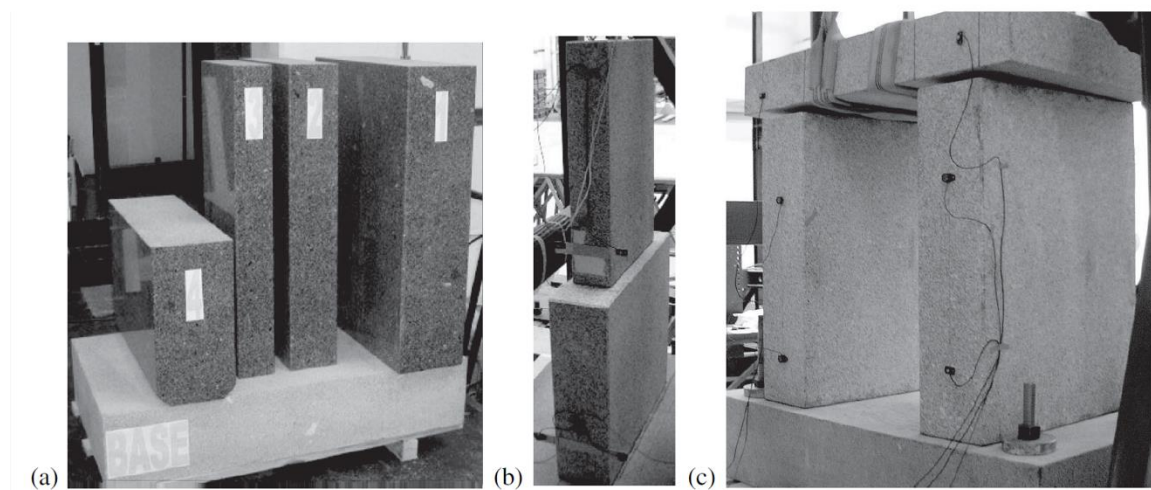


Figure 2.6 Granite stone experiment: (a) single block specimens; (b) dual-body specimen; and, (c) trilith frame-like specimen. (From Peña et al. 2008)

A very recent experimental campaign, presented by ElGawady et al. (2011), focused on the evaluation of the interface material or the rocking of slender, rectangular, symmetric blocks. This primary motivation was to gage the efficacy of the classical model's assumption of instantaneous, perfectly inelastic impacts, which are modeled through a velocity reduction factor termed the coefficient of restitution. The experimental specimens were of comparable aspect ratios to previous tests, namely values of 3 and 5. The experimental setup is pictured in Figure 2.7, where the uplift of the block was at distinct rocking points near a joint, which prevented any translation, sliding, uplift (jump), or twisting. At these joints, the various material interfaces were incorporated for testing in a free rocking motion. The free rocking response was further compared to the classical model assuming various values for the coefficient of restitution to obtain a best fit. This experimental campaign highlighted the inherent fluctuation in this value, and that the assumption of inelastic impacts is valid only for very stiff material impacts. Specifically, impacts of a rigid block upon a rubber foundation evidenced increased energy dissipation and required a lower value of the coefficient of restitution, which averaged approximately 80% the coefficient calculated in the classical model based solely on geometry.

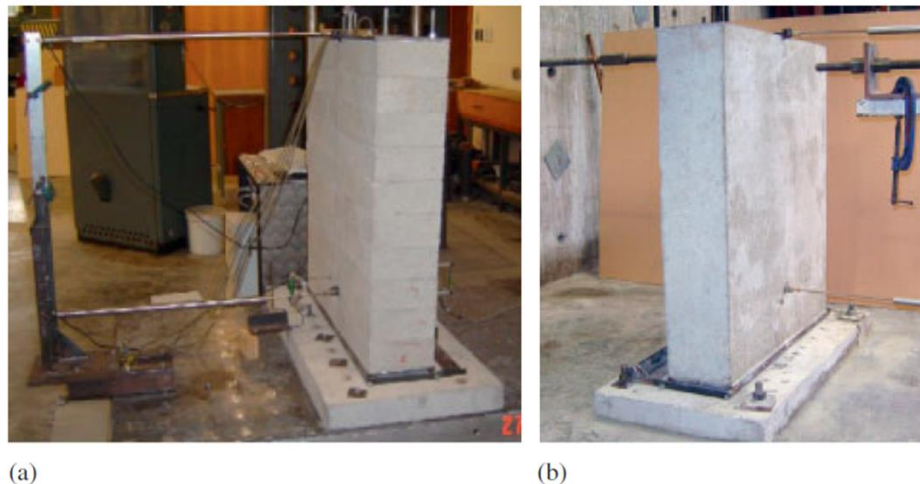


Figure 2.7 Experimental setup for the evaluation of interface material, incorporating a slender rigid block fixed from translation through joints at the base with various materials as the foundation material. (From ElGawady et al. 2011)

The final experimental campaign to be detailed focused on specific structures, rather than the general rocking body. In this study, numerous full-scale laboratory equipment components were tested on a shake table to earthquake excitation (Konstantinidis and Makris 2009). The specific equipment can be classified as stiff, rectangular, and symmetric, as shown in Figure 2.8. However, the experimental specimens were more realistic than those the classical model typically targets. As such, these specimens violated many of the classical assumptions and had inherently variable boundary conditions. The fully three-dimensional response of each specimen was monitored throughout the course of testing. The primary mode of response was sliding, with only minimal rocking occurring highlighting the necessity to incorporate multiple modes in the simulations. In addition, material failure was observed for the connected legs of one of the specimens, which further emphasizes the flexibility of realistic structures and that the stress and deformation of freestanding structures needs to be addressed for certain simulations.

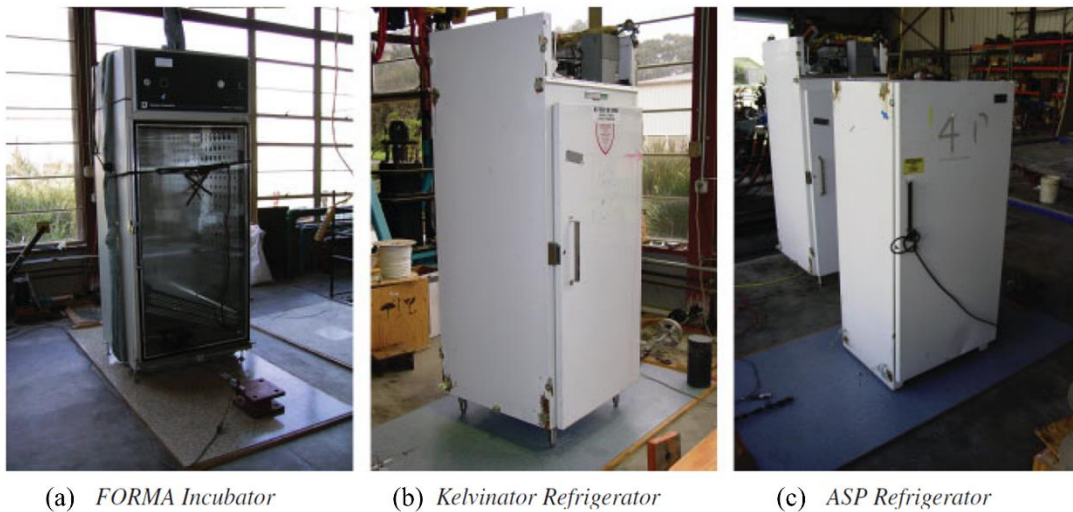


Figure 2.8 Experimental specimens used in shake table testing of laboratory equipment (from Konstantinidis and Makris 2009).

2.2.2 Multi-Body Systems

While numerous analytical and a handful of experimental studies have focused on the dynamics of single-body structures, very few have focused on the dynamics of multi-body structures. It is noted that there have been a number of studies on the dynamic response of unreinforced masonry walls (e.g. Benedetti et al. 1998; Costa et al. 2013); however, the objectives of these studies were aimed at the system-wide response and the calibration of finite element models. As such, works focused on unreinforced masonry are not included in this review of the literature. Similarly, trilith frame-like structures are not documented in this section, an example of which is shown from a recent experiment in Figure 2.6c. Rather, the focus of this multi-body literature review is on stacked dual-body or multi-body systems.

While the preliminary studies of Lipscombe and Pellegrino (1993) and Winkler et al. (1995) incorporated a stacked system of the single-body specimens, the results were not heavily detailed, nor analyzed by the authors. The first well-documented experiment of stacked multi-body systems was presented by Peña et al. (2008) in the same experimental campaign as numerous single-body tests. In these shake table tests, the dual-body system consisted of a top block with aspect ratio of 4 atop a bottom block with aspect ratio of 3, which is shown in Figure 2.6b. These manufactured blocks were modified to discourage sliding and three-dimensional response, as detailed in the previous section. The results of these tests emphasize the exponential increase in the complexity of the problem with the introduction of the second block. Specifically, repeatability of the single-body was achieved for harmonic base excitation, however the dual-body tests did not evidence any repeatability. This was largely attributed to the propagation of the minor geometric differences between tests and the precise initial location of the blocks with respect to each other. In addition, sliding and three-dimensional responses were observed in these dual-body tests, where these were not evidenced in the single-body tests. As a result, future numerical modeling is

recommended to account for the inherent variation of the interfaces and the resultant variation of the response.

A prevalent higher-order stacked multi-body system is the classical multi-drum column. This was the target of two recent experimental shake table testing campaigns, namely that of Mouzakis et al. (2002) and Drosos and Anastasopoulos (2014). The columns tested in both of these experiments are shown in Figure 2.9 and Figure 2.10 for Mouzakis et al. and Drosos and Anastasopoulos, respectively. In both tests, the individual blocks comprising the multi-body system are fairly squat, with aspect ratios less than or equal to 1 in both cases. In addition, it is noted that the interfaces of these blocks are geometrically similar, meaning that there is very little foundation for an additional block to rock – limiting the number of modes for this type of a multi-body system. Furthermore, in both tests, the blocks were marble and anticipated to have high-friction interfaces. Although, Drosos and Anastasopoulos measured the dynamic coefficient of friction to be close to 0.4, which is markedly lower than typically assumed for these materials. Both experiments highlighted the occurrence of sliding and relative motion of the individual blocks, with Mouzakis et al. observing this to be more likely for higher-frequency motions due to the accumulation of the many cycles of response. However, this relative motion was unable to be measured by Mouzakis et al, which was a primary motivation for the study of Drosos and Anastasopoulos. Specifically, this second multi-drum column experiment focused on the high-resolution dataset for the ultimate calibration and validation of a numerical model for this structural system.

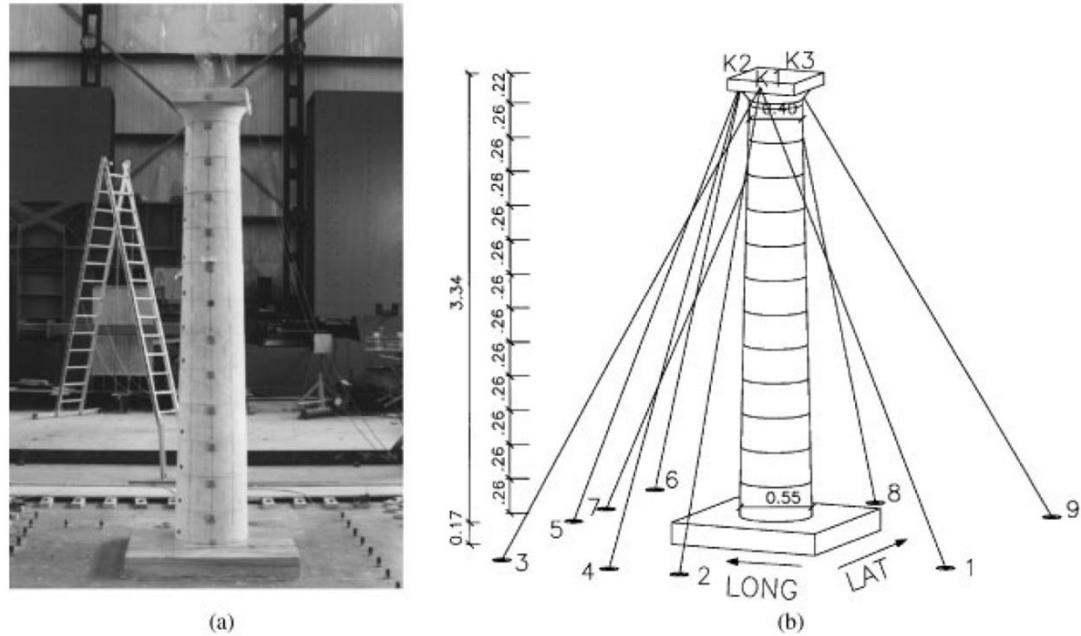


Figure 2.9 Scaled multi-drum column tested by Mouzakis et al. in (a) image, and (b) schematic including location of string potentiometers (from Mouzakis et al. 2002).

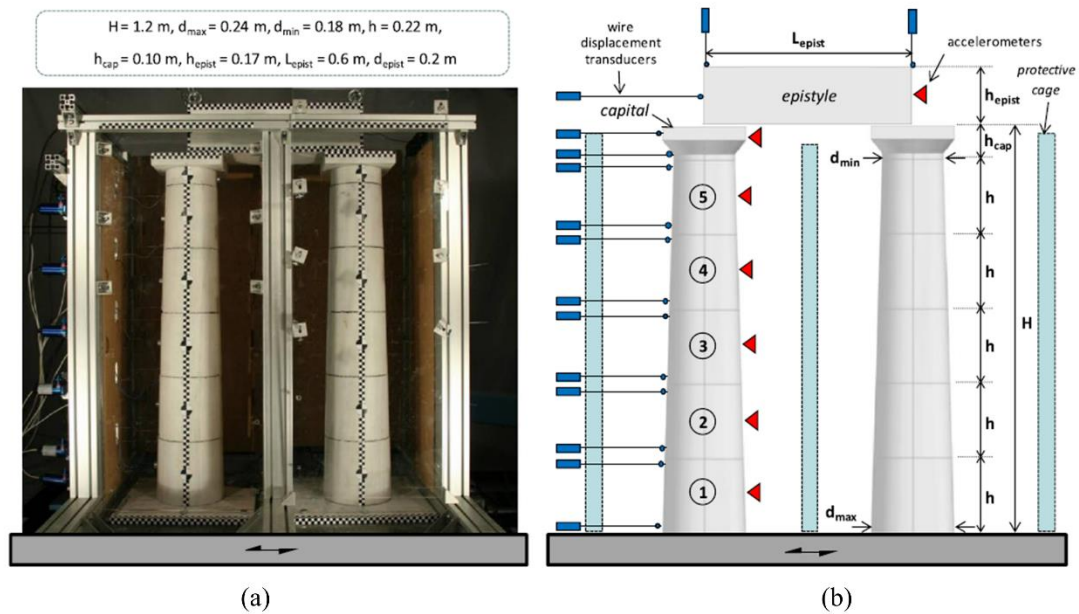


Figure 2.10 Scaled multi-drum column tested by Drosos and Anastopoulos, shown in a trilith form: (a) as built, and (b) in schematic with instrumentation schedule (from Drosos and Anastopoulos 2014).

2.3 State-of-the-Art Numerical Modeling

While analytical studies on the dynamics of freestanding structures are plentiful in the literature, a number of key limitations have been identified (e.g. Drosos and Anastasopoulos 2014). The primary limitation of analytical formulations is the cumbersome and infeasible implementation for realistic scenarios, which may incorporate three-dimensional bodies, multiple bodies in a stacked system, multiple modes of response, and flexible materials of the freestanding bodies or foundation. These variations on the classical model have been shown to be quite significant in recent experimental campaigns, as detailed in the previous section. As a result, numerical models have recently begun to be explored as an alternative method for the study of freestanding systems. The progression of these numerical models is discussed in this section in the context of a number of key studies presented in the literature.

Freestanding structural systems are comprised of individual or discrete units. There are two general classes of numerical approximations to this type of a system: 1) equivalent continuum or a 2) discontinuum approach (Lemos 2007). The first approach is the more widely understood and widely implemented approach in the engineering community – namely, the finite element method. In this modeling approach, a material model representative of the system-wide response is utilized for an equivalent uniform structural element, also known as macro-modeling. On the contrary, the second approach treats the structure as a system of distinct bodies that interact along their boundaries, also known as micro-modeling. Given the clear distinction between these two approaches, the majority of recent numerical modeling efforts have been geared towards the discontinuum approach for freestanding structural systems (e.g. Lemos 2007, and those cited therein). The most paramount efforts, in this regard, are presented herein.

The earliest known effort to model discontinuum systems was that of Cundall (1971), which combined rigid body dynamics for the simulation of multiple “blocky rock systems” that

interacted at their boundaries through springs. This was further developed to account for smaller particle systems, including soil, as the discrete element method or DEM (Cundall and Strack 1979). While many applications exist for discontinuum models, Winkler et al. (1995) presented the first thorough application of DEM for freestanding structures, including comparisons to experimental results and analytical predictions. In this study, Winkler et al. (1995) developed a computer implementation of DEM for single-body rectangular rigid blocks, which utilized normal and tangential springs and dashpots at points of contact between the block and foundation. At each time step in this simulation, contact forces as a result of the springs and dashpots were calculated for the body which generated forces and moments at the center of mass of the block. The acceleration of the body was then found through Newton's second law of motion, and ultimately the velocity and displacement of the body were found through numerical integration. The model and a flow chart of these computations are included in Figure 2.11. The investigation, presented by Winkler et al. (1995), showed agreement between the DEM and the classical model with respect to the initiation of a rocking mode; however, differences were observed for the experimental blocks. Furthermore, time histories of rotation were unable to be obtained in this experimental campaign, and calibration of the DEM was not incorporated. Nonetheless, this study generated the motivation for further study and use of discontinuum methods for the analysis of freestanding structural systems.

In more recent years, commercial implementations of DEM became available and were utilized in studies of freestanding systems, notably the Universal Discrete Element Code (UDEC). Early implementations of this software include the study of classical multi-drum columns by Papastamatiou and Psycharis (1993), in which UDEC was utilized for analysis of the Temple of Apollo. This early study emphasized the need for reliable calibration, and the uncertainty of results due to arbitrary selection of spring stiffness and damping coefficients. Another early study by Papantonopoulos (1997), which also utilized arbitrarily-chosen contact parameters, observed similar decay of free rocking motion between a UDEC model and the classical model. While many

of the salient features of a rocking response were observed in these early studies of DEM, there was little basis for selection of the contact parameters, namely the spring stiffness and the damping coefficient.

Whereas many early studies utilized DEM with arbitrary contact parameters, Peña et al. (2007) presented a methodology to determine contact parameters for a two-dimensional DEM based on corresponding parameters of the classical theory as well as based upon the results of shake table tests, as described in the previous section. In this methodology, the spring stiffness is a function of the size of the rigid block, and the damping ratio is fitted to the experimental data for a best-fit value. It is worth noting that fitted parameters showed variation smaller than 5%; however, variation of this order was observed to have a very significant effect on the response history. While this study addressed a significant dearth in the literature with respect to contact parameter selection, the experimental results were limited to rocking modes only and the numerical implementation was restricted to two-dimensions.

Many early DEM implementations were fairly cumbersome and not broadly available or easily implemented by other studies. In an effort to validate an easy-to-use and physically accurate model, Konstantinidis and Makris (2005, 2009) utilized the two-dimensional dynamic motion simulation software, Working Model 2D. This software utilizes rigid body dynamics for the analysis of individual bodies. The numerical predictions for a classical column as well as for laboratory equipment were compared to the results of analytical formulations for sliding, rocking, and slide-rocking, which served to validate the software. While this study emphasized the fidelity of the results and the ease of implementation, the treatment of impact with a coefficient of restitution and the treatment of simultaneous impacts is noted to be unclear by the authors of this study. Furthermore, the experimental results incorporated in the validation were predominantly

sliding; and, therefore, the capabilities with respect to rocking are not fully presented outside of the context of the classical model and its assumptions.

While early investigations emphasize the promise of discrete element methods and discontinuum modeling for freestanding structural systems, the majority focused on two-dimensional implementations. However, three-dimensional responses of these systems is known to be significant from the results of experimental studies, and serves as a primary motivation for the evaluation of numerical methods. Papantonopoulos et al. (2002) presents a significant effort in the three-dimensional application of DEM for a stacked multi-body system, specifically the classical multi-drum column. In this study, the numerical model was developed in the three-dimensional counterpart of UDEC, which is titled 3DEC. The model was built to simulate the response of the multi-drum column tested on a shake table, as shown in Figure 2.9 and detailed in Mouzakis et al. (2002). As the tested columns consisted of cylindrical bodies, the numerical representation was approximate with respect to this geometry. The numerical model, rather, consisted of 10-node polygonal cross-sections for each of the blocks, which were specified with a rigid material model, as shown in Figure 2.12. For the specified mesh of the rigid bodies, contact forces through spring and dashpot elements may be generated at the vertices and the edges of the mesh. Referring to the mesh in Figure 2.12, an initially adjacent block would result in contact at the central vertex as well as along multiple edges of this cross-section. Utilizing this numerical model, the experimental program was simulated and compared for efficacy of the method.

In general, the three-dimensional numerical model of Papantonopoulos et al. (2002) is shown to be able to reproduce the salient features of the multi-body response, including three-dimensional effects and multi-modal behavior. However, due to the nonlinearity of this type of system with respect to geometry, exact correspondence of the experiment and numerical results cannot be anticipated. This is reiterated by the low repeatability noted in the experimental portion

and the relatively high number of degrees of freedom. Furthermore, the authors emphasize the sensitivity of the response to the contact parameters, similar to the conclusion of Peña et al. (2007). However, in general, this study suggests utilizing contact parameters reflective of the interface material properties. The authors further suggest zero damping for the model, which allowed for a best fit of the experimental rocking behavior in many of the simulations. However, the authors also assert that the best-fit value of damping changes throughout the course of a motion, implying that further study is needed in this area. On the contrary, more recent applications, such as that of DeJong and Vibert (2012), indicate the necessity of damping in three-dimensional DEM to limit the high-frequency vibrations of the contact forces, which can cause erroneous computational results.

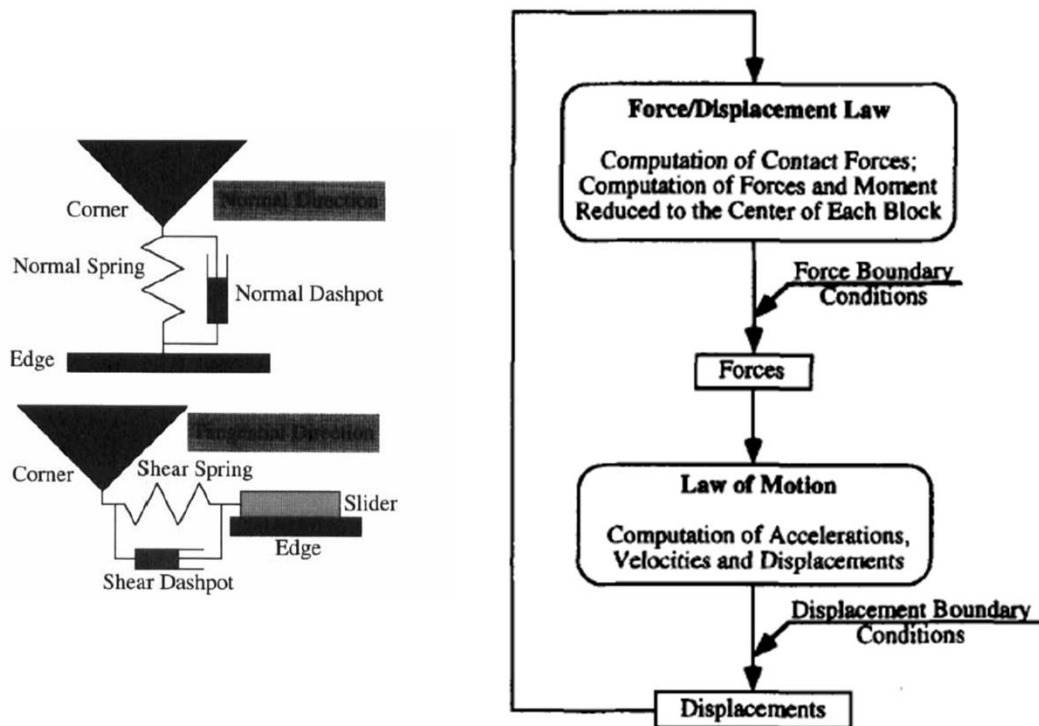


Figure 2.11 The distinct element model as implemented by Winkler et al. for the normal and tangential direction in two dimensions, as well as the flow chart of calculations for this implementation (from Winkler et al. 1995).

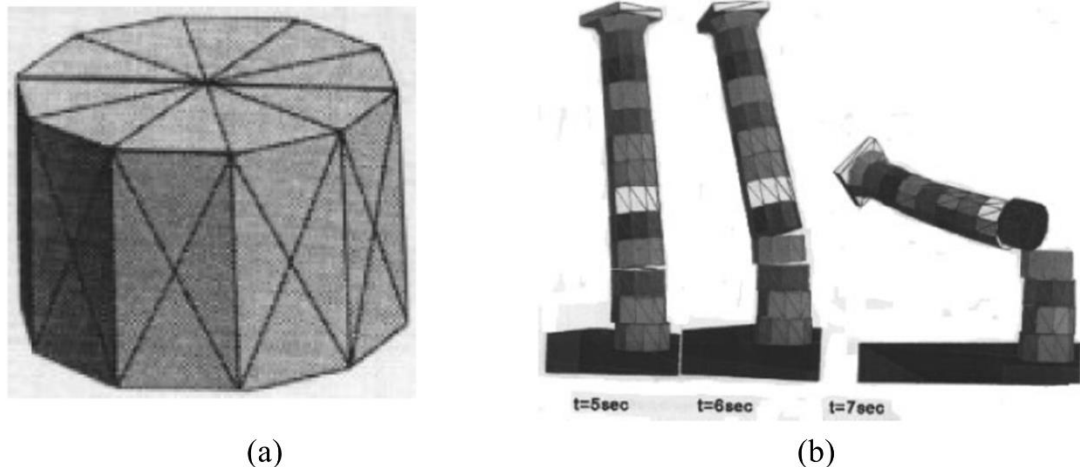


Figure 2.12 Three-dimensional discrete element model for the simulation of a multi-body system: (a) discretization of an individual body, and (b) simulated responses of the system showing the separation and interaction of the individual blocks (from Papantonopoulos et al. 2002).

2.4 Summary

The dynamics of freestanding structures is motivated by the broad range of critical or significant structural components that can be classified as such, compounded by the observed poor performance during earthquakes. As such, numerous studies have been presented which analyze the classical formulation of the freestanding structure, originally presented by Housner (1963). This classically derived analytical formulation is based upon a number of assumptions and idealizations, which include: 1) rigid bodies and rigid foundations, 2) perfectly inelastic, instantaneous impacts, 3) sufficient friction to preclude sliding, 4) continuous contact with no uplift or jumping, and 5) two-dimensional bodies and motion. Despite these numerous assumptions, a great deal has been gleaned from these analytical studies including the nonlinearity of the response with respect to geometry and the sensitivity of the response to small changes in the boundary conditions.

In efforts to understand the limitations of the classical model for the dynamics of freestanding structures, many studies have been presented in the literature which extend this model.

These studies have included the presentation of the equations of motion and impact for: multi-modal systems, three-dimensional systems, flexible systems, and dual-body systems. However, the cumulative effect of all of these extensions is not feasible. As a result, numerical methods were recommended in an attempt to simulate the response of more realistic structural systems. However, numerical methods require experimental data for calibration and validation. To this end, a handful of experimental campaigns for freestanding structures and systems have been conducted. However, due to the low number of tests, the current experimental database is quite limited with respect to multiple bodies, multi-modal response, and, most importantly, with respect to geometry.

As a result of the need for numerical models and the relative lack of comprehensive experimental data, this dissertation addresses three primary research objectives. The first is a database of extreme geometric configurations anticipated for freestanding structural systems. The second is the design and execution of a comprehensive experimental program, which addresses the broad range of anticipated geometries. The third and ultimate goal of this dissertation is the validation of a readily-available numerical model for the prediction of freestanding structures, which is validated with respect to the recorded response of a broad range of geometry and with respect to the fundamental and classical dynamics of the system.

Chapter 3 Geometric Survey and Characterization of Complex Freestanding Structures

Freestanding structural systems encompass a very broad range of structures and components, which range from commonplace to very unique or very critical. These systems have been observed to behave poorly during past earthquakes, as outlined in Chapter 1. As a result, a number of studies have been dedicated to the study of the dynamics of freestanding structures, as detailed in Chapter 2. Early analytical formulations of this problem emphasize the nonlinearity with respect to geometry. As such, quantification of realistic geometric configurations and ranges of anticipated geometry are critical for the development of experimental programs and the development of numerical models. It is therefore a primary objective of this dissertation, and this chapter specifically, to quantify this range of anticipated and extreme geometries. In this effort to examine the extreme geometric configurations, the stone statue-pedestal system is the focus of this chapter, as it is the most geometrically-complex freestanding structural system. Furthermore, these systems are exceptionally critical in the context of cultural heritage, which further motivates their study.

3.1 Introduction

Museum contents and cultural heritage artifacts, such as statues, are historic objects of importance culturally, nationally, or religiously and are regarded as unique and irreplaceable. Many of the human-form statues are one of a kind and hundreds of years old. However, these artifacts are often located in areas of moderate to high seismicity such as Italy, United States, Japan, Greece, Turkey, and many other countries. As a result, conservation and preservation have been ongoing for centuries. Despite society's efforts to preserve them for future generations, poor behavior such as overturning during earthquakes has been observed for decades around the world (e.g. Ericksen

et al. 1954; Thomas et al. 1963; Espinosa et al. 1977; Rosetto et al. 2012). A notable recent example is the overturning of the Captain Scott statue following the 2011 Christchurch earthquake (EERI 2015). Compounded by the irreplaceable nature and importance of these statues, detailed analysis with accurate geometry is required because inappropriate and misguided interventions may result in irreversible damage.

Human-form statues are by their nature structures with highly unique geometries and mass distributions which makes accurate prediction of their seismic response difficult. Analysis is further complicated by their varying boundary conditions and locations within a building. For example, statues may be floor or pedestal mounted; they may be freestanding or physically attached. Likewise, they may be placed at the ground level outside or at several levels above the ground level in a building. All of these pragmatic attributes change the type of potential input excitation to the artifact or statue. To address the need for characterizing these important structures, it is the goal of this chapter to outline and compare techniques for geometric data acquisition and their implications on analysis. In addition, this chapter aims to outline the acquired geometry and boundary conditions of a subsample of twenty-four culturally important statues. It should be noted that herein, the focus is on full-scale, culturally important statues constructed of homogenous marble due to their high prevalence and significance in society. The survey methodology does not apply to hollow statues (i.e. bronze or clay), or those comprised of non-uniform materials or multiple components connected at joints. This focus allows the presentation of dynamic analyses to concentrate on the dominant rigid body modes rather than material failures.

3.1.1 Brief Review of Past Surveys

In recent years, a handful of surveys and seismic analyses were conducted for various museum collections around the world. In addition, various methods for geometric data acquisition have advanced and have been applied in many aspects of civil engineering. In this section, major

contributions of both geometric data acquisition and seismic analyses are discussed with respect to marble statues as well as broader civil engineering applications.

Researchers at the University of Southern California in collaboration with the J. Paul Getty Museum (JPGM) in Los Angeles, CA, conducted perhaps the first most significant effort in the United States to understand the response of museum contents, including marble statues (Nigbor 1989; and, Agbabian et al. 1991). Nigbor (1989) surveyed the contents of JPGM and documented information for statues such as: artifact material, envelope shape and dimensions, and pedestal or mount materials. The marble statues documented were analyzed for rigid body modes given the estimated aspect ratio and the coefficients of friction. Due to the smooth modern pedestals used in the JPGM, it was concluded that the statues would predominantly respond in modes of sliding and rocking when subject to seismic excitation. A more recent survey by Monaco et al. (2014) quantified the friction coefficient for freestanding art objects and typical modern mounts (i.e. masonite, steel, concrete).

In the late 1990s, the Digital Michelangelo Project successfully created three-dimensional reconstructions of ten culturally important statues in the *Galleria dell'Accademia* in Florence, Italy, by the sculptor Michelangelo. The statues were scanned using a laser triangulation range finder with a computer-controlled motorized arm for placement. Researchers sought to obtain millimeter point cloud resolution, to eliminate as much occlusion as possible, and to develop advanced post-processing such as filtering and surface meshing capable of generating clean, highly detailed digital models (Levoy et al. 2000). This project did not evaluate the boundary conditions and the potential response of these artifacts to seismic excitation; however, it did provide much needed detailed geometric documentation and scanning methodology for some of the most historic full-scale statues.

Applications of laser scanning beyond statues have also significantly advanced following the seminal work of Levoy and the advent of commercially available laser scanners. Many studies have been presented which focus on the use of laser-based and image-based methods for obtaining geometric data in situations where manual measurements are unreliable or difficult to obtain. These situations include quantifying concrete flatness (Tang et al. 2011), building facades (Truong-Hong et al. 2012), road potholes (Koch et al. 2013), and coastal erosion of cliffs (Olsen 2013). In particular, Kim et al. (2002) used laser scans to retrieve volumes and aspect ratios of irregular stone aggregate for classification purposes. Similarly, Han et al. (2013) used commercially-available laser scanners to record cross-sections of tunnels for comparison with traditional measurements from a total station.

Given the aforementioned and other advances in geometric data acquisition as well as the motivation to further study Michelangelo's sculptures, Berto et al. (2012) presented a multidisciplinary methodology for assessing the state of health and seismic vulnerability of art objects. A survey was conducted documenting boundary conditions as well as providing detailed digital surface reconstructions of six of Michelangelo's statues in the *Galleria dell'Accademia*. Static analyses concluded that each of the six statues would tend most towards rocking during seismic excitation. Related analytical rigid body analysis methods have the potential for adaptation to human-form, marble statues. These studies include classical rigid body rocking using a symmetric approximation to statues (Yadav et al. 2010), classical rigid body rocking for non-symmetric boulders (Purvance 2008), as well as slide-rocking of non-symmetric structures (Di Egidio and Contento 2009).

These and other studies have provided the cultural heritage and earthquake engineering communities with general characteristics of culturally important artifacts as well as general modeling approaches for use in predicting their response when subjected to seismic motions.

However, no single broad multi-location survey of full-scale, human-form, culturally important, marble statues has been conducted where the emphasis has been to collect high-precision data needed to classify and perform these detailed seismic response analyses. In this context, full-scale refers to the size of the statues on the same order of magnitude as the subject (i.e. 1.5 – 2.5 m for human-form statues). The survey presented in this work attempts to fill this void and provide reference for future works to analyze the seismic response of statues as well as to discuss the impacts on relevant engineering parameters by varying techniques of geometric data acquisition.

3.1.2 Scope of Current Survey

This chapter summarizes a broad field survey of twenty-four culturally important human-form statues conducted in 2011 in Florence, Italy. Geometric data of the statues was acquired from various museums and is compared through use of standard linear measurements (Envelope Shape), image-based processes (Structure-from-Motion), and light-based processes (Light Detection and Ranging), also known as laser scanning. Three-dimensional digital reconstructions and the resultant geometric and mass properties are analyzed for their accuracy as a function of the method of acquisition.

3.2 Site Survey and Documentation

The database of statues detailed in this chapter is the result of a broad field survey conducted in 2011 in Florence, Italy. The database is limited to statues located in Florence, Italy, to provide focus while allowing manageable time and cost to the effort. However, it is noted that the sculpture and art collections held in Florence provide a substantial and quite reasonable representation of statues (particularly human-form) constructed in terms of dimensions and material of the Renaissance era (Avery 1970). The database includes statue surveys conducted at three sites as detailed in Table 3.1. The database is also augmented with five statues from the *Galleria dell'Accademia* by Stanford University (Levoy et al. 2000). At each site, a walk-through was

conducted identifying statues for database inclusion with respect to cultural relevance, structural relevance, and accessibility (defined by radius and height of viewpoint, as well as permissions).

Individual statue documentation included:

- Logistics: title, artist, owner, year constructed, and history of locations and restorations to account for damages and material inconsistencies.
- Location: location of statue within the site including building level, building room, and location within room to understand the potential seismic loading to the statue.
- General dimensions: a bounding box or envelope estimation of the pedestal and statue measured with a tape measure and/or a laser measurement device.
- Materials of construction: materials of ground, pedestal, and statue, including an estimation of the coefficient of friction.
- Boundary conditions: freestanding or details of attachment.

Following this documentation, the final step was to conduct imaging of the statue for three-dimensional digital reconstruction consisting of Structure-from-Motion (SfM) and/or Light Detection and Ranging (LiDAR) methods. A LiDAR scan of each statue was desirable but not possible for all statues due to time restrictions and/or access permissions. This implemented methodology for statue documentation is presented as a flow chart in Figure 3.1, including metadata of the survey as well as the various approaches to data capture which are explained in detail in the following sub-sections.

Table 3.1 List of sites and surveyed statues in Florence, Italy.

Site Name (physical address)	General Details	Surveyed Statue (Artist)
<i>Palazzo Vecchio</i> (P.zza Signoria 1, 50122, Firenze, Italia)	Florentine government building. 13 th century construction with 16 th century renovation.	<i>Genius of Victory</i> (Michelangelo) <i>Hercules and Centaur</i> (de Rossi) <i>Hercules and Diomedes</i> (de Rossi)
<i>Loggia dei Lanzi</i> and <i>Piazza della Signoria</i> (P.zza Signoria, 50122, Firenze, Italia)	Outdoor, covered gallery and surrounding plaza owned and operated by the city of Florence.	<i>Medici Lion</i> (Vacca) <i>Rape of the Sabine Women</i> (Giambologna) <i>Hercules Beating Nessus</i> (Giambologna/Francovilla) <i>Menelaus and Petroclaus</i> (Unknown) <i>Rape of the Polyxena</i> (Pio Fedi) <i>Hercules and Cacus</i> (Bandinelli)
<i>Museo dell'Opera del Duomo</i> (P.zza del Duomo 9, 50122, Firenze, Italia)	Museum originally constructed in 1891 and renovated in 1999.	<i>Florentine Pieta</i> (Michelangelo) <i>Zuccone</i> (Donatello) <i>Abraham and Isaac</i> (Donatello/di Bartoli) <i>Profeta</i> (di Bartolo) <i>Re Salomone</i> (Pisano) <i>Profeta</i> (Pisano) <i>Sibila Tiburtina</i> (Pisano) <i>Profeta</i> (Donatello) <i>Profeta</i> (dell' Armaturato) <i>Profeta</i> (di Banco)
<i>Galleria dell'Accademia</i> (Via Bettino Ricasoli 60, 50122, Firenze, Italia)	Owned and operated by the national Italian government. 18 th -19 th century construction.	<i>David</i> (Michelangelo) <i>St. Matthew</i> (Michelangelo) <i>Atlas</i> (Michelangelo) <i>Awakening</i> (Michelangelo) <i>Youthful</i> (Michelangelo)

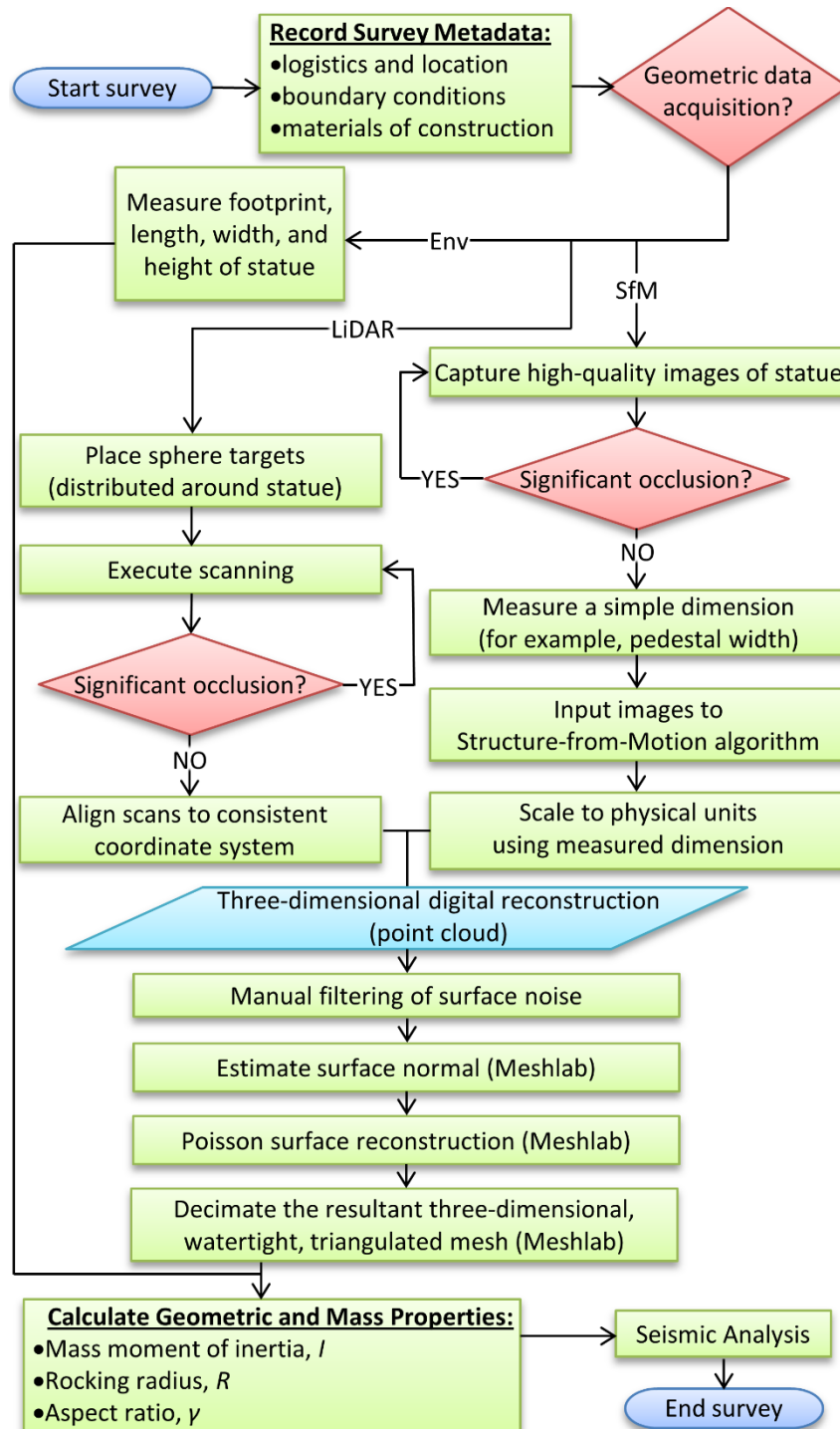


Figure 3.1 Flow chart of implemented methodology for statue documentation including the process of mesh generation in three-dimensional reconstruction.

3.2.1 Light Detection and Ranging

Light detection and ranging (LiDAR) systems comprise a broad spectrum of laser-emitting devices used for range measurement, or more typically known as laser scanning. The scanners provide dense depth maps of all objects within the line of sight including intensity and color information. The scanner used for acquisition during this survey was the FARO Focus 120 3D, a phase-based scanner that can acquire 976,000 points/second (FARO 2011). Provided the spot size of 3.8 mm, the step size of 0.009°, and the ability for close range scanning (approximately 1 m in the horizontal plane for a statue), sub-millimeter resolution point clouds are obtainable with this equipment. For the acquired data herein, the resolution of the scanner was typically set for a point-to-point distance of approximately 6 mm/10 m and approximately 44.4 million points per 360° scan. Given that the distance to the target statue was uniformly less than 2 m, up to sub-millimeter resolution was obtained for the statues scanned neglecting the patches of occlusion. Reflectance, scanner movement, and averaging of the divergent beam over multiple objects create noise in the resultant point cloud which is minimized by oversampling of the data. For an object scanned at a maximum distance of 2 m, the noise is estimated to be 0.12 mm uncompressed and the error to be ± 0.4 mm for a marble surface (FARO 2011).

LiDAR is a line-of-sight technology requiring multiple scans to minimize occlusion in the final point cloud. The number of scans (typically six to seven scans per statue), the horizontal and vertical position of the scanner were decided on site given the surface topology of the individual statue and accessibility. For example, the *Florentine Pieta* statue (shown in Figure 3.2) has a complex front and relatively flat back. In addition, a leg is extended which obstructs the view of other figures in the statue. For this reason, five scans were conducted in an elliptical shape around the front of the statue and a single scan of the back. Of the five front scans, three were conducted

at approximately mid-height while the remaining scans were conducted lower and higher to incorporate the areas of occlusion due to the leg.

To combine the multiple scans into a single point cloud with common axes and origin, points of reference must be identified amongst the scans. For this reason, ten retro-reflective spheres were positioned with additional flat checkerboard markers for redundancy. In the resulting individual scans, the retro-reflective spheres are identified as high-intensity low-noise zones to which a sphere can be fit with reasonable precision. In some instances, false positives are noted, such as the head of statues of certain size. However, the reference targets are manually verified to avoid these instances. Using at least three of these fitted spheres, the rotation of the point clouds is determined and results in a single point cloud with a single origin. The final step in processing the LiDAR point clouds is filtering. Common point cloud filtering techniques typically perform poorly for such detailed surfaces with sharp gradient changes, as is present for statues. Extraneous points and noise in proximity to the surface of the statue is manually filtered. The resultant aligned point cloud for a representative statue, *Florentine Pieta* by Michelangelo, is given in Figure 3.2a where the dense point cloud produces a near high-resolution image-like result with very fine details.

3.2.2 Structure-from-Motion

Structure-from-Motion (SfM) is three-dimensional scene reconstruction through correspondences of a series of 2D images. The technique is based upon the theory of passive stereo and the epipolar constraint, which dictates that given two projections of the same point in space, its location relative to the two rays can be determined through triangulation. SfM applies this concept to multiple points or features within a given set of images to triangulate the location of the cameras. The feature points combined with the relative position to the cameras creates an unscaled three-dimensional reconstruction of an object (must be scaled to physical units). Feature or point tracking

in the SfM algorithms searches for uniqueness of a pixel or a group of pixels from the surrounding in terms of color, edges, corners, shadows, and high contrast.

During this survey, three cameras for SfM documentation were used, namely: (1) Canon EOS 7D with a EF-S 28-135mm f/3.5-5.6 IS lens, (2) Canon EOS 5D Mark II with a EF 24-105mm f/4L IS lens, and (3) Nikon D7000 with a 18-105mm f/3.5-5.6 VR lens. It should be noted that only one high-quality camera is needed to reproduce this technique in this type of setting; however, the availability and use of any of these three allowed flexibility for the various scenes of interest and data collection efficiency. All selected cameras are digital AF/AE single-lens reflex cameras with a high-sensitivity, high resolution (ranging from 16.2 megapixels to 21.2 megapixels), large single-plate CMOS sensors. Cameras were operated manually, without flash, and at various focal lengths.

Approximately one-hundred images of each statue from multiple viewpoints and with significant overlap were captured to increase likelihood of correspondences. Data processing begins with sorting of the images, to either correct exposure or discard images which are out of focus. Statues presented in this database were reconstructed using VisualSfM (Wu 2011) as developed in Furukawa and Ponce (2010). The algorithm assumes an 8-parameter internal camera model including a single parameter for radial distortion. Object reconstruction in VisualSfM consists of four steps: (1) load images with exposure metadata; (2) conduct feature detection and pairwise image matching (linking of correspondences); (3) apply incremental reconstruction which aligns the images with respect to the cameras and the other images; and (4) conduct dense reconstruction. The result of this procedure is a series of points described by three-dimensional unscaled coordinates (x,y,z) , color (r,g,b) , and intensity. The point cloud is scaled to prototype coordinates using the easily measured pedestal dimensions.

Similar to the procedure for LiDAR, the first step in processing is to manually delete extraneous points and filter surface noise. Figure 3.2b contains a representative point cloud

reconstructed through SfM of the same statue scanned with LiDAR in Figure 3.2a. The SfM point cloud contains approximately 10-15% the number of total vertices of the LiDAR for these raw clouds. It is clear that SfM reconstruction is biased to areas of finer detail rather than in areas of relative simplicity as is seen through point coverage on the front compared to the back of the statue in Figure 3.2b. Furthermore, there is considerably more surface noise in the SfM point cloud potentially due to minor errors in correspondences and variations in feature resolution. In addition to the higher level of noise, stark differences arise compared to LiDAR with respect to collection and processing time. The described data collection for SfM requires approximately 1 hour, while the processing time to reconstruct the statues ranges from 4 – 6 hours with additional filtering time of another 4 – 6 hours. This is in contrast to the data collection and processing of the FARO: 1 hour for data collection, 1 hour for reconstruction, and 1 hour for filtering.

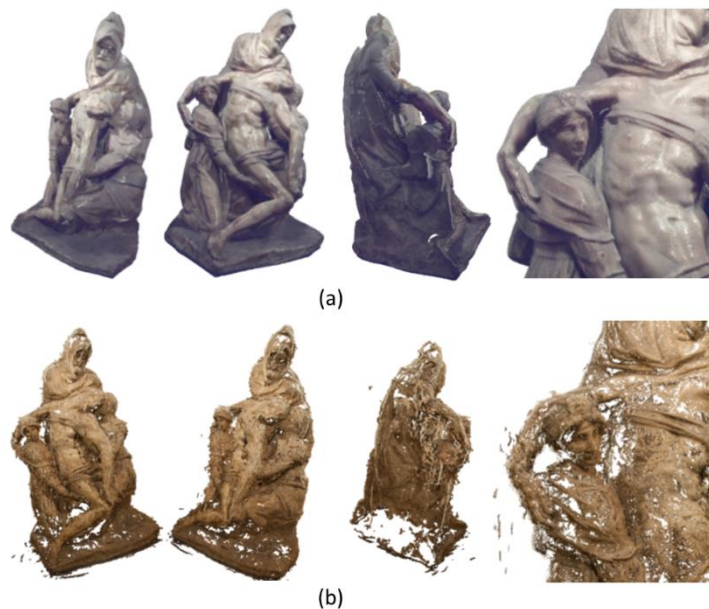


Figure 3.2 Isometric and detail view of *Florentine Pieta* by Michelangelo: (a) LiDAR point cloud consisting of approximately 3.4 million vertices, and (B) SfM point cloud consisting of approximately 560 thousand vertices.

3.2.3 Poisson Reconstruction

Meshing of point clouds is a very broad area of active research; however, the sharp gradient changes, non-uniform texture, and imperfect point coverage of the statues renders most common meshing algorithms inapplicable. Poisson surface reconstruction (PSR), on the other hand, considers a global solution rather than local and is constrained at all the surface points yielding a watertight (no holes in coverage) triangulated mesh with variable triangle size depending on coverage and input parameters, as well as only a single layer to define the surface. Furthermore, these properties of the algorithm inherently filter the existing noisy data in its surface approximation. Not only was the algorithm first presented and developed in the context of complex statue geometries (Kazhdan et al. 2006), a later study by Junior et al. (2011) visually compared PSR with alternate meshing algorithms specifically for art objects and concluded that PSR is the ideal choice. Due to the largely positive performance of PSR and the poor performance of other algorithms in these studies, PSR is the algorithm implemented for surface reconstruction in this work.

The Poisson reconstruction algorithm, as developed by Kazhdan et al. (2006), requires a set of points describing the surface of an object with variable levels of noise as well as a normal vector associated with each point. The normal vector for each point within the point cloud from either LiDAR or SfM was estimated by the normal of a fitted plane to the point's neighbors (typically, 10-20 neighbors were required) using a least-squares fitting method. Given the point set and corresponding normal set, the Poisson reconstruction algorithm solves for an approximate indicator function whose gradient best matches the normal vector field over a distinct patch of the surface points. The size of this patch for approximation of the indicator function is dictated by the octree depth, where a deeper octree allows for higher-order functions fit to the point set and creation of a finer resolution mesh. The maximum octree depth necessary for these statues is within the

range of 10-12, which is statue specific given the size of the statue and density of the cloud (SfM vs LiDAR). An octree depth of 10 corresponds to a regular grid size of 1024^3 , which for the average statue dimensions of this dataset corresponds to a 1 mm – 2 mm grid; whereas an octree depth of 8 corresponds to 64^3 or a 15 mm – 30 mm grid. The application of this filtering and meshing algorithm was completed in Meshlab (Cignoni et al. 2008).

The final step in the processing of the point clouds was to resample the mesh and subsequently the underlying point cloud in order to recover a resolution via a clustering decimation algorithm in Meshlab. A three-dimensional grid of specified size surrounds the mesh and collapses the vertices. Meshes and corresponding point clouds resulting from LiDAR scanning were able to be decimated to a uniform resolution of 1 mm neglecting areas of occlusion. These areas of occlusion (typically areas of statue flush with pedestal or very close to a wall) were manually estimated. It should be noted that following these filtering and meshing processes yielded underlying point clouds for SfM that contain only 1-3% as many vertices as those of LiDAR. This further substantiates the source of the more significant noise associated with the SfM reconstruction in comparison to LiDAR. The stages of reconstruction are included in the overarching flowchart (Figure 3.1). Meshes resulting from both LiDAR and SfM are included for visual comparison in Figure 3.3 which highlights the ability of SfM to capture the general shape. However, these meshes will be further compared quantitatively in the following section.

3.2.4 Mass Properties

The aforementioned three-dimensional digital reconstructions are used for calculation of geometric and mass properties of the statues including: volume, surface area, moment of inertia, and centroid, which are typically calculated by integration over mass. These mass integrals can be transformed into volume integrals and subsequently to surface integrals using an assumption of constant density (reasonable for solid marble statue) and application of the divergence theorem.

The surface integrals were numerically computed in MATLAB (2012) using an implementation of the efficient algorithm for triangulated surfaces of Mirtich (1996) and Eberly (2010). The integrals yield the mass, centroid, and moments of inertia. However, given the significant processing time for obtaining these properties by way of LiDAR or SfM, easily recorded dimensions such the height and the footprint are desirable for geometric characterization. Henceforth, these bounding dimensions are referred to as the envelope shape.

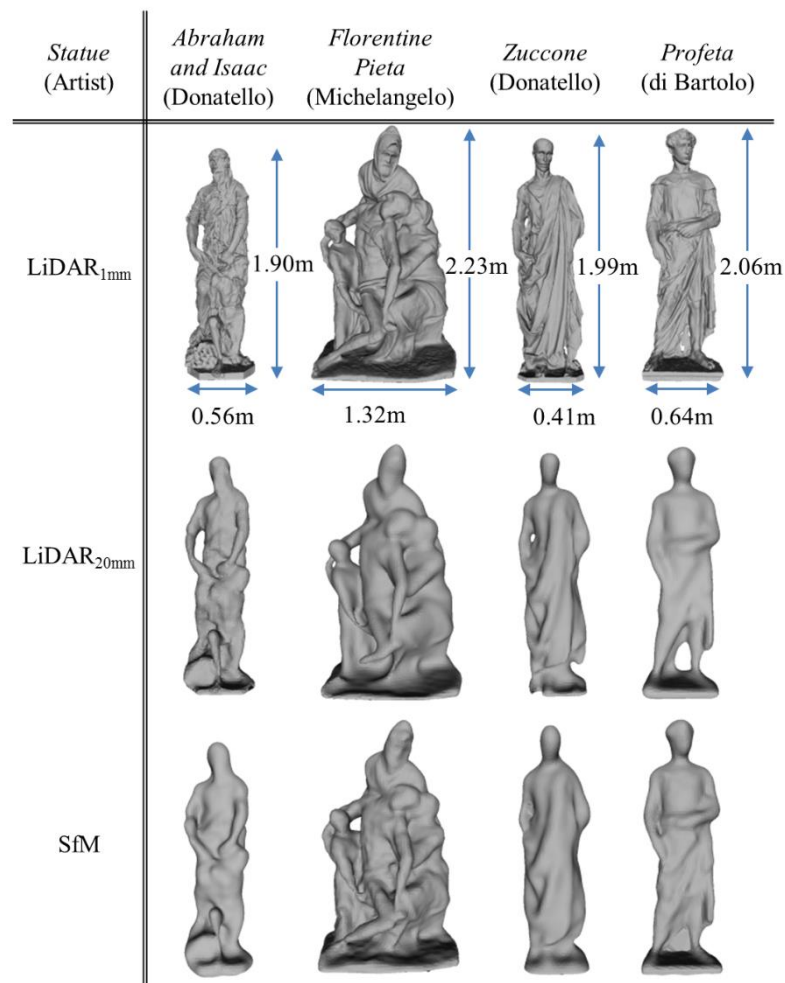


Figure 3.3 Snapshots of statue meshes of high and low resolution LiDAR and SfM.

3.2.5 Survey Results

This section introduces general observations regarding the boundary conditions and geometric properties of the twenty-four surveyed marble statues. The boundary conditions as well as the geometric and mass properties as calculated in accordance with the previous section are presented for a subset of four statues in Table 3.1. The four selected statues were each surveyed with LiDAR (decimated at 1 mm) and correspond to those meshes presented in Figure 3.3. This table is expanded to include properties of all twenty-four statues as well as photographs in Appendix A.

The range of geometries surveyed is significant, and presented statistically in Figure 3.4. In this figure, the minimum aspect ratio is plotted against the corresponding eccentricity, where the aspect ratio is defined as the height divided by a width and the eccentricity is defined as the ratio of two aspect ratios, as shown in the schematic in Figure 3.4a. There is no general trend between these geometric quantities for the surveyed statues, nor is one anticipated given the non-engineered designs. However, a number of general geometric observations can be made. Specifically, the aspect ratios presented range from values near 1.0 (fairly squat, or square in aspect ratio) to values approaching 10.0 (extremely tall). In addition, the eccentricities are seen to include such extreme values as 0.3, which indicates that one width to the center of mass is only 30% that of the opposite side indicating a very extreme mass eccentricity.

The survey concluded that all statues in the sample are constructed of marble and are observed to have an associated pedestal constructed of stone. Furthermore, all but one statue in the sample are freestanding and unrestrained on a pedestal. The outlier, *Florentine Pieta*, interface includes a cementitious material presumed to be an anti-theft measure of the past. A detailed friction study was unable to be completed as part of this survey as it requires contact with the pedestal, where physical contact was not permitted. However, the authors estimate that the coefficient of

static friction for marble on marble, marble on granite, and marble on limestone is at least 0.4, which corresponds to recent experimental results for marble-marble interfaces of classical multi-drum columns (Drosos and Anastasopoulos 2014).

Table 3.2 Summary of survey data and calculated geometric and mass properties for four statues using LiDAR_{1mm} meshes.

Parameter [units]	Abr. and Isaac (Donatello)	Florentine Pieta (Michelangelo)	Zuccone (Donatello)	Profeta (Bartoli)
mass [kg]	487	2604	576	484
Footprint (x,y) [m]	[0.49 0.56]	[0.97 1.32]	[0.55 0.41]	[0.41 0.64]
Height [m]	1.90	2.23	1.99	2.06
Center of mass (x,y,z) [m]	[0.21 0.24 0.82]	[0.46 0.58 0.81]	[0.27 0.19 0.91]	[0.20 0.31 1.03]
Inertia tensor [kg-m ²]	[122 123 11]	[842 940 293]	[146 149 14]	[146 151 12]
Boundary Conditions	Free-standing on pedestal	Restrained on pedestal	Free-standing on pedestal	Free-standing on pedestal
Construction Material	Marble	Marble	Marble	Marble

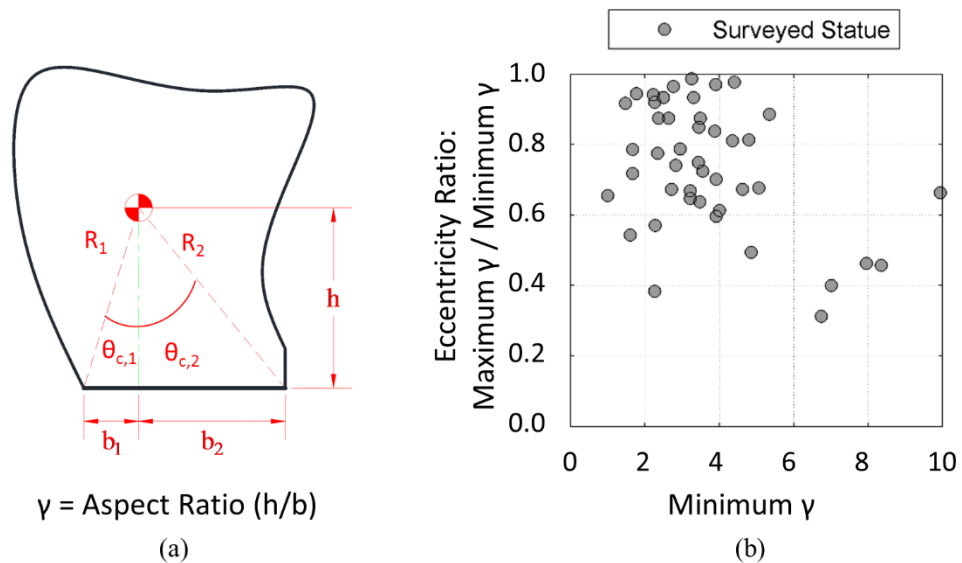


Figure 3.4 Two-dimensional schematic of an arbitrary statue with scatter plot of geometric data for surveyed statues.

3.3 Effect on Dynamic Response

Results from the survey indicate that human-form statues tend to be tall ($\gamma = \text{height}/\text{width} > 2.0$), asymmetric, and are commonly resting unattached on a squat pedestal with a rough interface. As a result, the statues can be studied in the context of rigid body dynamics. Significant research into the dynamics of two-dimensional rigid blocks has been done over the past several decades including derivation of the equations of motion for rocking (Housner 1963), sliding (Sinopoli 1997), and slide-rocking (Shenton 1996) as well as overturning (Zhang and Makris 2001), as detailed in Chapter 2 of this dissertation. Given the anticipated high coefficients of friction, this chapter only considers the rocking mode of response for the statues.

3.3.1 Equations of Motion

A detailed treatment of the classical rocking model is provided in Chapter 2. As such, the equations of motion and assumptions are only briefly described in this section. The geometric parameters for the two-dimensional idealization are illustrated in Figure 3.4a. While the footprint, mass moment of inertia, and mass are previously calculated for an individual statue, the remaining parameters can be calculated, including: 1) the slenderness, θ_c , and 2) the distance from the center of mass to a point of rocking, R . The two parameters are defined as:

$$\theta_c = \tan^{-1}(1/\gamma) \quad (3.1)$$

$$R = \sqrt{h^2 + b^2} \quad (3.2)$$

where $\gamma = h/b$, h is the height of the center of mass measured with respect to the base of the statue, and b is the horizontal distance to the center of mass from the extreme edge of the base of the statue. It should be noted that there are multiple values of α , γ , and R for an individual statue due to its asymmetry. In this chapter, the parameters associated with the more slender ‘side’ are termed ‘critical’ and given the subscript ‘1’, while those associated with the more squat ‘side’ are termed

‘noncritical’ and given the subscript ‘2’. The aspect ratio and rocking distance parameters of the four sample statues are included in Table 3.3 as calculated using the integrated properties in Table 3.2.

As detailed in Chapter 2, the equation of motion for rocking of a two-dimensional, nonrectangular rigid body are given in Equation (2.2) and restated here as:

$$\left(\frac{I}{m} + R_i^2\right) \cdot \ddot{\theta} = \ddot{x}_g \cdot R_i \cdot \cos(\theta_{c,i} - |\theta|) - \text{sgn}(\theta) \cdot R_i \cdot g \cdot \sin(\theta_{c,i} - |\theta|) \quad (3.3)$$

where the subscript i represents ‘critical’ or ‘noncritical’ parameters depending on the sign of rotation. Under the assumptions of rigid interfaces, no sliding, and perfectly inelastic impacts, as detailed in Chapter 2, the velocity adjustment factor for an impact is given in Equation (2.2) and restated here as:

$$r_i = \frac{1}{\left(\frac{I}{m} + R_i^2\right)} \cdot \left[\left(\frac{I}{m} + R_j^2\right) - B \cdot R_j \cdot \sin(\theta_{c,j}) \right] \quad (3.4)$$

where the subscripts i and j represent ‘critical’ or ‘noncritical’ parameters depending on the sign of rotation. It is noted that this coefficient is a function solely of the geometry of the block.

In this analysis, the equations of motion were integrated numerically using a 4th-5th order Runge-Kutta scheme and a state-space formulation in MATLAB (2012). At each time step, the algorithm solves for the rotation and rotational velocity; and, a velocity reduction is applied through the aforementioned velocity adjustment factor, or coefficient of restitution, at every detected impact. The rotation and reduced rotational velocity are then used in the computation for the next step. In addition to the velocity reduction, the geometric parameters (critical to noncritical or vice versa) alternate at each detected impact.

Table 3.3 Geometric and mass properties of four surveyed statues for rocking time history analysis in the transverse direction calculated using LiDAR_{1mm} meshes.

Statue (Artist)	$[\gamma_{crit} \ \gamma_{noncrit}] [-]$	$[R_{crit} \ R_{noncrit}] [m]$
Abraham and Isaac (Donatello/di Bartoli)	[3.89 2.96]	[0.84 0.86]
Florentine Pieta (Michelangelo)	[1.75 1.57]	[0.93 0.96]
Zuccone (Donatello)	[3.36 3.23]	[0.95 0.95]
Profeta (di Bartoli)	[5.04 4.98]	[1.05 1.05]

3.3.2 Effect of Point Cloud Resolution on Mass Properties

Prior to presenting time history analyses for individual statues, a sample study is presented of the variations in the relevant geometric parameters for the different methods of data acquisition. Figure 3.5 contains a series of plots presenting the variation in three geometric and mass properties for a subset of four statues of LiDAR at varying resolutions, SfM, and envelope shapes. The data is presented as a percent difference of the geometric or mass property with respect to a 1mm-decimated LiDAR mesh, considered the baseline or “ground truth”. The sample is limited to four statues due to the computational demand associated with developing and processing the point clouds and meshes, as well as the limited availability of statues with both LiDAR and SfM reconstructions. It is emphasized that these variations are unique to the individual statue and are not intended to be conclusive of all statues. Rather, these plots introduce the observed variations for this specific data set for better understanding of the dynamic time history analyses.

The scatter plots of Figure 3.5 emphasize the extremely poor approximation of the geometric properties by envelope shape for these statues. In particular, for the mass moment of inertia, the envelope shape yielded a value that varies from the high-resolution LiDAR by greater than 100%. The envelope shape shows marginal improvement with respect to calculation of R and

γ with variations up to 40%. The decimated LiDAR_{20mm} and SfM meshes showed variations up to 20% for each of the three presented geometric properties. This is in contrast to the snapshots provided in Figure 3.3 in which the meshes appear to superficially capture the statue geometry. The SfM meshes appear comparable or slightly more accurate than the decimated LiDAR_{20mm} or LiDAR_{50mm} for three of the four presented statues. The exception (*Abraham and Isaac*) yielded properties of SfM comparable to or less accurate than the envelope shape. This exception highlights the variability of SfM methods in terms of point coverage and resultant mesh due to minor occlusions or lack of surface texture.

In addition to the variations as a function of acquisition, large differences are observed among the geometric properties. While the aspect ratio and rocking distance are functions of the same two geometric properties, there is distinctly more variability in the aspect ratio. As the meshes decrease in resolution, the height of the center of mass tended to increase and the width of the base tended to decrease. This is evidenced in the snapshots of Figure 3.3 in which the mesh rounded out in the upper portion and the footprint narrowed. This proportional relationship of height of the center of mass and inverse proportional relationship of the width of the footprint with the aspect ratio can lead to significant increases in the aspect ratio. Whereas in the calculation of the rocking distance, the increase of the height and the decrease of the width largely balance each other.

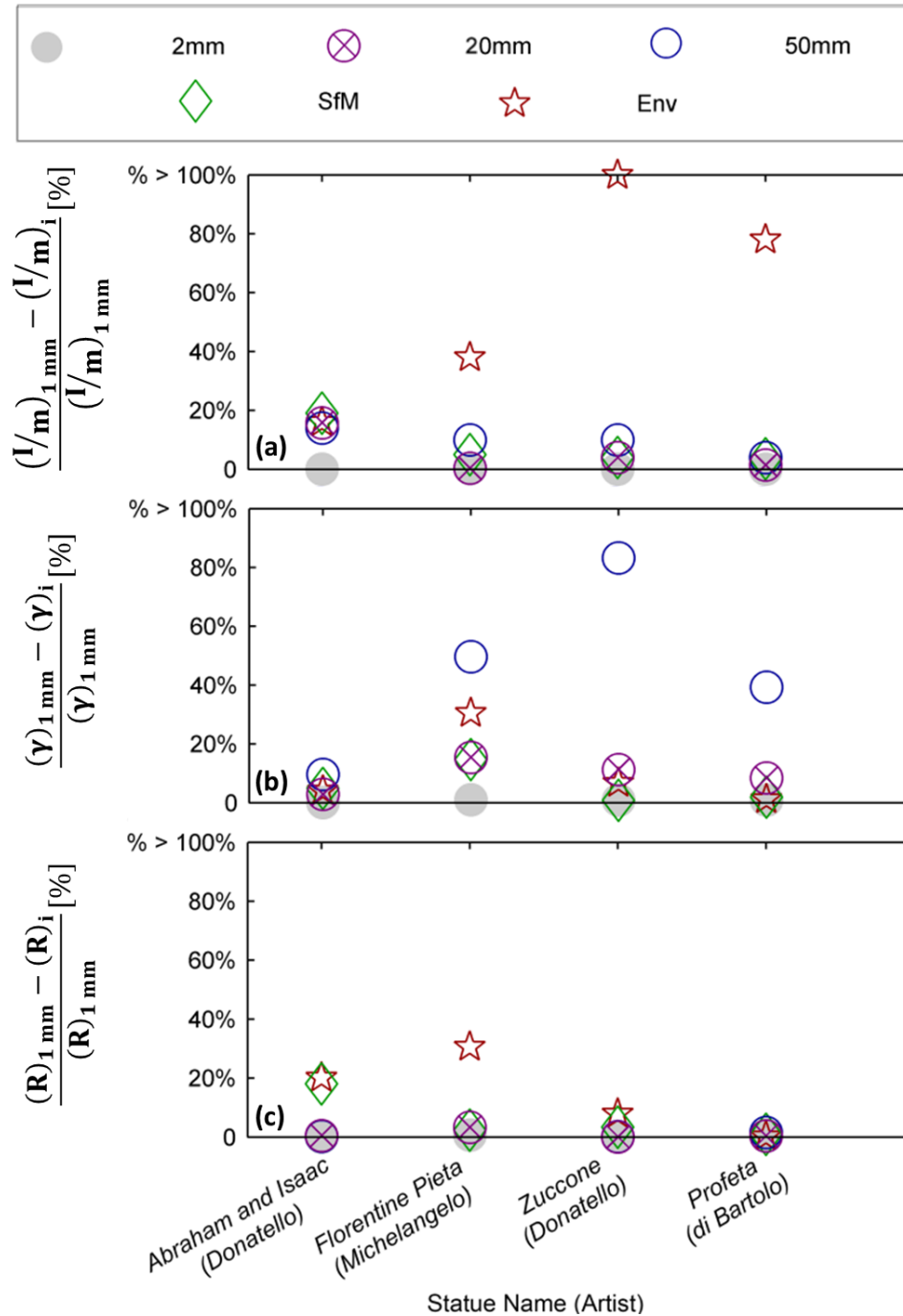


Figure 3.5 Percent difference between the LiDAR mesh at 1mm and the meshes at 2mm, 10mm, 50mm, and those generated by SfM and envelope shapes for four statues in terms of (a) normalized mass moment of inertia, (b) aspect ratio, and (c) rocking radius.

3.3.3 Effect of Point Cloud Resolution on Time History Analysis

The integrated time histories of the rocking response of two surveyed statues are included in Figure 3.6. The geometric parameters corresponding to the high-resolution LiDAR, the SfM, and the envelope shape are used in the integration to qualitatively compare the effects of the variation in the geometric properties. The sample input motion to these statues is the 1994 Northridge earthquake recorded at UCLA grounds (90-degree component) scaled to a peak ground acceleration of 0.90 g. This motion is selected in an effort to highlight the variable response of the statues due to the geometric data acquisition and is not intended to analyze the vulnerability of these statues. The acceleration time history of this earthquake record is also included in Figure 3.6. Refer to Table 3.2 and Table 3.3 for the geometric parameters in the transverse statue plane (YZ) as used in the equations of motion for the LiDAR mesh.

The response of the statue, *Abraham and Isaac*, is included in Figure 3.6a in which the overestimation of the rotations by envelope shape is clearly observed as well as the underestimation by SfM. The rotational overestimation by the envelope shape is most noticeable for positive rotations emphasizing the inability of the envelope shape to capture the statue's asymmetry. For example, the envelope shape records a maximum positive rotation of 0.201 radians compared to 0.136 radians computed using the properties of the LiDAR (a percentage error of 48%). It is important to note for this statue that the five geometric parameters used in this analysis each varied by no more than 20% between both the envelope shape and the SfM with the high-resolution LiDAR (refer back to Figure 3.5).

In contrast to *Abraham and Isaac*, the envelope shape and SfM of *Zuccone* were very similar to the LiDAR in terms of R and γ (less than 5% variation); however, the envelope shape overestimated the normalized mass moment of inertia, I/m , by over 200%. The response of *Zuccone* is included in Figure 3.6b. The geometry computed using the envelope shape does not yield a

conservative prediction as in the case of *Abraham and Isaac*. Rather, the envelope shape and the SfM produce stable responses with significantly lower maximum rotations of 0.113 radians and 0.145 radians, respectively, compared to 0.205 radians of the LiDAR model (percentage error of 45% and 30%). In addition to highlighting the importance of accurate mass moments of inertia, this example also emphasizes the large differences in response that can occur to relatively small perturbations in the geometric properties (such as the response due to SfM with less than 5% variation in each property).

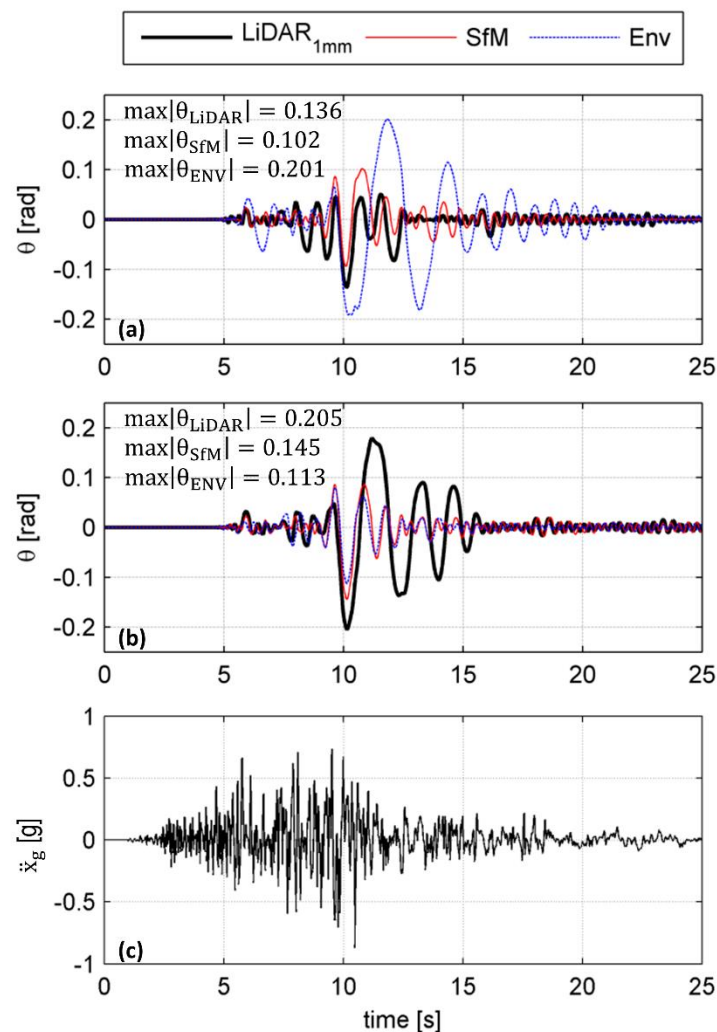


Figure 3.6 The analytical prediction of the rocking response of (a) *Abraham and Isaac*, and (b) *Zuccone* subject to (c) the acceleration history of Northridge earthquake at UCLA, scaled to a peak ground acceleration of 0.90g.

Although the findings presented in this section are specific to the input motion and to the individual statues, they elude to the possible impact, which may be either conservative or unconservative, that misrepresented geometry can have on the dynamic response of statues. In some cases, the envelope shape may yield a more slender geometry (γ increases) which would rock at lower values of acceleration and therefore may overestimate the response, as in the case of *Abraham and Isaac*. However, in other cases, the envelope shape may yield a larger (I/m and R increase) and potentially squatter geometry (γ decreases), which would rock at higher values of acceleration and therefore tend to be more stable (Housner 1963), as in the case of *Zuccone*. One cannot therefore conclude that approximate methods of geometric data acquisition are either conservative or unconservative due to their inconsistent overestimation and underestimation of the geometric parameters.

3.4 Conclusions

This chapter describes a survey of full-scale human-form culturally important marble statues in an effort to define their field characteristics essential for the analyses of statue response to seismic excitation. It further presents methods for geometric data acquisition and processing, and compares the results of such methods with respect to relevant properties needed for seismic analysis. The chapter concludes with the presentation of time history analyses using the classical rocking model for sample statues from the survey, illustrating the large variation in response due to the method of geometric data acquisition.

Field geometric data acquisition in this study involved use of Structure-from-Motion (SfM) and Light Detection and Ranging (LiDAR). While both are powerful strategies currently available to support geometric characterization, SfM and the use of envelope dimensions of the statue are simpler alternatives to LiDAR and the degree of accuracy is critical to characterize its seismic response. These methods can calculate aspect ratio and the distance to the center of mass

within 40%; however, differences greater than 100% may arise for the mass moment of inertia if computed using envelope dimensions. Furthermore, inappropriate geometric acquisition such as envelope shape rather than “ground truth” LiDAR can have a significant effect on the rigid body rocking time history analysis. In the analyses presented, variations up to 50% are observed in terms of the maximum rotational response.

3.5 Implications on Experimental Program

The first primary objective of this dissertation is to quantify a range of anticipated geometry and generate statistics on extreme geometric configurations of freestanding structural systems. The results of which guide an extensive shake table testing campaign, in the pursuit of the second primary objective. This chapter directly addresses this first objective and presents an extensive field survey of culturally-significant large, stone statue-pedestal systems, which is one of the most geometrically complex freestanding structural systems. Through this survey and subsequent analyses, the following conclusions and implications on shake table testing can be drawn:

- A very broad range of geometric configurations comprise the statue-pedestal systems surveyed. Aspect ratios calculated ranged from approximately 1.0 to values approaching 10.0. As a result, shake table testing needs to consider fairly squat and very tall configurations.
- The statues tended to incorporate varying degrees of mass eccentricity, with the majority of statues exhibiting eccentricity of the center of mass on the order of 70%. However, certain statues were calculated to have eccentricity ratios approaching 30%, which is severely asymmetric. As such, experimental specimens must incorporate varying levels of horizontal mass eccentricity – in both orthogonal directions.
- Nearly all of the surveyed statues were mounted freestanding atop a stone pedestal. The footprint of this pedestal is always greater than that of the statue, and a study of the

eccentricity shows that the pedestals are consistently symmetric. However, the aspect ratio of the pedestal varies from squat to tall, although this is to a much less degree than the variation of the statues. Therefore, shake table testing should account for the dual-body configuration in addition to single-body configurations, where the bottom body is of variable aspect ratio and consistent footprint.

- The statue-pedestal systems incorporated stone-stone interfaces. These interfaces were not polished; and, the experimental specimens should incorporate quarried stone material as-is, due to the untested interfaces of the surveyed statues.
- The statue-pedestal systems are located in buildings as well as outdoors. Therefore, shake table testing should include base excitations of varying frequency content, including filtered floor-level motions as well as free-field motions.

3.6 Acknowledgements

This work was supported by the National Science Foundation under IGERT Award #DGE-0966375. Additional support was provided by the World Cultural Heritage Society, Friends of CISA3, and the Italian Community Center of San Diego. The authors wish to thank the city of Florence, the city architect Giorgio Caselli, and the *Opera di Santa Maria del Fiore* for the permissions granted to access and scan the statue collections. The on-site assistance of Leonardo Rossi at the *Museo dell'Opera del Duomo* and Patrizio Mannucci at *Palazzo Vecchio* is greatly appreciated. The authors thank Marc Levoy and the Digital Michelangelo Project for providing additional data. Opinions, findings, and conclusions from this study are those of the authors and do not necessarily reflect the opinions of the sponsoring agencies.

This chapter, in part, is a reprint of the material as it appears in the American Society of Civil Engineers' Journal of Computing in Civil Engineering. Wittich, C.E. Hutchinson, T.C., Wood, R.L., Seracini, M., and Kuester, F. (2016). "Characterization of full-scale human-form

culturally important statues: case study” *J. Comput. Civ. Eng. (ASCE)*, 30(3), 05015001. The dissertation author was the primary investigator and first author of this publication.

Chapter 4 Shake Table Tests of Freestanding Structures:

Asymmetric Single-Body Tests

Freestanding structures have been observed to overturn and fail during earthquakes. The broad range of structures that fall into this classification serve to motivate their study. While a number of analytical studies have focused on the dynamic response of freestanding structures (e.g. Housner 1963), few experimental campaigns have been conducted. As such, the second primary objective of this dissertation is the generation of a comprehensive database of experimental response data for the seismic response of freestanding structures. Chapter 3 outlined the range of key geometric and material variables for consideration in shake table testing, which directly informs the design of the experiment detailed herein. Specifically, this chapter outlines the design, execution, and results of shake table testing of single-body freestanding structures considering mass eccentricity. The study of dual-body systems is detailed separately in Chapter 5.

4.1 Introduction

Initial studies on freestanding structures focused on the two-dimensional analytical formulation, which is based upon a number of assumptions and idealizations regarding rigidity and energy dissipation. As such, experimental campaigns are necessary to gage the limitations of the model and present a database for validation and calibration of numerical modelling approaches. A detailed review of experimental campaigns and shake table tests of freestanding structures is included in Chapter 2 of this dissertation, and only a brief overview is provided here.

Lipscombe and Pellegrino (1993) conducted one of the first campaigns for freestanding structures including an extensive experimental campaign for symmetric blocks of various aspect ratios and sizes. These results showed that the classical theory of Housner was highly inaccurate for very squat blocks (height-to-width ratio ≤ 1.0). The inaccuracies were attributed to the

introduction of bouncing and twisting upon impact. In recent years, additional experimental studies have focused on gaining further understanding of the response of symmetric blocks and systems of symmetric blocks (e.g. Mouzakis et al. 2002, Peña et al. 2008). In addition, the literature is rich with investigations focused specifically on a single type of unattached block, such as ancient columns (Drosos and Anastasopoulos 2014) or masonry walls (Costa et al. 2013). In particular, extensive experimental and numerical studies have been conducted focused on laboratory equipment which observed multiple modes of response (rocking and sliding) and validated a commercially available multi-physics solver for both modes (Konstantinidis and Makris 2009, 2010).

These and others, however, have primarily focused on bodies with symmetric geometries. Typically, geometric eccentricities have been accounted for on a case-study basis in which replicas of existing structures (e.g. statues) are tested under a limited number of ground motions or to demonstrate the applicability of a specific mitigation device (e.g. Agbabian et al. 1991, Podany 2008). A notable exception to this trend is the extensive shake table campaign of precariously balanced rocks by Purvance et al. (2008). The intent of this study was to understand the geometric and ground motion characteristics that produced overturning. While this study focused solely on the overturning rather than the entire rocking response, it concluded that variations in the slenderness due to eccentricity were more significant than variations in the size of the eccentric structure.

In this chapter, an extensive shake table campaign is presented consisting of more than 150 individual dynamic tests on single, stiff freestanding structures. The center of mass of the model structure was systematically translated vertically and horizontally to investigate the effects of geometric eccentricities on the bodies' seismic responses. Each configuration was subjected to a number of recorded and simulated earthquake motions on a uni-axial shake table. The main

variables in the test program were: 1) horizontal eccentricity in the direction of shaking, 2) horizontal eccentricity perpendicular to the direction of shaking, and 3) height of the center of mass. This experimental campaign is unique in that: 1) the geometric eccentricities were varied systematically in an effort to observe trends, and 2) multiple modes (e.g. rocking, sliding, and twisting) and modal transitions were allowed. It should be noted that this work is limited by the interface characteristics, which was selected as marble-marble, an interface commonly observed in culturally significant marble statues. In addition, this study is limited to structures with heights of the center of mass between 0.7 – 1.6 m and aspect ratios (height-to-width ratio) greater than 1.0. Due to the sensitivity of the response of unattached structures as noted in the literature, general trends are of particular focus in this dissertation and caution is suggested for extrapolation to other geometric configurations and interfaces outside of the measured frictional resistance.

4.2 Shake Table Test Program

4.2.1 Design and Construction of Model Statue Test Specimens

The large, culturally-significant statue-pedestal system has been identified as one of the most geometrically-complex freestanding structural systems; and, as such, serves as a primary motivator for this study. Chapter 3 presented a field survey of statue-pedestal systems and quantified a very broad range of geometry that these systems may include. Given the known nonlinearity with respect to geometry, it is a primary objective of this dissertation to generate a comprehensive database of experimental data across the range of anticipated geometry. As such, experimentation of real, culturally important, marble statues, in particular, would result in only limited knowledge and not be representative of the response of the range of systems surveyed. In addition, shake table testing of actual statues is not possible due to their irreplaceable nature and the high damage-risk associated with shake table tests. Furthermore, statue-specific testing would result in an inability to observe trends due to changes in certain aspects of geometry. Therefore, in

the present study, a stiff geometrically-variable specimen was designed to systematically vary the geometry of the statues. This conceptual design is presented in Figure 4.1, in which a sample surveyed statue-pedestal system is shown in the field juxtaposed with the statue-like experimental specimen. The link provided between these scenarios is the field survey of Chapter 3, which is summarized in this figure with two scatter plots. These scatter plots compare the range of the geometrically-variable specimen with the geometric quantities of the surveyed statues. As shown, the designed specimen can account for over 85% of the statues surveyed in the field in terms of size, slenderness, and eccentricity. The geometric parameters compared in these plots are defined in the schematic of Figure 4.2c.

The construction of the experimental specimen consists of: 1) a stiff, built-up steel tower, 2) a reinforced concrete-marble base, and 3) steel weight plates, which can be bolted in various configurations to induce geometric eccentricities. The tower is outfitted with holes and threaded rods at two different heights and on all four faces for installation of the weight plates. Figure 4.2 contains a sketch of the specimen with the weight plates in two configurations: symmetrically with a higher center of mass and eccentrically with a lower center of mass. Figure 4.2 also includes a schematic of a two-dimensional block including the relevant geometric parameters. The geometric parameters are as defined in the classical theory, namely: mass, m ; mass moment of inertia, I_0 ; rocking radius, R ; critical angle or slenderness, θ_c ; height of the center of mass, H ; width to the center of mass, B ; and corner or point of rocking, RP . The block is further characterized by a frequency parameter, p , which is a function of the geometry:

$$p = \sqrt{mgR/(I_0 + mR^2)} \quad (4.1)$$

where g is the acceleration due to gravity. It should be noted that there are two values of R , θ_c , RP , B , and p for an eccentric structure. In this chapter, a subscript ‘1’ indicates the geometric parameters associated with the smaller, more slender side; and, a subscript ‘2’ indicates the geometric parameters associated with the larger, more squat side.

Fifteen total configurations of the specimen were chosen for testing on the shake table. To observe trends in the results, at least three levels of variation were used for every parameter investigated. Therefore, the configurations are divided into three series corresponding to the height of the center of mass, three levels of in-plane (IP) eccentricity, and three levels of out-of-plane (OOP) eccentricity. A matrix of the configurations is included as Table 4.1. The three series are denoted as ‘U’, ‘L’, and ‘M’ corresponding to the location of the weight plates as ‘upper’, ‘lower’, or ‘moderate’ (distributed). Furthermore, in the present study, the level of eccentricity is defined as the ratio of the critical angles: $\theta_{c1} / \theta_{c2}$. Therefore, the level of eccentricity for the configurations is approximately 1.0, 0.80, and 0.50 for symmetric (IP1 or OP1), mildly eccentric (IP2 or OP2), and highly eccentric (IP3 or OP3). However, it should be noted that the frequency parameter (p) varies along with the critical angle, albeit to a significantly less degree. As the level of eccentricity ($\theta_{c1} / \theta_{c2}$) ranges from 0.5 – 1.0 for the tested configurations, the ratio of the frequency parameter (p_1 / p_2) ranges from 1.007 – 1.0. These ratios imply that the structure becomes more slender (reduced θ_c) and smaller (larger p) in the direction of eccentricity, and more squat (increased θ_c) and larger (smaller p) in the opposite direction.

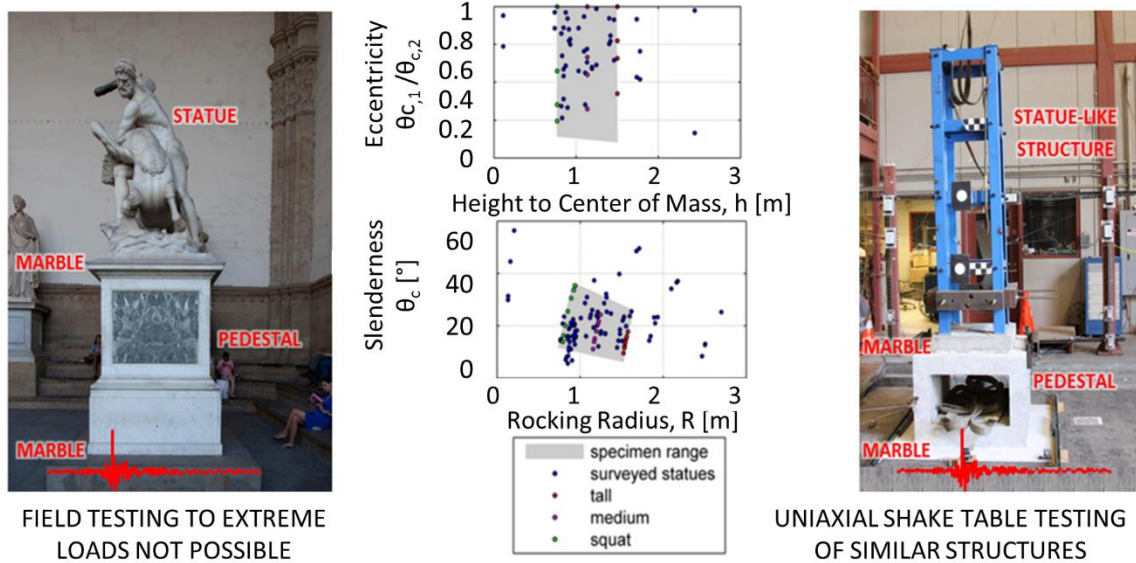


Figure 4.1 Conceptual design of experimental specimen and the range of the geometrically-variable statue-like structure.

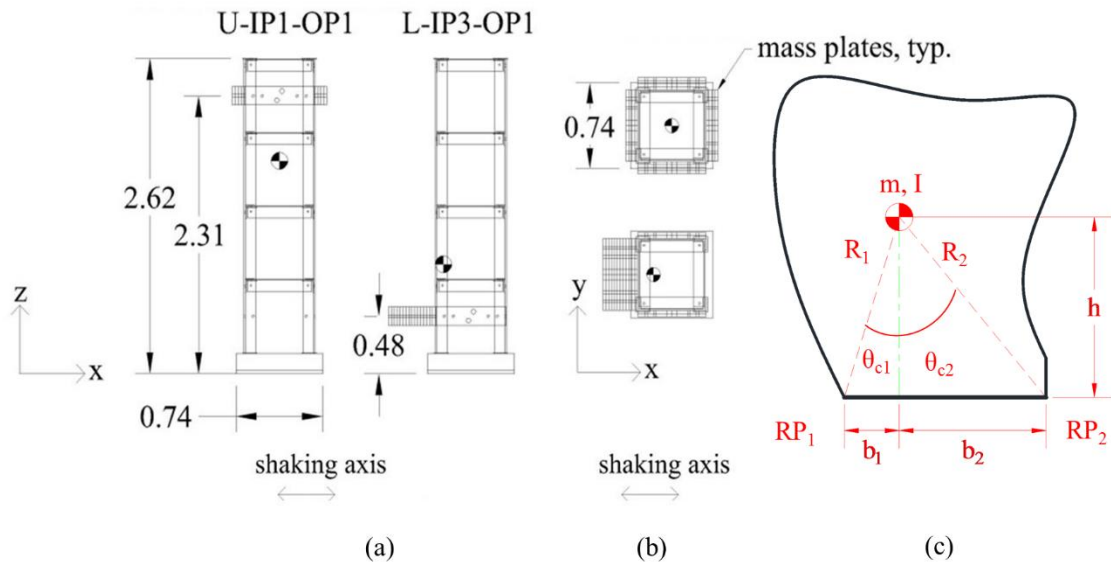


Figure 4.2 Key dimensions of the experimental specimen configured symmetrically with a higher center of mass and eccentrically with a lower center of mass, shown in (a) elevation and (b) plan views. (c) Arbitrary two-dimensional block and geometric labels. All units in meters.

Table 4.1 Geometric parameters of tested configurations.

Name ^[1]	H [m]	Direction ^[2]	θ_{c1} [°]	θ_{c2} [°]	R_1 [m]	R_2 [m]	p_1 [s ⁻¹]	p_2 [s ⁻¹]
U-IP1-OP1	1.45	IP	13.5	13.5	1.5	1.5	2.130	2.130
		OP	13.5	13.5	1.5	1.5	2.130	2.130
U-IP2-OP1	1.45	IP	12.0	14.9	1.5	1.5	2.134	2.128
		OP	13.5	13.5	1.5	1.5	2.129	2.129
U-IP3-OP1	1.45	IP	9.0	17.6	1.5	1.6	2.133	2.117
		OP	13.5	13.5	1.5	1.5	2.132	2.132
U-IP1-OP2	1.45	IP	13.5	13.5	1.5	1.5	2.129	2.129
		OP	12.0	14.9	1.5	1.5	2.134	2.128
U-IP1-OP3	1.45	IP	13.5	13.5	1.5	1.5	2.132	2.132
		OP	9.0	17.6	1.5	1.6	2.133	2.117
L-IP1-OP1	0.75	IP	26.3	26.3	0.8	0.8	2.559	2.559
		OP	26.3	26.3	0.8	0.8	2.559	2.559
L-IP2-OP1	0.75	IP	22.5	29.9	0.8	0.9	2.565	2.557
		OP	26.3	26.3	0.8	0.8	2.555	2.555
L-IP3-OP1	0.75	IP	16.9	34.4	0.8	0.9	2.546	2.526
		OP	26.3	26.3	0.8	0.8	2.568	2.568
L-IP1-OP2	0.75	IP	26.3	26.3	0.8	0.8	2.555	2.555
		OP	22.5	29.9	0.8	0.9	2.565	2.557
L-IP1-OP3	0.75	IP	26.3	26.3	0.8	0.8	2.568	2.568
		OP	16.9	34.4	0.8	0.9	2.546	2.526
M-IP1-OP1	1.10	IP	18.0	18.0	1.2	1.2	2.250	2.250
		OP	18.0	18.0	1.2	1.2	2.250	2.250
M-IP2-OP1	1.10	IP	16.5	20.0	1.2	1.2	2.255	2.248
		OP	18.0	18.0	1.2	1.2	2.252	2.252
M-IP3-OP1	1.10	IP	12.0	24.9	1.2	1.2	2.255	2.240
		OP	18.0	18.0	1.2	1.2	2.254	2.254
M-IP1-OP2	1.10	IP	18.0	18.0	1.2	1.2	2.252	2.252
		OP	16.5	20.0	1.2	1.2	2.255	2.248
M-IP1-OP3	1.10	IP	18.0	18.0	1.2	1.2	2.254	2.254
		OP	12.0	24.9	1.2	1.2	2.255	2.240

¹ Name is abbreviated using the series letter and two IP, OP levels: ‘U-IP3-OP’ becomes ‘U31’

‘IP’ refers to ‘in-plane’ or the XZ plane where Z is the elevation and X is the shaking direction

² ‘OP’ refers to ‘out-of-plane’ or the YZ plane where Y is the direction perpendicular to shaking

4.2.2 Measurement of As-Built Specimen Condition

In an effort to characterize the boundary conditions of the experimental setup, two tests were conducted throughout the program: 1) modal impact hammer testing of the specimen, and 2) friction tests at the marble-marble interface. The modal impact hammer testing consisted of instrumenting the specimen with magnetic accelerometers, exciting the specimen with a lightweight hammer, and analysis in the frequency domain through Fast Fourier Transform (FFT) and transfer functions. The fundamental frequency of the experimental specimen ranged from 17 – 32 Hz for all configurations, with an average value of approximately 25 Hz, which allows the specimen to be considered rigid (ICC 2007).

Measurement of the friction coefficient was first explored by conducting slow-pull tests, adding load until the specimen slipped across the marble base. The ratio of the applied load at the instant of slip to the weight of the sliding specimen yields an approximation of the static coefficient of friction. The friction test was repeated three times and yielded an average coefficient of static friction of 0.4. It is noted that this value is lower than the average measured and presented in the literature for marble-marble interfaces, where typical values range from 0.7 – 0.8 (refer to the experimental review of Ambraseys and Psycharis 2011). However, it is not outside of the bounds of what has been observed in past experiments. For example, tests reported in Peña et al. (2008) document initiation of sliding well below the threshold of static friction. Therefore, the as-built specimen was subject to harmonic motion with increasing acceleration amplitude of the shake table to understand its dynamic frictional behavior. During these tests, slip occurred at amplitudes greater than 0.37 g. Despite the significant difference between the static tests and the literature, the follow-on dynamic test yielded results similar to the present static tests. Moreover, they are quite similar to recent dynamic marble-marble tests reported in Drosos and Anastasopoulos (2014), which document an average value of 0.4 g. In general, the lower friction values in the present experiments,

compared with much of the literature, may be attributed to accumulated dust that filled the nominal imperfections at the interface as the marble was particularly soft. Moreover, the friction tests were conducted after the conclusion of the majority of rocking-dominated tests when asperities had likely smoothed.

In addition to the rigidity of the specimen and the frictional interface, the as-built specimen is characterized by an imperfectly level base due to concrete shrinkage and minor subsequent warping of the marble slab. This imperfection introduced an additional mode of response characterized by slight rocking or wobbling without uplift on the edges (true rocking). This wobble prevented perfect contact at the interface, while also preventing point impacts. This likely increased the rate of decay for large rotations of a rocking motion compared to a specimen with two distinct points of rotation. Furthermore, the increased impacts associated with the wobble mode may have smoothed asperities and reduced the frictional resistance. For complete details on the design of the experimental specimen and the as-built condition, refer to the experimental report (Wittich and Hutchinson 2014b).

4.2.3 Experimental Setup

The shake table campaign was carried out using a medium-sized uniaxial shake table at the University of California, San Diego. This single degree of freedom shake table consists of a 4.90 m by 3.05 m platen which slides horizontally on steel bearings driven by a double-acting hydraulic actuator. The table has a vertical load capacity of 350 kN, peak attainable acceleration of 9 g, a total horizontal stroke of 300 mm, and a maximum attainable velocity of 1 m/s. The mechanical setup atop the shake table consisted of: 1) experimental specimen, 2) fixed marble slab, and 3) safety catch system (Figure 4.3). A 1.2 m x 1.1 m slab of marble was fixed to the shake table platen to serve as the interface with the marble-base of the unrestrained experimental specimen. The unrestrained specimen was allowed to respond in all six degrees of freedom, despite the uniaxial

input. Due to the potential for overturning or excessive sliding of the specimen, a safety catch system consisting of a reaction frame and tow straps was installed, which allowed unrestrained rotation of the specimen up to $\pm 35^\circ$. Prior to each individual shake table test, the specimen was realigned to its original starting position. In addition, the marble-marble interface was cleared of any dust in an effort to maintain a consistent frictional interface.

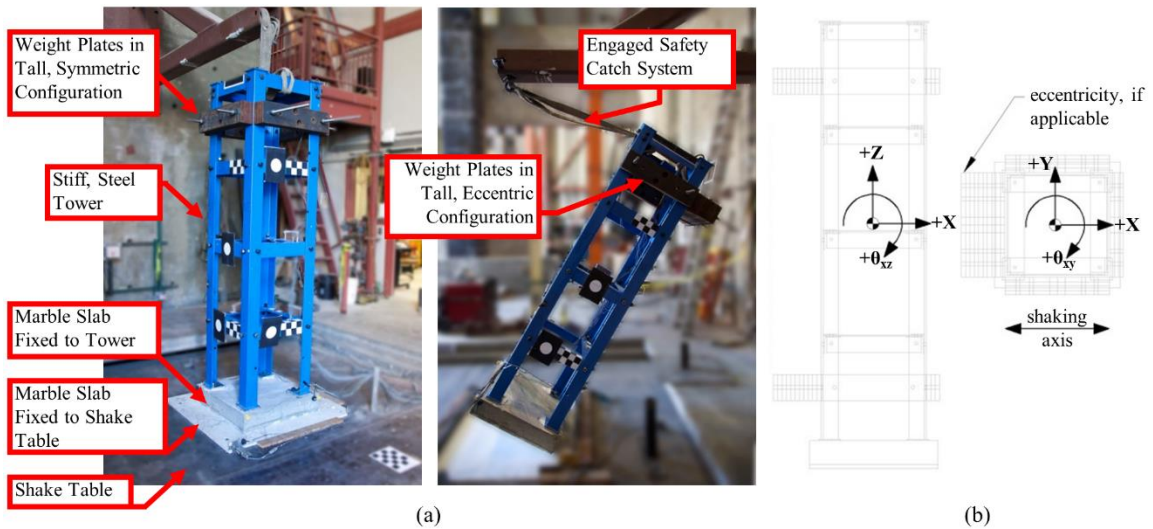


Figure 4.3 (a) Experimental setup including erect specimen and overturned specimen. (b) Elevation and plan views of the specimen indicating the primary directions and displacements. Note: θ_{xz} and θ_{xy} and Δ_x are referred to as “rocking”, “twisting”, and “sliding”, respectively.

4.2.4 Instrumentation

The input and the response of the specimen were monitored using a system of accelerometers, string potentiometers, and high definition video cameras. The input to the system was measured using a pair of horizontal accelerometers on either side of the system. This was further augmented by a string potentiometer for the shake table’s displacement as well as vertical accelerometers. The transfer of the input motion to the top of the fixed marble slab was similarly measured using a pair of horizontal accelerometers and a pair of vertical accelerometers. Linear potentiometers verified that the anchored slab did not translate or rotate during testing.

The translation and rotation of the specimen in the direction of shaking and in the perpendicular were calculated using measurements from pairs of string potentiometers. However, the rotation of the specimen about the vertical axis was measured using a high-frame rate (120 fps), high-definition (720p) video camera mounted on the safety catch reaction frame. Following correction for distortion, a pair of circular targets was tracked frame-by-frame to obtain the rotation. The translations and rotations of interest are illustrated in Figure 4.3b. In this chapter, the translation in the direction of shaking (Δ_x) is referred to as sliding. The rotation in the direction of shaking (θ_{xz}) is referred to as rocking, and the rotation about the vertical (θ_{xy}) is referred to as twisting. The remaining translations and rotations were not noticeably excited and are not further discussed. It should be noted that eccentricity (when incorporated) is added in the $-X$ direction. This yields a structure which is smaller and more slender (increased p , reduced θ_c) in the $-X$ direction while larger and squatter (reduced p , increased θ_c) in the $+X$ direction. This also corresponds to negative rocking, $-\theta_{xz}$, about the eccentric side of the structure.

4.2.5 Camera Layout

Although a wide system of instrumentation is previously outlined, the complex and large-displacement response of the specimen could not be adequately captured using traditional sensors alone. While three 100 in potentiometers were made available during this experiment, a large array of high-definition cameras was used for both imaged-based motion tracking and for simple recording. Figure 4.4 provides the location of each camera utilized in the testing program, whereas Table 5.2 lists the specifications of each camera employed and the viewpoint of the camera. Three standard camcorders recorded in full HD at 30 frames per second from non-critical viewpoints. Three GOPRO cameras recorded at high frame rates (60 frames per second or 120 frames per second) in positions on or above the shake table. Two of these cameras (one at 720p and one at 480p) recorded a close-up on the marble-marble interface at 120 frames per second. These critical

viewpoints convey additional information that the traditional sensors could not (e.g. any crushing of marble, bouncing, or mode transition). The remaining GOPRO camera was positioned for a top view and was used particularly for twisting time-history measurements, the data processing of which is discussed later in this chapter. Two additional digital single-lens reflex (DSLR) cameras were used for front and back views of the specimen due to their relatively low lens distortion compared to the camcorders.

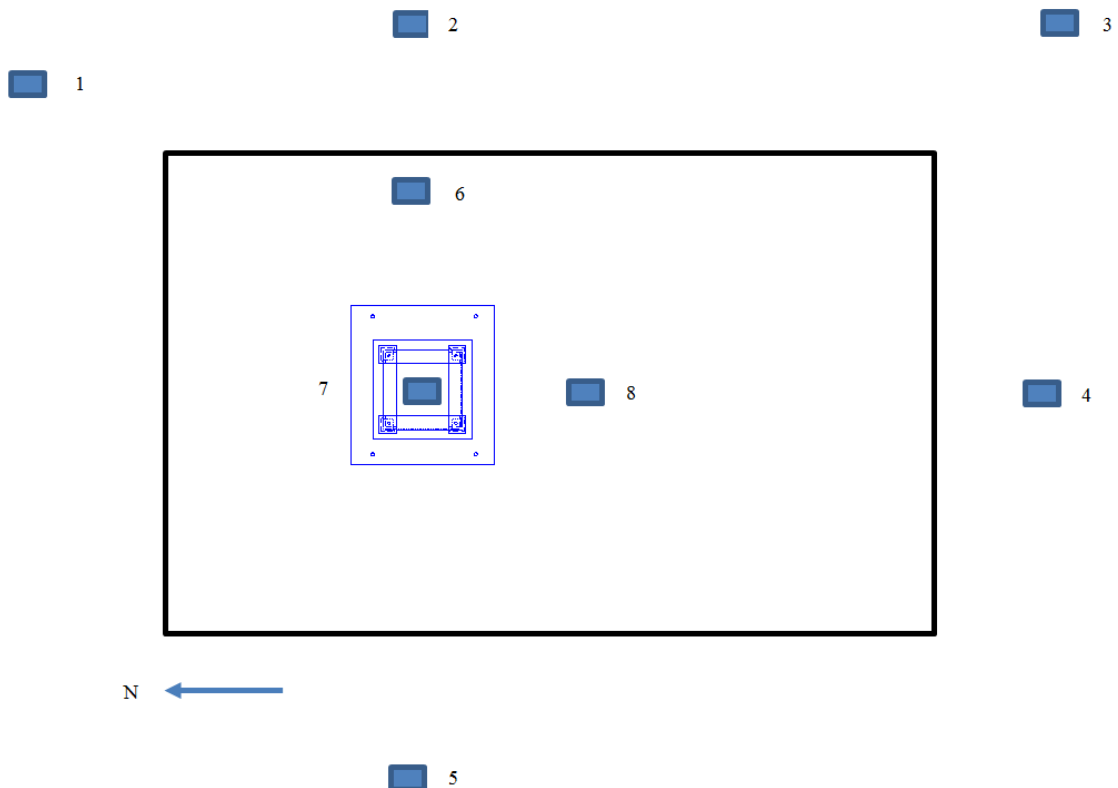


Figure 4.4 Plan view of locations of cameras used.

Table 4.2 Specifications of cameras used and sample viewpoints.

No.	Camera	Type	Frame Size	Frame Rate	No.	Camera	Type	Frame Size	Frame Rate
1	Samsung S10	Camcorder	1080 p	30 fps	3	Canon Vixia HFR30	Camcorder	1080 p	30 fps
									
2	Canon Mark ii 5D	DSLR	1080 p	30 fps	4	Canon Vixia HFS10	Camcorder	1080 p	30 fps
									
6	GOPRO Hero3	Camcorder	720 p	120 fps	7	Sony α35	DSLR	1080 p	30 fps
									
8	GOPRO Hero3	Camcorder	1080 p	60 fps	5	GOPRO Hero2	Camcorder	480 p	120 fps
									

4.2.6 Input Motions

Due to the anticipated rigid body response of the specimen and little anticipation of damage accumulation, the number and progression of selected input motions was limited only by timing and economical concerns. For these reasons, the number of ground motions per configuration was selected as no more than twelve. Three types of ground motion were chosen for testing: 1) pulse-like ground motions, both short-period and longer-period; 2) a broadband ground motion meant to be scaled multiple times for the same configuration; and 3) a simulated increasing sinusoidal protocol meant to induce many cycles of input. A table of the selected ground motions is included in Table 4.3.

Velocity pulses have long been correlated with overturning in rigid blocks – studies concluding this date back to the seminal work of Housner (1963). For this reason, pulses and pulse-like earthquakes were of particular interest for this experiment. Pulses occur in earthquakes due to either permanent displacement of the ground (fling step) or directivity effects, and are observed in the near-field (less than 10 km from the epicenter). Due to the shake table's displacement limitations, only pulses caused by directivity effects are considered and the total number of applicable ground motions is limited. Selection of the pulse-like motions was performed using wavelet analysis of the velocity time history, as proposed by Baker (2007). This method represents the time history as a sum of wavelets in which the predominant wavelet can be extracted. Two ground motions were selected from the PEER-NGA database with approximated wavelet periods of 0.9 s (i.e. 1999 Duzce Earthquake at Bolu, Chiou et al. 2008) and 1.8 s (i.e. 1989 Loma Prieta Earthquake at Gavilan College, Chiou et al. 2008). The extracted wavelet (referred to as pulse) and the transient component of the ground motion were also included for testing, where the transient is defined as the pulse component subtracted from the total motion. The pseudo-spectral acceleration spectra of the two selected motions including the extracted pulses and transient components are

included in Figure 4.5a-b. In addition, time histories of the achieved motions are included in Figure 4.6. It should be noted that the shake table produces significant high-frequency amplification due to the friction bearings; however, the low-frequency components of the input motion are well preserved. For comparison with the selected pulse-like ground motions, the selected broadband ground motion is the 1994 Northridge Earthquake at UCLA. The motion was selected so that it could be scaled multiple times to observe the progressive response of the specimen. Typically, the motion was scaled five times with the scale factors varying for each configuration in an effort to observe initiation of rigid body response through failure (overturning). The spectra and achieved time history of this motion is included in Figure 4.5c and Figure 4.6, respectively.

Due to the variability of earthquakes in terms of frequency content and amplitude, it is possible for rigid bodies to simply fail without exhibiting any classical rigid body modes (i.e. overturning with no rocking impacts or stick-slip sliding to failure). The primary focus of the shake table protocol developed herein is to induce many cycles of gradually increasing response; this is likely evidenced through large rotations, potential localized damage, and observation of both the initiation of response and failure. As such, the final input motion is a forward-oriented sinusoidal protocol increasing in a step-wise fashion. The protocol is based on normalized cycle-amplitude statistics garnered through rainflow cycle counting of the far-field and near-field ground motions of FEMA P695 (ATC 2009). The forcing frequency of the protocol varied according to the height of the center of mass of the configuration. Details on the development of the protocol are included in (Wittich and Hutchinson 2014a). The spectra and achieved time histories of the protocol are similarly included in Figure 4.5d and Figure 4.6, respectively.

Table 4.3 Specifications of selected input motions.

ID	Event	Station	M_w	PGA ^[1]	PGV ^[1]	PGD ^[1]	Tp ^[1]	ω_p/p ^[5]
				[g]	[cm/s]	[cm]	[s]	[-]
GM1A	Duzce, Turkey (1999) - original	Bolu	7.2	0.82	62.1	13.6	0.9	2.7 – 3.3
GM1B ^[2]	Duzce, Turkey (1999) - transient	Bolu	7.2	0.41	25.5	10.4	0.3	8.2 – 9.9
GM1C ^[3]	Duzce, Turkey (1999) - pulse	Bolu	7.2	0.61	63.2	10.6	0.9	2.7 – 3.3
GM2A	Loma Prieta, CA (1989) - original	Gavilan Coll.	6.9	0.79	61.3	13.6	1.8	1.4 – 1.6
GM2B ^[2]	Loma Prieta, CA (1989) - transient	Gavilan Coll.	6.9	0.88	38.9	11.6	0.1	25 – 30
GM2C ^[3]	Loma Prieta, CA (1989) - pulse	Gavilan Coll.	6.9	0.17	37.9	7.9	1.8	1.4 – 1.6
GM3 ^[4]	Northridge, CA (1994)	UCLA	6.7	0.28	21.9	4.1	0.2	12 – 15
GM4	Sinusoidal Protocol	-	-	[0.6 0.75]	[76.7 80.2]	[7.8 10.8]	[0.65 0.85]	2.9 – 4.6

¹ PGA = peak ground acceleration; PGV = peak ground velocity; PGD = peak ground displacement; Tp = predominant pulse period, ω_p = predominant pulse frequency.

² Transient component is equal to the total motion subtract the pulse component

³ Pulse component as determined by wavelet analysis for near-fault

⁴ Motion was implemented with various scale factors

⁵ Frequency ratio calculated using maximum and minimum values of p

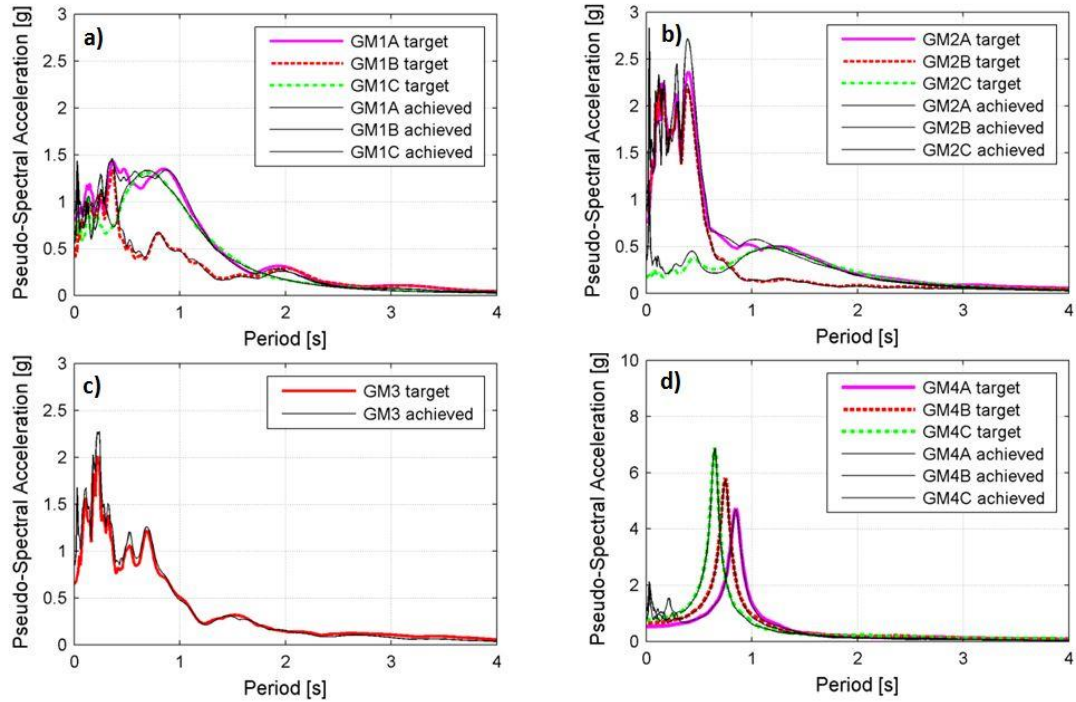


Figure 4.5 Pseudo-spectral elastic acceleration of the target and achieved motions atop the shake table for (a) GM1A-C, (b) GM2A-C, (c) GM3, and (d) GM4 (refer to Table 4.3).

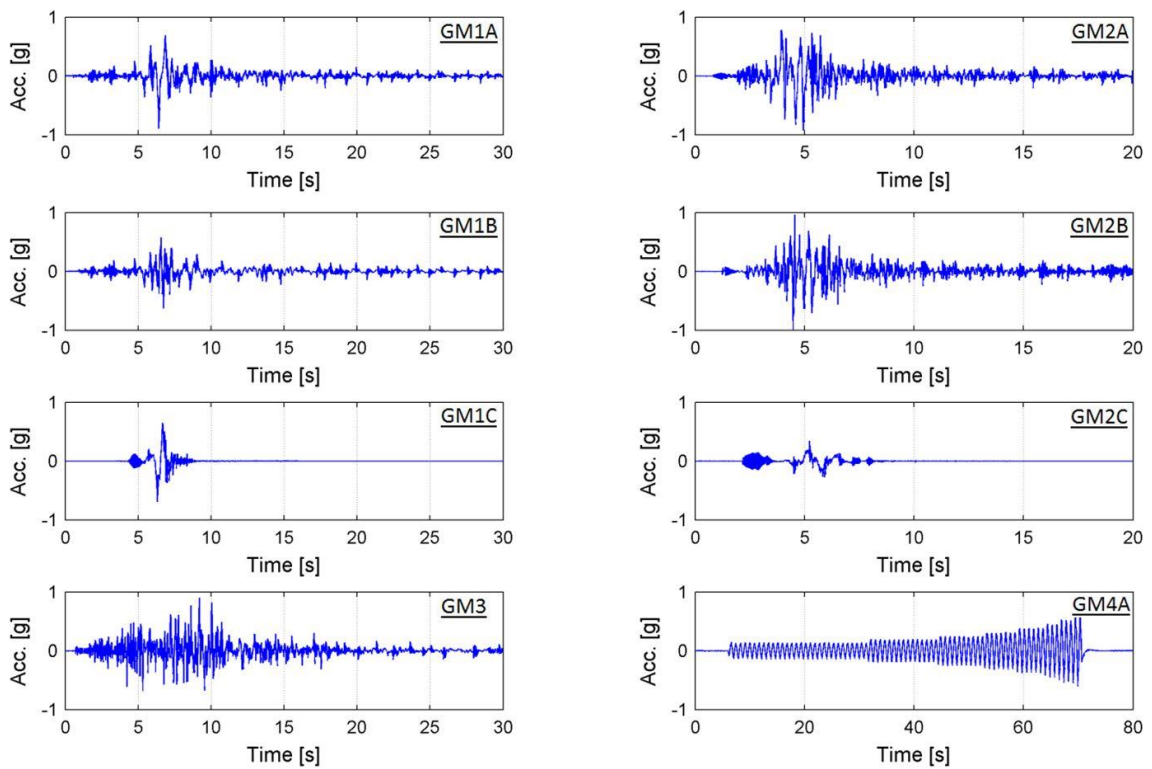


Figure 4.6 Acceleration time histories of the input motions as achieved on the shake table.

4.2.7 Test Procedure

With such a large test matrix consisting of over 150 individual tests, consistency amongst tests and configurations was critical. Consistency was sought for data recording through the DAQ, camera recording, and documentation. Each configuration and each ground motion needed to be properly carried out to facilitate comparisons amongst the tests. The procedures followed are included in the following two sub-sections for configuration and for ground motion, respectively.

The procedure for testing a configuration (typically completed in one day) is listed as follows:

1. Modify location of weight plate for configuration to be tested according.
2. Conduct modal hammer testing of the configuration to verify rigidity.
3. Place specimen on marble ensuring specimen is as square as possible to minimize any initial twist. Target starting location is marked on the fixed marble slab.
4. Warm up pumps and table (to be done by lab staff).
5. Exercise the valves of the table (to be done by lab staff).
6. Place tripods for digital video collection.
7. Place cameras and begin recording. (Note that sufficient memory was provided to each camera except the GOPRO cameras to allow for continuous recording during testing per configuration.)
8. Follow ground motion procedure for first GM indicated in test matrix.
9. Repeat step 8 for all ground motions in test matrix.
10. Stop recording on all cameras.
11. Remove specimen from marble.

12. Document the condition of the marble slab and measure permanent displacement and twisting marked (in colored pencil) on the marble.
13. Erase all pencil marks on marble.
14. Roughen or clean the marble slab, as necessary, in an effort to be consistent.
15. Download video data and clear internal memory or memory card.
16. Reduce data from the data acquisition system and save.
17. Repeat steps 1 – 13 for every configuration in test matrix.

The procedure for testing a ground motion is listed as follows:

1. Show white board in view of each camera (begin recording, if necessary). White board indicates date, configuration, and ground motion.
2. Bring table to high pressure (ready for testing).
3. Remotely start recording on GOPRO devices.
4. Begin countdown to motion.
5. Begin data acquisition, sampling at 200 Hz.
6. Execute ground motion. Abort the motion if specimen overturns.
7. Bring table to low pressure (safe for documentation).
8. Stop data acquisition, reduce data to text file.
9. Stop GOPRO recording.
10. Using a motion-specific colored pencil, outline final position (translation and rotation) of the specimen on the base marble.

11. Document final position and any material damage using Canon Mark ii 5D camera and a measuring tape.
12. Note predominant mode and pencil used in configuration data sheet.
13. Re-position specimen.

4.3 Data Processing for High Resolution Videos

This section presents the results and processing of the data obtained from the shake table experiment. While the processing of the string potentiometers was relatively straightforward for a shake table testing campaign, the motion tracking of the high frame rate cameras is discussed in detail in this section, which was particularly useful for tracking three-dimensional effects and twisting of the specimen. This section specifically details the pre-processing of the videos, treatment of lens distortion, and the final algorithm for motion tracking.

4.3.1 Raw Data

Due to the complicated motion of the specimen, a system of cameras was included for additional sensing. Although many cameras were incorporated in the instrumentation schedule, one camera was used specifically for measurements through a motion tracking algorithm. The camera employed for the motion tracking was a GOPRO Hero 3 Black Edition video camera. This camera recorded in full HD (1920 x 1080 pixels), 60 frames per second, and in the system's 'wide' field of view (higher levels of distortion). This field of view was necessary in order to maximize the viewable response of the specimen and the limited mounting locations. This camera was positioned on the safety catch frame, above the specimen. The camera's view included the top of the specimen including two flat, white-on-black targets fixed to the top beam of the specimen (see Table 4.2). These targets were used to track the in-plane and out-of-plane motion of the specimen at the top level on a frame-by-frame basis.

4.3.2 Lens Distortion

Prior to any measurements or calculation, the distortion associated with a camera and a lens must be accounted. Lens distortion is present in all cameras and causes straight lines in the field of view to appear curved in the image. For the GOPRO, the distortion is specifically barrel distortion in which the image magnifies with distance from the optical axis giving the appearance that the image has been mapped around a sphere. This spherical image can be unmapped to a flat image through a coordinate transformation from the three-dimensional sphere to a two-dimensional plane provided certain information regarding the lens.

The camera model used for the GOPRO lens was that of Bouguet (2004) which is modeled after Heikkila and Silven (1997). The parameters that define the camera in this model are: focal length (f_c), principal point (cc), skew ($ac = 0$, for square pixels), and distortion coefficients (kc). The Camera Calibration Toolbox for MATLAB (Bouguet 2004) was used to determine these parameters for the GOPRO camera in the ‘wide’ field of view, whereby the following steps were taken:

1. A printed, flat, black and white grid of 30 mm x 30 mm (1.18 in x 1.18 in) was created.
2. Video recorded at many angles of the grid with the GOPRO camera at 60 fps, 1080p, and at the ‘wide’ field of view.
3. Fifteen frames were extracted from the video file so that the grid was at a different angle and position in the field of view for each frame. This step was completed using MATLAB.
4. Using the toolbox functions, pixel locations of the corners of the grid are manually selected.
5. Using the toolbox functions, calibration of the fifteen images is completed using a nonlinear optimization yielding the distortion coefficients.

This procedure yielded the following parameters for the GOPRO lens in the ‘wide’ field of view: $fc = [852.03; 872.06]$; $cc = [947.47; 556.25]$; $ac = 0$; and, $kc = [-0.2374; 0.0519; 0.00033; 0.0016; 0.0000]$. Provided these parameters for the camera lens, undistortion of an image is implemented by two-dimensional linear interpolation. A function written in MATLAB (2012) by the author then reads in each video and undistorts it frame-by-frame, exporting a new video file which can be used for measurements and calculations. Figure 5.2 contains snapshots of an example video from the GOPRO camera, both original distorted video and undistorted video.



Figure 4.7 Example frames from top-view GOPRO: (a) distorted, color frame, and (b) undistorted, uncolored frame.

4.3.3 Motion Tracking Algorithm

In order to track the motion of the specimen through the camera data, two flat, circular, white-on-black targets were fixed to the top of the specimen. The circular targets, which are seen in Figure 4.7, were of the same specific diameter (4.0 in or 10.1 cm) to aid in any calculations. The motion is tracked on a frame-by-frame (undistorted) basis by locating the pixel location of the center of the circles. Although the targets are circular, the center of each was not found by standard circle detection algorithm beyond the first time step. Rather, the video frame was converted to a binary (pure black and white) image which separated the targets from the complicated background. This was done to account for rotation of the specimen, blurring of the targets, and lighting changes. The centroid of each target could then easily be calculated, along with many other quantities such

as the minor axis length and the major axis length which aid in unit conversion on a frame-by-frame basis from pixels to distance measurements. The motion tracking algorithm which results in the aforementioned eight response quantities is outlined as:

1. Open first undistorted frame of video.
2. Estimate location of two circles' centers using Hough transform (MATLAB command *imfindcircles* enforcing a radius range of [70 105] pixels to eliminate false positives. This estimation will serve to bound the field of view for the next frame to maximize processing speed.
3. For each of the two targets, track the motion of the center (internal MATLAB function):
 - a. Open next undistorted frame of video.
 - b. Convert image to binary (black-and-white) based upon threshold of 0.7 where 0 is black and 1 is white. This threshold was determined based on visual inspection for typical frames.
 - c. Specify the field of view for motion tracking defined as a square with length 130% of the previous radius and centered on the previous centroid (or results of Hough transform for second frame).
 - d. Determine the geometric properties of the all contiguous white (1 in binary) space in the field of view:
 - i. 'Centroid' for tracking
 - ii. 'Area' for elimination of false targets
 - iii. 'Minor Axis Length' to aid in unit conversion (typically in the local x-direction)
 - iv. 'Major Axis Length' to aid in unit conversion (typically in the local y-direction)
 - e. Save the centroid (x,y) and axes lengths of the largest area in an array by frame.

- f. Repeat sub-steps a-e for second frame of video.

This algorithm was developed and implemented in a series of MATLAB functions progressing from distortion correction to motion tracking and saving of the final eight centroid and axes length quantities parameters. The saved quantities will be synthesized with the data from the DAQ and used to characterize the response of the specimen which will be discussed in the following section. The accuracy of the algorithm with respect to locating the targets and calculating the respective centroids is illustrated in Figure 4.8. It can be seen that the algorithm correctly locates both targets both while it is centered in the frame and when it is highly rotated and non-circular.

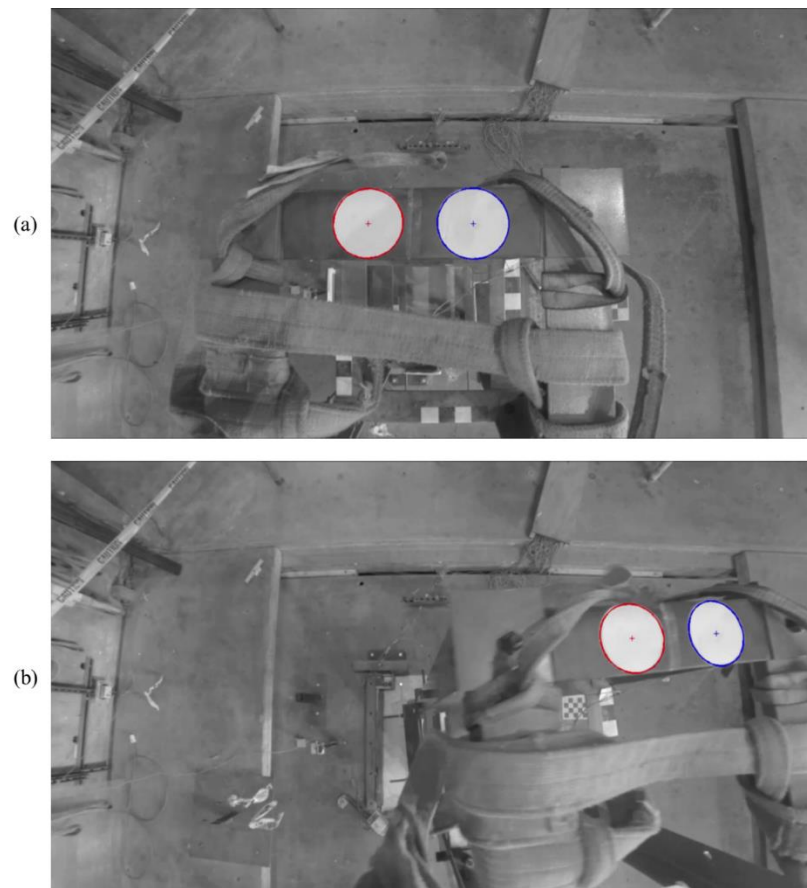


Figure 4.8 Motion tracking of specimen from top-view GOPRO: (a) original position of targets identified, (b) targets automatically detected in elliptical form for rotation calculations.

4.3.4 Time Alignment

The GOPRO positioned above the specimen on the safety catch frame was used in conjunction with the string potentiometers to record the complex motion of the specimen undergoing seismic excitation. The potentiometers were sampled at 200 Hz using the central data acquisition system; whereas, the cameras were sampled at 60 Hz and are not synchronized. As a result, time alignment based on peak displacements and re-sampling of the data were necessary.

Data from the string potentiometers was acquired through the UCSD Data Acquisition System (UCSD-DAQ) at an approximate rate of 200 Hz, or more specifically at a time step of 0.004992 s. All of the displacement transducers were controlled by the UCSD-DAQ and each began recording simultaneously – there is no time delay for these sensors. However, the cameras were not able to automatically begin recording with the UCSD-DAQ. The camera was controlled remotely using the GOPRO's Wi-Fi capabilities and recording began approximately 5 seconds before the DAQ began recording. As a result, there is a variable time delay associated with any measurements taken from the camera. Furthermore, the camera sampled at 60 frames per second requiring re-sampling of the data to facilitate syncing with the potentiometers.

Time synchronization of the data from the UCSD-DAQ and the motion tracking cannot be done explicitly because the two systems do not directly measure any of the same quantities. Therefore, the time synchronization is based on similar quantities from the systems, namely the total in-plane displacement of the specimen (recorded at various heights). The total in-plane displacement of the specimen was recorded by two string potentiometers at heights of 1.02 m and 1.40 m above the base. This displacement at 2.54 m can also be obtained from the motion tracking algorithm. These time histories will be similar in shape and zero-crossings, but will have varying magnitudes depending on the height along the specimen. As such, the time delay associated with the motion tracking data can be determined through a cross-correlation of these time series. The

cross-correlation function is a measure of similarity between two separate time histories as a function of a time lag. The cross-correlation equation for two arbitrary time series f and g is: $(f * g)[n] \stackrel{\text{def}}{=} \sum_{m=-\infty}^{\infty} f^*[m]g[n + m]$, where f^* is the complex conjugate. The location of the peak of the cross-correlation function would indicate the time delay which results in the most similarity between the two time series. The procedure for this time synchronization and data resampling followed is:

1. Re-sample the in-plane potentiometer at 1.40 m from base to 60 Hz using linear interpolation. Save this vector as $X_{55-60Hz}$.
2. Read in the in-plane displacement calculated from the motion tracking algorithm, X_{100} . This quantity will be discussed further in the following section.
3. Compute the cross-correlation function of the two time series using the *xcorr* function in MATLAB.
4. Locate the maximum of the cross-correlation function, n_{max} .
5. Calculate the time delay: $t_{lag} = 0.01668s(n_{max} - n_{X55-60})$, where n_{X55-60} is the total number of points in the time series X_{55-60} .
6. Shift the time series X_{100} : $t_{X100-shifted} = t_{X100} - t_{lag}$

These steps are further illustrated in Figure 4.9 which shows the time synchronization process step-by-step using as an example the M_IP1_OP3 configuration subject to GM1C (extracted pulse of the Duzce earthquake recorded at Bolu). The synchronization is verified in the part (d) of the figure with the time correctly aligned between the camera system and the potentiometer. In addition, the displacement is larger than the lower potentiometer (as expected) due to the large in-plane rotation of the specimen.

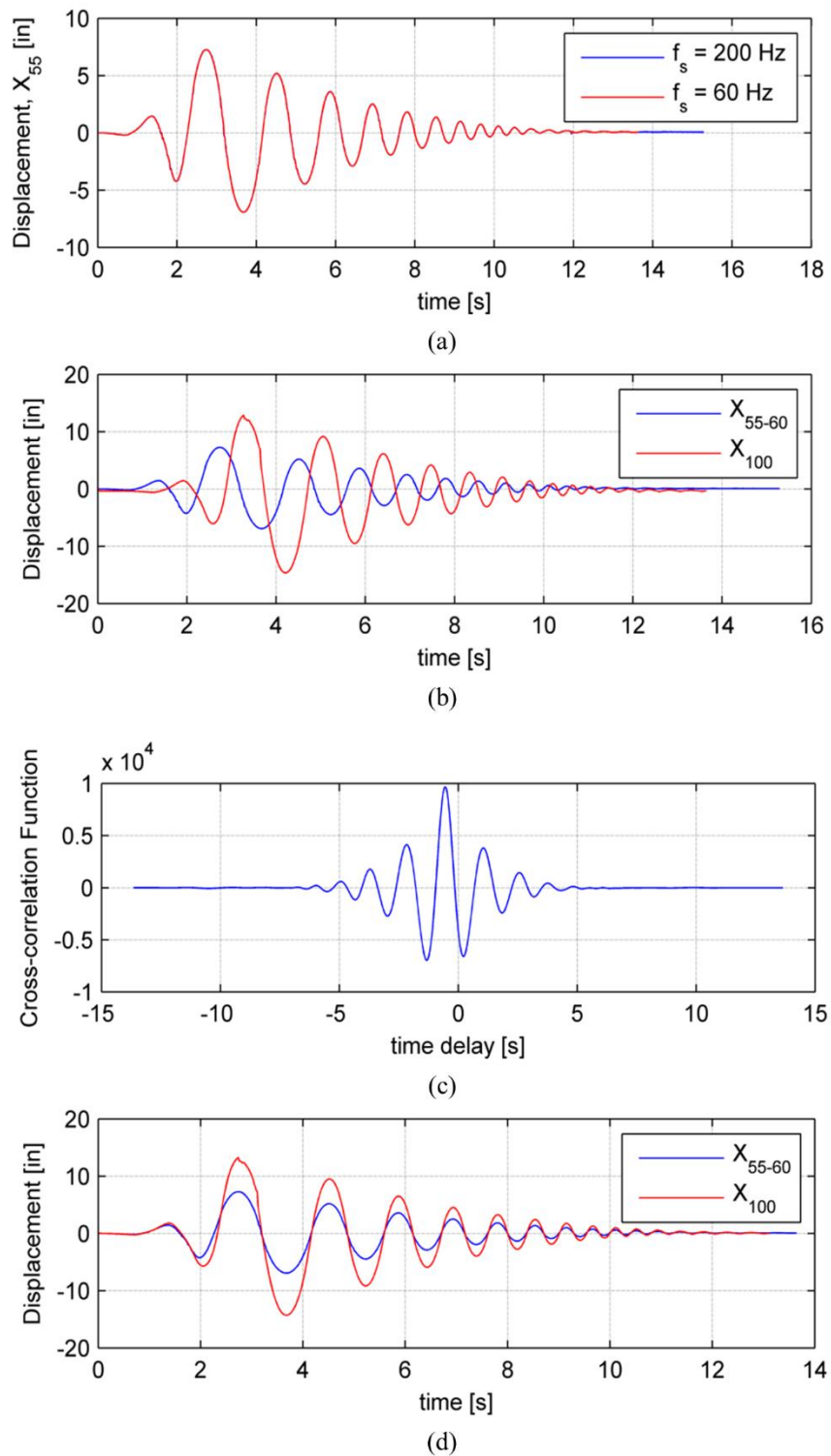


Figure 4.9 Time synchronization of potentiometer and camera data: (a) Original and down-sampled potentiometer data, (b) down-sampled potentiometer data and horizontal motion tracked by camera, (c) cross-correlation, and (d) synchronized time histories.

4.4 Results and Interpretation

A primary goal of this experimental campaign was to analyze the primary modes of response of freestanding structures and to develop trends which correlate the geometric variations and eccentricities with type, magnitude, and direction of these modes. The main variables in this experiment which will be discussed in detail in this chapter are: 1) horizontal mass eccentricity, both in- and out-of-plane, 2) vertical mass eccentricity in which the height of the center of mass varies, and 3) input excitation, particularly pulse effects.

To guide the discussion and analysis of the results, representative time histories are included in Figure 4.10 of both symmetric (IP1-OP1) and in-plane eccentric (IP3-OP1) for smaller, squatter (L) and larger, taller (U) configurations. It should be noted that the 'L' and 'U' configurations are presented for GM1C and GM3C, respectively, in an effort to highlight the salient characteristics of behavior. One of the most prominent observations in the time histories is that rocking, sliding, and twisting behavior were observed in nearly all tests to some degree. In addition, there is a drastic difference between the responses of the two series when in-plane eccentricity is incorporated. The squatter, smaller, symmetric (L11) configuration responds in both sliding and twisting with minimal rocking. However, its eccentric counterpart (L31) not only responds in a solely rocking mode, it also overturns. Unlike the 'L' series, the taller, larger, symmetric (U11) configuration responds in a solely rocking mode; however, the eccentric configuration (U31) responds with significant motion in each of three modes. This mode change is further examined later in this chapter.

Due to the observation of multi-modal response, interaction diagrams of each of the modes are produced and analyzed. The interaction diagrams are simply the time history response of one mode plotted against the other. If two modes occur simultaneously, the plot has a defined non-zero slope. Representative interaction diagrams are presented in Figure 4.11 for slide-rocking, rock-

twisting, and slide-twisting. The slide-rocking interaction diagram is from the response of M11 configuration to GM1A in which slide-rocking is observed only for the first quarter-cycle of rocking response. In other motions and configurations, the interaction may take place throughout most or all of the duration of the response. This is the case for the out-of-plane eccentric L12 configuration to GM3 in which the specimen twists positively on each half-cycle of rocking (Figure 4.11b). In addition to duration, the modal interaction is also characterized by direction. For example, the response of the out-of-plane eccentric U13 configuration to GM3 is nearly linear in which the sliding and twisting response are only positive. The likelihood of occurrence and correlation of the primary modes and interactive modes with geometry is presented in the following sections.

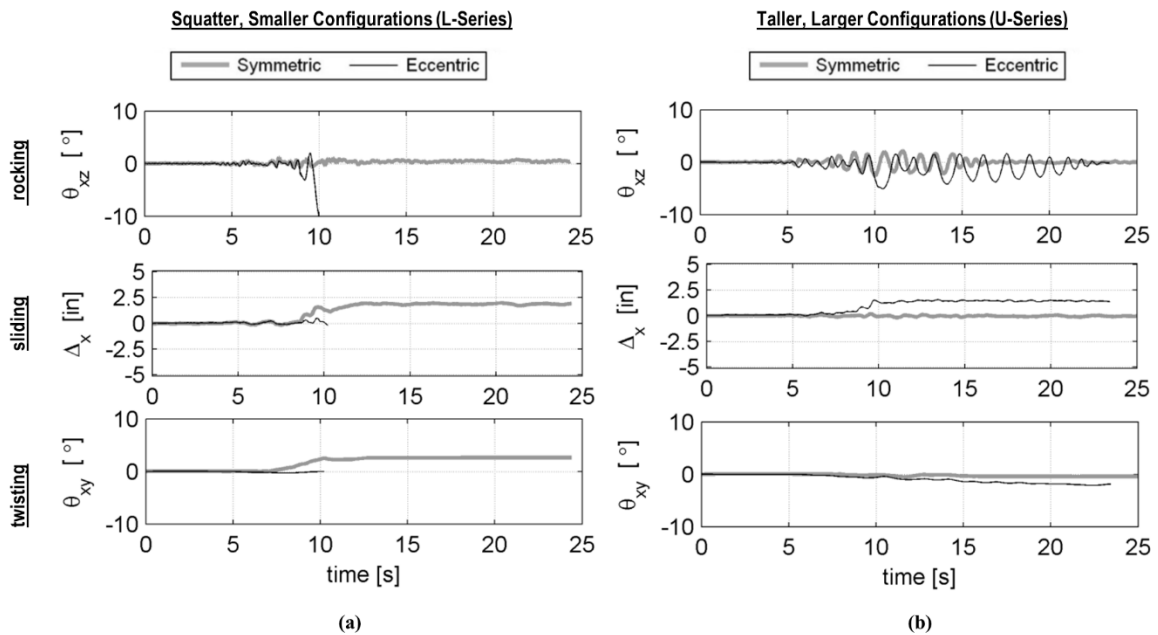


Figure 4.10 Time history responses of symmetric and in-plane eccentric configurations for (a) smaller, squatter configurations (L11, L31) and (b) larger, taller configurations (U11, U31). The ‘L’ configurations are subject to GM1C and the ‘U’ to GM3-90%.

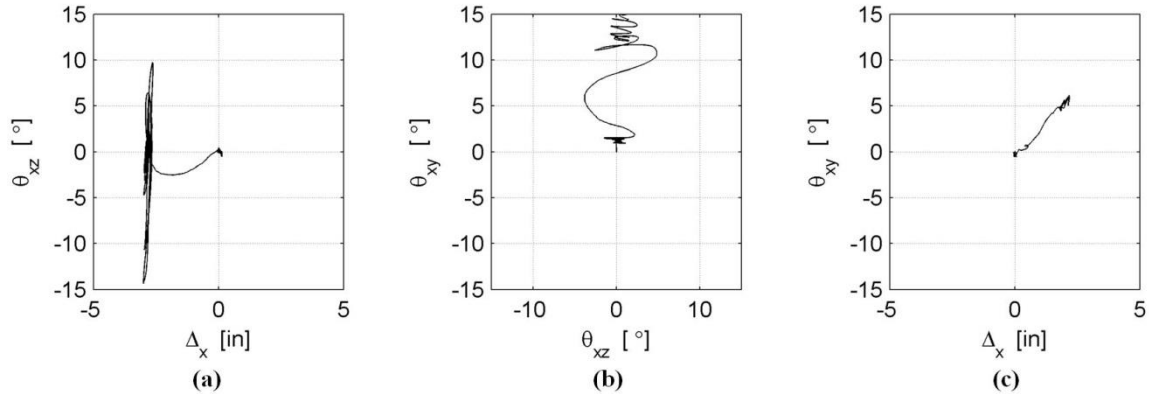


Figure 4.11 Modal interaction diagrams for (a) slide-rock (M11, GM1A), (b) rock-twist (L12, GM3-225%), and (c) slide-twist (U13, GM3-175%).

4.4.1 Effect of Horizontal Mass Eccentricity

As previously presented in the time history responses, multiple modes are possible including three-dimensional effects even when the structure is symmetric and the loading is uni-axial. Furthermore, the multiples modes of response may or may not interact or occur simultaneously. Although the initiation into a mode is a very straight-forward determination based upon simple statics and physics relationships, most structures and boundary conditions are not perfect yielding highly complex multi-mode response and transitions between modes.

To understand the likelihood of certain modes and interactions with various levels of horizontal eccentricity, bar charts of modal occurrences are included in Figure 4.12. An occurrence for a primary mode (i.e. rocking, sliding, or twisting) is counted only for those motions and scale factors, which were consistent across all configurations to avoid bias. In addition, a modal occurrence is identified only if the mode was distinctly excited to avoid false positives as a result of the inability to directly measure the quantities. The criteria for an occurrence are: 1) rocking greater than 0.5° , 2) sliding greater than 10 mm, and 3) twisting greater than 0.5° . The occurrences of modal interaction are determined visually for each response using the modal interaction diagrams.

The occurrences of each primary mode by direction of response are presented in Figure 4.12a. It should be noted that the in-plane eccentric configurations were more slender (and smaller) in the negative sliding and rocking directions. The occurrences of rocking increase with increasing in-plane eccentricity, as would be expected. However, it is seen that the rocking occurrences become entirely in one direction as the in-plane eccentricity increases. This suggests that the eccentricity nearly renders the response of the sides separate. That is, the structure becomes smaller and more slender in one direction tending towards rocking while it becomes larger and squatter in the other tending towards sliding. Out-of-plane eccentricity does not lead to the same behavior; rather, the out-of-plane eccentric structures have similar occurrences of rocking with only increased twisting when compared to symmetric. The occurrences of the modal interactions are presented in Figure 4.12b. While no distinct trend is observed regarding the occurrence of modal interaction, it is apparent that the symmetric configurations observed the fewest instances of modal interaction and that any amount and direction of eccentricity increases the likelihood of modes occurring simultaneously.

In addition to the occurrence of a mode, the magnitude of response is also of interest. The maximum rocking, sliding, and twisting of each test included in the bar charts are plotted in Figure 4.13. Overlaid on each set of maxima is the median value and interquartile range to aid in trend and scatter identification. Similar to the observation of modal occurrence, the magnitude of rocking response increases nearly linearly with increased in-plane eccentricity. In addition, the interquartile range (scatter) of the rocking response increases with increased in-plane eccentricity. However, the median sliding response and corresponding interquartile range are reduced with in-plane eccentricity indicating that larger displacements and rotations are inherently more variable. Regarding the out-of-plane eccentricities, the median rocking magnitudes of these configurations are very similar to the median of the symmetric configurations suggesting that the out-of-plane eccentricity does not have a distinct correlation with the rocking mode. A similar trend is observed

for the twisting in which a nearly linear relationship is seen for the twisting with increased out-of-plane eccentricity. However, eccentricity in either direction correlates to a reduction in sliding.

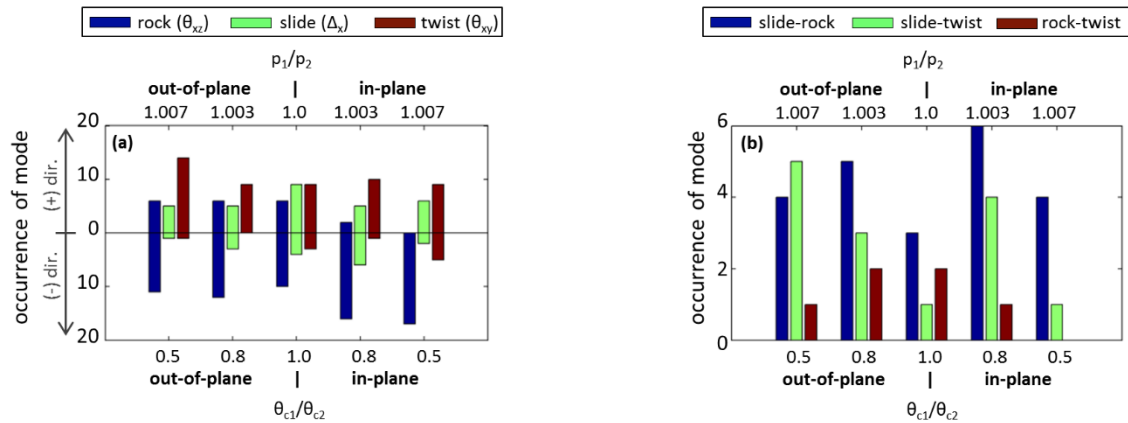


Figure 4.12 Bar charts of occurrence of rigid body modes categorized by horizontal eccentricity level for all configurations: (a) primary modes of rock, slide and twist, and (b) interactive modes of slide-rock, slide-twist, and rock-twist.

- Notes:**
1. An occurrence was counted only for input motions at the same scale for all configurations for consistency.
 2. Modal occurrence was differentiated as ‘positive’ and ‘negative’ according to whether response was observed in one or both directions (i.e. sliding in +X or -X direction).

Due to the nature of the geometric eccentricities, the scatter plots of Figure 4.13 are divided into positive and negative responses for the rocking and sliding modes in Figure 4.14. While the total sliding response in Figure 4.13 shows a distinct correlation with eccentricity, no effect of direction can be observed. However, the increase of rocking with in-plane eccentricity shows distinct directivity effects. Whereas the negative response increases with increasing eccentricity similar to the total maxima in Figure 4.13, the positive response remains nearly constant similar to the out-of-plane eccentric and symmetric configurations. This suggests that, in general, mass eccentricity is more significant to structures undergoing a rocking mode. The effect of this in combination with vertical eccentricities is further studied in the following section.

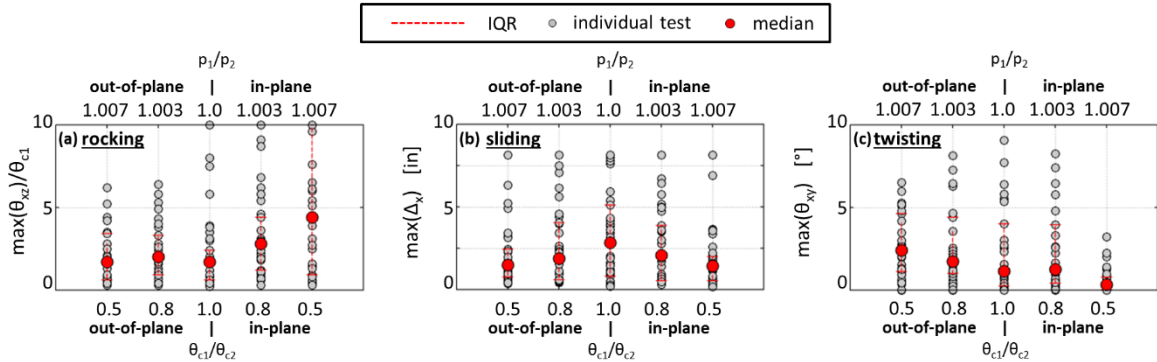


Figure 4.13 Scatter plots of the absolute maximum for (a) rocking, (b) sliding, and (c) twisting for each level of horizontal eccentricity for all configurations.

- Notes: 1. A point was plotted only for input motions and scales that were consistently implemented across all configurations.
 2. Additional larger twisting points are not visible in (c) to emphasize the trend seen by the median values; however, twisting up to 30° was observed.

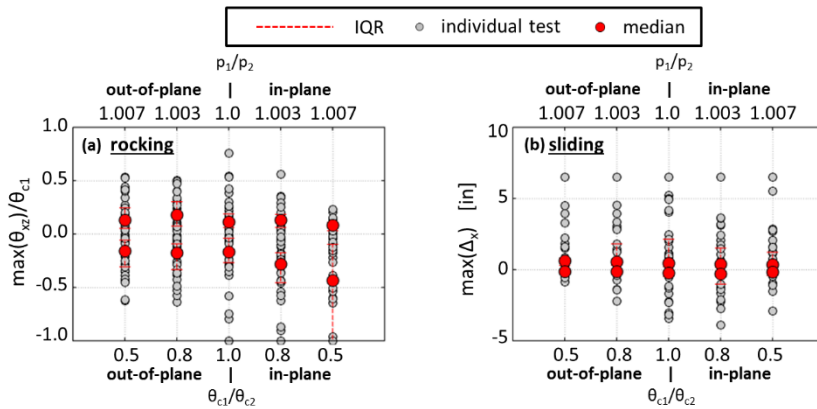


Figure 4.14 Scatter plots of the maximum (a) rocking and (b) sliding by direction of response for each level of horizontal eccentricity including all configurations. Note: A point was plotted only for input motions at the same scale for all configurations for consistency.

4.4.2 Effect of Height of the Center of Mass

Similar to prior discussions regarding the horizontal mass eccentricities, bar charts and scatter plots are presented to correlate the modes with the height of the center of mass (h) or size of the structure by way of the frequency parameter (p). Figure 4.15 presents the occurrences of the primary and interactive modes by height of the center of mass and size for all levels of eccentricity. It is observed that the larger, taller configurations (U-series) are most likely to respond in a rocking mode; although, rocking appears to be the most common mode of response for all heights of the center of mass. However, the more interesting observations are regarding the modal interaction occurrences. Whereas the two smaller, squatter (L and M) series do not appear to be more likely to experience one interactive mode instead of another, the larger, taller configurations (U-series) are significantly likely to observe a slide-rocking mode.

To observe the general behavior of the combined horizontal and vertical eccentricities, scatter plots are presented of the maximum response of the in-plane eccentric configurations (IP3) normalized by that of the corresponding symmetric configuration (IP1). The plots for the amplification of response due to in-plane eccentricity are included in Figure 4.16a and b for rocking and sliding, respectively. The scatter plot is further categorized by the height of the center of mass (and size) and broken down by direction of the maxima. For clarity, each individual time history response yields a maximum and a minimum which are then normalized by the maximum and minimum of the corresponding symmetric response.

Referring to the rocking amplification scatter plot, an increase of in-plane eccentricity affects the 'L' (squatter, smaller) and 'U' (taller, larger) configurations very differently. The 'U' configurations have a median rocking amplification of approximately 1.5 in the direction of the eccentricity and a reduction of approximately 0.25 in the opposite direction. However, the sliding of these configurations presents a reduction of approximately 0.5 in the direction of the eccentricity

and a significant amplification greater than 4.0 in the opposite direction. This likely stems from the sliding (or slide-rocking) tendency of the structure in the positive direction which becomes larger and squatter (increased θ_c and reduced p). Therefore, this suggests that certain eccentric structures (e.g. configuration U31) may actually have a much increased risk of sliding (and rocking) compared to their rocking-dominated symmetric counterparts; however, the risk of overturning due to amplified rocking is also present. Refer to the time history comparison of the ‘U’ configurations in Figure 4.10, as well, for observation of the increased sliding and rocking demands to the eccentric configuration compared to the symmetric (U31 vs. U11).

The median sliding response of the squatter, smaller (L) configurations with increased in-plane eccentricity is reduced in both directions. However, a very significant amplification of the rocking in the direction of the eccentricity is observed with a median value greater than 4.0. The rocking in the opposite direction has a median value close to 1. This suggests that the ‘L’ configurations with eccentricity have a significantly increased risk of overturning and a reduced risk to excessive sliding, as would be expected given the more slender and smaller geometry of the eccentric side of the structure (reduced θ_c and increased p). Although not explicitly plotted, it is worth noting that the in-plane eccentric ‘L’ configuration experienced the most overturning of any configuration tested – twice the occurrences of overturning compared to the in-plane eccentric ‘U’ configuration.

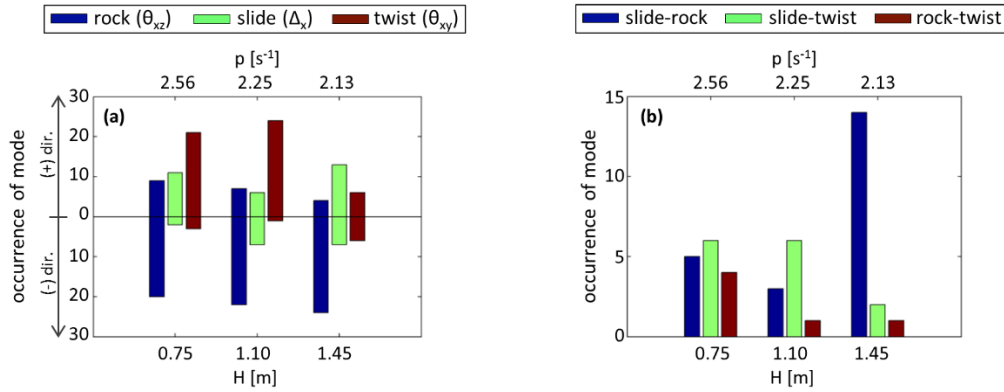


Figure 4.15 Bar charts of modal occurrences by the height of the center of mass (and frequency parameter p) for all configurations: (a) primary modes; (b) interactive modes. Note: An occurrence was counted only for input motions at the same scale for all configurations for consistency.

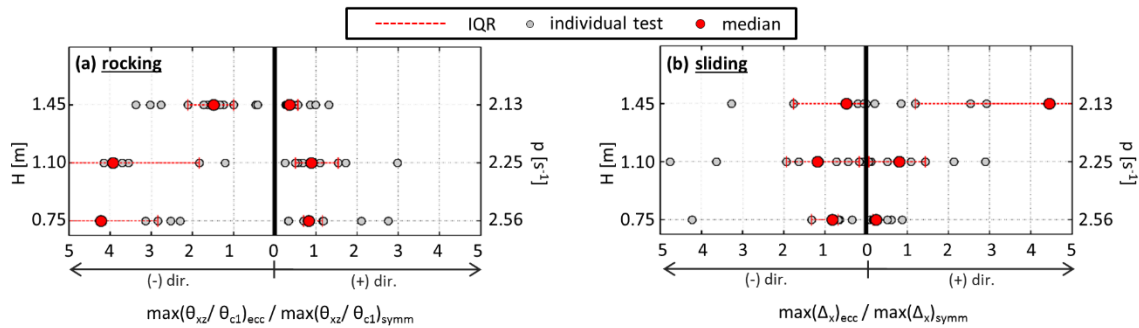


Figure 4.16 Scatter plots of the maximum (a) rocking and (b) sliding by direction, for the eccentric (IP3) normalized by the symmetric (IP1) configurations for the same motion. Note: The amplification is limited to +/- 5; although, larger amplifications are included in the statistics.

4.4.3 Effect of the Input Motion Pulse

It is well known in the literature that pulses and near-fault ground motions particularly excite unattached structures and render them highly susceptible to overturning. Housner (1963) introduced the fundamental concept that smaller blocks (larger p) are more susceptible to overturning than larger blocks of similar aspect ratio (similar θ_c). Housner's work in this area has been further studied by many researchers (e.g. Yim et al. 1980, Makris and Roussos 2000). Many

of these studies have likened seismic excitations to a simplified pulse given the correlation of the pulse to the vulnerability of overturning. In particular, the overturning response has been correlated to the ratio of the pulse frequency to the frequency (size) parameter of the block: ω_p/p , where $\omega_p = 2\pi/T_p$. Smaller values of this ratio indicate greater tendency towards overturning. However, the work of Makris and Roussos (2000) considered the entire pulse-like ground motion and concluded that smaller blocks overturn due to short duration, high acceleration pulses and larger blocks overturn due to long duration pulses with lower acceleration. It should be noted that all configurations tested in the current work are considered small, by these standards, and susceptible to short-duration, high acceleration pulses. Therefore, in this chapter, a simple presentation of the response of two configurations with varying heights of the center of mass to two pulse-like input motions is discussed.

Referring to the discussion of the input motions, GM1A and GM2A are recorded pulse-like ground motions with similar peak ground acceleration, velocity, and displacement, but with different values of the pulse period. Motion GM1A has an approximated pulse period of 0.9s and motion GM2A has an approximated pulse period of 1.8s. The time history of rocking response of the taller, larger (U11) and squatter, smaller (L11) symmetric configurations subject to GM1A and GM2A is included in Figure 4.17. The ω_p/p ratio is overlaid on each time history in which the motion with the highest value of this ratio produces the most significant rotation. This unanticipated observation is associated with the lower value of θ_c . Furthermore, it should be noted that the squatter, smaller (L) configurations also partially responded in a sliding mode to both ground motions. Despite the additional mode, the ‘L’ configuration observes similar rocking amplitudes to both motions. However, the ‘U’ configuration has a drastically reduced rocking response when considering the longer duration pulse-like motion (GM2A). The maximum rocking and sliding response of the configurations to GM1A normalized by that of GM2A is included in Figure 4.18a and b. These plots show that whereas the ‘U’ configurations respond to GM1A with rocking

amplitudes 400% greater than that of GM2A, the sliding response is relatively constant with little effect from the pulses. The ‘L’ configurations have a nearly opposite effect in that the rocking response to the two motions is nearly constant; however, the sliding amplitudes are nearly 400% greater than that of GM2A. This suggests that, regardless of the mode of response, this type of structure is more susceptible to the shorter duration pulse – which also corresponds to slightly larger values of ω_p/p as seen in Figure 4.17.

The configurations were tested to the pulse-like motion with and without the pulse content, as discussed previously. If possible, it is ideal to simplify this type of problem to a single pulse which greatly reduces the numerical computing expenses and increases the predictability of the analytical system. Therefore, the maximum rocking response of each configuration subject to the total, transient, and pulse content is plotted in Figure 4.18c. Recall, the spectra of these motions included in Figure 4.5 emphasizes the predominance of the low-frequency components to the input motion and the high contribution of the pulse (GM1C) to the total motion (GM1A). It is expected that the transient component of the motion excite the structure significantly less. However, it is interesting to note that the median response of the pulse component of GM1A is less than 50% the median response of the total input motion. While outlier (overturned) configurations are observed in the scatter plot, particularly for the total recorded motion, the interquartile range is relatively small indicating the total motion often excited the system much more than the extracted pulse.

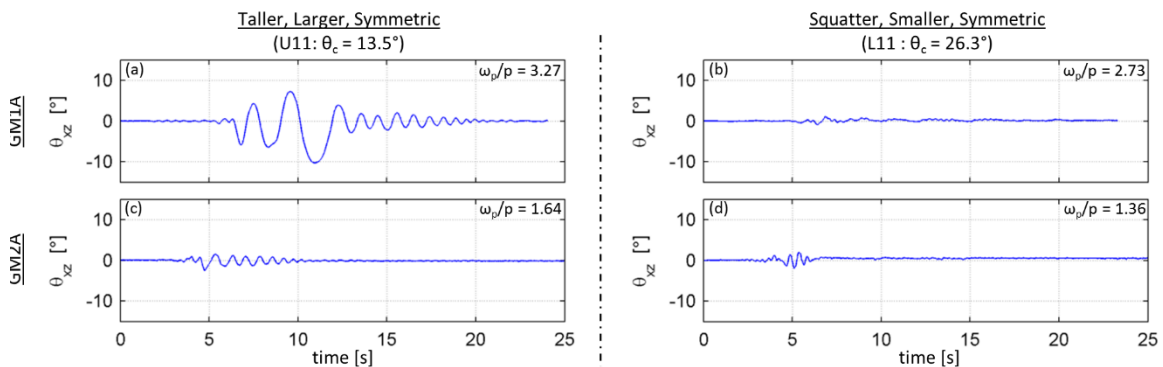


Figure 4.17 Rocking time history of the (a, c) symmetric ‘U’ and (b, d) symmetric ‘L’ configurations for the two pulse-like input motions.

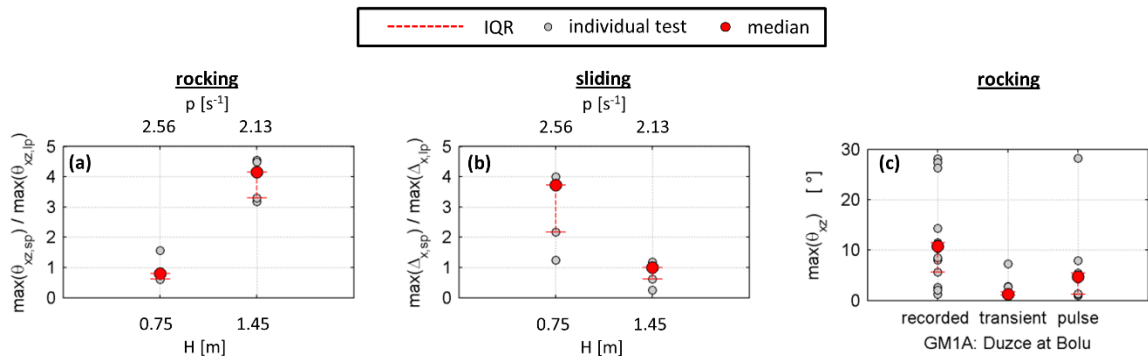


Figure 4.18 Scatter plot of the maximum response of the specimen to GM1A ($T_p = 0.9s$) normalized by that of GM2A ($T_p = 1.8s$) for (a) rocking and (b) sliding. (c) Scatter plot of maximum rocking response of each configuration to total pulse motion, transient, and extracted pulse motions.

Note: 1. The subscript lp denotes “long-period” for GM2A and the subscript sp denotes “short-period” for GM1A.

4.5 Comparison with Classical Model

Although it is clear that the specimen responded in multiple modes more often than not, it is of interest to gauge the applicability of the classical rocking model. Moreover, the specimen responded in a pure rocking mode when excited into a free rocking response following an input of a single pulse. Therefore, this section presents a comparison of the experimental free rocking response with that of an analytical simulation based on the classical rocking model as first introduced by Housner (1963) and further studied and expanded by many (refer to Chapter 2 of this dissertation). A number of studies have shown that this classical rocking model is able to produce results comparable to experiments as long as the specific boundary conditions such as friction and coefficient of restitution are accurate (e.g. Konstantinidis and Makris 2009, ElGawady et al. 2011, Costa et al. 2013). However, Lipscombe and Pellegrino (1993) noted the inability of the model to capture the response of squat blocks defined by an aspect ratio of 1.0 or less. Although the configurations tested in this experiment were taller than this limitation, structures with such large

eccentricities and resultant aspect ratio variations have not yet been verified to be accurately represented by the simple rocking model. This section outlines the governing differential equation and boundary conditions of the simple rocking model and its implementation followed by a comparison to the free rocking response of the symmetric and eccentric ‘U’ configurations.

The derivation of the equations of motion and detailed explanation of the assumptions that form the basis of the classical model are detailed in Chapter 2, and summarized in this chapter in brevity. The equation of motion is a function of the geometric and mass properties shown in Figure 4.2c, and is given as:

$$\left(\frac{I}{m} + R_i^2\right) \cdot \ddot{\theta} = \dot{x}_g \cdot R_i \cdot \cos(\theta_{c,i} - |\theta|) - \text{sgn}(\theta) \cdot R_i \cdot g \cdot \sin(\theta_{c,i} - |\theta|) \quad (4.2)$$

where the subscript i indicates the rocking point and its corresponding geometric parameters. Recall this model assumes rigid interfaces, no sliding, and perfectly inelastic impacts, as detailed in Chapter 2, where the velocity adjustment factor (coefficient of restitution) for an impact is given in Equation (2.2) and restated here as:

$$r_i = \frac{1}{\left(\frac{I}{m} + R_i^2\right)} \cdot \left[\left(\frac{I}{m} + R_j^2\right) - B \cdot R_j \cdot \sin(\theta_{c,j}) \right] \quad (4.3)$$

where the subscripts i and j indicate the rocking points. Equation (4.2) can be cast in a state-space formulation to allow the use of standard solvers for ordinary differential equations. Specifically, the equation is solved using a 4th-5th order Runge-Kutta scheme in MATLAB (2012). During the solution, the velocity reduction is applied through Equation (4.3) at every detected impact.

The experimental specimen was set into free rocking following a single acceleration pulse of the shake table. The time of free rocking was considered to be the motion following the first peak of rotation after impact at the cessation of the acceleration pulse. That is, the first half-cycle of response is entirely free rocking with no forcing. The free rocking response of the specimen is

studied in detail for comparison with the simple rocking model due to its single-mode response. Free rocking tests of two configurations are presented: 1) tall, symmetric U-IP1-OP1, and 2) tall, eccentric U-IP3-OP1.

To evaluate the applicability of the classical rocking model to this problem, simulated time histories of the free rocking response are overlaid with the experimental response in Figure 4.19 for the two configurations. These simulations used the configuration geometry (Table 4.1) as input to the equation of motion along with the geometry-based velocity reduction factor. Included with these time histories are two scatter plots which show the decay of the peak rocking amplitudes, per side, for each of five experimental trials along with median values. It can be seen that after three cycles of rocking, the analytical (theoretical) simulation overestimates the experimental data by 50% and 90% for the symmetric and eccentric, respectively. This stark difference in decay suggests additional factors other than solely geometry impact the rocking response, such as minor marble crushing and base imperfections.

The simulated responses using the theoretical values for the coefficient of restitution are compared with additional simulations using a modified value of the coefficient of restitution. The modified coefficient was selected to best fit the experimental data. The large overestimation of the simulation using theoretical values is pronounced for both configurations; however, the classical rocking model is able to match the experimental response quite well using the modified values for the coefficient of restitution. The value of the coefficient of restitution was reduced to $0.87r_{theo}$ in the case of the symmetric configuration, where the subscript '*theo*' represents the theoretical coefficient and '*mod*' represents the modified value. For the eccentric configuration, the coefficients were also reduced to $0.87r_{theo}$ for both directions. The need for a modified coefficient of restitution has similarly been reported in prior experimental campaigns with modified values both greater and less than the theoretical values (e.g. Priestley et al. 1978, ElGawady et al. 2011,

Costa et al. 2013). The observed reduction value in this experiment is consistent for both configurations and is likely a function of the experimental setup as well as geometric anomalies and material. It is emphasized that this reduction is specific to this experiment and is not meant to characterize marble interfaces in general. However, it is apparent that the simple rocking model is not able to accurately predict the response of the experimental free rocking of the specimen; however, the performance of the model significantly improves with adjusted values for the coefficient of restitution.

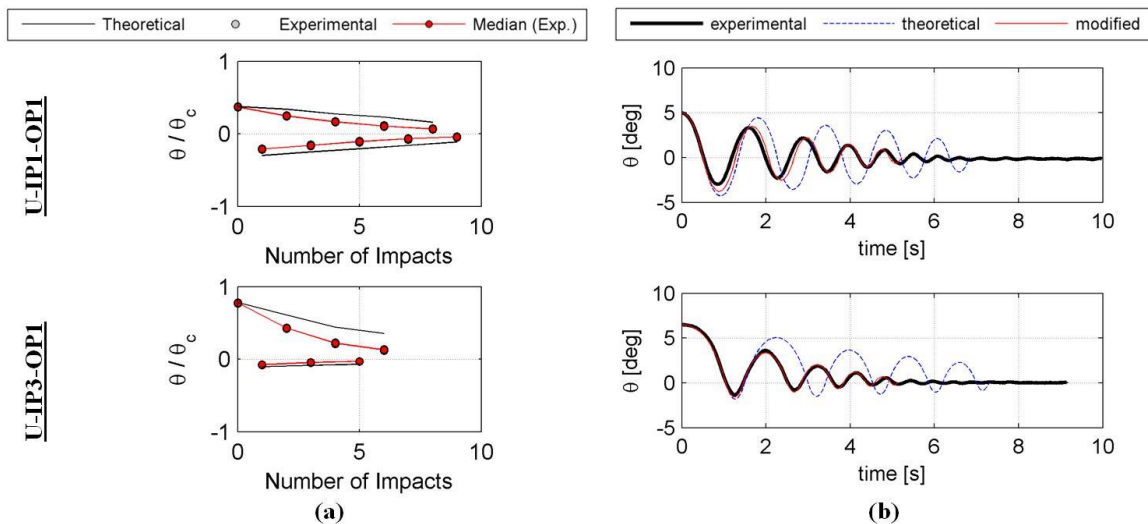


Figure 4.19 Experimental free rocking behavior compared to the classical model: (a) decay of peak rocking amplitudes, and (b) rocking time history including simulation with theoretical and modified values of the velocity reduction factor (coefficient of restitution).

4.6 Conclusions

The vulnerability of unattached, stiff structures has been observed in numerous post-earthquake field investigations. In an effort to better understand the dynamic behavior of these types of structures and to support validation of numerical models, an extensive shake table testing campaign is detailed in this chapter. The range of geometries tested in this program incorporates heights of the center of mass from 0.75 m through 1.45 m, frequency parameters 2.13 through 2.56, and slenderness ratios ($\theta_{c1} / \theta_{c2}$) from 0.5 through 1.0. This geometric range and the marble-marble

interface selected for study are specifically geared towards understanding the response of large, human-form, marble statues; however, this study and its findings may be useful to understanding the behavior of a wider range of structures in this class with similar coefficients of friction ($\mu \approx 0.4$) and geometry such as electrical transformers, nuclear radiation shields, office equipment, and simple masonry structures. In the detailed experiment, fifteen unique geometric configurations were tested using a number of both recorded and simulated earthquake motions on a uni-axial shake table at the University of California, San Diego. The large-displacement rigid body motion of each configuration was continuously recorded and analyzed in an effort to correlate the geometry and motion characteristics with response mode, magnitude, and direction. The main findings presented in this chapter are as follows:

- Multi-mode and three-dimensional responses were observed in nearly all tests including symmetric configurations in which the loading was along an axis of symmetry. The multi-mode response can be observed as either simultaneous modal interaction or as unique modes per direction of the response. Symmetric configurations were the least likely to observe this type of response; however, it was still evident.
- Horizontal mass eccentricity perpendicular to the direction of shaking has little effect on the magnitude of rocking response; however, the three-dimensional effects and twisting are significantly increased with this increased eccentricity. This highlights the necessity for three-dimensional analyses even in the case of planar symmetry.
- Horizontal mass eccentricity in the direction of shaking (increased p , reduced θ_c in the direction of eccentricity) does not significantly increase the three-dimensional and twisting response; however, the likelihood of occurrence and the magnitude of a rocking response are greatly increased.

- In general, horizontal mass eccentricities have the greatest effect on structures undergoing a rocking mode and can increase the risk of overturning.
- In this experiment, taller, larger structures ($h \approx 1.45$ m; $p \approx 2.13$; $\theta_c < 15^\circ$) and squatter, smaller structures ($h \approx 0.75$ m; $p \approx 2.56$; $\theta_c > 20^\circ$) respond very differently when mass eccentricity is present. The taller, larger configurations have only a slightly increased rocking response, yet also a significantly increased sliding response due to modal interaction on the larger, squatter side of the structure. The squatter, smaller configurations have significantly increased rocking response and risk of overturning with a much reduced sliding risk. The squatter, smaller structures with eccentricity were observed to be the most susceptible to overturning.
- For the tested pulse-like motion, Duzce earthquake at Bolu station (1999), considerable reduction (less than 50%) in the rocking response was observed for the extracted pulse compared to the total recorded motion. This highlights a potential pitfall of analyses making use of approximated pulses. However, additional variables such as the transient frequency content limit the extension of this finding to other pulse-like earthquake motions.
- The classical rocking model significantly overestimates the free rocking response of both symmetric and eccentric configurations, up to 90% in this study. The overestimation is likely related to the additional sources other than geometry which affect the rate of decay such as material effects, base imperfections, and/or mild bouncing. A reduced value for the coefficient of restitution to account for these additional factors greatly improves the performance of the simple rocking model and the agreement with this specific set of experimental results.

4.7 Implications on Numerical Modeling

This chapter partially addresses the second primary objective of this dissertation, which is to generate a comprehensive database of the experimental response of freestanding structural systems. The following chapter completes the treatment of this objective, with the incorporation of dual-body tests for comparison presented in the following chapter. The combination of these two chapters, in response to the second primary research objective, is intended to inform the ultimate objective, which is to develop and validate a numerical model for the seismic response of freestanding structures. As such, key conclusions of the detailed experimental campaign are summarized here along with their implications on numerical modeling of freestanding structural systems:

- The response of symmetric and asymmetric configurations varied greatly – not only in magnitude of response, but also in the mode of response. As such, the numerical model must be able to adequately represent asymmetric and arbitrary geometries.
- Three-dimensional responses (e.g. twisting) were observed in many cases, even for configurations with apparently planar symmetry. As such, the numerical model must be conducted in a three-dimensional framework.
- Multi-modal responses were observed often for many configurations. These responses included both simultaneous response in two or more modes, as well as transitioning from one mode to another in the same response. As such, the numerical model must allow rotation and translation at all times and in all directions throughout the simulation.
- The classical model was not able to adequately represent the free rocking response of the experimental specimen. This can be attributed to a difference in the energy dissipation of the classical model with the actual specimen. Therefore, a numerical model should allow for some degree of flexibility at the interface.

4.8 Acknowledgements

The experimental investigation presented was supported by the National Science Foundation under IGERT Award #DGE-0966375, "Training, Research and Education in Engineering for Cultural Heritage Diagnostics." Additional support was provided by the Qualcomm Institute at the University of California San Diego, the Friends of CISA3 and the World Cultural Heritage Society. The use of Carrara marble in the experiment was made possible by a generous donation from Florentine Stone Company. The technical input and continuous support of Professor Falko Kuester is highly valued. Additional assistance during testing was provided by Professor Richard Wood and numerous undergraduate students. The assistance and support of the Charles Lee Powell Laboratory staff is greatly appreciated – namely, Paul Greco and Darren McKay. The opinions, findings, and conclusions expressed in this chapter are those of the authors and do not necessarily reflect those of the sponsoring organizations.

This chapter, in part, is a reprint of the material as it appears in the journal *Earthquake Engineering and Structural Dynamics*. Wittich, C.E. and Hutchinson, T.C. (2015). "Shake table tests of stiff, unattached, asymmetric structures." *Earthquake Eng. Struct. Dyn.*, 44(14): 2425-2443. The dissertation author was the primary investigator and first author of this publication.

Sections 4.2.5, 4.2.7, and 4.3 are based upon a technical report as it appears in the Structural Systems Research Report Series. Wittich, C.E. and Hutchinson, T.C. (2014). *Shake Table Tests of Stiff, Unattached, Asymmetric Structures – Phase 1: Floor-Mounted*. Structural Systems Research Project Report Series, SSRP-2013/18, Department of Structural Engineering, University of California, San Diego, La Jolla, CA. The dissertation author was the primary investigator and first author of this publication.

Chapter 5 Shake Table Tests of Freestanding Structures:

Dual-Body Systems

Freestanding structural systems comprise a very broad variety of structural systems, which tend to perform poorly during earthquake excitation. While a significant number of studies have been presented focused on the analytical response of single-body systems, only a handful of experimental campaigns have been conducted, as detailed extensively in Chapter 2. Even fewer studies have analyzed or tested the response of multi-body systems. This dissertation aims to fill this gap with respect to the experimental response of both single-body and dual-body systems. Chapter 4 presents the results of the single-body tests, whereas the dual-body tests are presented herein.

5.1 Introduction

Analytical studies of freestanding structural systems are typically accredited to having originated with the landmark study of Housner (1963). Since then, numerous studies have been presented that extend Housner's classical rocking model to account for multiple modes, flexibility of the foundation, flexibility of the rocking body, and three-dimensional responses. (e.g. Shenton and Jones 1991, Chatzis and Smyth 2011, DeJong and Vibert 2012, Zulli et al. 2012, respectively). Psycharis (1990), however, presented the first extension of this two-dimensional, rectangular, symmetric, rigid body, rigid foundation, rocking model for the dual-body system (two bodies in a stacked configuration). However, these classical extensions result in cumbersome implementations, are not easily combined to represent realistic structures, and evidence an exponential increase in complexity with additional degrees of freedom (e.g. number of bodies in a stacked configuration).

Validating analytical and numerical methods for the analysis of the multi-body system requires significant experimental response data. Unfortunately to date, only a handful of tests on

the freestanding multi-body system have been documented, as detailed in Chapter 2 and summarized in brevity in this chapter. For example, in one experimental program, Mouzakis et al. (2002) presented the shake table tests of a scaled model of a Greek classical multi-drum marble column. Rocking and sliding of the individual blocks were observed; however, only the displacement of the top drum was recorded, which limited its ability to accurately document the response. In a similar experiment presented by Drosos and Anastasopoulos (2014), a scaled model of a different multi-drum marble column was tested in which the response of each drum was recorded in time. In both of these experiments, the individual drums of the column were squat (height/width < 1.0), which limits the extensibility to systems of alternate geometries. While the aforementioned studies focused on systems of squat blocks (i.e. multi-drum column), Peña et al. (2008) tested a dual-body configuration consisting of tall, rectangular stones. However only a single geometric configuration was tested, therefore extensibility is limited.

While previous test programs provide insight into the behavior of a subset of multi-block configurations, a systematic study specifically considering variable block geometries, eccentricities, and interface characteristics, has yet to be performed. In particular, the importance of geometric variations was highlighted for the single-body configuration in the shake table tests presented in Chapter 4. Recall that in these experiments, geometric configurations, which systematically varied the slenderness, size, and eccentricity of the structure (height to the center of mass varied from 0.75 m – 1.45 m with a width of 0.74 m) were tested. Significant three-dimensional and multi-modal responses (e.g. slide-rocking, rock-twisting) were observed for all configurations, particularly the squatter, smaller configurations. These tests also revealed that the presence of eccentricity had a more profound effect on the smaller, squatter structures, manifesting in a high level of interaction amongst modes and corresponding modal transitions.

This chapter extends the first phase of testing, presented in Chapter 4, to understand the seismic behavior of dual-body systems. Test models considered varied geometry, interface conditions, and eccentricities. The experimental data acquired serves to complement the existing database of multi-body tests in the literature, which is currently limited by tested geometry and is biased towards systems of symmetric, squat blocks. Furthermore, it will provide valuable data for validating numerical modeling strategies for capturing a broader range of dual-body systems under a wider range of earthquake motions. It should be noted that the test setup, specimen, and protocol are consistent with that of the first phase of testing for single-body systems, as presented in Chapter 4, and thus background in this regard is provided only in brevity in the current chapter. Detailed technical reports of both tests suites may be found in (Wittich and Hutchinson 2014b, 2015).

5.1.1 Design and Construction of Experimental Specimens

Recall from Chapters 3 and 4 that the statue-pedestal system is one of the most geometrically-complex freestanding structural systems; and, as such, serves as the primary basis for the experimental design detailed herein. A schematic of the generalized two-dimensional dual-body system is provided in Figure 5.1a. The individual structures are characterized by: mass, m ; mass moment of inertia, I ; height of the center of mass, h ; width to the center of mass, b , slenderness or critical angle, $\theta_c = \tan^{-1}(b/h)$; rocking radius, $R = \sqrt{h^2 + b^2}$; and, the frequency or size parameter, $p = \sqrt{mgR/(I + mR^2)}$, where g is the acceleration due to gravity. It should be noted that there are two values of R , θ_c , B , and p for an eccentric structure. In this dissertation, a subscript ‘1’ indicates the geometric parameters associated with the smaller, taller side; and, a subscript ‘2’ indicates the geometric parameters associated with the larger, squatter side. Furthermore, a superscript ‘t’ indicates the top-body or “tower” in the stacked configuration; and, a superscript ‘p’ indicates the bottom-body or “pedestal” closer to the ground or floor support location. For example, θ_{c1}^t represents the slenderness of the tower in the direction of eccentricity (the smaller, taller side).

The dual-body configuration is also characterized at the interfaces by the coefficient of friction, μ . The two interfaces are distinguished with the superscripts ‘t-p’ for the tower-pedestal interface and ‘p-st’ for the pedestal-shake table interface.

The top structure of the dual-body experimental configuration was the geometrically-variable tower specimen utilized in the first phase of testing, as presented in Chapter 4. A detailed drawing of the specimen in a dual-body configuration is included in Figure 5.1 and shows the overall dimensions and locations of the incorporated weight plates, which is identical to that of the single-body tests. This allowed the height of the center of mass of the top-body to vary from 0.75 m to 1.45 m. The resultant slenderness (θ_c) is 13.5° or 25.6° and the resultant frequency parameter (p) is 2.13 or 2.56 when the weight plates are placed symmetrically at the top or bottom locations, respectively. The geometric and mass properties of each configuration of the tower are included in Table 5.1. The tower configuration naming convention is based on the height of the weight plates (i.e. ‘L’ for lower, ‘U’ for upper), where the abbreviated configuration names of Chapter 4 are incorporated for simplicity within the dual-body configurations. The second and third numbers in this convention represent the horizontal geometric eccentricity in the direction of shaking and perpendicular to the direction of shaking, respectively. For example, L31 is characterized by weight plates in the lower section of the tower, eccentrically in the direction of shaking and symmetrically in the perpendicular direction.

In an effort to observe multiple modes of dual-body response, two distinct pedestal geometries were designed. One pedestal was designed to have a squatter aspect ratio ($H/B < 1.0$ or $\theta_c > 45^\circ$) and tend to sliding while not anticipated to initiate a rocking mode. The second pedestal was designed to have a taller aspect ratio ($H/B > 1.0$ or $\theta_c < 45^\circ$) which was anticipated to initiate into a rocking or a slide-rocking response. All other pedestal attributes were designed to be the same for both pedestals, namely: constructed of hollow, lightweight concrete to target a mass

similar to the tower; symmetric geometry with a 1.02 m square footprint and a height of 0.76 m or 1.52 m; and, two marble-clad surfaces to maintain the in-situ material and interface characteristics. The geometries of the pedestals were also selected to correspond to observations of culturally significant statue-pedestal systems from the field survey presented in Chapter 3. It is noted that in the current test program, an alternate low-friction steel plate system was used beneath the marble at the interface with the shake table. This system is further discussed in the following section on the experimental setup. A sketch of the pedestal is included in Figure 5.1 and a summary of the geometric and mass properties are included in Table 5.1. The combinations of pedestal specimens and tower configurations tested are summarized in Table 5.2. The system naming convention consists of the tower name followed by the pedestal name and the pedestal material. For example, L31sm is the L31 (squat, eccentric) tower configuration atop the ‘sm’ pedestal (squat pedestal with a marble interface).

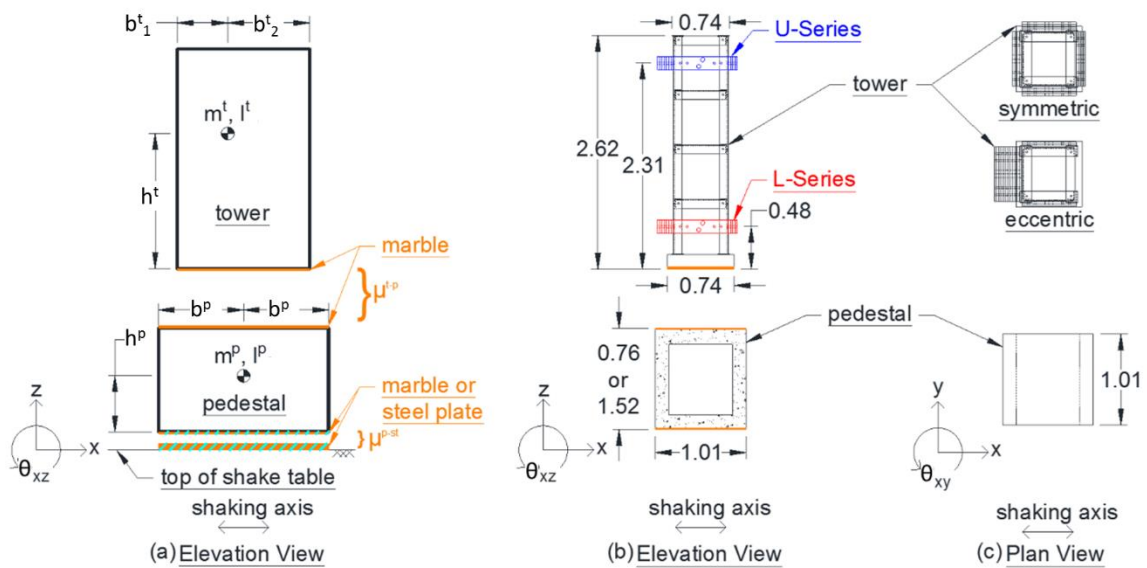


Figure 5.1 (a) Idealized dual-body system of arbitrary top-block geometry atop symmetric bottom block. Key dimensions shown in (b) elevation and (c) plan views. Notes: all units in meters, orange lines indicate marble interface, hatched lines indicate marble or steel interface.

Table 5.1 Geometric and mass properties of the individual experimental specimens.

Spec. No.	Spec. Type	General Description	h^p or h^t [m]	m [kg]	θ_{c1} [$^\circ$] ¹	θ_{c2} [$^\circ$] ¹	p_1 [s^{-1}] ²	p_2 [s^{-1}] ²
1	Tower (L11)	Squat, small, symmetric tower	0.75	817	26.3	26.3	2.56	2.56
2	Tower (L31)	Squat, small, eccentric tower	0.75	817	16.9	34.4	2.55	2.53
3	Tower (U11)	Tall, large, symmetric tower	1.45	817	13.5	13.5	2.13	2.13
4	Tower (U31)	Tall, large, eccentric tower	1.45	817	9.0	17.6	2.13	2.12
5	Pedestal (T)	Tall pedestal	0.76	1134	33.7	33.7	2.21	2.21
6	Pedestal (S)	Squat pedestal	0.38	1089	53.1	53.1	3.07	3.07

¹ The slenderness or critical angle is defined as: $\theta_c = \tan^{-1}(B/H)$

² The frequency or size parameter is defined as: $p = \sqrt{mgR/(I + mR^2)}$, where R is the rocking radius defined as: $R = \sqrt{H^2 + B^2}$.

Table 5.2 List of tested configurations including tower and pedestal combinations.

No.	Name ¹	Pedestal Spec. ²	Tower Specimen ²	Bottom Interface (p-st) ³	Top Interface (t-p) ³
1	L11np	n/a	1: L11 (squat, symmetric)	n/a	marble-marble
2	L31np	n/a	2: L31 (squat, eccentric)	n/a	marble-marble
3	U11np	n/a	3: U11 (tall, symmetric)	n/a	marble-marble
4	U31np	n/a	4: U31 (tall, eccentric)	n/a	marble-marble
5	L11tm	6: Tall	1: L11 (squat, symmetric)	marble-marble	marble-marble
6	L31tm	6: Tall	2: L31 (squat, eccentric)	marble-marble	marble-marble
7	U11tm	6: Tall	3: U11 (tall, symmetric)	marble-marble	marble-marble
8	U31tm	6: Tall	4: U31 (tall, eccentric)	marble-marble	marble-marble
9	L11sm	5: Squat	1: L11 (squat, symmetric)	marble-marble	marble-marble
10	L31sm	5: Squat	2: L31 (squat, eccentric)	marble-marble	marble-marble
11	U11sm	5: Squat	3: U11 (tall, symmetric)	marble-marble	marble-marble
12	U31sm	5: Squat	4: U31 (tall, eccentric)	marble-marble	marble-marble
13	L11ss	5: Squat	1: L11 (squat, symmetric)	steel-coated steel	marble-marble
14	L31ss	5: Squat	2: L31 (squat, eccentric)	steel-coated steel	marble-marble
15	U11ss	5: Squat	3: U11 (tall, symmetric)	steel-coated steel	marble-marble
16	U31ss	5: Squat	4: U31 (tall, eccentric)	steel-coated steel	marble-marble

¹ Configuration name consists of the tower name (e.g. 'L11'), the pedestal name (e.g. 's'), and the base interface material (e.g. 'm'). Note that 'np' stands for 'no pedestal'.

² Refer to Table 5.1 for specifications on the pedestal and tower specimens. Light grey denotes squat pedestal configurations; darker grey denotes tall pedestal configurations. No shade denotes the single-body, no pedestal condition.

³ Interfaces are denoted as: $p-st$ (pedestal-shake table) and $t-p$ (tower-pedestal)

5.1.2 Experimental Setup

The shake table campaign was carried out using a uniaxial shake table at the University of California, San Diego, as detailed in Section 4.2.3. The mechanical setup atop the shake table for the dual-body tests consisted of: 1) a fixed marble slab or low-friction steel plate system, 2) a pedestal specimen, 3) a tower specimen, and 4) a safety catch system to preclude total collapse of the system during testing. Select images of various configurations of the experimental setup are included in Figure 5.2. This figure also includes images and a schematic of the low-friction steel plate system, which includes a thin, corrugated stainless steel plate fixed to the shake table with another thin, polymer-coated steel plate resting unattached above the base plate. The resultant frictional properties of this system as well as the marble-marble interface are discussed later. It is noted that prior to each individual shake table test, both specimens were lifted and re-oriented to their original starting position. In addition, the interfaces were cleaned of any dust in an effort to maintain consistent frictional resistance.

5.1.3 Instrumentation

The responses of the shake table and dual-body system were monitored using a system of accelerometers, string potentiometers, and high-definition video cameras. The acceleration was recorded on the surface of the shake table as well as along the height of both specimens. The three-dimensional translation and rotation of both pedestal and tower were recorded in time using a system of nine string potentiometers attached to the specimens in groups of three. The translation and rotation were post-processed using the intersection of three spheres. While the fully three-dimensional displacement response was recorded, only select response quantities are explored in this study. Figure 5.3 illustrates the three primary response quantities: 1) the translation in the direction of shaking, Δ_x , referred to as sliding; 2) the rotation in the direction of shaking, θ_{xz} , referred to as rocking; and, 3) the rotation about the vertical, θ_{xy} , referred to as twisting. The remaining

translations and rotations were not noticeably excited and therefore not further discussed. It should be noted that the rocking is often presented in terms of the slenderness, also known as the “critical angle”. Therefore, the normalized rocking is introduced as: $\phi = \theta_{xz}/\theta_c$.

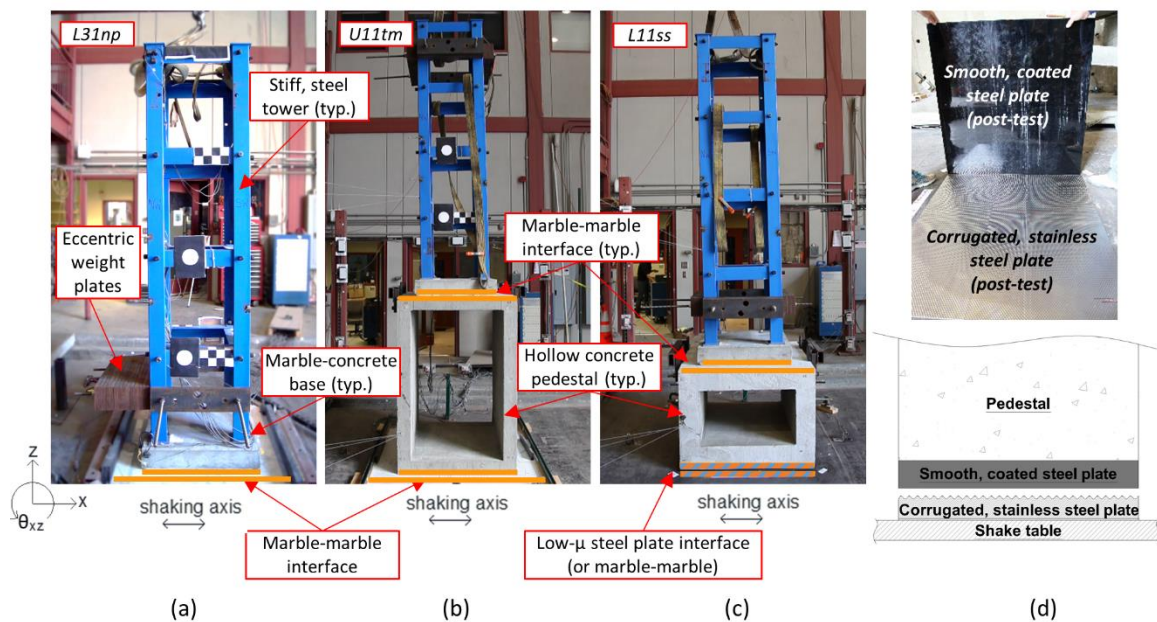


Figure 5.2 Experimental setups: (a) single-body tests, and (b-c) dual-body tests with (b) tall pedestal and marble interface, and (c) squat pedestal on steel plate interface. (d) Low-friction steel plate interface in image and schematic forms. Note orange and hatched lines added for emphasis.

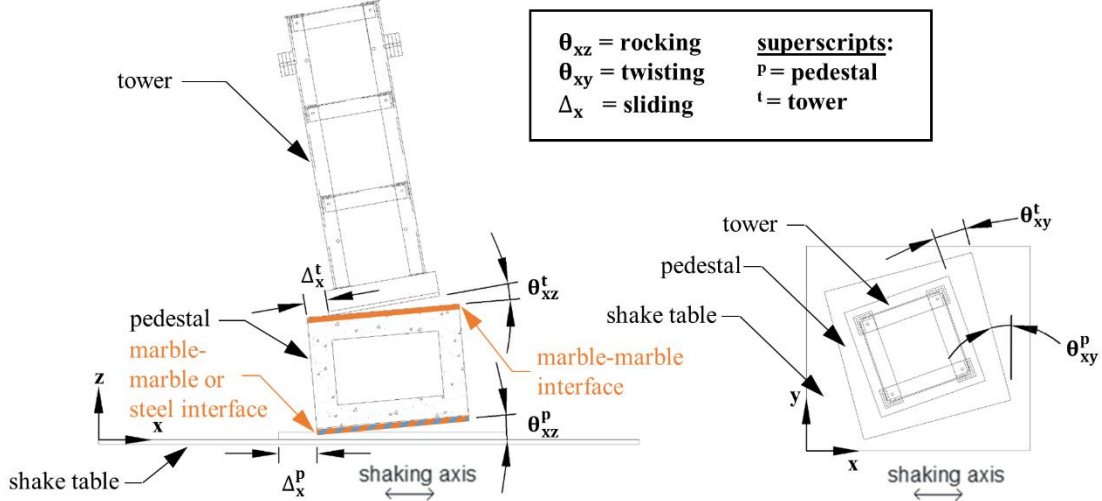


Figure 5.3 Nomenclature adopted to characterize the displaced shape of the dual-body system. Note that tower displacements are always taken relative to the pedestal, unless otherwise stated.

5.1.4 Input Motions

Each tested configuration was subjected to at least five different input motions. The selected motions largely correspond to those utilized in the single-body tests, as detailed in Chapter 4. The selected input motions are detailed in Table 5.3 and include Motion ID, event and station, source mechanism, and other characteristics such as peak achieved quantities. Each of the first five motions was obtained through the PEER-NGA database (Chiou et al. 2008), with modifications to the first motion for the extraction of the near-fault pulse, as detailed in the previous chapter. An additional recording, which was not utilized in the previous experiment, was selected from the 1985 Valparaiso Earthquake from the COSMOS database (COSMOS 2014). This motion was selected due to its significant duration of strong shaking, which is in excess of 40 s. The acceleration time histories and the pseudo-spectral acceleration of each of the aforementioned motions are provided in Figure 5.4 and Figure 5.5, respectively.

Table 5.3 Input motions and select intensity characteristics, as achieved on the shake table for the dual-body tests.

ID	Event (date)	Station (component)	Mechanism	M_w	PTA ^[1] [g]	PTV ^[1] [cm/s]	PTD ^[1] [cm]	Tp ^[1] [s]
GM1A	Duzce, Turkey (1999) - original	Bolu(90°)	Strike-slip	7.2	0.82	62.1	13.6	0.9
GM1B ^[2]	Duzce, Turkey (1999) - transient	Bolu(90°)	n/a	7.2	0.41	25.5	10.4	0.3
GM1C ^[3]	Duzce, Turkey (1999) - pulse	Bolu(90°)	n/a	7.2	0.61	63.2	10.6	0.9
GM2 ^[4]	Loma Prieta, CA (1989)	Gavilan(67°)	Reverse Obl.	6.9	0.79	61.3	13.6	1.8
GM3 ^[4]	Northridge, CA (1994)	UCLA(90°)	Reverse	6.7	0.81	63.5	11.1	0.2
GM4	Valparaiso, Chile (1985)	USFM(70°)	Reverse	8.0	0.94	50.3	12.5	1.4

¹ PTA=peak table acceleration; PTV=peak table velocity; PTD=peak table displacement; Tp=predominant pulse period

² Transient component is calculated as the total motion subtracted by the pulse component, in time

³ Pulse component as determined by wavelet analysis.

⁴ Motion was scaled to the PTA listed

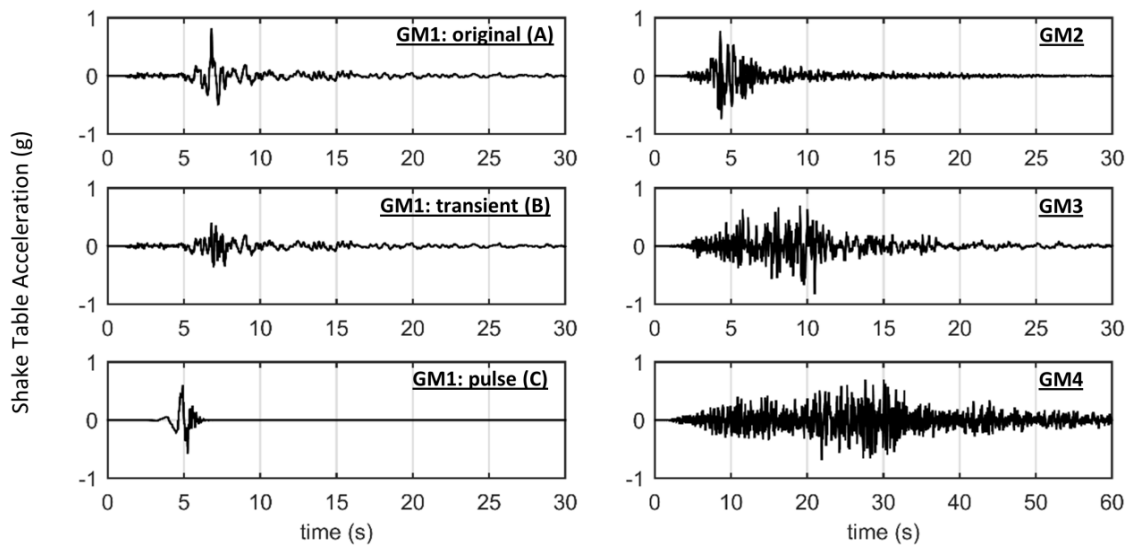


Figure 5.4 Achieved acceleration on the shake table for each input motion during the dual-body tests. Note that the x-axis range for GM4 is double that of the other plots.

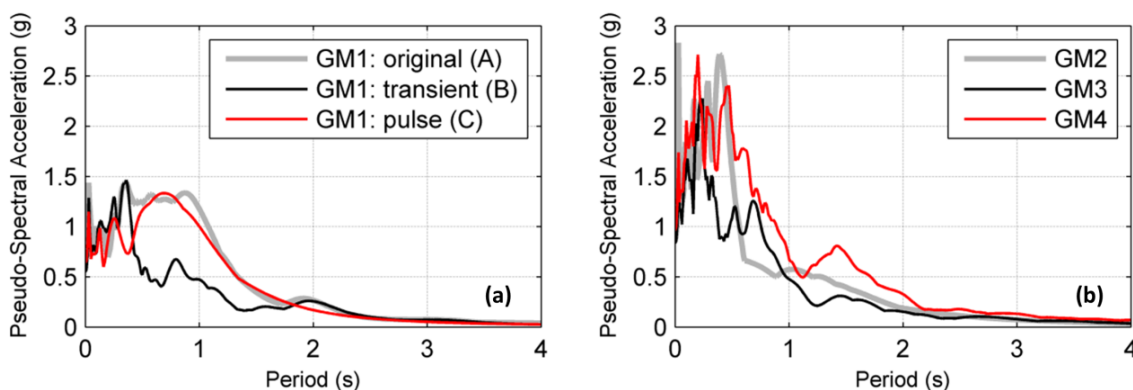


Figure 5.5 Five percent damped elastic pseudo-spectral acceleration of the achieved input motions for (a) GM1, and (b) GM2-4.

5.2 Inter-phase Comparison of Achieved Motions

Due to the nature of the experiment, it is of interest to compare the results of specific tower configurations atop each of the pedestals with that of the tower as a single-body, as detailed in Chapter 4. As a result, a comparison of the motion transfer and motion repeatability at the top of the shake table platen is of interest. For this reason, the pseudo-spectral acceleration of the mean achieved motion atop the shake table from the single-body tests, conducted in 2013, and the dual-body tests, conducted 2014, are overlaid with that of the target spectrum in Figure 5.6. Upon inspection, the spectra of the single body tests, denoted as phase-1, and the dual-body tests, denoted as phase-2, are very similar in the range of the longer periods ($T > 0.5$ s). In the short-period range, the spectra of phase-2 appear to be amplified indicating further degradation of the friction bearings of the shake table as the amplification is likely due to the stick-slip behavior.

In order to further understand the variation of the input motion, scatter plots of the peak acceleration or average spectral acceleration within a period range are given in Figure 5.7. In addition to the absolute maximum acceleration over the time series, the data in the remaining plots consist of the average pseudo-spectral acceleration within two distinct period ranges of interest: 1) $0 \text{ s} < T \leq 0.25 \text{ s}$, and 2) $0.25 \text{ s} < T \leq 0.5 \text{ s}$. Each of the three sets of data is plotted for the achieved

motions in phase-1 and phase-2 against that of the target. The individual data markers represent the maximum acceleration or the average spectral value for the mean time history or the mean spectrum, as previously defined. In addition to the individual data markers, bars are included which represent the total range of data for each of the achieved motions and are a simple measure of the scatter and variability of the data. Upon inspection of the absolute maximum acceleration plot, it is emphasized that the shake table consistently amplifies the peaks. The peaks were amplified by approximately 10% in phase-1, whereas the peaks were amplified by nearly 40% in phase-2. In addition to the significant amplification, the range of achieved peaks also increased from phase-1 to phase-2. This increased variability may be related to the manual lubrication of the bearings which occurred before each configuration during phase-2.

The amplification of the target motion is not very severe when analyzed in terms of the average spectral acceleration in critical period ranges. In addition, the effect is reduced as the period increases. For example, in Figure 5.7, the short-period spectral acceleration was amplified by approximately 10% during phase-1 and no greater than 20% during phase-2. The amplification in the period range of 0.25 – 0.50 s is further reduced in which both phases of experimentation observed amplification of less than 5%. However, it is still noted that larger amplifications in this period region were observed during phase-2. Due to the sensitivity of the freestanding system to long-period contributions, these amplifications are not likely to have a significant effect on comparisons of results between the phases. In addition, the response of the pedestals in terms of rocking and sliding also act as a low-pass filter of the input motion due to the nature of rocking and sliding compared to vibration.

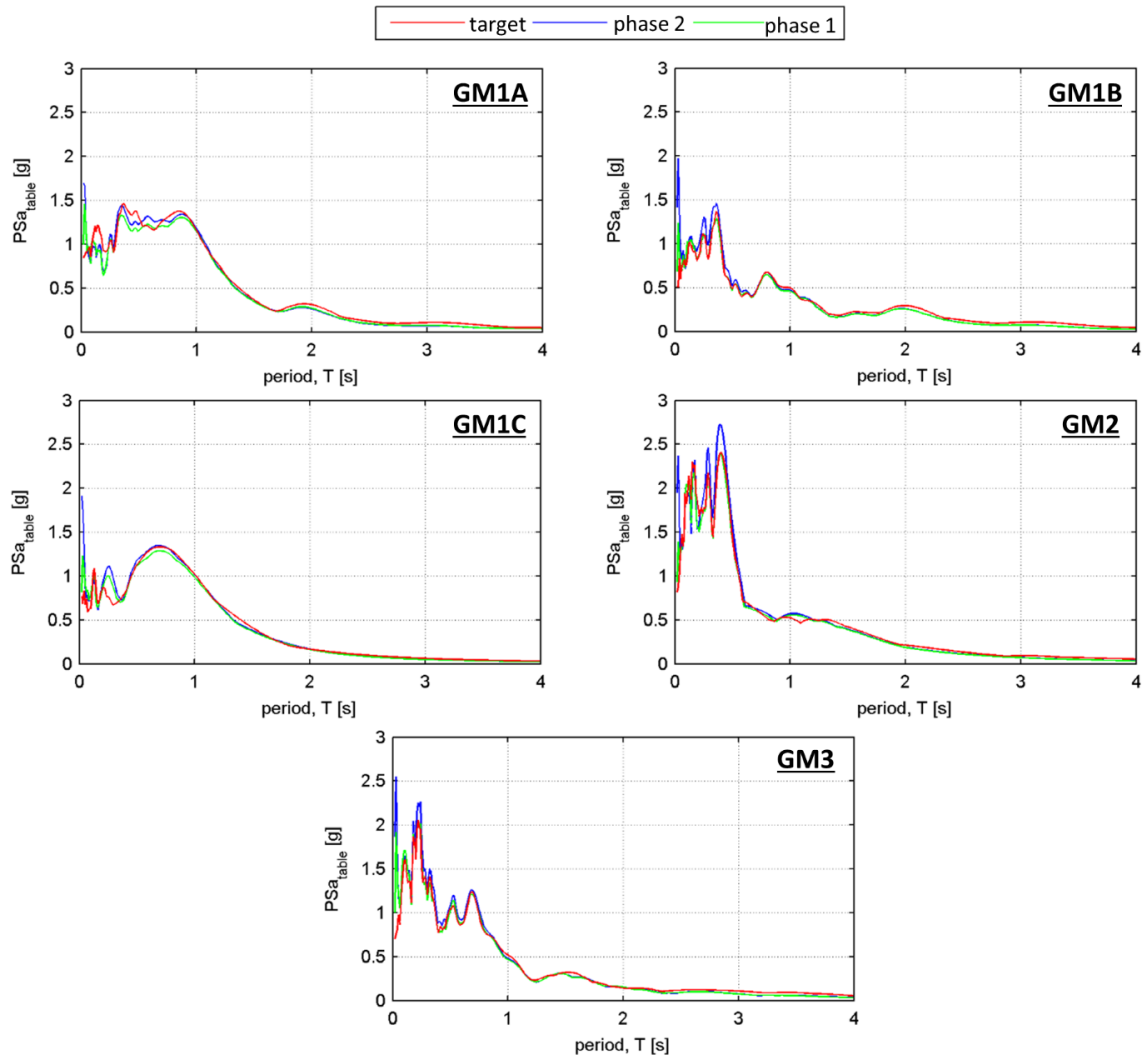


Figure 5.6 Pseudo-spectral acceleration (5% damped) of the target input motions overlaid with that of the mean achieved recording during both the single-body tests (phase-1) and the dual-body tests (phase-2).

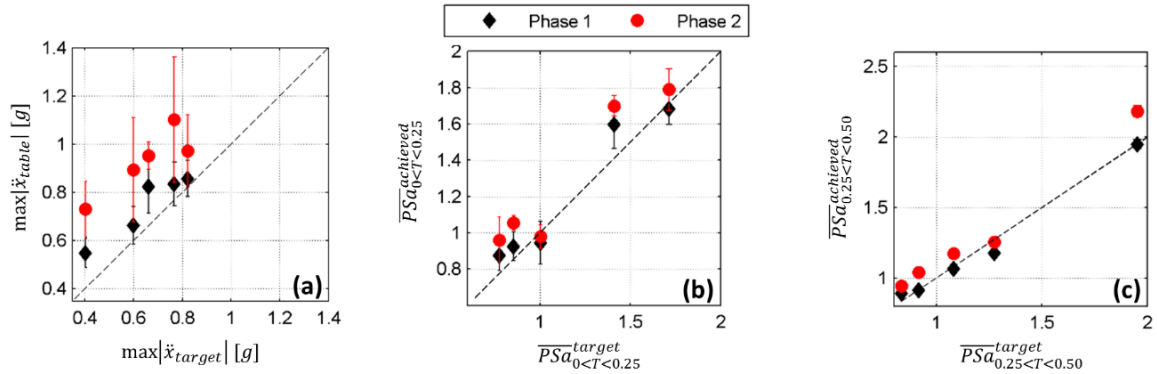


Figure 5.7 (a) Maximum absolute acceleration, (b) pseudo-spectral acceleration averaged over $T = [0, 0.25]$ s, and (c) pseudo-spectral acceleration averaged over $T = [0.25, 0.50]$ s, against that of the peak target acceleration for each of the input motions for single- and dual-body tests.

5.3 Interface Characterization Tests

Due to the anticipated sliding response of both tower and pedestal, friction characterization tests were conducted at each of the interfaces throughout the duration of the shake table testing. The three tested interfaces include the tower-pedestal, pedestal-shake table with marble, and pedestal-shake table with steel plates. These interface characterization tests aimed to quantify the coefficient of friction and any potential variation of the frictional resistance. The tests were conducted by restraining the specimen above the interface and inducing slip at the interface by displacing the shake table at a constant velocity. Tests were conducted at various levels of constant velocity (i.e. 10 mm/s, 50 mm/s, 100 mm/s), with velocity of 50 mm/s thought to be most representative of the typical velocity range during earthquake motions. The specimen was restrained from motion using a chain system, which was anchored to a strong wall adjacent to the shake table. A load cell was placed in parallel with the chain system to measure the restraining force. The displacement of the shake table and the specimens were monitored using the previously discussed string potentiometer system. The coefficient of friction was extracted from the recorded data as the ratio of the restraining force and the weight of the specimen, where the experimental setup and schematic for extraction are provided in Figure 5.8.

Typical results of the calculated coefficient of friction over time for three trials of each of the three interfaces are presented in Figure 5.9a. The time histories show a gradual increase in the coefficient of friction, which is indicative of the chain system becoming taut, after which the force levels off and an average coefficient of friction can be determined. The pedestal-shake table marble interface yielded an average coefficient of friction of approximately 0.68, which is only slightly less than values typically reported in the literature (i.e. 0.7 – 0.8, Ambraseys and Psycharis 2011). However, the marble interface between the tower and the pedestal was much lower with an average coefficient of friction of approximately 0.40. This value agrees well with the dynamic values reported in Chapter 4 and in prior studies (e.g. Drosos and Anastasopoulos 2014). For a more detailed treatment of the interface characterization tests, refer to the general experimental report (Wittich and Hutchinson 2015), and a thesis focused specifically on the interface characterization tests (Grossi 2014).

It should be noted that the histories presented in this section were obtained after most of the earthquake tests were completed. A comparison of the results before and after the earthquake tests is included in Figure 5.9b. Scatter on the order of 0.04 is observed for both marble interfaces (tower-pedestal and pedestal-shake table), which includes both pre-earthquake and post-earthquake tests. Results for the steel plate interface indicate a much higher level of repeatability amongst the pre-earthquake and post-earthquake tests. However, there is a distinct difference between the coefficient of friction recorded prior to earthquake testing and that after earthquake testing. While the friction was initially measured at approximately 0.15, the value at the conclusion of testing was approximately 0.21 indicating degradation and wear of the polymer-coated surface. Due to this behavior, a total of four plates were used during the testing with a new plate placed for each pedestal-tower configuration.

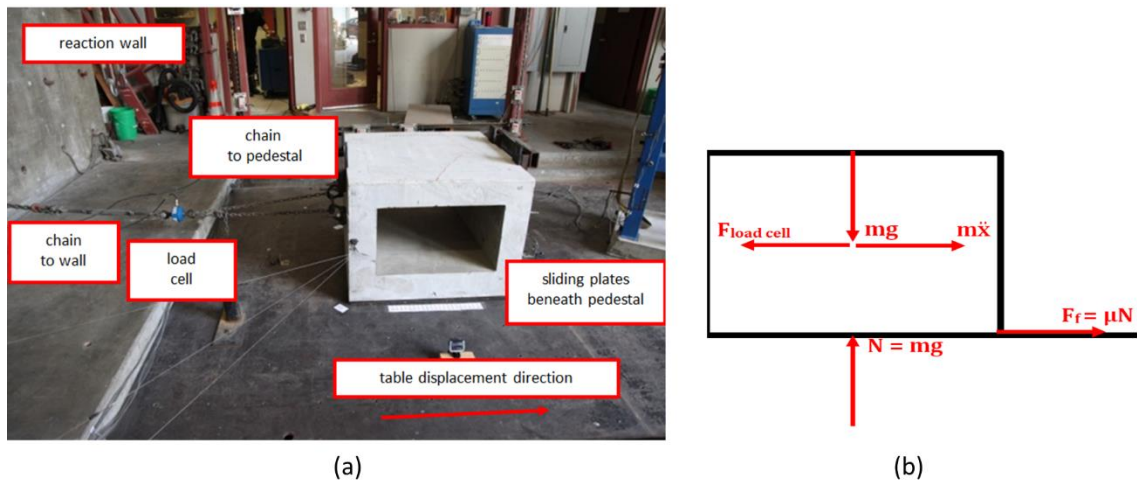


Figure 5.8 (a) Experimental setup for the interface characterization tests, shown for the squat pedestal. (b) Free body diagram for the extraction of coefficient of friction.

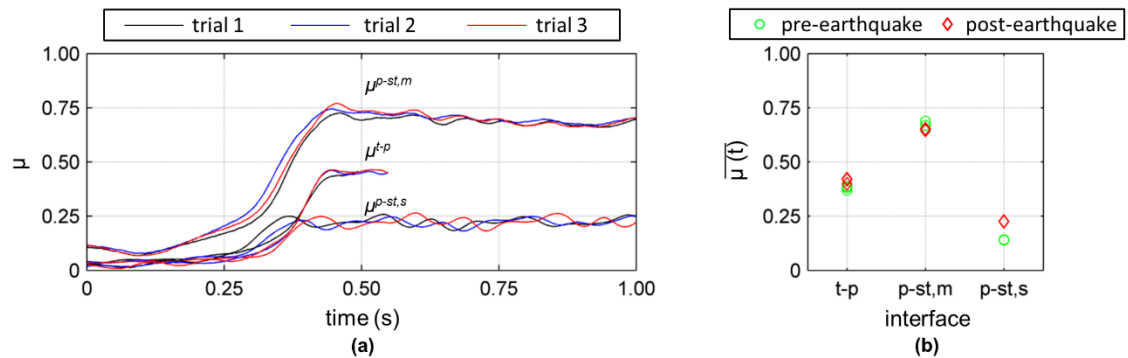


Figure 5.9 (a) Three trials of pull tests for the three interfaces at constant velocity (50 mm/s) after dynamic testing. (b) Comparison of extracted coefficients for each interface before and after dynamic testing.

5.4 Repeatability of Dynamic Tests

5.4.1 Marble-Marble Interfaces

Previous experiments on multi-body response, such as those by Peña et al. (2008), have reported decent repeatability for harmonic or pulse input motions with low repeatability for earthquake or random input motions. However, many of these previous experiments were focused

on the response of stacked systems in excess of two bodies which incorporated largely squat geometries. Therefore, a number of repeatability tests were incorporated into the test matrix of the current experiment for implementation on the various geometric configurations. An attempt was made to incorporate at least two repeatability tests for each configuration into the overall test matrix in an effort to understand the inherent variability of the results. Ideally, each test of each configuration would be repeated under identical conditions; however, this is not possible for many reasons including scraping of the interfaces, minor crushing of the tower edges, imperfect starting locations, and high-frequency disturbances of the input motion.

Time history comparisons for two repeatability trials of GM1A are presented for L11sm, L11tm, L31sm, and L31tm in Figure 5.10 - Figure 5.13, respectively. In these plots, the rocking, sliding, and twisting are presented separately for the pedestal and tower with the two trials overlaid. In general, the twisting of the tower appears to be the most highly variable with significantly different shape, magnitude, and direction. However, this variability appears to have little effect on the other modes of the tower. This can be linked to the relatively small magnitudes of the twisting and the resultant small effect on the component of motion transferred. For example, a twist of approximately 5° has an effect of less than 0.5% on the accelerations inputted in the primary direction. Therefore, variations in terms of the twisting are not considered significant and do not significantly impact the collapse potential of the system (i.e. overturning or excessive sliding). Furthermore, the rocking and sliding modes appear fairly repeatable even in the presence of large twisting variations. The shape of the response history and the magnitudes are quite similar between the two trials for each of these four configurations. In addition, there appears to be little correlation of the repeatability with any particular tower or pedestal configuration.

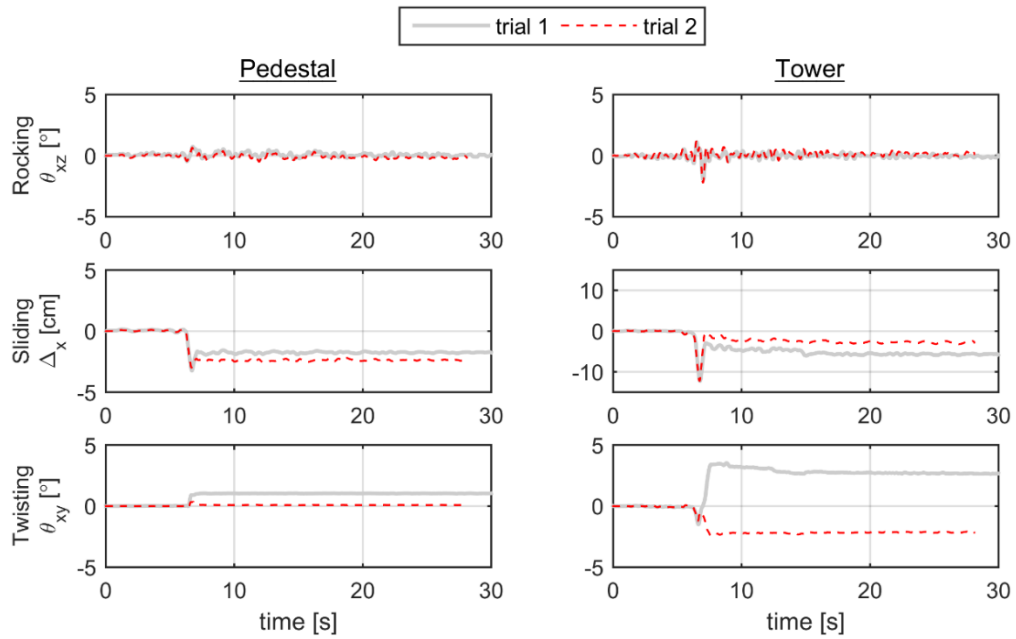


Figure 5.10 Time history comparison of repeatability trials for L11sm configuration to GM1A.

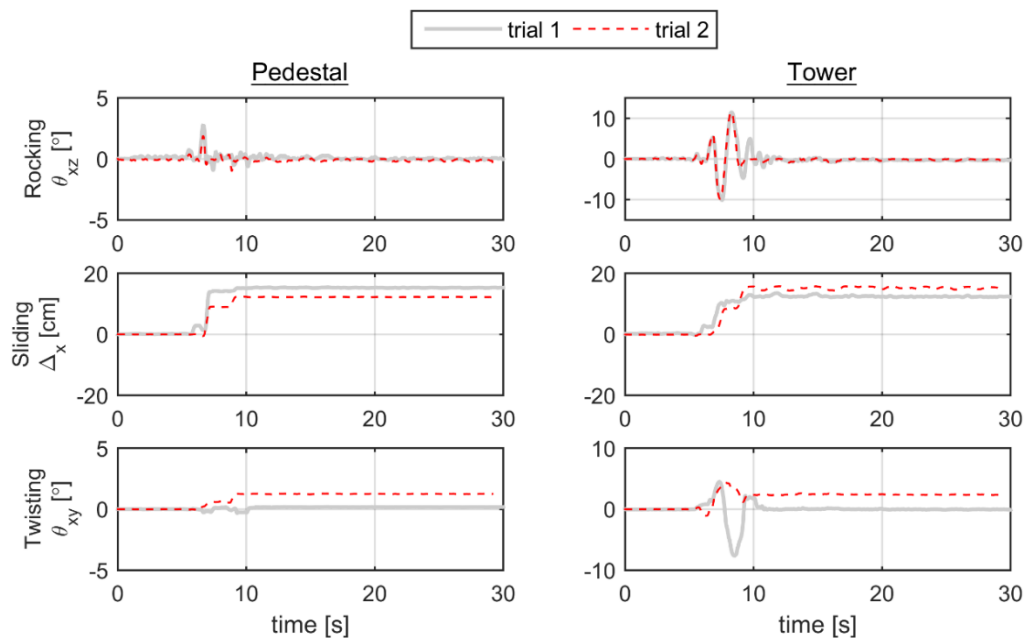


Figure 5.11 Time history comparison of repeatability trials for L11tm configuration to GM1A.

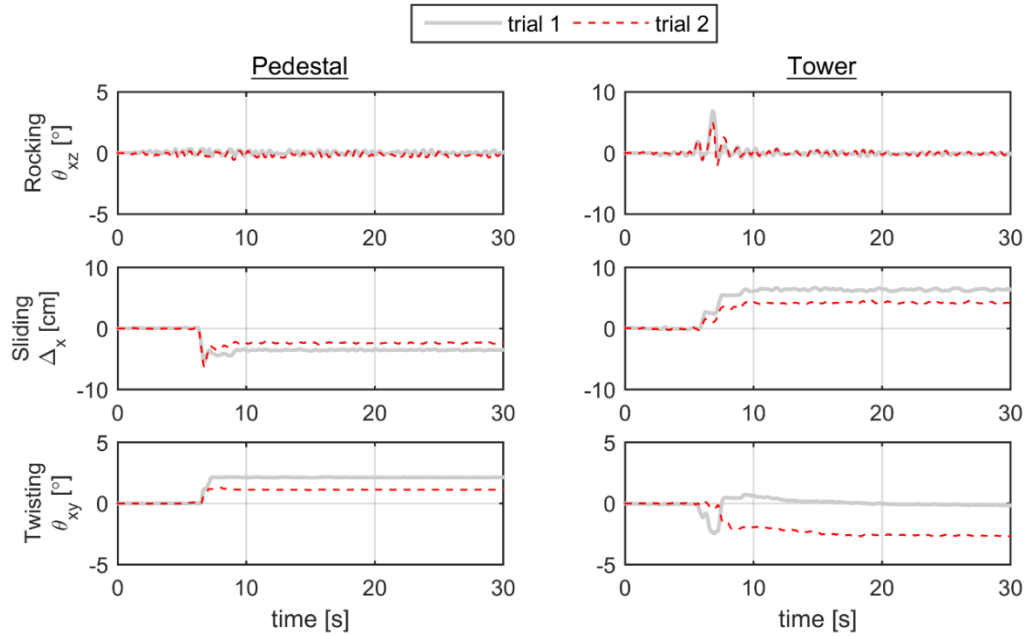


Figure 5.12 Time history comparison of repeatability trials for L31sm configuration to GM1A.

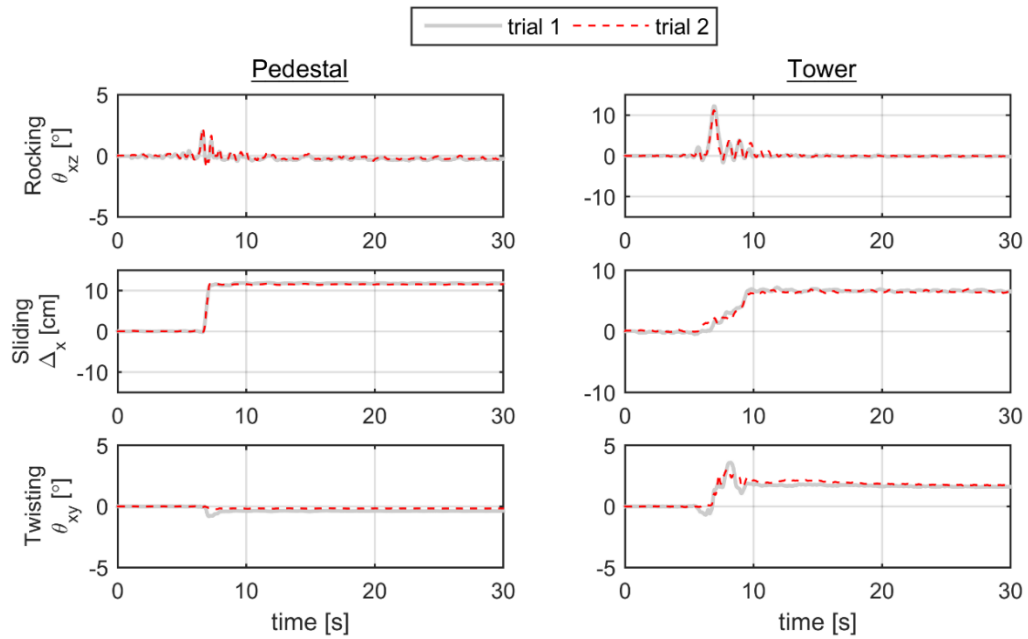


Figure 5.13 Time history comparison of repeatability trials for L31tm configuration to GM1A.

Referring again to Figure 5.10 - Figure 5.13, the rocking appears to have slightly more variation than the sliding. While very good agreement is possible (e.g. L31tm in Figure 5.13), other configurations show slight differences in the rocking histories. For example, for L11tm in Figure 5.11, the maximum achieved rocking of the tower is quite similar between the two trials, but the rocking appears to decay much more rapidly in the second trial. This is related to the complex interaction between two moving blocks and the uneven surfaces. Furthermore, rocking impacts and decay are correlated with material interactions; and, an impact located precisely at a crack, imperfection, or warp could potentially dissipate less energy than at a more even or rigid location. In addition, the fabrication-induced wobble of the pedestal can be a factor in the rocking decay of the tower. The rocking decay of the single block was fairly uniform for the single-body experimentation, detailed in Chapter 4, due to the impacts with the very stiff base slab and shake table; however, the dual-body system involved two moving bodies.

While previously presented time history comparisons of repeatability tests were largely positive, a final set of comparisons is included in Figure 5.14, which presents a more abnormal situation. The U11sm configuration was tested four times to the GM1A input motion. The rocking, sliding, and twisting response histories of each the four trials are overlaid in this figure. The motion of the pedestal is small during this motion due to the significantly more slender tower and the high friction, squat pedestal. However, the response of the tower is quite drastically different amongst the trials. Although sliding and twisting of the tower are observed, the magnitude of sliding is no greater than 2 – 3 cm and the twisting is no greater than 5 – 10° at any point in any trial. The overlaid rocking time histories are nearly identical up until approximately 7 s when the tower reaches a rotation of approximately 10°. At this point, the tower remains at this rotation for a highly variable amount of time depending upon the trial. This rotation is approaching the critical angle and even very small modifications to its input can cause very different results. This observation has been made in much of the early literature on the analytical response of single blocks (e.g. Housner

1963; Yim et al. 1980; Konstantinidis and Makris 2009). This sensitivity near the critical angle appears to be exacerbated when in this dual-body configuration due to the inevitable variations in the pedestal response, even if in nearly indiscernible, as well as the constantly evolving interface characteristics.

In an effort to understand to the general repeatability of the various configurations, a series of bar charts are presented in Figure 5.15. In these charts, the measure of repeatability is the difference of the maximum achieved response (e.g. rocking rotation, θ_{xz}) of a given repeatability trial with that of the median of all *identical* tests (all repeatability trials). This study includes all configurations of the SM- and TM-pedestals. Referring to the individual subplots which represent an individual mode, the data appear fairly symmetrically distributed with no distinct skew towards either direction of response. In addition, the data have a very strong central tendency and the frequency falls off rapidly as the deviation moves further from zero. This strong central tendency can be characterized by a range of values within which 90% of the deviations were included for each mode. The following list summarizes these ranges of 90% repeatability:

- Rocking of the pedestal, θ_{xz}^p : $\pm 0.4^\circ$
- Rocking of the tower, ϕ^t : ± 0.1
- Sliding of the pedestal, Δ_x^p : ± 1.0 cm
- Sliding of the tower, Δ_x^t : ± 1.7 cm
- Twisting of the pedestal, θ_{xy}^p : $\pm 0.6^\circ$
- Twisting of the tower, θ_{xy}^t : $\pm 2.4^\circ$

Note that the provided 90%-repeatability ranges are representative of the raw data and may be smaller than the ranges shown in the bar charts which were developed with even bins according to the total range. This largely affected the sliding mode which was characterized by very large, yet infrequent deviations. These sliding anomalies may be attributed to the evolving surface and the

development of marble dust at the interfaces which can create a very smooth surface during an individual dynamic test.

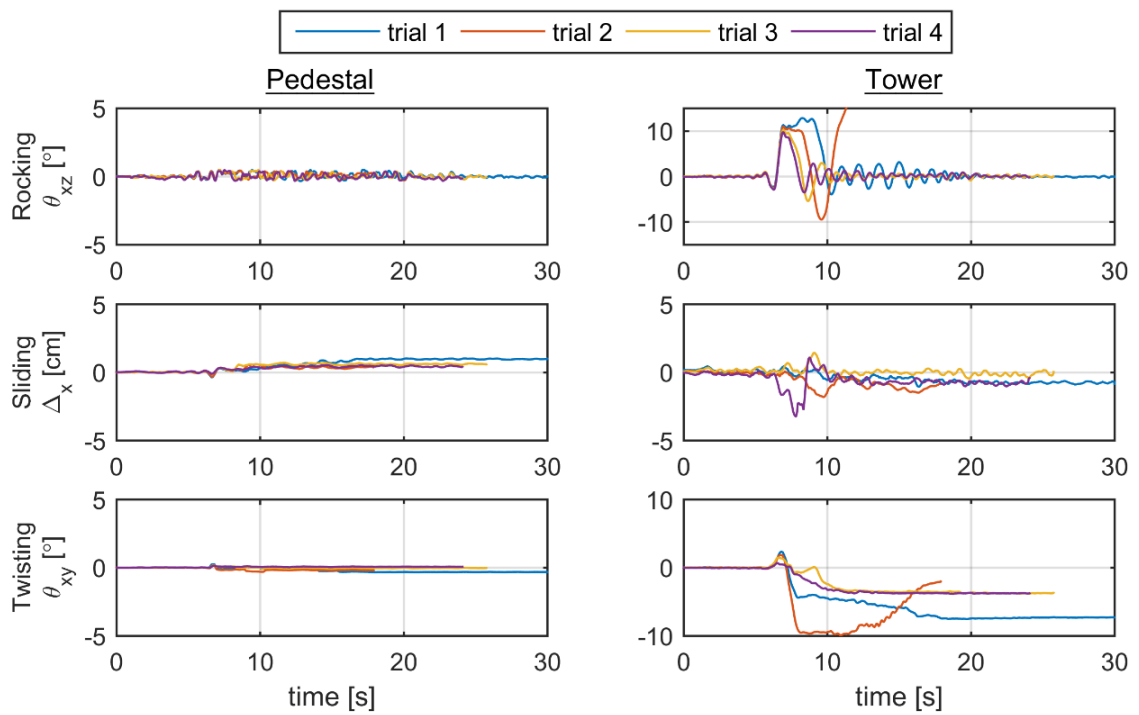


Figure 5.14 Time history comparison of repeatability trials for U11sm configuration to GM1A.

Deviation from Median of All Repeatability Trials

$$\Gamma = \max |RQ_{dir}^{spec}| \Big|_{\substack{GM \\ Config \\ i}} - Md (\max |RQ_{dir}^{spec}|) \Big|_{\substack{GM \\ Config}}$$

where: $RQ = \theta, \phi, \Delta_x$
 $spec = t, p$
 $dir = xz, xy, x$
 $i = trial$

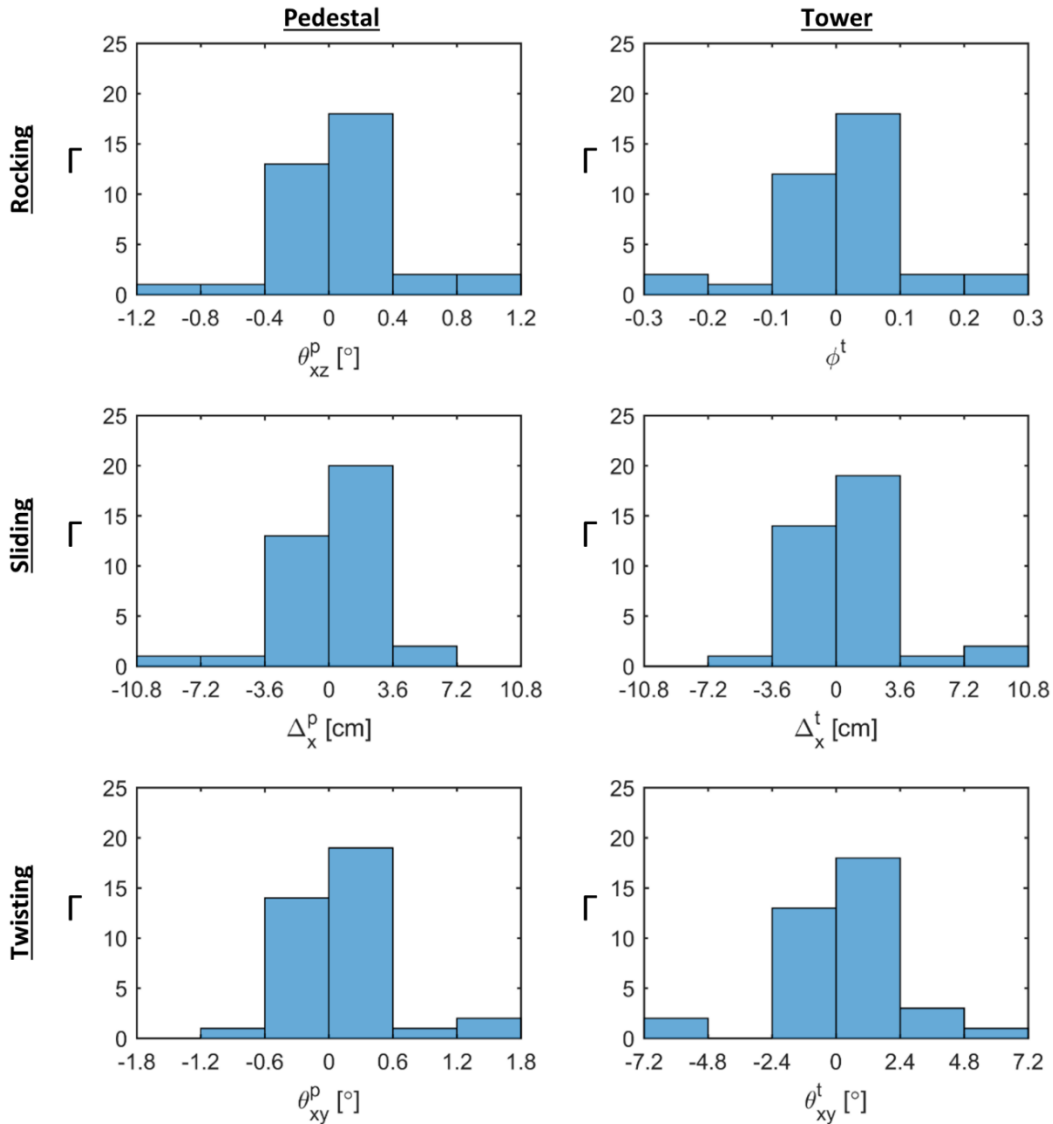


Figure 5.15 Repeatability of various response quantities for pedestal and tower in which histograms of deviation from the median are presented.

5.4.2 Comparison with Low Friction Steel Interfaces

To evaluate the repeatability of response of the system, at least one motion was repeated for each configuration tested in the current experiment. To assure consistency in protocol, the specimens were re-oriented and interfaces cleaned prior to each test in an attempt to produce an identical configuration. Representative measured rocking and sliding response for a pedestal and tower structure (U31sm: tall, eccentric tower atop squat marble pedestal) for two trials of the pulse-like Duzce motion (GM1A) are included in Figure 5.16. While both trials result in eventual overturning, the responses prior to overturning are not identical. The pedestal responds in a sliding mode during both trials with one trial achieving a peak displacement of approximately 2.5 cm and the subsequent trial achieving about half of this amplitude at 1.2 cm. This variation indicates potentially high dependence on the marble interface for the repeatability. Furthermore, the tower exhibited differences not only in magnitude of response but also the mode. The first trial observed a largely rocking response with sliding occurring during the final overturning event. However, the second trial observed a distinct slide-rocking response prior to the point of instability. Despite these non-identical results, the ultimate failure and residual displacements were similar.

To compare the effect of the frictional resistance on the repeatability, a second set of time history results are presented in Figure 5.17 in which the rocking and sliding of the tower and pedestal on the steel plate interface were subject to the pulse-like Loma Prieta motion (GM2). Significantly increased repeatability is observed for these tests in terms of the response of both specimens compared to that of the same system with the marble interface at the base. There is no discernible difference in the sliding response of the pedestal and negligible differences in terms of the rocking and sliding of the tower. This emphasizes the high correlation between the base interface and the repeatability of the entire system response. The steel interface allows for very smooth sliding responses and a relatively constant frictional resistance across the interface. On the

contrary, the marble-marble interface produces a more stick-slip response due to distinct asperities. Furthermore, the marble interface is more likely to change throughout testing due to accumulation of dust or damage during impact.

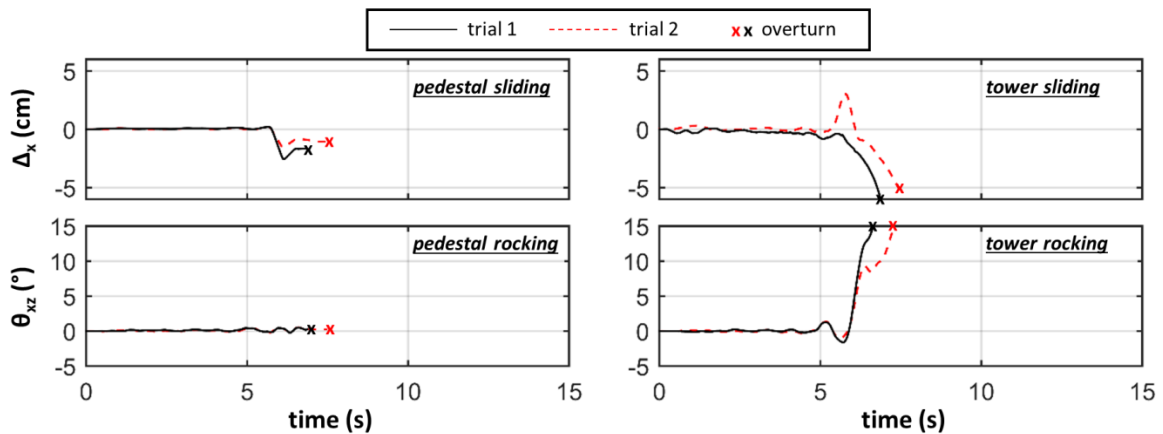


Figure 5.16 Specimen U31sm (tall, eccentric tower atop squat pedestal with marble interface) subject to repeated trials of motion GM1A (1999 Duzce Earthquake at Bolu Station).

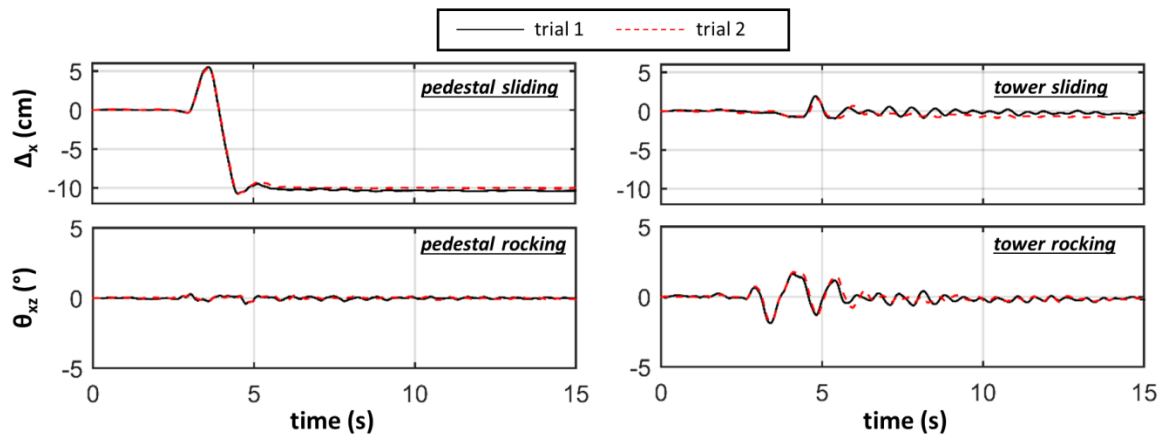


Figure 5.17 Typical repeatability tests for U31ss (tall, eccentric tower atop squat pedestal with steel plate interface) subject to GM2 (1989 Loma Prieta Earthquake at Gavilan College).

5.5 Results and Interpretation of Dynamic Tests

5.5.1 Effect of Pedestal Geometry

To investigate the effect of the presence and geometry of the pedestal, three unique variations were incorporated into the test program: 1) ‘np’ which is a single-body configuration with a marble-marble base interface (i.e. no pedestal); 2) ‘sm’ which is a dual-body configuration in which a squat pedestal is present with a marble-marble base interface; and, 3) ‘tm’ which is a dual-body configuration in which a tall pedestal is present with a marble-marble base interface. In order to understand the general effects of the pedestal, the maximum achieved rocking and sliding of the tower in one pedestal configuration are plotted against another in Figure 5.18. In these plots, the data markers correspond to the tower configuration (i.e. L11, L31, U11, U31) and the pedestal type is defined along the x- and y-axes. In addition to the data markers, each plot includes a 1-to-1 line to aid in evaluating trends.

Referring to the top row of plots in which the response is plotted with no pedestal against that with the tall pedestal, an increase in the maximum achieved rocking of the tower is observed with the presence of the pedestal. This relative increase is least noticeable for the U-configurations of the tower, which are quite tall as single-bodies and this single-body response remains dominant, even in a dual-body configuration with a tall pedestal. The increased response is particularly noticeable for the L11 configuration, as it is dominated by a sliding response when it is in a single-body configuration. However, the center of mass of the dual-body configuration can produce a taller system compared to that of the single-body; and, this would lead to rocking initiating at lower values of acceleration and ultimately a rocking-dominated response. While the aforementioned observations regarded the case of the tall pedestal compared to the case of no pedestal, similar observations are seen with respect to the squat pedestal compared to the tall pedestal, although much less drastic (refer to second row of plots in Figure 5.18).

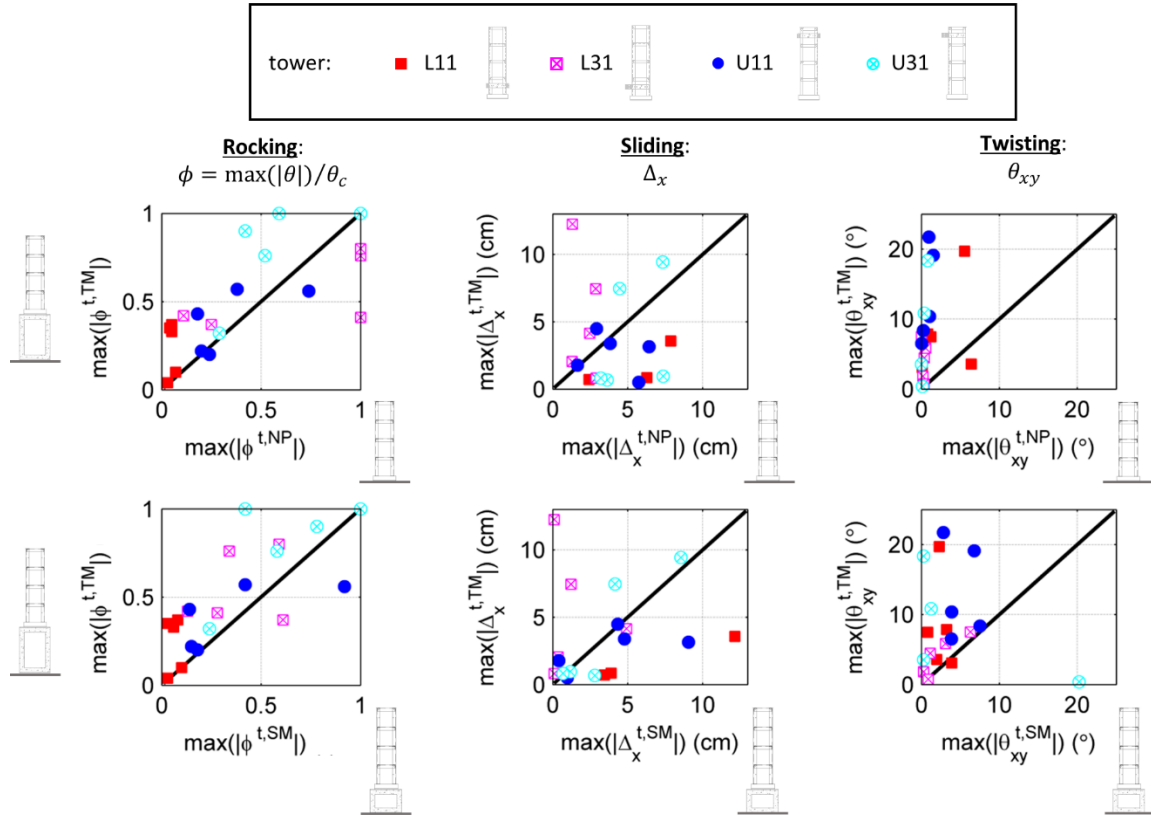


Figure 5.18 Scatter plot of maximum absolute (normalized) rocking, sliding, and twisting for individual motions and tower configurations atop the taller ('tm') pedestal versus that (top row) as a single-body ('np') and (bottom row) atop the squat ('sm') pedestal on the marble interface.

In contrast to the other tower configurations, the L31 (squat, eccentric) tower configuration observed lower rocking demands in the dual-body configuration than it does as a single-body configuration. As a single-body, this configuration is prone to overturning; however, this configuration overturned only after multiple impacts. Therefore, the reduced demands are likely attributed to the complex interaction of the tower and pedestal at impact. Whereas a single body impacts a fixed boundary, the tower impacts an inclined plane rotating with a finite value of angular velocity when atop a pedestal. For example, Figure 5.19 presents the rocking time history of this tower in a single-body configuration and the corresponding time history in a dual-body configuration atop the tall ('tm') pedestal. It is clear that the tower atop the tall pedestal attains a

higher initial rotation at approximately 3 s; however, the motion is drastically reduced after this first peak. The impact with the pedestal, in this case, results in significantly more energy dissipation as the pedestal is uplifting with positive angular velocity prior to impact while the tower has negative angular velocity (time section denoted as *i* in the figure). After impact, the tower remains in contact with the pedestal as evidenced by the overlapping time histories for a period of time following impact (time section denoted as *ii*). The noticeable change in slope of the rocking history at this point indicates the significant reduction in angular velocity and the decay of the motion. This is in stark contrast to the impacts exhibited by the single-body configuration which result in noticeable uplift about the opposite rocking point after impact due to lower energy dissipation.

While the effect of the pedestal on the rocking effect was quite profound, the effect of the pedestal on the sliding mode does not present a distinct overall trend as presented in Figure 5.18. However, the L31 (squat, eccentric) configuration does evidence a clear increase in sliding on the tall pedestal compared to both the squat pedestal and no pedestal cases. When placed in the dual-body configuration, the tower is not resting on a level surface at times which increases the likelihood of sliding. This is most pronounced in this configuration due to the very high overturning rate and low modal interaction for this particular tower as a single-body.

Referring to the final column of plots in Figure 5.18 focused on the twisting, a very clear increase in the three-dimensional effects (i.e. twisting) is seen for both pedestal cases. This is anticipated due to the increased degrees of freedom which amplifies minor response changes from the base to the top block. While this increased twisting response has also been observed in other multi-body experiments (e.g. Peña et al. 2008), the twisting observed in this experiment is quite distinct with many instances of twisting in excess of 5° . This substantial response can also be attributed to the uneven interfaces which were slightly warped due to the wet-bonded fabrication of the concrete-marble pedestals. Furthermore, the effects of twisting were more noticeable for the

tall ('tm') pedestal cases. This is likely attributed to the rocking response of this pedestal which caused the uneven surface to be inclined. It should be noted that the outlier response in this plot (20° of twist atop the squat pedestal and no twist atop the tall pedestal) is due to the overturning of the tower atop the tall pedestal at the very beginning of the motion.

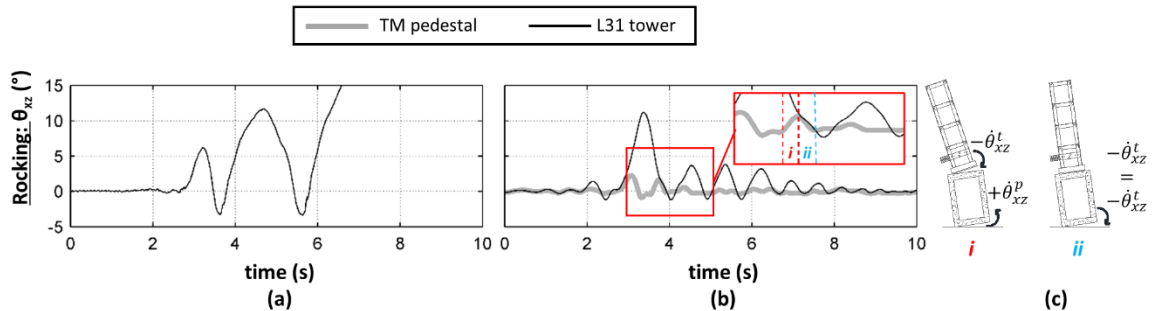


Figure 5.19 Time history of rocking for L31 (squat, eccentric) tower in (a) single-body, and (b) dual-body atop tall ('tm') pedestal with detail view of impact and (c) schematic of impact. Note that the tower rocking is plotted absolutely and is not with respect to the pedestal.

5.5.2 Effect of Tower Geometry

While the effect of the pedestal on the tower was analyzed in a previous section, the impact of the tower geometry on the pedestal was not explicitly evaluated. This section aims to study why the pedestal affected certain configurations less than others. Referring back to Figure 5.18, the rocking response of the L11 configuration (squat, symmetric) drastically increased with the inclusion of the tall pedestal. However, the response of the tall (i.e. U11, U31) tower configurations was much less amplified. To investigate further, the responses of L11tm overlaid with L11np as well as U11tm with U11np are included in Figure 5.20. For this plot, all configurations are subject to GM1A. The time histories include the response of the pedestal, as well. For this reason, the absolute response of the tower is provided meaning that the plotted rocking of the tower includes

that of the pedestal. For example, if the plot of the tower response does not deviate from that of the pedestal, the tower did not move relative to the pedestal.

Regarding the case of the L11 (squat symmetric) tower, the tower-only configuration observes very minimal response for any of the modes with the primary response being sliding. However, the L11 tower atop the tall pedestal (L11tm) initiates into a system-wide slide-rocking mode. This means that initially the pedestal uplifts and slides while the tower maintains contact with the pedestal surface. This system-wide mode then transitions to uplift of both structures in which the tower rocks in-phase with the pedestal (see inset of Figure 5.20 for schematic of response). Upon impact, the rocking of the pedestal fades and the configuration is dominated by tower-only rocking. Therefore, the initiation of rocking of the L11 tower atop the tall pedestal is due to the increase in system slenderness rather than a tower-only attribute. However, a different response is observed for the U11tm (tall, symmetric tower atop tall pedestal) tower. Rather than a system-wide response, the tower initiates into a single-body rocking mode. It is anticipated that a transition to a dual-body rocking mode would occur at a later time. However, this is not observed in the time histories due to limitations of the instrumentation. An examination of the high-resolution, high-frame rate video recordings reveals uplift of the pedestal to very small angles. This indicates that although a system-wide mode is eventually observed, the response remains dominated by the tower rocking due to the corresponding tower-pedestal geometry. Therefore, the response of the single-body test would likely be rocking-dominated, as well, which is true. However, the time history of the corresponding U11np tower is quite different than the U11tm tower. This is due to minor differences in the interface and motion transfer through the pedestal. The maximum achieved rocking for the 'tm' and 'np' towers are actually quite close (9.0° vs. 10.4°).

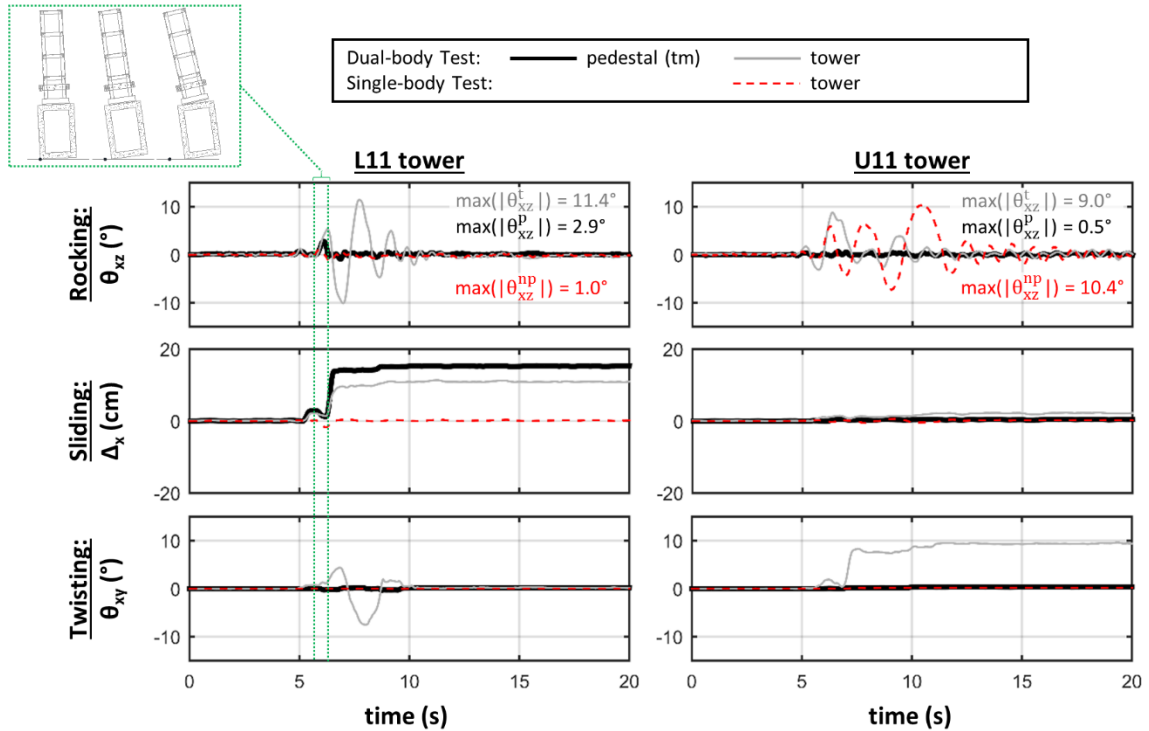


Figure 5.20 Rocking, sliding, and twisting time histories for L11tm (squat, symmetric tower on tall marble pedestal) and U11tm (tall, symmetric tower on tall marble pedestal) subject to GM1A overlaid with response of single-body towers. Note that tower responses are absolute.

5.5.3 Effect of Pedestal Friction

Two interface conditions were incorporated for study in this experiment beneath the pedestal, namely the as-built marble-marble (i.e. high-friction) interface and an alternative low-friction steel plate system. This steel-plate system is meant to both study the effect of the coefficient of friction on the response of the system as well as demonstrate the effect of a simple seismic isolation system with applicability to such dual-body systems. A set of scatter plots similar to those in a previous section is presented in Figure 5.21 to interpret the effects of the friction. The data markers indicate the tower configuration, whereas the interface beneath the squat pedestal is a variable on each of the x- and y-axes. The initial observation is a fairly significant reduction in the twisting and sliding of the tower atop the pedestal with the low-friction interface compared with

that of the marble interface. This is anticipated due to the reduction of acceleration and forces transferred to the tower. However, a less significant reduction is observed for the majority of the configurations in terms of maximum achieved rocking. Certain tower configurations, particularly eccentric towers, responded in a similar (near the 1-to-1 line) or even in an increased rocking response atop the lower-friction interface compared to that of the marble interface.

In an effort to further investigate the seemingly limited benefits in terms of rocking response of certain configurations, a set of time history results are plotted in Figure 5.22. The selected plots include the acceleration response of the shake table and the pedestal, as well as the rocking response of the tower for the U31 (tall, eccentric) configuration subject to the pulse-like motion GM1A as well as the broadband motion GM3. Referring to the response to GM1A, a very clear acceleration saturation is observed, which corresponds to the unit-less coefficient of friction. However, the prominent long-period pulse is still largely transferred through the pedestal. Despite the reduced amplitude of the pulse, the sensitivity of freestanding structures is still evident as the tower ultimately overturns. In contrast, motion GM3 does not contain any significant long period pulse contributions. The tower does not overturn during this motion; however, significant rocking is still observed with the maximum rocking at approximately 30% of critical. The poor isolation of the tower, in this case, cannot be attributed to the transfer of energy at long periods through the pedestal. Rather, the acceleration saturation (coefficient of friction) is very close to the acceleration which initiates rocking (slenderness). This case emphasizes that the coefficient of friction of a sliding plate system benefits from design tailored to the geometric configuration of the bodies to assure effective isolation.

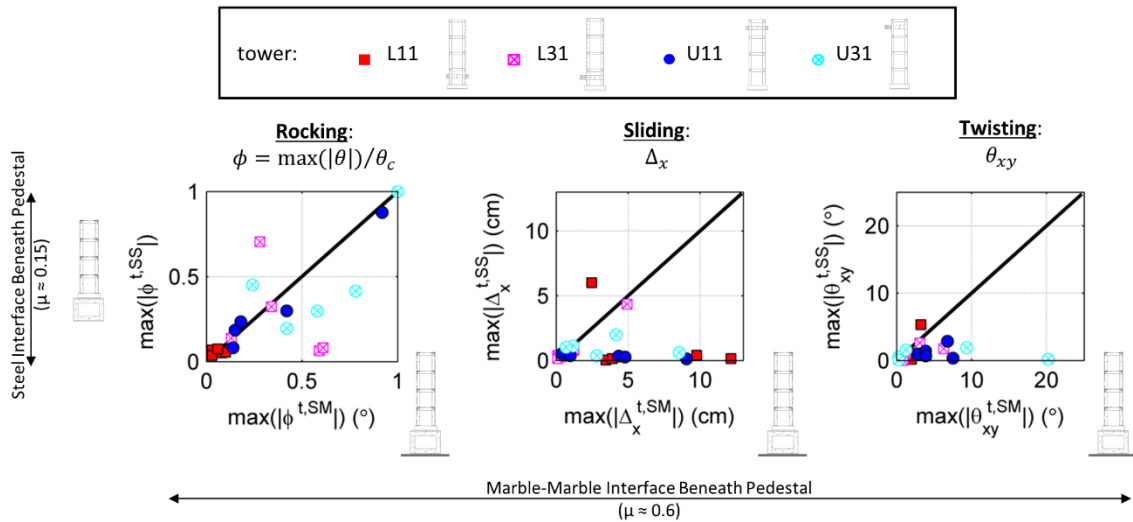


Figure 5.21 Scatter plot of maximum absolute rocking, sliding, and twisting for individual motions and towers atop the squat pedestal on steel plate interface ('ss') versus the marble interface ('sm'). Note: The thick grey line represents the marble-marble interfaces in schematics.

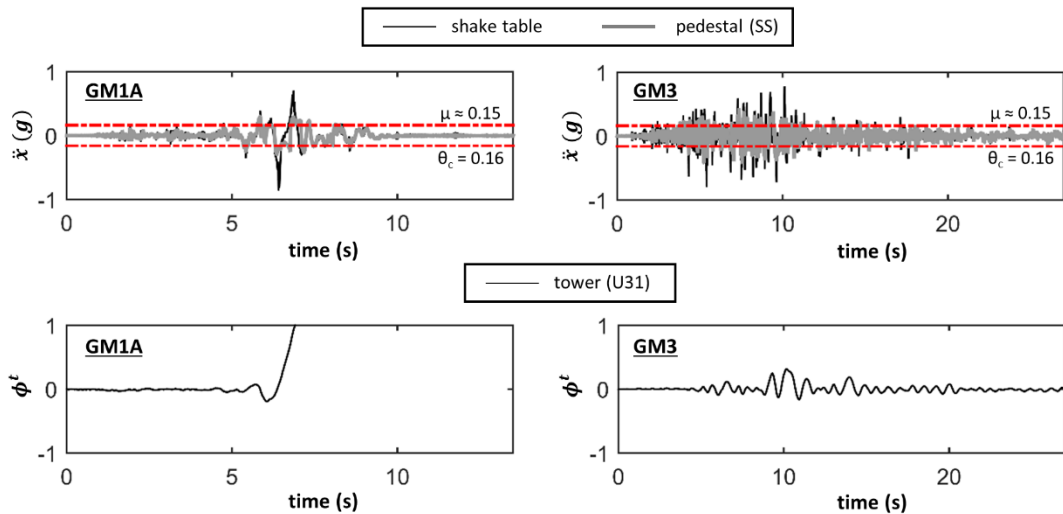


Figure 5.22 (top) Acceleration history of the shake table and squat pedestal on the steel plate interface ('ss') as well as (bottom) the tower rocking response, to GM1A and GM3.

5.5.4 Combined Effects on Multi-Modal Response

While previous sections attempted to isolate the effect of a single experimental variable, the combined effects of all parameters in terms of both primary demands is presented herein. Figure 5.23 plots the maximum sliding demand versus the maximum rocking demand for the same motion and same configuration. To facilitate interpretation, the symbols correspond to a unique tower configuration while the color of the symbol corresponds to the associated pedestal condition. In addition, the plot is separated into four quadrants associated with low or high rocking demands and low or high sliding demands. While the limit demarcating low and high demands is specific to a given situation, 20% of the maximum possible sliding and rotation for a given configuration is selected. This limit corresponds to approximately 20% of the rotation necessary for overturning as well as 20% of the distance to the edge of the pedestal (approximately 3 cm).

Use of the 20% limit highlights a number of general trends that were not necessarily apparent in previous sections. The upper-right quadrant (IV) presents those tests which exhibited both significant rocking and sliding of the tower. Nearly 70% of the tests in this quadrant included an eccentric tower configuration. While this heavy modal interaction for eccentric configurations was noted in the single-body tests of Chapter 4, it is now apparent that the tall pedestal has a similar effect. Approximately 50% of those tests in quadrant IV were for configurations incorporating the tall ('tm') pedestal, including almost half with a symmetric tower. This is likely attributed to both the finite angular velocity of the pedestal, which may result in tower rocking, and the inclined interface, which results in tower sliding. While the increased modal interaction is noted for the tall pedestal configurations, this does not necessarily correspond to an increase in the instances of failure or overturning. Of the seven cases which exhibited overturning, three were in a single-body ('np') configuration while only two were on the tall ('tm') pedestal. While the modal interaction and sliding of the tower atop the tall ('tm') pedestal may dissipate additional energy, the complex

interaction of both the pedestal and tower at impact is also a key contributor to the overturning potential. Referring back to Figure 5.19, this interaction may yield a markedly reduced angular velocity after impact and increased decay of the response. However, it should be noted that there are instances where the pedestal can increase the angular velocity of the tower at impact and potentially lead to overturning.

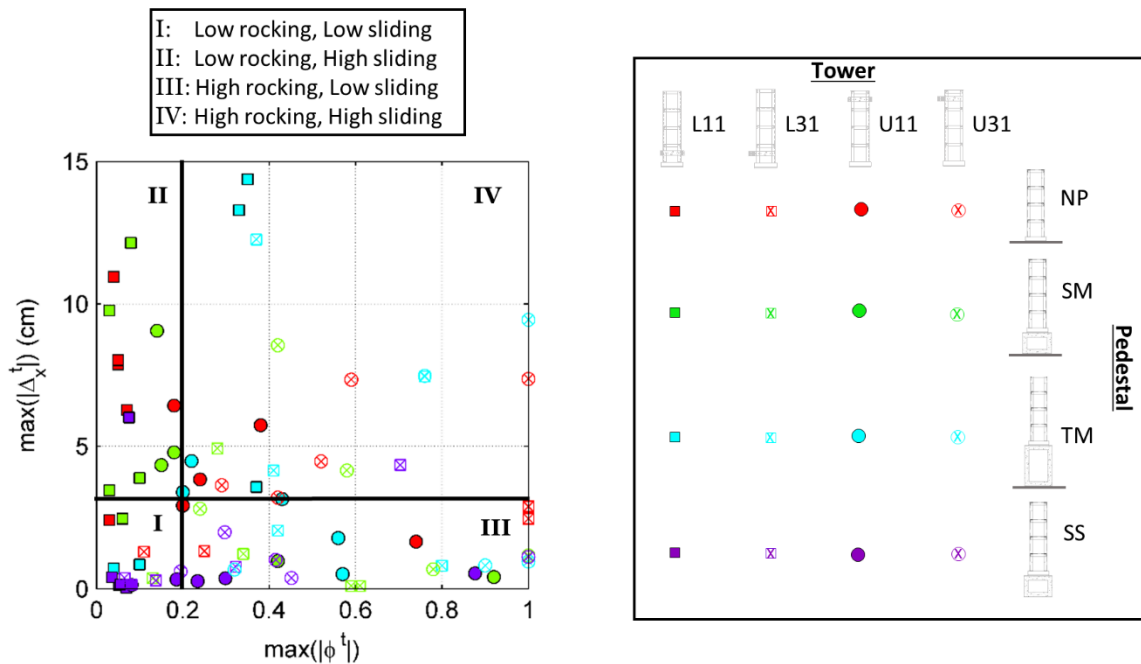


Figure 5.23 Maximum sliding of a single test against the maximum rocking of the same test. Symbols correspond to a specific tower configuration and the color corresponds to the pedestal configuration.

5.5.5 Effect of Tower Restraint with Low-Friction Pedestal Interface

This section introduces the results of a modified L11ss configuration, denoted L11ss_mod1, and compares these results with those of the L11ss configuration. The L11ss_mod1 configuration consists of the same specimens and interfaces as the L11ss configuration (squat, symmetric tower atop the squat pedestal with low-friction sliding plates beneath the pedestal). However, the L11ss_mod1 configuration has an additional restraint system fixing the tower to the pedestal. The restraint system, shown in Figure 5.24, utilized the existing bumper system. The bumper system (on the north/south sides of the pedestal) consisted of embedded threaded rod in the concrete pedestal, two short tube steel sections oriented vertically, and one horizontal crossbar bolted on the outside of the two vertical members. The restraint system consisted of an additional two tube sections placed across the concrete surface of the tower which were welded to two short vertical sections and subsequently welded to the bumper system. The connections of the bumper system were wrench-tightened to ensure vertical compression at the tower-pedestal interface. Little movement of the system was observed throughout the testing of this configuration.

While significantly less motion of the tower is anticipated in this configuration, variations in the pedestal response as well as the acceleration and forces in the tower are explored. The time histories of the response of the pedestal and tower to the test GM4 is plotted in Figure 5.25 with overlaid time histories of the L11ss configuration (restrained vs. unrestrained). Significant variations are noted in each response category for both specimens. While the rotation of the tower was significantly reduced, the rotation of the pedestal was increased to nearly 1° . This increased rotation of the pedestal is not technically rocking (uplift on the edge); however, this exacerbated wobble is due to the increased height of the center of mass of the system which could be detrimental to alternate configurations. Similarly, the sliding and twisting of the tower were drastically reduced to essentially zero. On the contrary, the acceleration at the top of the tower in the direction of

shaking significantly increased in the restrained configuration. At its peak, the tower experienced accelerations in excess of 1.5g in this configuration.

In an effort to summarize and generalize the observations from the single presented test (GM4), scatter plots of the maximum absolute normalized rocking and maximum absolute tower acceleration are plotted for the restrained configuration versus the unrestrained configuration in Figure 5.26. These scatter plots are overlaid with a thick, black line at a 1-to-1 ratio of restrained to unrestrained for comparison. It is clear that in all tests, the rotation of the tower is drastically reduced as anticipated due to the restraint mechanism. In addition, the increase of the tower acceleration is also observed in each of the tests. Although the range of accelerations observed in the unrestrained cases was very narrow (0.55 – 0.80 g), the restraint mechanism did not uniformly amplify these accelerations. Instead, a much broader range of accelerations was observed (0.95 – 1.55 g) due to the vibratory response dominating rather than a rigid body system response.

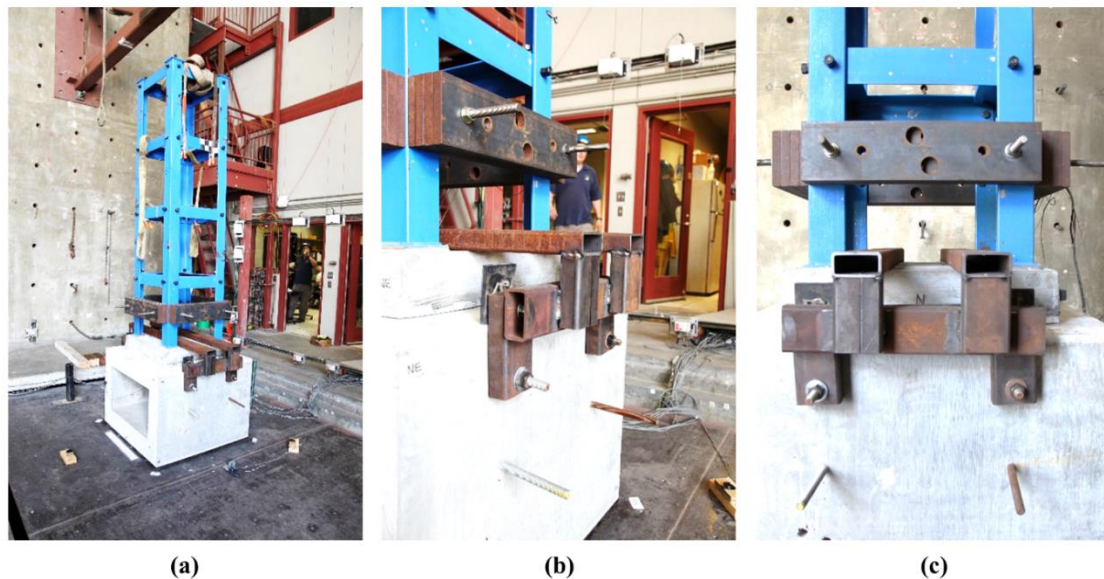


Figure 5.24 Images of L11ss_mod1 configuration highlighting the restraint mechanism.

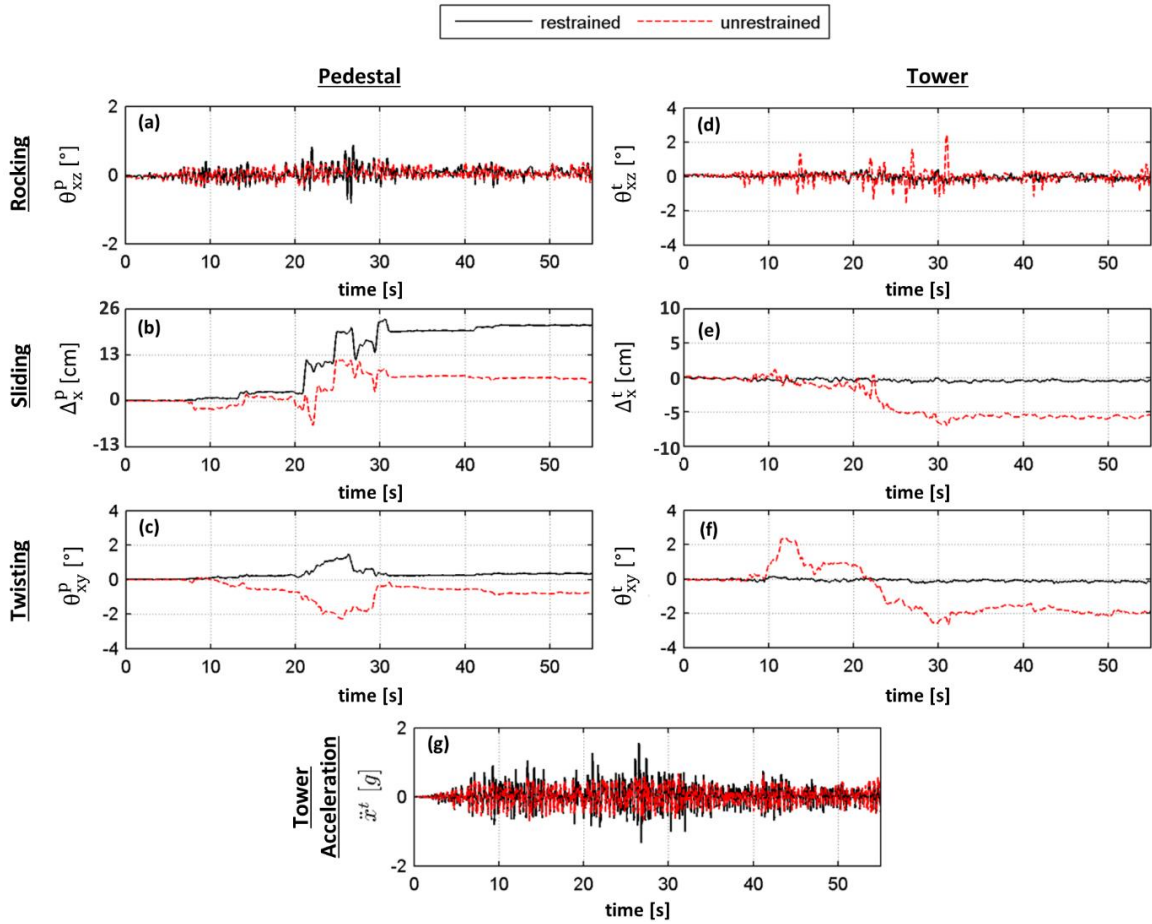


Figure 5.25 Time history of L11ss_mod1 configuration with response of L11ss to GM4 in terms of rocking, sliding, and twisting for (a-c) the pedestal and (d-f) the tower, as well as (g) acceleration of table.

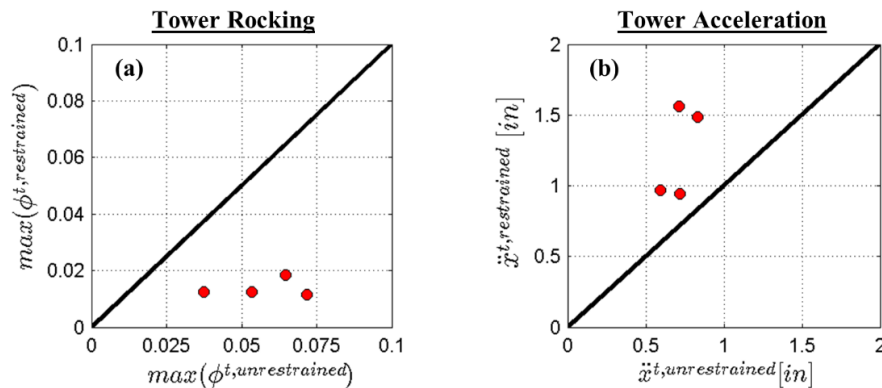


Figure 5.26 Scatter plots comparing (a) maximum normalized rocking of the tower and (b) acceleration at the top of the tower in shaking direction for L11ss versus L11ss_mod1.

5.5.6 Effect of Ground Motion

Identifying a measure of earthquake intensity, which reasonably predicts collapse of single and stacked systems of rigid blocks, is an active area of research. Presently, a single measure does not exist which has been definitively shown to be an accurate predictor. Nonetheless, some have shown promise. For example, most recently, Drosos and Anastasopoulos (2014) presented a quite reasonable correlation of the characteristic length as an intensity measure in the prediction of collapse potential of a multi-drum column using experimental results and Ricker pulse excitations. This parameter is typically obtained using a velocity quantity combined with a dominant frequency or period of the motion. Recent studies compute this using the period of an approximated pulse and the maximum velocity of the approximated pulse (e.g. Makris and Black 2004, Drosos and Anastasopoulos 2014). However, the current experiment utilized both near- and far-fault motions with variable frequency content. Therefore, an alternate version of the characteristic length is employed, which is similar to that presented by Karavasilis et al. (2010). Namely, the characteristic length is computed as:

$$L_c = T_m \cdot PTV \quad (5.1)$$

where T_m is the mean period based on the Fourier Spectrum and PTV is the peak table velocity of the motion. As a result of this product, the characteristic length is a measure of the intensity of the dominant velocity pulse.

The effect of the characteristic length on the response of the single- and dual-body configurations of this experiment are evaluated using a series of scatter plots in Figure 5.27. These plots contain the maximum achieved rocking and sliding for each of the four setups ('np', 'sm', 'tm', and 'ss') with the data markers representative of the tower configuration (L11, L31, U11, and U31) and trendlines corresponding to each tower by color. While little correlation is seen in terms of the sliding, there is fair correlation for the individual configurations in terms of rocking with the

exception of L11 (which correlates well in terms of sliding). Therefore, it is interesting to note that while L_c correlates with sliding for sliding-dominated configurations, it does not correlate with comparable sliding demands when the response is multi-modal (significant rocking and sliding). As a result, the present results show less correlation and increased scatter than other recent experiments (e.g. Drosos and Anastasopoulos 2014), due to the strong presence of multi-modal behavior. However, a particular outlier in terms of the trends observed is the L31ss configuration which had lower rocking demands for higher values of the characteristic length (negative slope).

To further study the atypical ‘ss’ configuration trend, a second set of scatter plots are included in Figure 5.28. In Figure 5.28a, the maximum absolute sliding of the ‘ss’ pedestal for all tests is plotted against the characteristic length. A positive trend is observed indicating that the ‘ss’ pedestal slides more during pulse-like motions. This indicates that the sliding plate system dissipates the most energy during those motions with significant velocity pulse content. The repercussions of this are shown in Figure 5.28b which plots the ratio of the maximum rocking on the ‘ss’ pedestal to the maximum rocking on the ‘sm’ pedestal. A value less than 1 in this plot indicates a reduction in rocking demand when the sliding plate system is incorporated. For all tower configurations, the rocking demand on the ‘ss’ pedestal is either similar or less than that on the ‘sm’ pedestal for the motions with high values of the characteristic length. This indicates that greater isolation is provided during pulse-like motions. However, this conclusion must be understood incorporating the observations of the previous section on the pedestal friction effects. This sliding plate system enforces an acceleration amplitude cutoff and has little effect on the transfer of energy at long periods to the tower. For this reason, the long-period pulse content, which is positive for the sliding plates is also detrimental to the tower. This is the likely reason for the cases which presented similar rocking demands on both the ‘ss’ and ‘sm’ pedestal (scatter plot values near 1.0) which may correspond to overturning in both cases.

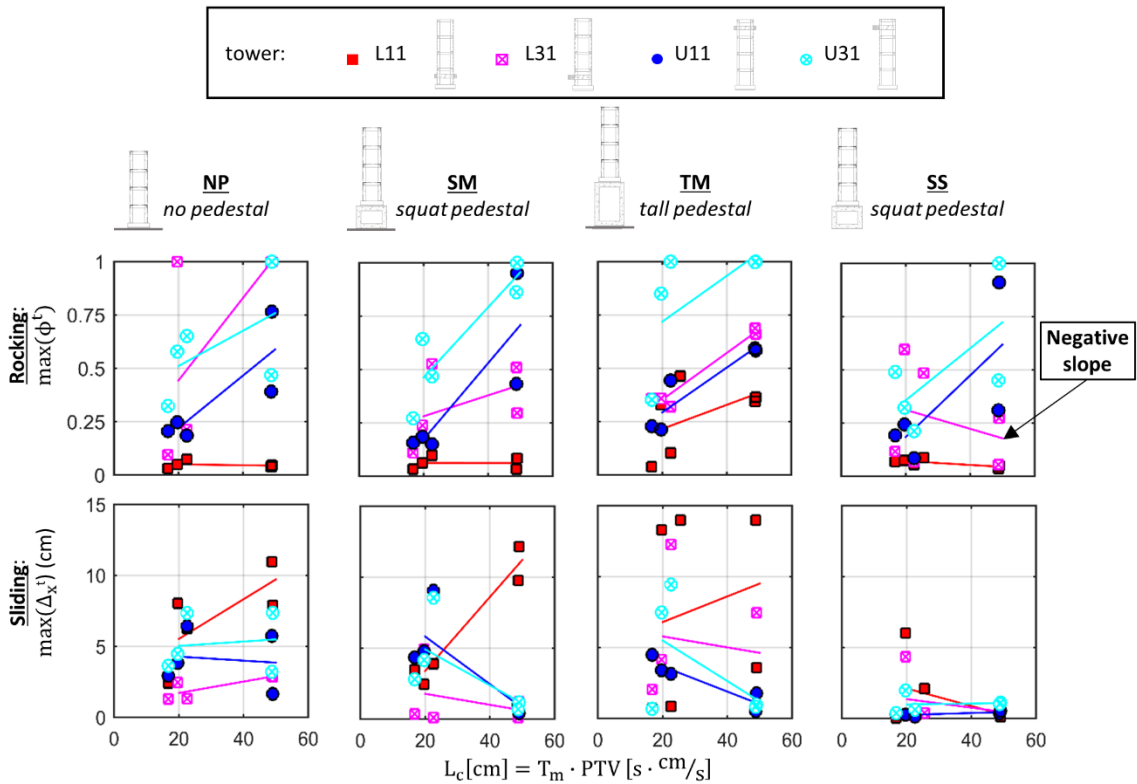


Figure 5.27 Maximum rocking and sliding of individual tower configurations for each of the four pedestal configurations versus the characteristic length of the input motion. Note that the trendlines correspond to individual configurations by color.

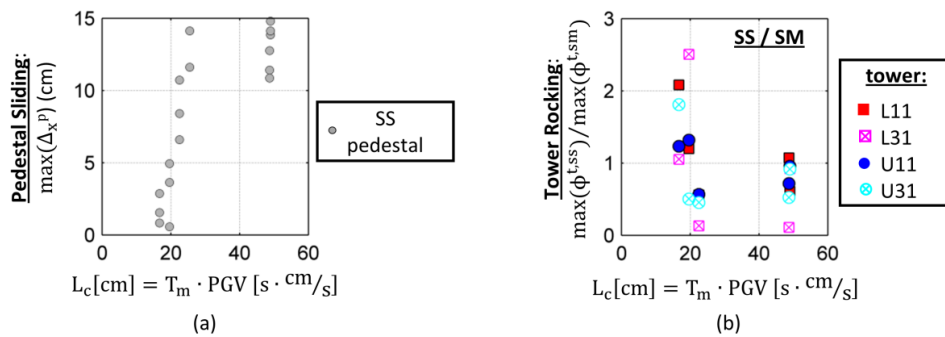


Figure 5.28 (a) Maximum sliding of SS pedestal versus the characteristic length of the input motion. (b) The maximum rocking of the tower on ‘ss’ pedestal normalized by that of the ‘sm’ pedestal versus the characteristic length of the input motions.

5.6 Conclusions

Systems of unattached, stiff, single or multiple bodies are particularly susceptible to earthquake damage, as they inherently lack protection from earthquake-induced accelerations. To better understand the dynamic behavior and interactions of these structures, large-scale experiments are necessary. In an effort to complement the limited experimental database, an extensive shake table testing campaign is detailed in this chapter. The current experiments expand upon tests conducted for single-body systems, as detailed in Chapter 4, in an effort to incorporate a second body (referred to herein as the pedestal). The range of geometries for the top-body in the dual-body configuration of these tests ranged from 0.75 m through 1.45 m for the height of the center of mass, from 2.13 through 2.56 for the frequency parameter, and from 0.16 through 0.60 for the slenderness. The range of geometries for the symmetric bottom-body ranged from 0.38 m through 0.76 m for the height of the center of mass, from 2.21 through 3.07 for the frequency parameter, and from 0.59 through 0.93 for the slenderness. The dual-body configuration was further characterized by two marble-marble interfaces of approximate coefficients of friction of 0.68 beneath the pedestal and 0.40 beneath the tower. An alternate steel plate system was incorporated beneath the pedestal to observe the effects of the friction coefficient as well as to test a simple seismic mitigation system. The corresponding coefficient of friction of this system was approximately 0.20. The tower and pedestal specimens were combined into sixteen unique combinations and tested on the uni-axial shake table at the University of California, San Diego. The three-dimensional displacement response of each specimen was continuously recorded in time and analyzed in an effort to correlate the geometry, friction, and motion characteristics with the dynamic response. The key findings presented in this chapter are summarized as follows:

- Repeatability of the dynamic response of the dual-body system is attainable provided a smooth interface with relatively constant frictional resistance. The potential

repeatability of specimen response is less viable when rougher interfaces such as the marble-marble interface are utilized.

- In general, observations of collapse and rocking demands on the tower increase with the presence of a pedestal. This is further increased as the pedestal increases in height (reduced slenderness angle, increased size). However, certain configurations of the tower were observed to be more stable in the stacked configuration than in the single-body configuration. This is likely related to the increased sliding on an inclined surface and the complex interactions at impact associated with two rotating bodies.
- The results of these experiments reveal the dependence of the response of the pedestal (bottom-body) on the geometry of the tower (top-body). Certain configurations of the dual-body system initiate into a system-wide mode, whereas others initiate into a single-body mode due to the height of the center of mass of the system compared to the tower only.
- A low-friction interface beneath the pedestal ($\mu \approx 0.2$) reduces demands on the tower; however, long-period energy content may still be transferred through the pedestal and these demands can be detrimental to the tower response if the frictional coefficient is not less than the slenderness of the tower. However, the sliding response of the pedestal on a low-friction interface observed high-correlation with the length-characteristic of the input motion ($L_c = T_m \cdot PTV$). This indicates that the system produces increased isolation during pulse-like motions.

5.7 Implications on Numerical Modeling

This chapter, along with the previous chapter on single-body tests, concludes this dissertation's treatment of the second primary objective, which is to generate a comprehensive database of the experimental response of freestanding structural systems. The generation of this database and the subsequent data analysis are intended to inform the ultimate objective, which is to develop and validate a numerical model for the seismic response of freestanding structures. As such, key conclusions of the single-body experimental campaign were detailed in Chapter 4, along with the implications on numerical modeling. These findings included:

- Asymmetry of the body impacts not only the magnitude, but also the response mode for a single-body. Therefore, the numerical model must adequately represent asymmetric and arbitrary geometry.
- Three-dimensional responses (e.g. twisting) were observed in many cases, even for configurations with apparently planar symmetry. As such, the numerical model must be conducted in a three-dimensional framework.
- Many configurations, including those which are symmetric, evidenced multi-modal behavior. As such, the numerical model must allow rotation and translation at all times and in all directions throughout the simulation.
- Experimental free rocking was unable to be captured by the classical model, which can be attributed to the assumed perfectly inelastic impacts of the classical model. Therefore, numerical models must allow for flexibility at the interface.

Building upon the results of the first phase of testing on single-body freestanding systems, the second phase of testing aimed to analyze the impacts of a dual-body system. Similarly, key

conclusions of the experimental campaign can be used to inform numerical modeling efforts. These findings for dual-body systems include:

- Geometry of upper bodies in a multi-body system distinctly impacts the response of lower bodies. As such, the dynamic response may not be solved in a cascade analysis fashion. Rather, the response of each block must be solved simultaneously.
- The response of a given freestanding structure as a single-body is oftentimes more stable than when the same structure is placed at the top of a multi-body system. However, many geometric configurations evidence an opposite trend. This is attributed to the complex interactions and dynamics between two moving bodies. As such, the motion of each discrete body in the multi-body system must be solved as a discontinuum, rather than an equivalent continuum system.
- Three-dimensional responses for symmetric bodies were observed, similar to the results of single-body tests, but to a much more significant degree. As such, the numerical model must allow for the fully three-dimensional response of the individual bodies.
- Multi-modal behavior was observed for both bodies of the dual-body system, to an even greater degree than observed for the single bodies. This is attributed both to the propagation of small interface changes and geometry, as well as to the response of the upper bodies on an inclined plane due to rocking of the bottom block. As such, the numerical model must allow for rotation, translation, and separation at all times and in all directions throughout the simulation.

5.8 Acknowledgements

The experimental investigation presented was supported by the National Science Foundation under IGERT Award #DGE-0966375, "Training, Research and Education in Engineering for Cultural Heritage Diagnostics," and award #CNS-1338192, "MRI: Development of Advanced Visualization Instrumentation for the Collaborative Exploration of Big Data." Additional support was provided by the UC San Diego Academic Senate, the Qualcomm Institute at UC San Diego, the Friends of CISA3, and the World Cultural Heritage Society. The sliding plate system was donated by EQX Global with installation assistance from Mr. Don Clyde. The assistance and support of the Charles Lee Powell Laboratory staff is greatly appreciated, particularly Mr. Darren McKay. Additional laboratory assistance was provided by Ms. Sara Grossi of the University of Bologna. The continuous support of this project and guidance of Professor Falko Kuester is greatly valued. The opinions, findings, and conclusions expressed in this chapter are those of the authors and do not necessarily reflect those of the sponsoring organizations.

This chapter, in part, has been submitted for publication to the journal *Earthquake Engineering and Structural Dynamics*. Wittich, C.E. and Hutchinson, T.C. (201X). "Shake table tests of unattached, asymmetric dual-body systems." *Earthquake Eng. Struct. Dyn.* The dissertation author is the primary investigator and first author of this publication. Sections 5.2, 5.4, and 5.5.5 are based upon a technical report as it appears in the Structural Systems Research Report Series. Wittich, C.E. and Hutchinson, T.C. (2015). *Shake Table Tests of Stiff, Unattached, Asymmetric Structures – Phase 2: Pedestal-Mounted*. Structural Systems Research Project Report Series, SSRP-2015/05, Department of Structural Engineering, University of California, San Diego, La Jolla, CA. The dissertation author was the primary investigator and first author of this publication.

Chapter 6 Numerical Model Development and Validation

Freestanding structural systems represent a variety of structures and components, including very unique and irreplaceable artifacts as well as equipment and contents critical for the functionality of a facility. However, freestanding systems are poorly understood in terms of their dynamic response. Housner (1963) first presented the classical two-dimensional rocking block model to understand the dynamics of this system. Since this pioneering study, a number of analytical studies have been presented in the literature that extend this model to account for multiple modes, multiple dimensions, multiple bodies, or flexibility of the body and foundation (e.g. Psycharis 1990, Shenton and Jones 1991, Konstantinidis and Makris 2007, Chatzis and Smith 2011). These studies have provided significant understanding of the effects of these variables on the general dynamics of the system, which is of great significance. However, given the infeasibility of a combined analytical model that accounts for all of these pragmatic variables, the development and validation of numerical models is warranted.

Numerical models for freestanding structural systems have been the focus of a number of studies presented in the literature in recent years (e.g. Papantonopoulos et al. 2002, Peña et al. 2008). These studies have largely utilized a discontinuum or micro-modeling approach, oftentimes an implementation of the discrete element method (DEM). This modeling approach simulates the dynamics of systems of rigid bodies or particles that interact with each other at their surfaces through spring and dashpot elements. These spring and dashpot elements are not explicitly modeled, rather the elements are generated only when contact is detected between two bodies and only at the location of the detected contact. While a handful of studies have demonstrated the promise of these modeling methods for freestanding structural systems, the numerical models are reliant upon the availability of experimental response data for calibration and validation. In the studies that have been presented, experimental data and the resultant numerical models have been

biased towards systems of very squat blocks, such as a classical multi-drum column. As a result, this dissertation aims to address three primary research objectives. The first is to identify a range of extreme geometries for freestanding geometries, as addressed and detailed in Chapter 3. The second is to generate a comprehensive database of experimental response data across the broad range of anticipated geometries, as addressed and detailed in Chapters 4 and 5. The third and final objective is to develop and validate a numerical model that can sufficiently reproduce the dynamic response of freestanding structures across a broad range of geometric configurations. This chapter attempts to address this final objective by detailing the development and validation of a numerical model for freestanding structures using the experimental data from a large range of geometry, as presented earlier in this dissertation.

The ultimate goal of this chapter and of this dissertation is the validation of a numerical model for the prediction of the seismic response of freestanding structures across a broad range of geometry. However, this chapter initially presents an extension of the classical analytical, two-dimensional rocking model to account for an arbitrary number of rocking points at the interface. This analytical study is critical to understand the unique effects of this variation on the dynamics of the system, as mild warping was present at the interfaces of the experimental specimens (refer to Section 4.2.2 of this dissertation). Therefore, the effects of this geometric variation must be clearly outlined prior to the development and validation of the numerical model. Following the analytical derivation and parametric study, the primary conclusions of the experimental campaigns are summarized with respect to their implications on numerical modeling. This is followed by a detailed discussion on the development and calibration of a multi-physics discontinuum numerical model; and, ultimately, the model is validated with respect to multi-modal behavior, multi-body interaction, and classical rocking dynamics.

6.1 Extension of Classical Model for Warped Interfaces

6.1.1 Introduction

The classical rocking model was first introduced in the pioneering work of Housner (1963), as detailed in Chapter 2. This rocking model considers a two-dimensional, symmetric, rectangular, rigid block that oscillates about two rocking points at its base atop a rigid foundation. The model further assumes that there is sufficient friction to prevent sliding and that the block transitions smoothly between rocking points through an inelastic impact with conservation of angular momentum. The response of this block is modeled as a set of piecewise equations of motion and an instantaneous reduction of angular velocity at the moment of impact.

In efforts to understand the dynamics of more realistic structures, a number of variations to the classical rocking model have been presented in terms of the number of modes, number of dimensions, flexibility of the block, and flexibility of the foundation. For example, Zulli et al (2012) derived the equations of motion of a three-dimensional, rigid block for dynamic base excitation. Related to flexibility of the block, Acikgoz and DeJong (2012) derived the equations of motion for a linear elastic oscillator able to uplift at its rigid base. Similarly, Vassiliou et al. (2015) extended previous models for flexible rocking structures to account for the distributed mass of the column and foundation. In these models, the authors derived expressions for the energy dissipation at impact for a rigid interface, similar to previous studies. On the contrary, Chatzis and Smyth (2011) extended the classical rocking model to account for flexibility at the interface. In this model, the authors incorporated a bed of distributed or concentrated springs at the interface, allowing for non-instantaneous energy dissipation.

In an effort to validate the classical rocking model and its variations, a number of experimental investigations have been presented. For example, Aslam et al. (1980) tested multiple concrete blocks in free and forced rocking behavior. The classical model was unable to accurately

predict the response of the block, however relatively good agreement was found between the experimental results and the model with an arbitrary value of the coefficient of restitution. Lipscombe and Pellegrino (1993) further tested the free rocking response of four steel blocks of varying aspect ratios. The authors similarly noted the inability of the classical model to accurately predict the experimental response. However, rather than an arbitrary variation of the coefficient of restitution, the authors suggest the use of a bouncing model, which allows complete separation of the block from the foundation, to enhance agreement. In more recent tests, ElGawady et al. (2011) observed a correlation of the coefficient of restitution with various materials at the interface of the rocking block and the foundation. The authors presented significantly improved agreement between the experimental results and the classical model utilizing modified values of the coefficient of restitution.

While previous studies have highlighted the importance of the value of the coefficient of restitution at impact (e.g. Aslam et al. 1980, Peña et al. 2007, ElGawady et al. 2011), few have analyzed the effect of geometric interface defects, which result in multiple rocking points and an increased number of impact events. Such studies have been limited with the exception of a recent experiment by Purvance et al. (2008), in which three boulders incorporating jagged bases were tested on a shake table to the point of overturning. The authors found that these boulders overturned at lower accelerations than geometrically similar counterparts with flatter interfaces. However, a detailed study of the effects of geometric interface defects and multiple rocking points on blocks of various geometry has not been presented in the literature. In this chapter, the equations of motion for a two-dimensional rocking block with interface defects are derived in a Newtonian formulation. Furthermore, the coefficient of restitution assuming classical impact theory is presented; and, the effect of this modified energy dissipation is studied parametrically and compared with recent experimental results. A final comparison of block stability is presented for geometrically similar blocks with and without geometric interface defects in the form of overturning spectra.

6.1.2 System Description

The presented system consists of a two-dimensional, rigid body resting on a rigid foundation with sufficiently high friction to preclude the mode of sliding, similar to the classical rigid body rocking problem. An arbitrary shape further characterizes the system, as presented in Figure 6.1, with account for the ensuing mass eccentricities. The block with a perfectly level base is shown schematically in Figure 6.1a, while a single geometric defect is present at the base of the block in Figure 6.1b. In this case, the geometric defect results in three potential rocking points, rather than the typical assumption of two. Additional geometric defects, including jagged edges, yield further rocking points, as presented in Figure 6.1c. Each of the blocks is described by its mass, m ; mass moment of inertia about its center of mass, I_{cm} ; total width, B , which is measured between extreme rocking points; and total height, H . Each rocking point, RP , is described by a rocking radius, R ; width, b ; height to the center of mass, h ; and, a slenderness, or critical angle, α , which is measured from the rocking radius to the vertical line extended from the center of mass for the at-rest block. It should be noted that herein the slenderness angle is a signed quantity, which differentiates rocking points on either side of the center of mass. This is in contrast to much of the literature on rigid body rocking; however, the presented equations of motion are markedly simplified with this minor change in notation. Furthermore, the notation for the slenderness angle in this chapter deviates from prior chapters of this dissertation, from θ_c to α , where the literature is largely split in the adoption of this alternate variable. This notation change is similarly incorporated for a simplified presentation of the equations, which otherwise would incorporate multiple subscripts and could potentially lead to misinformation. In addition, it is reiterated that the presented geometric properties are specific to an individual rocking point, where rocking point 1, RP_1 , is the left-most rocking point increasing sequentially through rocking point n , RP_n .

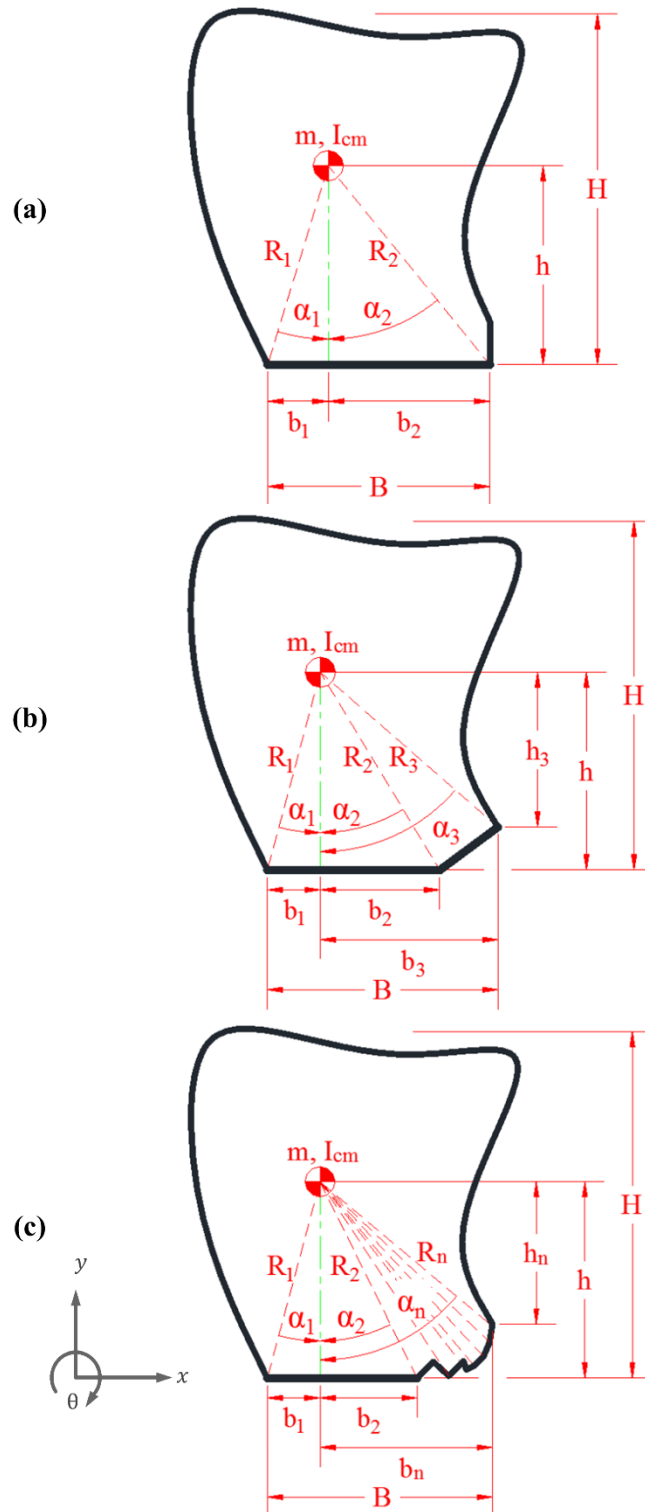


Figure 6.1 Schematics of an arbitrary rigid block overlaid with relevant geometric and mass parameters for (a) level interface and two rocking points, (b) singular interface defect and three rocking points, and (c) highly jagged interface and multiple rocking points.

6.1.3 Equations of Motion

The system of interest consists of a two-dimensional, rigid block of arbitrary shape with any number of potential rocking points at its base. The following derivation presents the equation of motion for a rocking mode of the considered block with three rocking points. However, it should be noted that this derivation and resultant equation of motion is valid for any number of rocking points, including the typical assumption of two rocking points. The rigid block, subject to horizontal ground acceleration, \ddot{x}_g , will uplift and rotate about a rocking point when the overturning moment due to the ground acceleration exceeds the restoring moment due to gravity about the rocking point of interest. A schematic of the uplifted block is provided in Figure 6.2. The ground acceleration which will cause the block to uplift and enter a rocking mode can be represented as:

$$\ddot{x}_g > -g \tan(\alpha_1) \quad (6.1)$$

$$\ddot{x}_g < -g \tan(\alpha_2) \quad (6.2)$$

where g is the acceleration due to gravity, and α_1 and α_2 are the signed slendernesses corresponding to the rocking points, RP_1 and RP_2 , which are positioned positively and negatively with respect to the block's center of mass, respectively, for the coordinate system shown in Figure 6.1 and Figure 6.2. The initiation of rocking motion can be generalized for negative rotation and positive rotation, respectively, as:

$$-\frac{\ddot{x}_g}{g \tan(\alpha_i)} > 1 \quad (6.3)$$

where i corresponds to the rocking point about which rotation is initiated. Note that this expression is only valid for rocking points which are in contact with the foundation prior to the initiation of rocking.

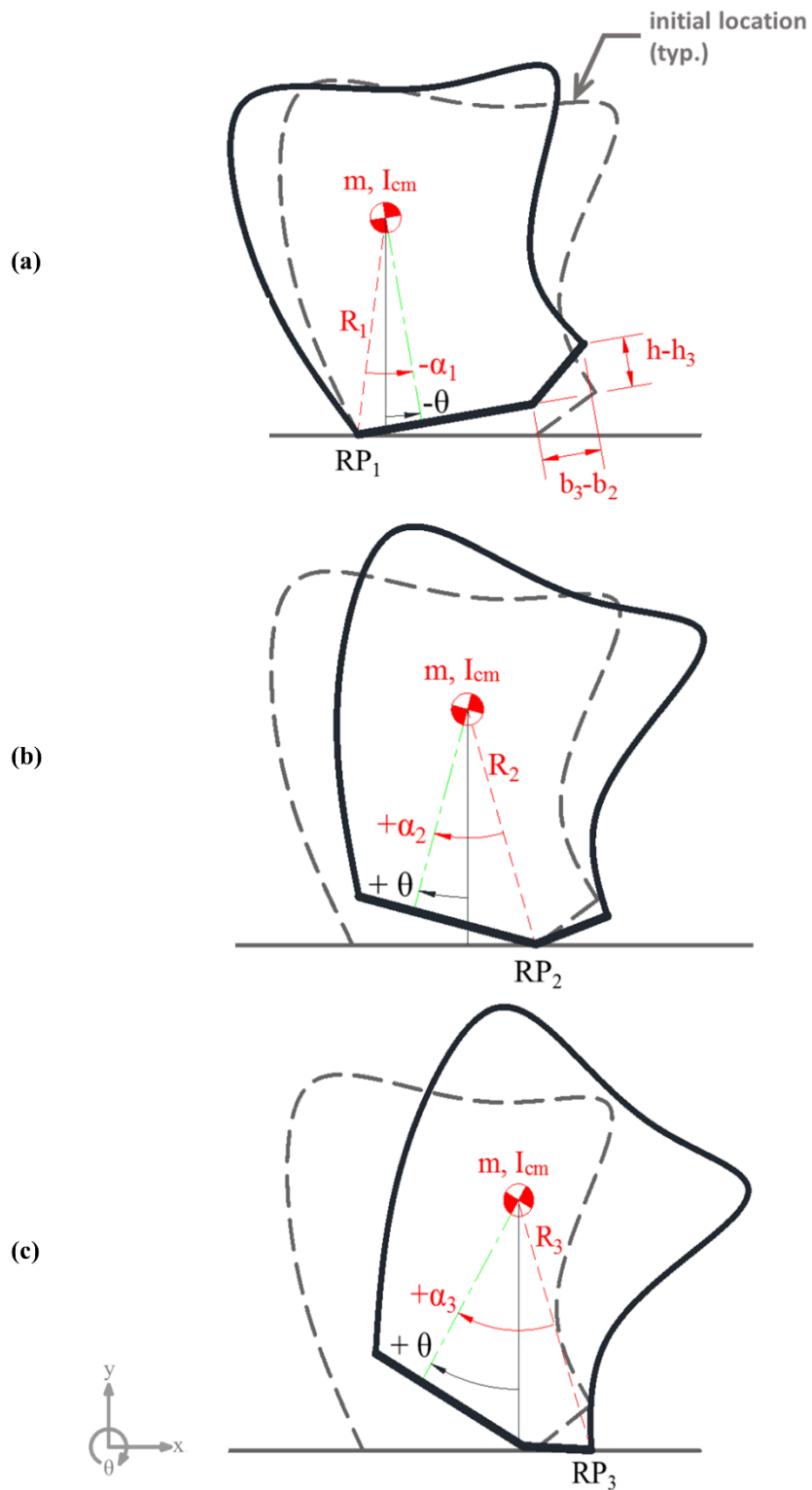


Figure 6.2 Uplifted rigid block subjected to horizontal acceleration at the base.

Once the rigid block has uplifted about a rocking point, the equation of motion is derived by summing the overturning and restoring moments about the specified rocking point and equating this to the inertial term. Referring to Figure 6.2, the equation for each rocking point, RP_1 , RP_2 , and RP_3 , respectively, becomes:

$$(I + mR_1^2)\ddot{\theta} = mgR_1 \sin(\alpha_1 - \theta) - m\ddot{x}_g R_1 \cos(\alpha_1 - \theta), \theta \leq 0 \quad (6.4)$$

$$(I + mR_2^2)\ddot{\theta} = -mgR_2 \sin(\alpha_2 - \theta) - m\ddot{x}_g R_2 \cos(\alpha_2 - \theta), 0 < \theta \leq \text{atan}\left(\frac{h - h_3}{b_3 - b_2}\right) \quad (6.5)$$

$$(I + mR_3^2)\ddot{\theta} = -mgR_3 \sin(\alpha_3 - \theta) - m\ddot{x}_g R_3 \cos(\alpha_3 - \theta), \theta > \text{atan}\left(\frac{h - h_3}{b_3 - b_2}\right) \quad (6.6)$$

where each equation is valid only for the given range of angles, which reflects the rotation necessary for uplift on the given rocking point with respect to the initial vertical. Equations (6.4) – (6.6) can be expressed as a singular equation, which represents the rocking about any arbitrary rocking point:

$$(I + mR_i^2)\ddot{\theta} = -mgR_i \sin(\alpha_i - \theta) - m\ddot{x}_g R_i \cos(\alpha_i - \theta) \quad (6.7)$$

where i corresponds to the i -th rocking point. Recall that α is a signed quantity in this equation. Further substitutions in terms of the rocking radii and slendernesses are incorporated resulting in the following limits for rocking points characterized by slenderness angles greater and less than zero, respectively:

$$\theta_{i-1} \leq \theta < \theta_i = \operatorname{atan} \left(\frac{R_{i-1} \cos(\alpha_{i-1}) - R_i \cos(\alpha_i)}{R_i \sin(\alpha_i) - R_{i-1} \sin(\alpha_{i-1})} \right), \quad (6.8)$$

for rocking points with $\alpha_i > 0$

$$\theta_{i-1} \leq \theta < \theta_i = \operatorname{atan} \left(\frac{R_{i+1} \cos(\alpha_{i+1}) - R_i \cos(\alpha_i)}{R_i \sin(\alpha_i) - R_{i+1} \sin(\alpha_{i+1})} \right), \quad (6.9)$$

for rocking points with $\alpha_i < 0$

$$\theta_0 = -\frac{\pi}{2} \text{ and } \theta_{n+1} = \frac{\pi}{2} \quad (6.10)$$

where θ_i is the upper bound angle for rotation will occur about RP_i , and i corresponds to the i -th rocking point from $i = 1$ to $i = n$. Note that the angle θ_k corresponds to the angle of the segment with the horizontal. In addition, the rotation is bounded on one-side only for the extreme rocking points.

The general equation of motion, Equation (6.7), is equivalent to that of a two-dimensional, rectangular, rigid block with two rocking points, accounting for the signed slendernesses. The primary difference when multiple rocking points are present can be observed from the schematics of Figure 6.1 and Figure 6.2. The initiation into a rocking mode is now a function of a much more slender block, indicating that rigid body motion would initiate at much lower acceleration amplitudes than a similar block with two rocking points. However, this initial rocking mode is very low-amplitude for mild geometric defects.

6.1.4 Impact and Energy Dissipation

Following the initiation of uplift on a given rocking point, the block will either overturn if the point is an extreme rocking point, or it will impact the foundation at an adjacent rocking point. For slender aspect ratios ($H/B > 2$), it is typically assumed that this impact will be smooth, without bouncing, and result in the instantaneous pivoting about an alternate rocking point. Due to the assumption that both the block and foundation are rigid, energy loss can be assumed only at this instant of impact. This relates to the classical concept of the coefficient of restitution, which is a measure of the kinetic energy remaining after an impact. Specifically, the coefficient of restitution, e , is defined as the ratio of the angular velocity of the block just after impact to that just prior to impact. This velocity ratio can be derived by the conservation of angular momentum of the rigid block about the new pivot point, due to the assumption of the smooth transition to rocking about the alternate rocking point.

Similar to the previous section, the derivation is first presented for the block with a single geometric defect (Figure 6.1b). Then, a general equation is presented, which can be applied to a block with an arbitrary number of rocking points. Referring to the schematic of Figure 6.2, there are four unique instances of impact: 1) impact at RP_1 with previous rotation about RP_2 ; 2) impact at RP_2 with previous rotation about RP_1 ; 3) impact at RP_3 with previous rotation about RP_2 ; and, 4) impact at RP_2 with previous rotation about RP_3 . For each impact scenario, respectively, conservation of angular momentum yields:

$$(I_{cm} + mR_1^2) \dot{\theta}^+ = I_{cm} \dot{\theta}^- + (mR_2 \dot{\theta}^-) \cdot (R_1 \cos(\alpha_1 - \alpha_2)) \quad (6.11)$$

$$(I_{cm} + mR_2^2) \dot{\theta}^+ = I_{cm} \dot{\theta}^- + (mR_1 \dot{\theta}^-) \cdot (R_2 \cos(\alpha_1 - \alpha_2)) \quad (6.12)$$

$$(I_{cm} + mR_3^2) \dot{\theta}^+ = I_{cm} \dot{\theta}^- + (mR_2 \dot{\theta}^-) \cdot (R_3 \cos(\alpha_2 - \alpha_3)) \quad (6.13)$$

$$(I_{cm} + mR_2^2) \dot{\theta}^+ = I_{cm} \dot{\theta}^- + (mR_3 \dot{\theta}^-) \cdot (R_2 \cos(\alpha_2 - \alpha_3)) \quad (6.14)$$

where $\dot{\theta}^+$ and $\dot{\theta}^-$ are the angular velocities of the rigid block immediately following and just prior to impact, respectively. The ratio of velocities, r , is then extracted from each equation and can be generalized as:

$$r_{i/j} = \frac{\dot{\theta}_+}{\dot{\theta}_-} = \frac{I + mR_i R_j \cos(\alpha_j - \alpha_i)}{I + mR_i^2} \quad (6.15)$$

where $r_{i/j}$ is the ratio of post- to pre-impact velocities for impact at RP_i with previous rotation about RP_j . It is worth noting that the ratio in Equation (6.15), which is valid for any arbitrary number of rocking points and arbitrary shape, is equivalent to the commonly used expressions in rigid body rocking analyses, as first derived by Housner (1963). In the classical model, the block is assumed to be symmetric and rectangular resulting in $I_{cm} = 1/3mR^2$, $R_i = R_j$, $\alpha_i = -\alpha_j$, which results in the classical expression, termed $r_{classical}$:

$$r_{classical} = 1 - \frac{3}{2} \sin^2 \alpha \quad (6.16)$$

The commonly used expression of Equation (6.16), often referred to as the coefficient of restitution, approaches a value of 1 for extremely slender blocks (i.e., $\alpha \rightarrow 0$). Correspondingly, squatter blocks exhibit more significant velocity reductions at impact than more slender blocks. Classical dynamics indicates that coefficients less than 1 indicate an inelastic impact, with a value of 0 for a perfectly plastic impact. While this classical coefficient of restitution is primarily a

function of the materials properties of the colliding bodies, the derived expressions in Equations (6.15) and (6.16) are solely functions of geometry. As such, these expressions represent a maximum value of the post-impact velocity associated with the specific geometry due to energy radiating into the rigid foundation. Other mechanisms of energy loss would serve to reduce the presented coefficient. These mechanisms may include vibrations of a non-rigid block, elasticity of the interface material, or crushing at the interface.

In contrast to the commonly used expression in Equation (6.16), the expression in Equation 6.15 for the block with multiple rocking points may yield ratios very close to a value of 1. In fact, the ratio can even exceed 1.0 for certain impacts in which the angle between the pre- and post-impact rocking radii is small and the post-impact rocking radius is smaller than the pre-impact rocking radius. Referring to Equation (6.15), this is represented by $R_i < R_j$ and the cosine term approaching a value of 1. This situation can be compared to the classical dynamics problem of the figure skater, in which the angular velocity of the skater is smaller with arms outstretched and increases when the arms are brought inward (radius reduces). This potential for a finite increase in angular velocity at impact reflects the geometry of a single rocking point, and is not necessarily indicative of a net angular velocity increase over the duration of the switch from one extreme rocking point to the other. However, the net change in angular velocity is still likely to be less than that associated with a geometrically similar block with a perfectly flat interface.

The low energy loss of the block with multiple rocking points can be further understood in the context of the weight vector at impact. Referring to the rectangular, symmetric block, the weight of the block always produces a “restoring” moment about the impacted corner. However, the weight of the block can produce an overturning moment about an interior impact point, depending on the direction of the angular velocity (e.g. impact at RP_2 with previous rotation about RP_3). Due to the possibility for values greater than 1 combined with the use of angular velocities rather than linear

velocities, the expression in Equation (6.15) will not be referred to as a coefficient of restitution as is typically done in the literature. Rather, this ratio will be referred to as a velocity adjustment factor, r . Furthermore, the possibility of $r \geq 1$ implies that the rocking response of a block may be increased by the presence of multiple rocking points, compared to that of the classical model with two rocking points. This may appear counter-intuitive as energy loss and the decay of rocking response are often associated with the number of impacts. However, these additional impact events are associated with rocking points of effectively more slender geometry and are characterized by increased values of the velocity adjustment factor. This concept can potentially explain the increase in overturning, observed by Purvance et al. (2008), for the three boulders with multiple jagged rocking points. The variation of this velocity adjustment factor and its effect on the rocking response is explored parametrically in a subsequent section.

6.1.5 Experimental Comparison

Free rocking tests of stiff, freestanding structures were conducted as part of the experimental campaigns detailed in Chapters 4 and 5 of this dissertation. The experimental results of this are compared to the responses predicted by the classical model as well as the extended model accounting for an interface defect. As noted in the description of the experimental specimens in previous chapters, the marble base was characterized by a mild warp due to fabrication of the tower specimen in which the slab was wet-bonded with the concrete. As a result, the tower specimen exhibited a “wobble” mode during low-amplitude shaking. A general overview of the specimen is included in Figure 6.3, as well as detail images of the warped interface highlighting the regions that were in contact at two different times during a dynamic response. It should be noted that no appreciable sliding was observed during these free rocking tests; although it was not restricted from translation.

The freestanding tower was initiated into a free rocking response by a sinusoidal acceleration pulse of the shake table. However, the presented free rocking time histories do not include the initial forced response. Figure 6.4a presents the angular displacement of the experimental specimen undergoing a free rocking motion. In the presented time history, the tower was characterized as a fairly squat, symmetric body (i.e. L11, see Table 4.1) with: $\alpha = 0.46$, $R = 0.84$ m, $I_{cm} = 480$ kg-m², and $m = 817$ kg. The numerically integrated response of the classical model characterized by these geometric and mass parameters is overlaid with the experimentally measured angular displacement in Figure 6.4a. The time history was solved in a state space formulation with a 4th-5th order Runge-Kutta numerical scheme in MATLAB (2012). The numerical prediction drastically underestimates the rocking response. In particular, the classical model predicts the peak angular displacement after the first impact to be only approximately 80% of the measured response. In addition, the experimental specimen exhibited a rocking motion for approximately 5 s, whereas the classical model predicts the motion ceases in less than 2.5 s. Thus, the classical model overestimates the rate of decay of the rocking motion.

In an effort to better predict the response of the squat tower specimen, the equations of motion for a rigid body with multiple rocking points were numerically integrated (Equations (6.7) and (6.15)). The geometry of the interface modeled is included in the schematic at right in Figure 6.4. The geometry of the interface modeled is included in the schematic at right in Figure 4. The interface was modeled with three rocking points, where the intermediary rocking point is located at approximately one-third of the total width, with a defect height of approximately 1 mm. The resultant time history is overlaid in Figure 6.4a with the response of the experimental specimen and the prediction of the classical model. This alternate model results in significantly better agreement with the experimental results. While minor deviations are noticed, this is attributed to the inability to accurately measure the defect as well as variations of the defect with depth (non-symmetric warp). The enhanced agreement of the model with defect can be better understood in terms of the

angular velocity, which is compared with that of the classical model in Figure 6.4b. For the geometry of the experimental specimen, the velocity adjustment factor of the classical model is approximately 0.7. This is in stark contrast to the factors associated with the proposed alternate model, which are 0.85, 1.02, 0.95, and 0.95. The increased velocity reduction of the classical model at the first impact is highlighted in the inset of Figure 6.4b. Furthermore, the response of the model with defect not only includes lower energy dissipation at impact, but also includes a finite increase in angular velocity in the negative angular velocity direction (see inset of Figure 6.4b).

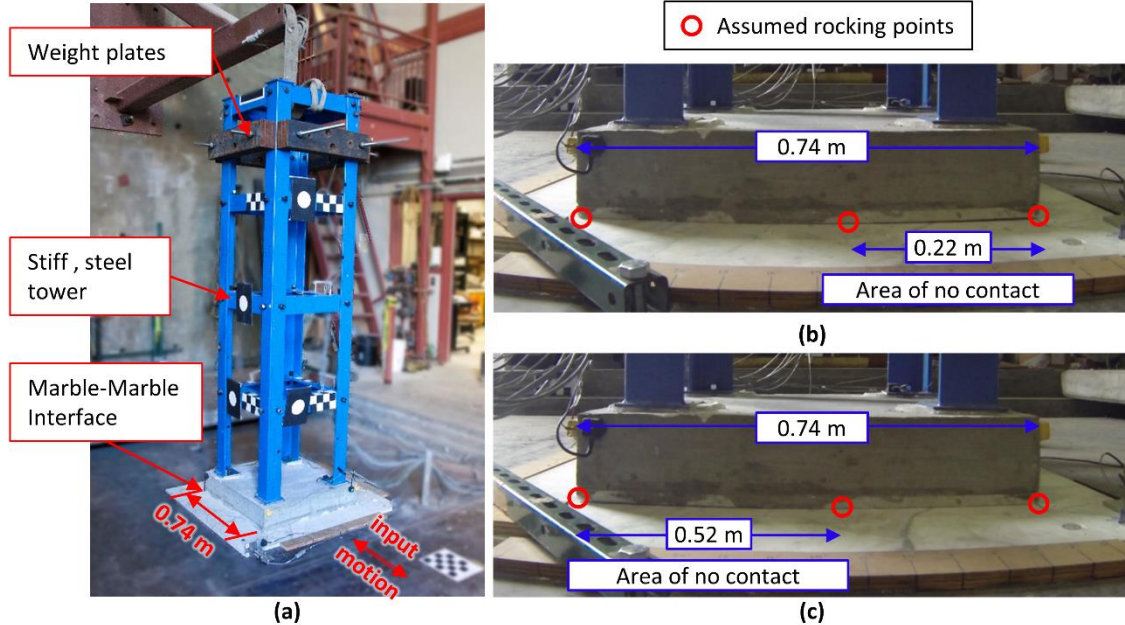


Figure 6.3 Setup for free rocking tests of L11 configuration (see Chapter 4) with (b - c) highlights of the areas of no contact which allow a wobble mode to occur.

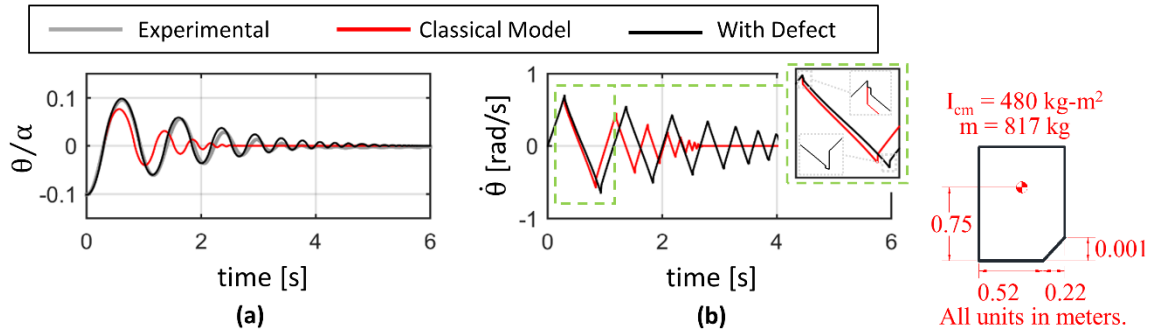


Figure 6.4 Experimental free rocking in (a) rotation and (b) rotational velocity, overlaid with the results of the classical model and the extended model with three rocking points (shown at right).

6.1.6 Parametric Study: Effect of Defect Size

This section presents a parametric study of the equations of motion and the velocity adjustment factor, as previously defined. The velocity adjustment factor is studied in the context of the size of the defect and the aspect ratio of the block in this section, and with respect to the number of rocking points defining the defect in the following section. Time histories of the angular displacement and rotation of representative blocks are also presented. In this and the following sections, the time histories are solved in a state space formulation with a 4th-5th order Runge-Kutta numerical integration scheme in MATLAB (2012). At each detected impact according to the limits set forth in Equations (6.8) – (6.10), the angular velocity is adjusted by the factor defined by Equation (6.15) prior to continuation of the numerical integration scheme.

To evaluate the effect of the defect size on the response of the block, a parametric study of the velocity adjustment factor is first presented followed by individual time history comparisons. This parametric study is limited to the symmetric, rectangular block with three rocking points to emphasize the effect of individual parameters. The size of the defect is defined by h_{defect} and b_{defect} , each of which is given as a fraction of the height to the center of mass or total width of the block. In this way, the effect of the defect size can be evaluated for varying levels of the block aspect ratio.

It should be noted that studies of the velocity adjustment factor are presented for a constant size of the block, with respect to the rocking radius. The contribution of the rocking radius effectively cancels out of the definition for the velocity adjustment factor, as seen in Equation (6.15).

Figure 6.5 presents the velocity adjustment factor for each unique impact of the three rocking points of the block as a function of the block's aspect ratio. The value associated with the classical model, assuming two rocking points at the block's extreme edges, is also plotted for comparison. In this figure, the height of the defect is defined as either $0.0025h$ or $0.05h$, and the width of the defect is defined as either $0.25B$ or $0.45B$, as shown in the schematic. From this figure, it is foremost observed that the velocity adjustment factor from the classical model is markedly lower than that of the block with three rocking points. This is most noticeable for the lower aspect ratios (e.g. $H/B < 6$), where the lowest value of the velocity adjustment factor for the block with defect is 25% greater than that of the classical model. However, for very tall blocks (e.g. $H/B > 8$) the velocity adjustment factors of each of the rocking points, including those of the classical model, largely approach a value of 1. The increase in this factor for the more squat blocks relates to the increased slenderness (reduced α) of the block with the defect, where the equivalent block at impact is much more slender and therefore dissipates less energy at impact.

Referring to Figure 6.5, the velocity adjustment factor for individual rocking points shows significant variation for a given block aspect ratio, as well as variation for an individual rocking point as the aspect ratio increases. For the squatter blocks (e.g. $H/B = 2$), the factor associated with the interior rocking point with prior rocking about the highest point ($r_{2/3}$) is the largest factor for the block, with values greater than 1 for certain sizes of the defect. However, the largest factor for more slender blocks (e.g. $H/B = 8$) is the extreme point associated with the defect with prior rocking about the interior point ($r_{3/2}$). This relates to the geometry of the block and the interface, specifically the variation of the rocking radius at impact. For more slender blocks, the rocking radius associated

with the extreme rocking point is smaller than that associated with the interior rocking point. However, the interior rocking radius is smaller than that of the extreme rocking point for squatter blocks. This is true for the plots presented in Figure 6.5 because the size of the block is constant for the variation with respect to aspect ratio. Therefore, the slender blocks are more sensitive to differences in the height of the rocking point, which is a more significant contributor to the calculation of the rocking radius. Similarly, the squatter blocks are more sensitive to differences in the horizontal location of the rocking point. Due to this varying sensitivity, the largest velocity adjustment factor varies with aspect ratio according to the rocking point with the smallest value of the rocking radius.

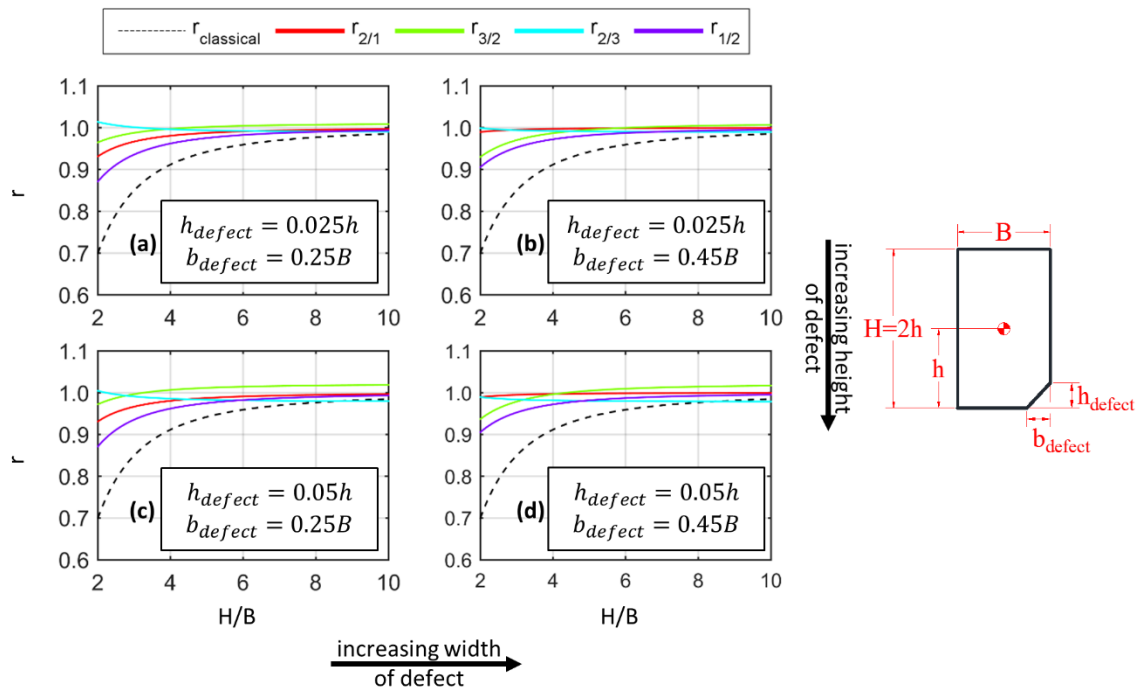


Figure 6.5 Velocity adjustment factor, r , for each rocking point as a function of aspect ratio for a symmetric, rectangular block with three rocking points, as shown at right, where the height and width of the defect, are: (a) $0.025h$, $0.25B$, (b) $0.025h$, $0.45B$, (c) $0.05h$, $0.25B$, (d) $0.05h$, $0.45B$.

The identification of the rocking point with the smallest rocking radius can be used to further explain the variation of the velocity adjustment factor for varying width and height of the defects. As the rocking radii of slender blocks are more sensitive to variations in the height of the defect, it follows that the velocity adjustment factor would show greater variation for defects of increasing height with constant defect width. This is verified in the plots of Figure 6.5, specifically the value of $r_{3/2}$ for a block with an aspect ratio of 10 is 1.006 and 1.017 for defect heights that are 0.025 and 0.050 of the height to the center of mass, for a constant defect width of $0.45B$. This increase in the height of the defect results in a reduced rocking radius at RP_3 , and therefore an increase in the velocity adjustment factor. This is in comparison to the effect of the width of the defect, which is much less noticeable. For example, the same block with aspect ratio of 10 has $r_{3/2}$ values of 1.019 and 1.017 for defect widths of $0.25B$ and $0.45B$ of the block's total width. However, the impact of the defect width is much more noticeable for squatter blocks (e.g. $H/B = 2$) due to the larger contribution of the block's width to the aspect ratio.

The presence of imperfections at the interface of a symmetric, rocking block is shown to cause variations in the velocity adjustment factor for each unique impact scenario. Whereas Figure 6.5 presented these individual variations, Figure 6.6 presents an effective factor, which represents the combined effect of multiple impacts for comparison with an idealized block of two rocking points. In this context, the effective factor can be calculated as the product of the velocity adjustment factors at all impacts that occur while the block is transitioning between the extreme rocking points, which is calculated as follows:

$$r_{n/1} = \prod_{k=1}^{n-1} r_{(k+1)/k} \quad (6.17)$$

$$r_{1/n} = \prod_{k=2}^n r_{(k-1)/k} \quad (6.18)$$

for positive and negative angular velocities, respectively. Considering the symmetric, rectangular block with a single interface defect and three rocking points, the effective velocity adjustment factors are presented as a function of block aspect ratio for various defect sizes and for both positive and negative angular velocities in Figure 6.6. From these comparisons, it can be seen that the effective velocity adjustment factor is smaller than that of the classical model for slender blocks, while it is larger than that of the classical model for squatter blocks. Recall from Figure 6.5 that the individual velocity adjustment factors for each rocking point were consistently larger than that of the classical model regardless of aspect ratio. However, the effective velocity adjustment factor for a slender block is smaller than that of the classical block due to the compounding of multiple impacts that have velocity adjustment factors close to 1. While this compounding effect is still present in the effective factors of the squatter blocks, the effect is much less significant due to the drastic difference of the individual factors of the rocking points with the classical factors. It can be seen from these plots that the threshold for which the effective velocity adjustment factor is less than that of the classical model occurs at an aspect ratio approximately $4 < H/B < 5$, which varies according to the defect size. However, it should be further noted that this observation is only valid for negative angular velocity of the described block, whereas the effective velocity adjustment factor is always greater than that of the classical model for positive angular velocity, given that the defect is located in the positive direction.

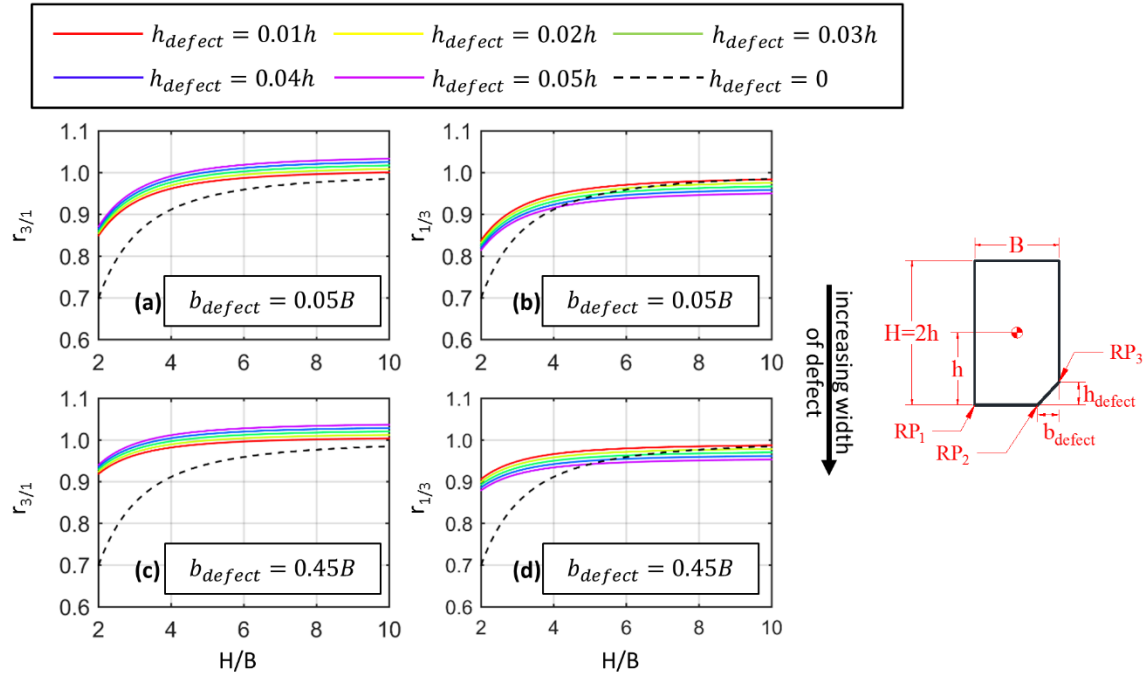


Figure 6.6 Effective velocity adjustment factor for (a, c) impact at the defect (positive angular velocity) and (b, d) impact away from the defect (negative angular velocity) for the block at right with varying height and width of the defect.

Due to the consistently higher values of the effective factor for squatter blocks, it is anticipated that these blocks may have an increased free rocking response characterized by low energy dissipation compared to the classical model with two rocking points. The effect on slender blocks is likely much less given the similar magnitude of the velocity adjustment factors for the block with three rocking points and the classical model. However, the magnitude of the energy dissipated at an impact is a function of the magnitude of the angular velocity; and, therefore, the impact of the variation of the velocity adjustment factor on the rocking response is explored through free rocking time histories in this section and through overturning spectra in the next section.

Figure 6.7 and Figure 6.8 present free rocking time histories of angular displacement and velocity for a symmetric, rectangular block with aspect ratios, H/B , of 2 and 6, respectively. The responses of the block with and without a single interface defect are presented, which is modeled

as a block of two or three rocking points, respectively. In these plots, the angular displacement is presented as a normalized quantity with respect to the slenderness of the block with two rocking points. For ease of comparison, the two blocks are of identical size with a rocking radius of 1 m. The interface defect is characterized by a width of $0.25B$ and a height that yields an angle equal to 0.3α , which enforces that the transition to the third rocking point will be easily identified and compared. In each of these plots, the block has an initial angular displacement of -0.45α about RP_1 , then impacts for rotation about RP_2 , and RP_3 , and ultimately reaches zero angular velocity and returns to rotation about RP_2 and RP_1 .

The initial observation for the blocks of both aspect ratios is the increase in magnitude of the peak angular displacement post-impact compared to that of the classical model. This behavior can be explained by an examination of the angular velocity time history. The blocks with and without the interface defect have an identical response until the first peak in angular velocity, which occurs at the first impact. Due to the very slender intermediate rocking point, less energy is dissipated at this impact, as seen in the detail views of Figure 6.7c and Figure 6.8c. In addition to the lower energy dissipated at this impact, the block is then rotating about a very slender rocking point which approaches an angle close to its slenderness. This is observed as the reduced slope of the angular velocity immediately after impact. Upon impact at RP_3 , the block is rotating about a rocking point with similar slenderness to RP_1 and is able to maintain its stability. However, this cycle of reduced energy dissipation and rotation about a very slender intermediary point compounds throughout the time history resulting in a much increased rotational response of the block with three rocking points compared to the block with two rocking points – regardless of aspect ratio. This further influences the general shape of the rocking time history which resembles that of a highly eccentric body, despite the interface defect being relatively small in comparison to the size of the symmetric body.

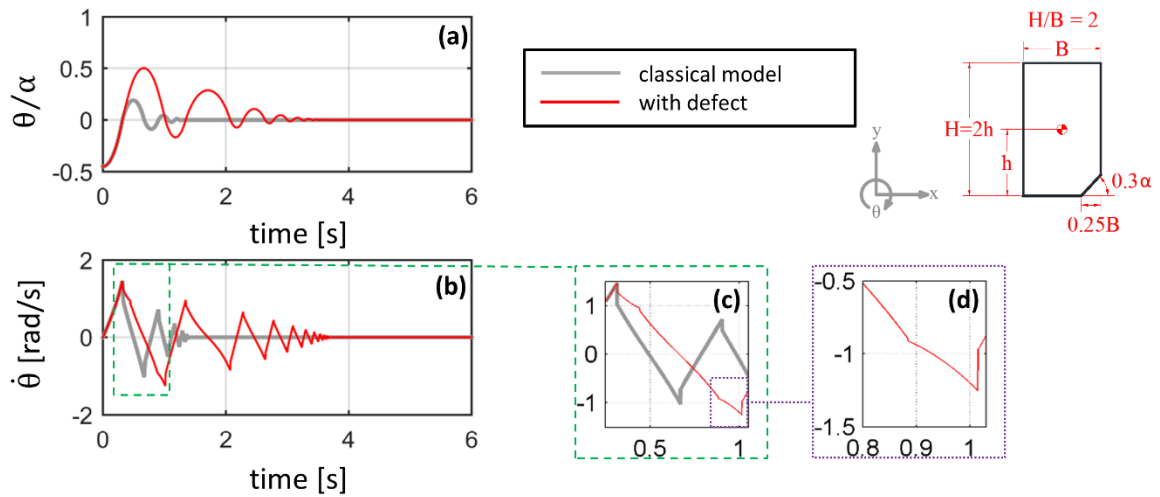


Figure 6.7 Time history of free rocking of symmetric, rectangular block with aspect ratio of 2 and $R_I = 1$ m with and without a single interface defect, shown at right: (a) angular displacement, (b) angular velocity, and (c, d) detail inset of first two reversal events.

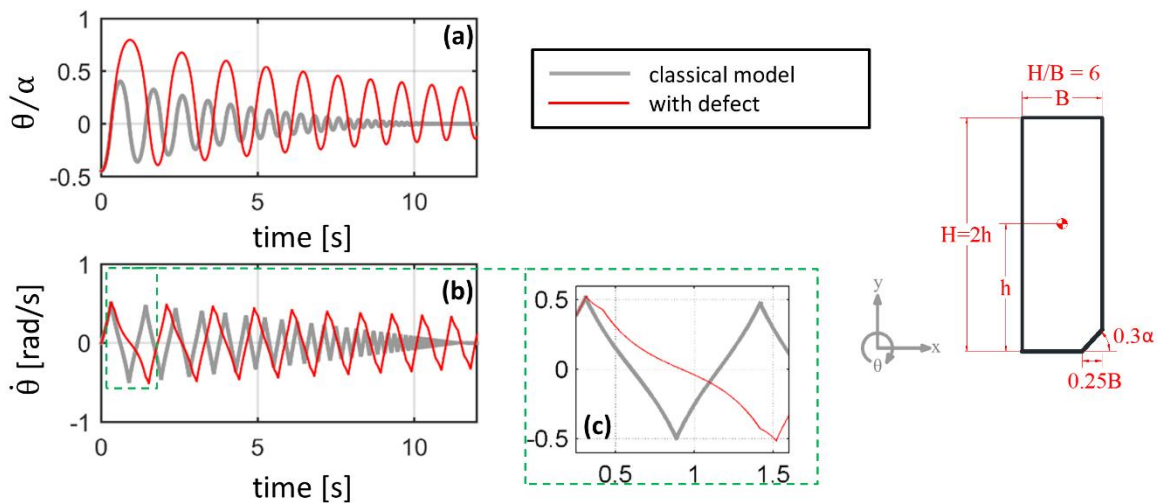


Figure 6.8 Time history of free rocking of symmetric, rectangular block with aspect ratio of 6 and $R_I = 1$ m with and without a single interface defect, shown at right: (a) angular displacement, (b) angular velocity, and (c) close-up of angular velocity for the first two reversals.

The time histories presented in Figure 6.7 and Figure 6.8 can be further compared for the relative effects of the interface defect on blocks of various aspect ratios. While the rotational response is amplified in both cases, the effect of the deformity on the squatter block (Figure 6.7) is more severe, as previously asserted in the discussion of the velocity adjustment factor. For example in the response of the squatter block, the peak angular displacement after the first impact is 0.50α . Whereas, the response of the block without the interface defect reaches a peak angular displacement of 0.19 – an amplification greater than 250% due to the defect. While still significant, the same comparison for the taller block in Figure 6.8 yields an amplification less than 200%. This variation can, in part, be explained by the previously studied velocity adjustment factor which is more sensitive to the presence and size of the defect for squatter blocks. This reduced energy dissipation can be clearly observed in the impacts of Figure 6.7c as well as the finite increase in angular velocity seen in Figure 6.7d. These significant effects are not seen in the impacts of Figure 6.8c, where the rocking response of the taller block with the defect is largely related to the change in slenderness rather than the change in the energy dissipated at impact.

6.1.7 Parametric Study: Effect of Number of Rocking Points

To evaluate the effect of the number of rocking points which define a geometric interface defect, a parametric study is presented similar to that focused on the size of the defect. In this section, the study is limited to the case of a symmetric, rectangular block of constant size and variable aspect ratio; however, the number of linear segments which define the surface defect is variable rather than the size of the defect. For ease of comparison, the location of RP_2 and RP_n are held constant, while the number of segments between these points is increased. A schematic of the defect is provided as an inset within Figure 6.9, where it is shown that a larger number of rocking points approaches a rounded corner.

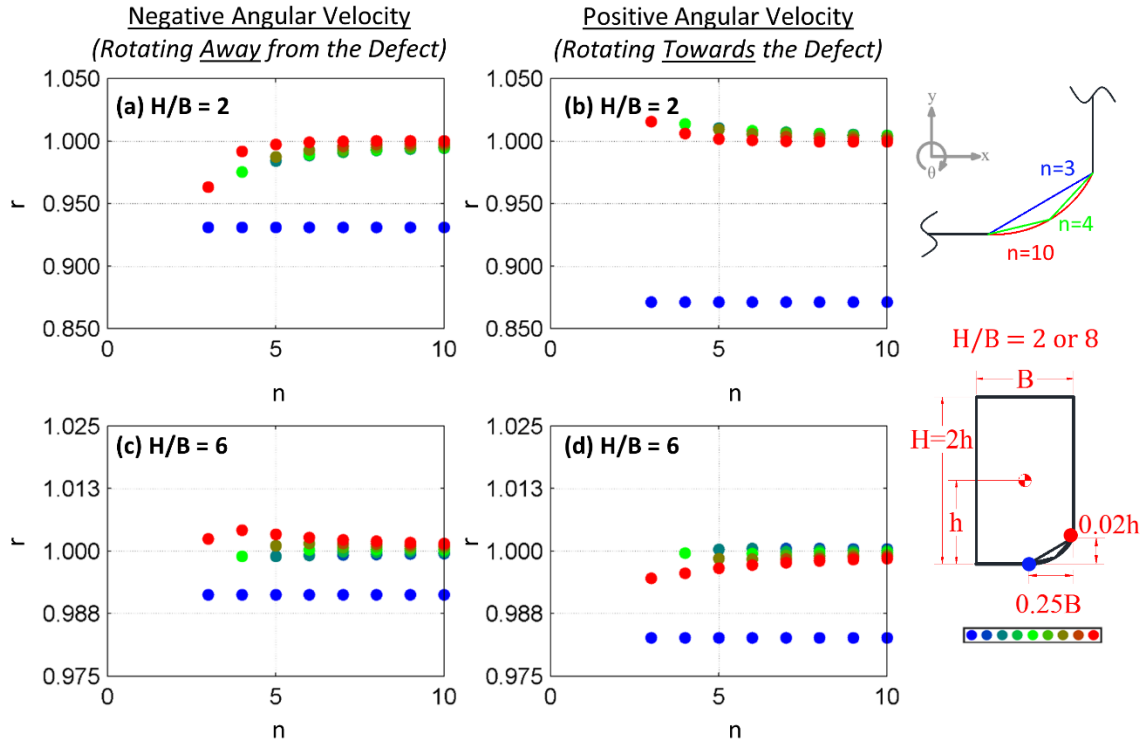


Figure 6.9 Velocity adjustment factor, r , as a function of the number of rocking points when the block is moving with (a, c) negative angular velocity and (b, d) positive angular velocity for aspect ratios of (a, b) 2 and (c, d) 8. Note that the color is mapped according to schematic at right.

Figure 6.9 presents the velocity adjustment factor, r , as a function of the number of rocking points along the defect. Individual plots are provided for negative and positive angular velocity as well as for blocks of squatter ($H/B = 2$) and taller ($H/B = 6$) aspect ratios. The velocity adjustment factor is differentiated for each rocking point by color, where blue indicates the factor at RP_2 , red indicates the factor at RP_n , and colors ranging from blue to red indicate the intermediate rocking points. A colormap is provided beneath the schematics in Figure 6.9 for reference. Similar to observations in the previous section, the velocity adjustment factor is largest in magnitude for the squatter block in the positive angular velocity direction, whereas the opposite is true for the taller block. This is related to the variation in the rocking radius, where R_2 is smallest for the squatter block and R_n is smallest for the taller block. However, regardless of the aspect ratio, the largest

velocity adjustment factors are associated with the block with only three rocking points. This is again related to the variation in the rocking radius, where the difference between adjacent rocking radii diminishes as the number of rocking points increases. This ultimately leads to the convergence of the velocity adjustment factor to a value of unity for all rocking points along the defect as the number of rocking points increases. This observation suggests that if a geometric interface defect is rounded (i.e. many segments), its energy dissipation will be that of an eccentric body where the rocking radius and slenderness of the eccentric side will correspond to RP_2 , where the defect initiates. However, this does not necessarily indicate that the rocking response will be identical to that of an eccentric body, which will be further explored through time history comparisons.

The effective velocity adjustment factor, as defined in Equations (6.17) and (6.18), is plotted as a function of the number of rocking points in Figure 6.10 for various aspect ratios and for positive and negative angular velocities. As anticipated, in all cases, the effective velocity adjustment factor is much greater than that of the block with only two rocking points (i.e. classical model), where this effect is further diminished for taller structures. Whereas, the largest variations of individual velocity adjustment factors are associated with the block of three rocking points, the effective factor is observed to gradually increase and converge as the number of rocking points increases. This reflects the convergence of the velocity adjustment factors to a value of unity at the rocking points along the defect. This indicates that the effect of the number of rocking points on the energy dissipation of a rocking block is quickly diminished for a number of rocking points greater than three. In these cases, the energy dissipated is again likened to that of an eccentric body characterized by the geometry at the initiation of the defect (RP_2). However, the time history of rocking response is still likely to vary due to the many changes in slenderness for the impacts along the impact, which is more like a rolling response rather than a true rocking response.

Figure 6.11 presents the time history response of the symmetric, rectangular block with an interface defect for a variable number of rocking points and for both squatter ($H/B = 2$) and taller ($H/B = 6$) blocks. These blocks are consistent in size and are identical to those presented in Figure 6.7 and Figure 6.8 for the cases of two and three rocking points. The most striking observation, for both aspect ratios, is the marked increase in the peak angular displacement after the first impact. While it was noted in the previous section that the presence of a defect results in larger rotations, it is further observed in the plots of Figure 6.11 that the peak angular displacement increases with the number of rocking points. Recall that the velocity adjustment factors converge to a value of 1 for defects with many rocking points, as seen in Figure 6.9. This indicates that the increased rocking response of the block, as seen in Figure 6.11, is largely due to the changes in rocking radius and slenderness at impact, rather than due to energy dissipation. For example, the block with $n = 3$ (three rocking points) rotates about the quite slender RP_2 for a longer duration and to a greater angular displacement than blocks with higher numbers of rocking points. While rotating about RP_2 , this block maintains a higher level of angular velocity allowing it to achieve the necessary rotation to impact at RP_3 , which is much squatter and allows the block to switch directions (angular velocity changes from positive to negative). However, the block with many rocking points (i.e. $n = 18$) approximates a rolling response, in which the angular displacement of the block increases faster than the slenderness, α , of the many rocking points.

The plots of Figure 6.11 provide further insight into the differences between the taller and squatter blocks with multiple rocking points. For the taller block, each increase in the number of rocking points resulted in an increase in the peak angular displacement after the first impact. However, the rocking response of the squatter block ($H/B = 2$) with six rocking points actually produces a rocking time history that is smaller in magnitude than that of the block with three rocking points. For this case of the block with six rocking points, the block is not yet approximated by a rolling response. Rather, as the rocking point progresses towards RP_n , the rocking radii is

increasing and, as such, reducing the magnitude of the angular displacement. In addition for the squatter blocks, the increased number of rocking points expedites the motion decay. Specifically, the squat block with eighteen rocking points has a lower peak angular displacement than the squat block with three rocking points in the second cycle, despite the peak angular displacement of the first cycle being orders of magnitude larger. The differences associated with these geometric subtleties are further explored in the following section on stability and overturning spectra.

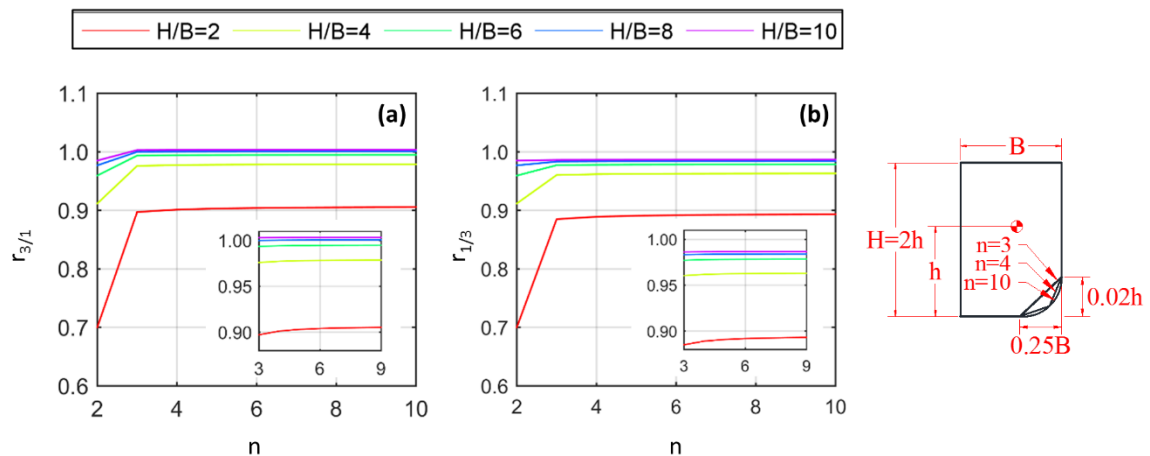


Figure 6.10 Effective velocity adjustment factor, r , as a function of the number of rocking points (see schematic at right) for (a) negative angular velocity, and (b) positive angular velocity with detail view inset.

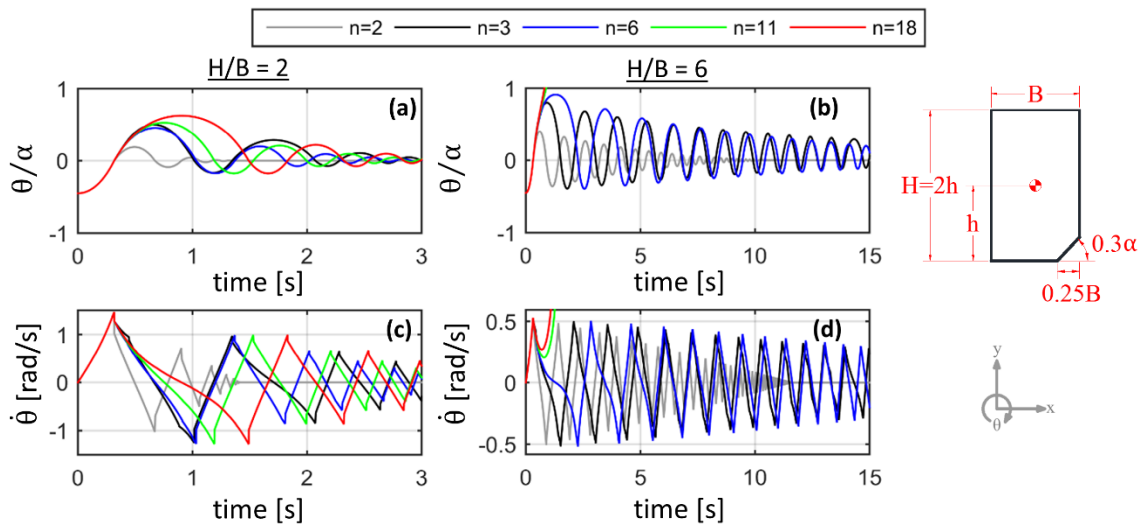


Figure 6.11 Time history of free rocking response of symmetric, rectangular block with an interface defect as shown at right with variable number of rocking points for (a, b) angular displacement and (c, d) angular velocity and aspect ratios (a, c) of 2 and (b, d) 6.

6.1.8 Effect of Interface Warps on Overturning Spectra

The response of a freestanding body to an arbitrary ground motion is nonlinear with respect to its orientation, and therefore a particular block which overturns in a given motion may not necessarily overturn in a motion of greater intensity. However, systematic trends can be observed in overturning spectra for simple pulse motions, as first presented by Zhang and Makris (2001). As the results of the parametric studies emphasize the significant differences between the classical and the presented multi-point model, overturning spectra are presented in an effort to generalize conclusions on the effects of interface defects on blocks of various aspect ratios. It is noted, however, that these spectra are not intended to be predictive of the response of a given block to an arbitrary motion, such as earthquake, but to provide qualitative insight into the effect of multiple rocking points.

The overturning spectra presented in this section consist of the normalized angular displacement of the block at discrete pairs of amplitude and frequency of a single sinusoidal pulse, which is used as the horizontal base acceleration and is given as:

$$\ddot{x}_g(t) = A_p \sin(\omega_p t), \text{ for } 0 \leq t < \frac{2\pi}{\omega_p} \quad (6.19)$$

$$\ddot{x}_g = 0, \text{ for } t \geq \frac{2\pi}{\omega_p} \quad (6.20)$$

where A_p is the amplitude of the sinusoidal pulse and ω_p is the pulse frequency. For ease of comparison, the amplitude and frequency are varied and presented in the spectra as normalized quantities. Specifically, the amplitude is normalized by the acceleration criteria for rocking

initiation, $\tan \alpha$, and the frequency is normalized by the size parameter of the block, which is defined as:

$$p_i = \sqrt{\frac{mgR_i}{I + mR_i^2}} \quad (6.21)$$

For the models with three rocking points, the slenderness and rocking radius values used in the normalization quantities are associated with RP_1 , which coincides with the values associated with the classical model. The equations of motion are numerically integrated for each normalized amplitude-frequency pair, and the angular displacement is plotted as an intensity value normalized by the corresponding slenderness of RP_1 .

Figure 6.12 plots the overturning spectra corresponding to a squat block with $H/B = 2$ as modeled with two rocking points (classical model) and with three rocking points. Two spectra are presented for the block with three rocking points corresponding to the direction of the sinusoidal pulse. The interface defect incorporated in this model is the same as that presented in the Figure 6.7 and Figure 6.8, in which the width of the defect is $0.25B$ and the height of the defect corresponds to an angle of 0.30α . The spectra associated with two rocking points in Figure 6.12a highlights the two well-known overturning regions for rocking blocks subject to a sinusoidal pulse (Zhang and Makris 2001). The dark blue region of this plot indicates overturning without impact, whereas the dark red region indicates overturning after a single impact event.

Figure 6.12b plots the overturning of the same block subject to the same input motions as Figure 6.12a, with the incorporation of a geometric defect and a third rocking point in the positive direction. As such, the dark blue overturning region, indicating overturning without impact, is identical to that of the classical model with two rocking points; however, the dark red overturning region is significantly increased. While the increased overturning region (dark red) emphasizes the

marked reduction in stability due to the presence of a geometric defect at the interface, it is noted that this dark red region extends below the minimum amplitude threshold of the dark blue region. This indicates that overturning is possible for blocks with an interface defect subject to base excitation that would not even induce uplift of the block with two distinct rocking points. This reduction in the amplitude threshold for overturning is similarly observed in Figure 6.12c, which differs from Figure 6.12b only in the direction of the sinusoidal input motion. Given the negative sinusoidal pulse, the initiation of rocking motion is in the direction of the geometric defect. As such, the dark red region represents overturning in the direction of the defect, prior to any rotation about the opposite rocking point. This region is much larger than the corresponding dark blue region in Figure 6.12b, as the initiation of rocking at the very slender intermediary point occurs at lower amplitudes. However, overturning in the direction opposite to initiation (dark blue in Figure 6.12c, dark red in Figure 6.12b) is much reduced. This corresponds to the increased velocity adjustment factor at rocking points in the direction of the defect, which in this case is the positive direction (see Figure 6.6). Whereas, the block with initial rotation in the direction of the defect (Figure 6.12c) dissipates more energy upon impact away from the defect, and subsequent rotation about a more squat rocking point.

Figure 6.13 plots the same overturning spectra as Figure 6.12, but for blocks of a taller aspect ratio ($H/B = 6$). As anticipated, the dark red region (overturning after an impact event) is increased for Figure 6.13b compared to Figure 6.13a, similar to the observation of Figure 6.12, with overturning possible below the amplitude threshold to initiate rocking for the classical model with two rocking points. Figure 6.13c presents the overturning of the same block as Figure 6.13b, but with the sinusoidal input in the opposite direction. Similar to Figure 6.12c, the dark blue region of overturning in the negative direction is quite small, which is again attributed to the more squat geometry and lower velocity adjustment factors in this direction. However, a third region of overturning emerges for these taller configurations with three rocking points. This second dark red

region is separate from the high-amplitude, low-frequency region, which is characterized by overturning in the direction of the defect with no impact or rotation about the opposite rocking point. Rather, this second region is characterized by initial rotation in the direction of the defect, impact and rotation about the opposite point, and then ultimately overturning in the direction of the defect. This can be attributed to the asymmetry of the block with an interface defect subject to higher frequency motions, which terminate before the first impact.

The final observation of the spectra regards the apparent increased stability of the block with a defect for certain high-amplitude, high-frequency input motions. This is most noticeable in Figure 6.13c compared to Figure 6.13a, where the overturning regions would be swapped in Figure 6.13a for a negative sinusoidal input. Due to the more slender geometry of the rocking points associated with an interface defect, this block achieves a higher initial rotation compared to the block without a defect subject to a sinusoidal pulse of the same amplitude and frequency. In doing so, the block avoids overturning due to the decelerating portion of the sinusoidal pulse, and then rotates about a more squat geometry following impact.

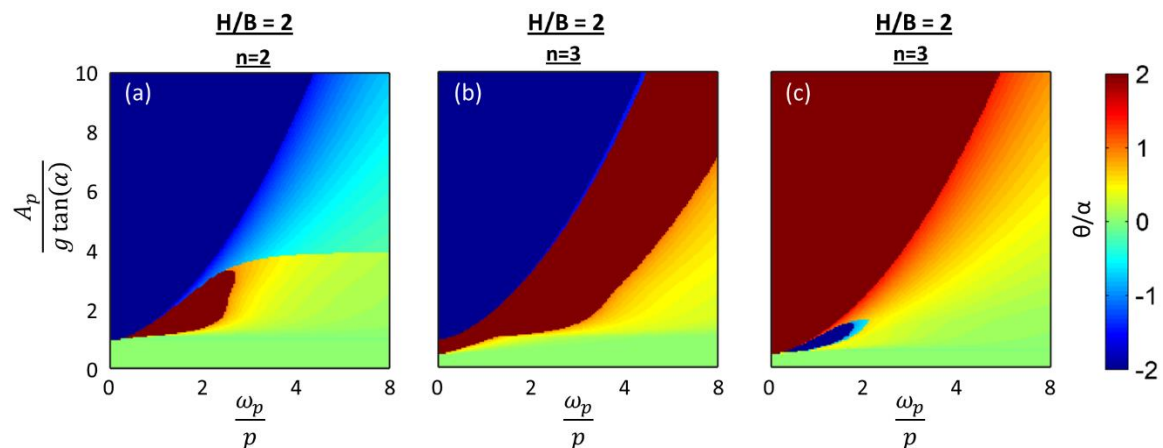


Figure 6.12 Overturning spectra for a squat block ($H/B = 2$), where the defect is characterized as $0.25B$ and $0.3a$ for (a) two rocking points or no defect, (b) three rocking points, and (c) three rocking points with the sinusoidal input in the direction of the defect.

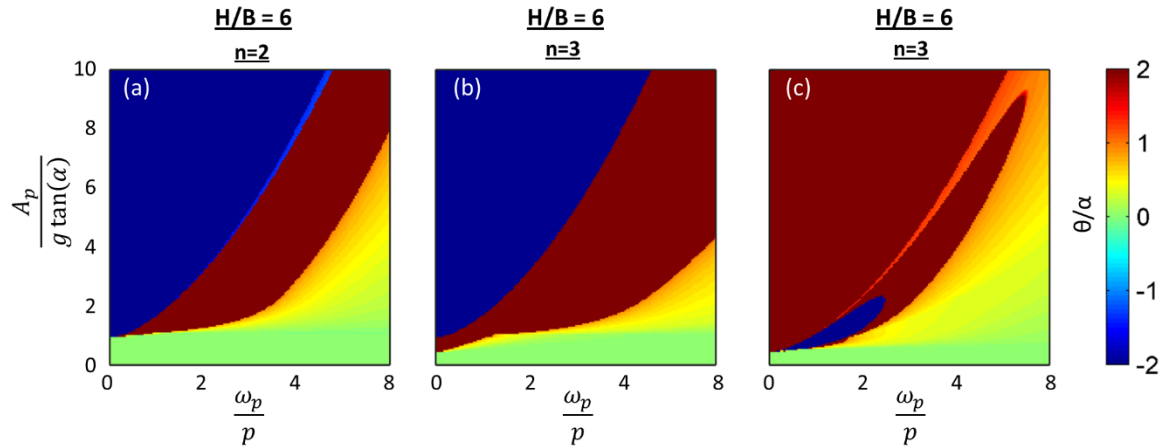


Figure 6.13 Overturning spectra for a tall block ($H/B = 6$), where the defect is characterized as $0.25B$ and $0.3a$ for (a) two rocking points or no defect, (b) three rocking points, and (c) three rocking points with the sinusoidal input in the direction of the defect.

6.1.9 Conclusions

Freestanding structures comprise a wide variety of systems such as water towers, gravestones, nuclear radiation shields, mechanical and electrical equipment, as well as culturally significant statues and columns. Many of these systems have a significant effect on the functionality of a facility post-earthquake or are culturally significant and irreplaceable, necessitating the accurate prediction of this system's response to an earthquake. These structures are typically modeled as symmetric, rectangular, two-dimensional rigid blocks with two points of rotation at the base. This section extends this classical model for an arbitrary number of rocking points at the base, reflecting small interface defects or warping. The equations of motion are presented in conjunction with a velocity adjustment factor, which accounts for potential energy dissipation at each impact of a rocking point. The effect of minor interface defects is then studied parametrically with respect to the classical model as well as compared to recent experimental free rocking tests. The primary conclusions of this work are summarized as:

- The presented model enhances agreement with recent free rocking tests of stiff, freestanding bodies. This agreement is possible without arbitrary modification of the

velocity adjustment factor (or coefficient of restitution for the classical model), rather by considering three rocking points at the interface, as an approximation to base defects.

- The velocity adjustment factor, which represents energy dissipation, is the instantaneous result of point impacts and can have a value greater than 1 in the presented model, resulting in a finite increase in the angular velocity of the block due to the instantaneous reduction in rocking radius. This is in stark contrast to the classical model, in which this factor is referred to as a coefficient of restitution and always less than 1. In the proposed model, the velocity adjustment factor may be up to 25% larger than that specified in the classical model for squatter blocks ($H/B < 4$). As a result, the classical model may be unconservative and underestimate the rocking response of blocks with interface defects.
- The velocity adjustment factor is unique to each rocking point; and, the rocking point with the highest velocity adjustment factor (least energy dissipation) will vary, depending upon the size of the defect and the aspect ratio of the block. Specifically, the factor is highest at the extreme rocking point associated with the defect for taller blocks ($H/B > 4$), while an intermediary point is highest for squatter blocks.
- Despite little variation in the velocity adjustment factor for taller blocks, the rotational response of the block with a defect is quite different than that predicted by the classical model. Specifically, the first peak after impact can be nearly 200% greater; however, the decay of the motion is much more rapid. Overturning spectra for a single sinusoidal pulse input further emphasize the significantly increased rate of overturning for both squat and tall blocks, with overturning possible for blocks of three rocking points at amplitudes less than the threshold to initiate rocking motion in the classical model with two rocking points. However, a sinusoidal pulse that overturns a block modeled with two rocking points may not necessarily overturn a block modeled with three rocking points due to its asymmetry.

6.1.10 Implications of Analytical Study on Numerical Modeling

The ultimate goal of this chapter is the validation of a numerical model for the seismic response of freestanding structures of varying geometry. This validation aims to compare the predictions of the numerical model with carefully monitored shake table testing of twenty-seven unique geometric configurations of single- and dual-body systems. However, the experimental specimens were characterized by mild interface warps, due to fabrication. The warp effectively introduces intermediary rocking points, which violates the assumptions of the classical rocking model that is characterized by perfect contact at the base and two distinct points of rocking. As such, the effects of this mild variation are not understood in the classical context. Therefore, the extension of the classical model to account for an arbitrary number of rocking points was presented in this first section of the current chapter.

It was observed through the parametric study presented in this section that a minor warp or defect at the base of squatter structures is much more significant for the dynamic response than for taller structures. However, there is still a noticeable effect on the rate of overturning for blocks of all aspect ratios. Therefore, the numerical modelling approach must be able to physically model intricate surface geometries as well as arbitrary body geometry, as noted in the experimental conclusions of Chapters 4 and 5. In addition, it was observed through numerically integrated time histories that squatter structures with warped interfaces will decay much less rapidly when set into a free rocking motion. However, taller structures with a warped interface may decay much faster. Therefore, it is emphasized that the validation of the numerical modeling approach should carefully consider the energy dissipation for freestanding structural systems of varying aspect ratios, which will serve to validate the model with respect to the fundamental rocking dynamics of the system.

6.2 Summary of Implications on Numerical Modeling

While the objective of this chapter is the development and validation of a numerical model for freestanding structures, the results of previously discussed experimental and analytical studies were intended to directly inform the development of this model. As such, the findings of these studies and the combined effects on model development are summarized herein, while the primary conclusions and the individual implications of each study are summarized within each of the corresponding chapters. In an effort to collocate all of this pertinent information, Table 6.1 outlines each of the preceding studies, the key findings, as well as the implications on numerical modeling, which are elaborated upon in this section.

The first phase of experimentation focused on the dynamics of single-body systems, as detailed in Chapter 4. In these tests, symmetric and asymmetric freestanding structures of various size and aspect ratio were subjected to seismic excitation, and the fully three-dimensional motion was recorded in time. During these tests, the asymmetric bodies responded not only with varying magnitude, but also in completely different response modes compared to their symmetric counterparts when all other variables remained the same. As a result, numerical models cannot assume simplified geometries – as is typical of the analytical and classical methods. Furthermore, three-dimensional responses were frequently observed emphasizing that modeling must be conducted in a three-dimensional framework and that key information would be lost in a two-dimensional idealization. In addition, these structures tended to exhibit multi-modal behavior; and, as such, the numerical modeling scheme must allow the bodies to rotate and translate at any time and in all directions throughout its response. While this multi-modal behavior is a key attribute of the system, the free rocking behavior of the experimental specimen is also of further interest. Specifically, the experimental results did not agree with analytical predictions, which is largely attributed to the classical assumption of perfectly inelastic impacts. As a result, the numerical model

must be able to account for flexibility at the interface to some degree. However, experimental modal analysis of the tested structures indicates the rigidity of the individual bodies, which allows the freestanding bodies to be modeled as rigid with lumped flexibility at the interface during impacts.

Following the first phase of experimentation on single-body systems, a second phase considering dual-block systems built upon or reconfirmed previous conclusions. For example, multi-modal behavior and three-dimensional effects increased with the additional degrees of freedom for the dual-body system. This finding re-emphasized the criticality and necessity of the numerical model to be conducted in a three-dimensional framework without restrictions on the rotation, translation, and separation of the individual bodies that comprise the freestanding system. In addition, the geometry of the upper body of the dual-body system was observed to have a very significant effect on the response of the lower bodies. This was often evidenced by system-wide responses compared to the motion of the upper body atop the lower body, where this actually increased the stability of the upper body in certain configurations. The combination of these key findings highlight the applicability of a discontinuum approach for the simulation of freestanding structures, in which the motion of each discrete body is modeled with contact forces developing at their boundaries allowing both individual and system-wide motion.

The final considerations for the numerical model development arise from an analytical study, as described earlier in this chapter. This analytical study was conducted to gauge the impact of minor geometrical defects in the base or interface of a freestanding structure, as was evident in the experimental specimens due to fabrication error. Through this study, the impact of warps at the interface of these systems is noted to be profound, with differences in the impact observed for squatter and taller systems. As such, the numerical model not only should be able to incorporate finely detailed interface geometry, but also should be validated with respect to its ability to capture the complexities of impact with finely discretized interfaces.

Table 6.1 Summary conclusions from shake table testing and analytical modeling with the corresponding implications on numerical model development.

No.	Study	Primary Conclusion	Implication on Modeling
1	Single-Body Testing	Asymmetry of body impacts not only magnitude but also response mode	Able to represent asymmetric and arbitrary geometry bodies
2	Single-Body Testing	Twisting was a significant mode of response, even for symmetric bodies	Conducted in a three-dimensional framework
3	Single-Body Testing	Multi-modal behavior was typical	Bodies must be free to rotate and translate at all times
4	Single-Body Testing/Analytical Modeling	Coefficient of restitution of classical model must be reduced to mimic experimental free rocking.	Material effects and flexibility must be incorporated at interface.
5	Single-Body Testing	Experimental modal analysis yields natural frequencies in excess of 17 Hz	Freestanding bodies can be modeled as rigid
6	Dual-Body Testing	Geometry of upper bodies affects response of lower bodies	Solution scheme must account for motion of all blocks simultaneously – discontinuum approach
7	Dual-Body Testing	Stability can increase in a dual-body system due to impacts between moving bodies	Impacts and contact must be a function of the individually impacting blocks – discontinuum approach
8	Dual-Body Testing	Twisting was a significant mode of response, even for symmetric systems	Conducted in a three-dimensional framework
9	Dual-Body Testing	Multi-modal behavior was common and varied for the individual bodies of a system	Each body in a system must be free rotate and translate at all times
10	Analytical Modeling	Minor warps or geometric interface variations can have significant impact on rocking	Able to physically model interface geometries

6.3 Numerical Modeling Methodology

This section details the numerical modeling methodology, which is further studied and validated in subsequent sections. Specifically, the experimental conclusions and implications on numerical modeling directly inform the development of this modeling technique. Each implication and the ultimate treatment in the numerical model is provided in Table 6.2, which corresponds to the list of key findings and implications in Table 6.1. To this end, this section is divided into subsections that detail the modeling platform, model discretization, material model, contact-impact algorithms, and finally the dynamic analysis method.

6.3.1 Modeling Platform

The numerical model was developed in the explicit, multi-physics solver LS-DYNA (LSTC 2013). LS-DYNA is a robust platform which incorporates the finite element method, rigid body dynamics, and advanced contact-impact algorithms, which are particularly attributable to freestanding structural systems. This software has both two-dimensional and three-dimensional capabilities, with a broad library of material models, element types, and contact algorithms. Furthermore, LS-DYNA is a readily-available and widely-used engineering software allowing for ease of implementation and further analyses of freestanding systems, including fluid-structure interaction and other multi-physics simulations. This multi-physics platform is additionally used across a broad range of engineering disciplines, including mechanical and aerospace engineering. This extensive user base further justifies its use as the dynamics of freestanding systems extends well beyond structural and earthquake engineers. Furthermore, the input files for LS-DYNA simulations consist of standard text files, consisting of 80-character lines, which can be generated on any text-editing platform. These files consist of “keywords” which define the model geometry and relevant parameters, as described in the following sections.

Table 6.2 Implications of preliminary analyses on numerical modeling and treatment within the proposed numerical model.

<u>No.</u>	<u>Implication on Modeling</u>	<u>Treatment in Model</u>
1	Able to represent asymmetric and arbitrary geometry bodies	Solid elements of arbitrarily shaped finite element mesh. Geometric and mass parameters can be manually overwritten
2	Conducted in a three-dimensional framework	Three-dimensional version of LS-DYNA utilized
3	Bodies must be free to rotate and translate at all times	Horizontal and tangential springs and dashpots at points of contact
4	Material effects and flexibility must be incorporated at interface.	Tangential springs and dashpots account for local flexibility
5	Freestanding bodies can be modeled as rigid	Solid elements with rigid (undeformable) material model
6	Solution scheme must account for motion of all blocks simultaneously – discontinuum approach	Rigid body dynamics with advanced contact model allows independent motion of blocks – discontinuum approach
7	Impacts and contact must be a function of the individually impacting blocks – discontinuum approach	Contact model accounts for material properties of both impacting bodies in the discontinuum approach
8	Conducted in a three-dimensional framework	Three-dimensional version of LS-DYNA utilized
9	Each body in a system must be free rotate and translate at all times	Horizontal and tangential springs and dashpots at all points of contact between all bodies and boundaries
10	Able to physically model interface geometries	Discretization of bodies utilizes solid elements for arbitrarily shaped finite element mesh

6.3.2 Model Geometry and Discretization

A primary implication of both phases of experimentation as well as preliminary analytical studies is the need for the numerical model to incorporate arbitrary, detailed, and three-dimensional geometry. This need originates from the significantly different responses of symmetric and asymmetric bodies, the high number of occurrences of twisting modes, and the noted impact of mild geometric warps in the interface, as detailed in Table 6.1 items 1, 2, 8, and 10. The ability to model complex geometries and multiple objects is well incorporated within LS-DYNA, which can be implemented using the corresponding pre-processor, LS-PrePost, or by manual specification in the input files (i.e. keyword files) as described in this section and identified in Table 6.2.

The definition of geometry and the discretization of the proposed discontinuum model is identical to that of traditional finite element modeling. LS-DYNA keywords include a list of nodes with corresponding nodal identifier and xyz coordinates. Manual input of these nodes allows for arbitrary geometry to be easily incorporated, such as a resultant point cloud from LiDAR or SfM, as described in Chapter 3. The nodes define not only the surface, but the interior of the objects as well, as discussed in the context of elements. Specifically, individual nodes define the boundaries of solid or shell elements within the program. For the proposed model, solid elements were utilized; however, the contact-impact algorithms, material model, and analysis procedure are identical for shell elements. The specific solid element incorporated is an 8-node brick, constant stress solid element, the default element type in LS-DYNA (EQ.3 in *SECTION_SOLID). It is noted, however, that the choice of solid element formulation does not impact the solution for the presented analyses due to the choice of material model, as discussed in the following sub-section.

The definition of nodes and elements, as described, is identical to that of finite element modeling. However, the proposed model is a discontinuum indicating that the elements do not necessarily comprise the same structure. Rather, the elements are defined not only by the eight

nodes that form the geometry, but also by a part number. The part definition specifies the material model and the element formulation (i.e. *PART keyword). Each individual part can be defined using any number of nodes and elements; and, the interaction or the connectivity between individual parts is dictated by the contact-impact algorithms, which are discussed in the following sections. In addition, the part definition can be used to override mass and inertial quantities, which are calculated as a summation over the nodes by default. Specifically, the *PART_INERTIA keyword enables the user to define the center of mass, the total mass, and the six components of the inertia tensor for the part, or freestanding structure in this study. This enables the use of significantly coarser meshes than typically necessary for finite element analyses. However, it is noted that the discretization of the meshes significantly impact the contact-impact algorithms, and this is further explored in terms of the model sensitivity in the next section.

A schematic of a representative model is included in Figure 6.14. Two parts are modeled in this figure, Part 1 representing a freestanding body and Part 2 representing a foundation. Both of the parts shown incorporate 8-node brick solid elements, where the meshes are shown to be finely discretized. However, Part 1 consists of two very different degrees of discretization. The part is shown with a highly discretized interface and a single element representing the bulk of the structure. It is noted that the inertial properties of the structure would be exceedingly inaccurate provided the shown mesh; and, as such, these properties are overridden as previously described. While the parts shown in the figure are exaggerated, the multiple levels of discretization were incorporated throughout the numerical models described in this chapter. This was specifically done for the distribution of the contact forces while reducing computational time and file size.

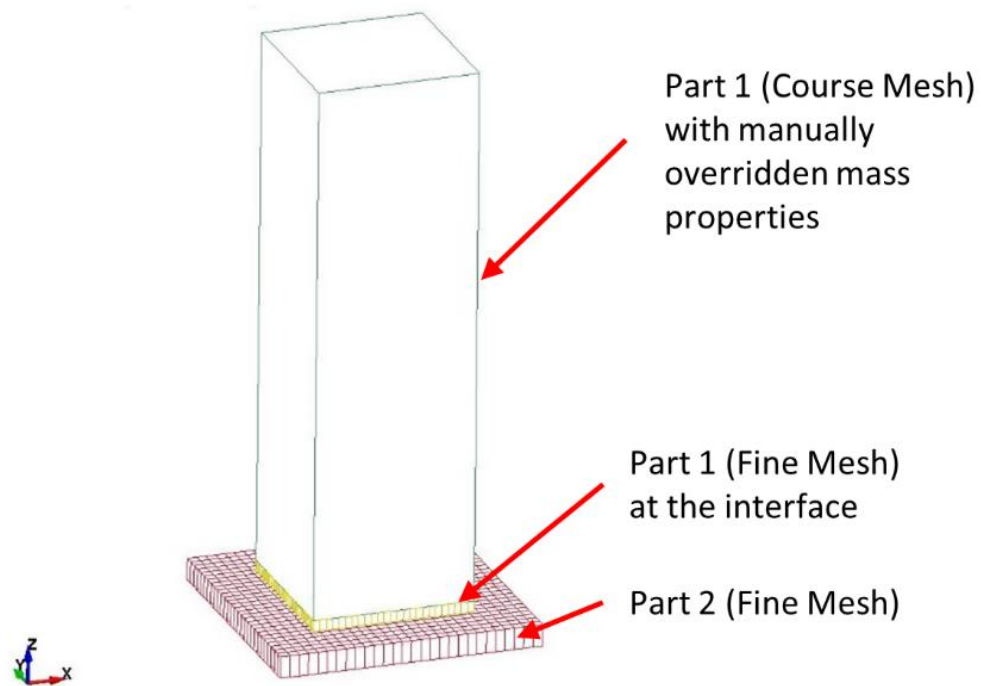


Figure 6.14 Geometry of baseline numerical model showing one part for each freestanding structure with variable discretization at the interface.

6.3.3 Material Model

All elements that comprise an individual part in the numerical model are specified with an appropriate constitutive or material model. As evidenced by experimental modal analysis, all tested systems discussed in Chapters 4 and 5 can be considered rigid, with negligible deformation during earthquake excitation. As such, all parts were specified with a rigid material model (refer to Table 6.2, line 5), as defined by the keyword `*MAT_RIGID`. In LS-DYNA, the specification of an element as rigid indicates that the element will be bypassed during element processing, and no space is allocated for storing history variables such as stress. As a result, only part-specific data is recorded, such as the rigid body displacement and rotation. This results in significant time and computational savings; however, it is noted that the model is easily extended to account for

flexibility of a freestanding body, which would incorporate an elastic material or an alternative constitutive model.

While the rigid material model essentially indicates an infinite stiffness, material properties are still defined for the rigid elements. This is done specifically for the treatment of contact and lumped flexibility at the interfaces, as described in the following sub-section. Specifically, the following parameters are defined for a rigid material in LS-DYNA:

- Material ID: unique identifier for the material;
- Poisson's Ratio (ν): material property that defines the ratio of transverse to axial strain, and further used to convert Young's modulus to bulk modulus;
- Density (ρ): mass density for the calculation of mass (note this can be overridden using *PART_INERTIA as discussed in previous sub-section); and
- Young's Modulus (E): modulus of elasticity for the calculation of spring stiffness during contact-impact calculations.

Additional parameters may be defined to constrain the motion of the body or define a local coordinate system; however, these are not necessary for the simulations described in this dissertation.

6.3.4 Contact-Impact Algorithm

Contact-impact algorithms are the general class of algorithms that define how various parts interact within a simulation in LS-DYNA. While this can apply to tied constraints and folding of deformable surfaces, the contact-impact algorithm utilized within the proposed model is a penalty-based contact algorithm, which generates springs and dashpots to resist the penetration of a node into another element. In this way, the model accounts for lumped flexibility at the surfaces of the freestanding bodies. Furthermore, these spring and dashpot elements, which are generated only at the time and location of a detected penetration, provide flexibility in all directions, allowing the

bodies to rock, slide, impact, and separate. Therefore, the incorporation of penalty-based contact within the numerical model directly addresses implications 3, 4, and 9 within Table 6.2.

Penetration of a node into an element, or detection of contact, is determined by LS-DYNA through a bucket sorting algorithm, in an effort to improve computational efficiency for automatic contact types (i.e. *CONTACT_AUTOMATIC). Specifically, at every time step in the simulation, each node that is specified for contact is located with respect to a nearest segment, where a segment is a face of a solid element. However, the distance between the current node and every segment in the model is not calculated. Rather, the bucket sorting algorithm categorizes all the nodes based upon previous locations; and, only the nearest segments are checked for being the ultimate nearest segment. The specific implementation described in this chapter utilized contact that was defined by the individual parts, meaning that contact was defined to act between two parts. This allows for arbitrary motion of the bodies as any node on either part could interact with any element of the other part. However, a new contact definition is required for each individual pair of bodies. As such, two contact definitions were implemented for the dual-body system.

Once a nearest segment has been identified for each node, the nodes are checked for penetration into the master surface. If the node is found not to be penetrating any element, nothing is done and no spring nor dashpot is generated at that node. However, if it is found to penetrate, an interface force is applied between the node and the point of contact. The contact force that lies within a segment is proportionally applied to the segment nodes. The magnitude of this contact force is proportional to the penetration, as shown in Figure 6.15, and defined in:

$$F_R = K\Delta_{node} \quad (6.22)$$

where F_R is the resultant contact force acting in the direction opposite that of the nodal velocity vector, Δ_{node} is the nodal penetration into the master element, and K is the contact stiffness, which is a function of the master segment stiffness (not the default option):

$$K = \frac{K_b A^2}{V} \quad (6.23)$$

where K_b is the master segment's bulk modulus, as computed through the Young's modulus and the Poisson's ratio specified in the material model, A is the area of the segment that has been penetrated, and V is the volume of the penetrated element. This resultant contact force acts in the direction opposite that of the nodal velocity vector. This force can then be decomposed into normal and tangential components with respect to the master segment. However, the calculation of these components is conducted with respect to Coulomb friction, and limiting the tangential force accordingly.

In addition to the generation of spring forces at each penetration, the model provides the option for dashpot elements or contact damping to be incorporated. While many DEM implementations utilize Rayleigh damping (Itasca 2003), the LS-DYNA model presented in this dissertation utilizes viscous contact damping. This viscous contact damping is intended to remove high frequency noise in impact problems and oscillations normal to the contact surfaces. The damping model is specified in the input file as a viscous damping coefficient (VDC) or a percentage of critical damping, where c_c is the corresponding critical damping coefficient:

$$c_c = 2m\omega \quad (6.24)$$

where m is the minimum of the slave nodal mass and the effective nodal mass for the master segment, based upon the basis function for the contact point of the slave node, and where ω is defined as:

$$\omega = \sqrt{\frac{K(m_{slave} + m_{master})}{m_{slave}m_{slave}}} \quad (6.25)$$

where K is the interface stiffness as previously defined and the masses correspond to the slave nodal mass and the interpolated effective master nodal mass at the point of contact. The sensitivity of these parameters is further explored in later sections of this dissertation. A more detailed treatment of the contact-impact algorithms in LS-DYNA can be found in the accompanying theory manual (LSTC 2006).

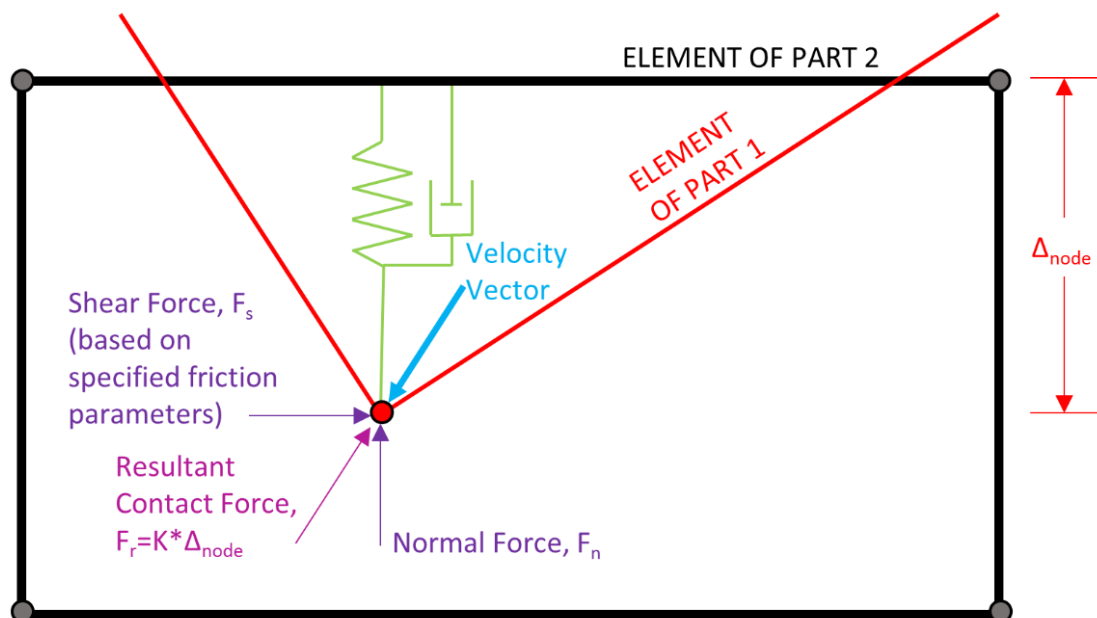


Figure 6.15 Penalty-based contact algorithm as utilized within LS-DYNA.

6.3.5 Dynamic Analysis Method

The time stepping procedure performed within this LS-DYNA numerical model is very similar to that of the discrete element method (Cundall 1971). This analysis approach is specifically applicable to the problem as it simulates the response of a discontinuum. As such, it allows for the fully three-dimensional rigid body dynamics of many individual bodies simultaneously, and allows these bodies to interact at their boundaries. At these points of contact, spring and dashpot type elements are generated for contact forces. This separate motion of each body and the distinct interaction at contact directly addresses the experimental implications denoted in lines 6 and 7 of Table 6.1 and Table 6.2.

The general procedure, which applies to DEM, is provided as a flow chart in Figure 6.16a; whereas, the detailed steps performed by LS-DYNA are included as a flow chart in Figure 6.16b. The three primary steps are: 1) the determination of external forces; 2) solving rigid body acceleration through Newton's Second Law of Motion; and, 3) numerically integrating the acceleration for the displacement and position. The steps are the basis of the discontinuum or micro-modeling approach of many bodies in a system. However, the specific implementation and subsequent efficiency of the numerical scheme varies depending upon the platform. While an overview of the procedure is provided herein, a more detailed treatment of the implementation in LS-DYNA can be found in the theory manual (2006) as well as the original derivation of the rigid body dynamics algorithm by Benson and Hallquist (1986).

Referring to Figure 6.16b, the initial step in the analysis is the application of boundary conditions. For the numerical simulations described in this chapter, this primarily consists of gravitational forces and the prescribed motion of the foundation to represent the base excitation or the motion of the shake table. This step is followed by the contact-impact algorithm, as described in the previous sub-section, in which a search for nodal penetration is conducted and tangential and

normal forces are generated to resist that penetration through the generation of springs and dashpots as well as the enforcement of Coulomb friction. At this point in the simulation, all of the external forces on the individual rigid bodies are current, and the sum of the forces and moments on the rigid body centers of mass is calculated. Provided the individual rigid body's forces and moments, the linear and angular acceleration can be solved by a simple application of Newton's Second Law of Motion. The central difference method is then used to numerically integrate the rigid body accelerations into rigid body velocities, which inform the updating of the rotation matrix and the updated nodal positions.

While the updated nodal positions are the intended outcome of the time stepping procedure and can be used to solve for the three-dimensional motion of the bodies, it is essential to have updated nodal velocities for the calculation of the contact forces at the subsequent time step. For this reason, the nodal velocities are numerically differentiated from the updated nodal displacements. The procedure described appears roundabout in that it does not directly integrate the rigid body accelerations into rigid body displacements. However, the calculation of nodal accelerations is more computationally expensive than LS-DYNA's current algorithm and the numerical integration in this method would likely introduce distortion to the rigid bodies. As a result, the nodal accelerations are never calculated in the described algorithm, but can be obtained by post-processing the nodal velocities.

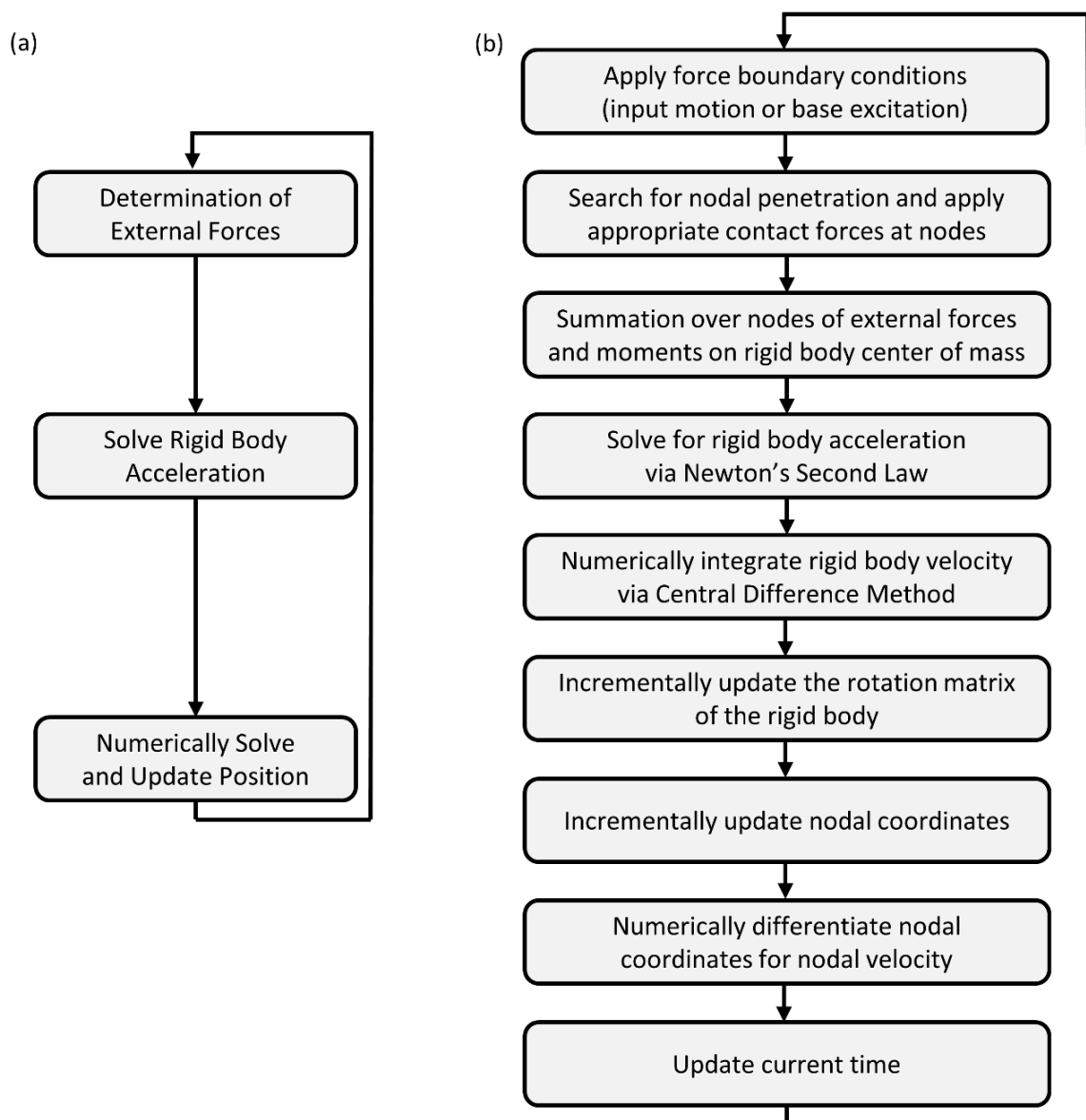


Figure 6.16 Flow chart of time stepping process in the developed LS-DYNA model: (a) primary steps, and (b) detailed steps.

6.4 Numerical Model Calibration and Sensitivity

The primary goal of this section is the development and calibration of the numerical model, as previously discussed, to fit the experimental data, as described in Chapters 4 and 5. In this effort, a generic tower structure is modeled as seen in Figure 6.14, which incorporates a rectangular tower of variable interface discretization that can represent a more complex geometry through the manual input of mass and inertia properties. This generic model is characterized by geometric and mass properties similar to that of the experimental tower specimen including a 0.74 m square footprint, a center of mass located 2.4 m symmetrically above the base, a total mass of 760 kg, and an inertia tensor with diagonal components of [700, 700, 100] kg-m² in x, y, and z-directions. The contact damping, interface stiffness, and interface discretization of this generic model are varied to understand the sensitivity of the response to these critical parameters as well as to inform the selection of appropriate parameters for the experimental specimens, as ultimately described at the conclusion of this section.

6.4.1 Contact Damping

At every time step in the dynamic simulation, the contact-impact algorithm generates spring elements to resist nodal penetration. The spring stiffness is a function of material properties; and, the spring generates a force proportional to the penetrated distance. The nodal mass that penetrates a master segment and the generated interface spring effectively form a simple mass-spring system. As such, this system will tend to oscillate causing fictitious high frequency vibrations at the interface, which may lead to erroneous results. In an effort to reduce these high frequency oscillations, contact damping is a typical element in contact-impact algorithms. Specifically, viscous damping is incorporated in the proposed numerical model described in this dissertation. This sub-section aims to investigate the effect of this viscous damping in terms of the nodal penetration, the contact force, and ultimately the rocking response.

The free rocking response of a representative rigid, symmetric tower structure atop a rigid foundation is released from an initially rotated condition and, subject to gravity, undergoes a free rocking response, as shown in Figure 6.17. The general procedure is described in the previous section. For the present study, material properties close to that of marble are used to define the rigid material model and subsequently the interface stiffness. Specifically, the material model was defined by a density of 2700 kg/m^3 , Poisson's ratio of 0.3, and Young's modulus of 50 GPa. Given the baseline interface discretization of four elements in both horizontal directions (refer to Figure 6.14), the approximate interface stiffness is 150 GPa/m. Furthermore, the contact model ignored friction for the study of free rocking, and included a variable viscous damping coefficient (VDC), which is a percentage of critical based upon the nodal mass and interface stiffness.

Figure 6.17 presents the results of the free rocking simulations within the contact damping parametric study. This sequence of plots includes the displacement of a tracked corner node in the direction normal to the foundation or master segments. When this node is in contact with the master segment, this quantity is equivalent to the nodal penetration, Δ_{node} . In addition, the normal contact force and the rigid body rotation, or rocking, are included over time for the first two cycles of rocking. The results are presented for three values of the viscous damping coefficient: 0% (no damping), 50%, and 100% (critical damping). It is clearly observed that there is no noticeable difference in the results prior to the first impact event. However, significant variation in the results begins at this instance of impact, near 0.8 s. Specifically, the model with no contact damping exhibits very significant high frequency oscillations of the contact force following this impact event, with duration of the oscillations in excess of 1 s. Furthermore, the nodal penetration is observed to bounce, and creates a stark contrast to the very smooth behavior of the models with damping. However, these high frequency oscillations do not carry over into the rocking response, which is the ultimate product of the model. Rather, the model with no damping that is characterized

by significant bouncing at the interface yields slightly higher peak rotations and a slower decay of rocking motion.

In order to take a deeper look at the effect of damping at the impact event, detail views of an individual impact event are included in Figure 6.18 and Figure 6.19. These detail views initially highlight the very significant bounce of the model with no damping, with bouncing approaching 2 mm and durations in excess of 0.04 s of no contact between the tower and the foundation. The degree of bouncing reduces significantly in the models with higher levels of viscous damping, however the bouncing is always present. In addition, it is apparent that the high frequency contact force oscillations are directly correlated to this bouncing, with spikes at each subsequent impact event. It is clear that the level of viscous damping has a significant effect on the free rocking response. The response to a random base excitation would result in greater variation due to the increased number of impacts anticipated during a random event. Therefore, it is recommended to utilize high levels of viscous damping in the experimental predictions. Specifically, critical damping values are incorporated ($VDC = 100\%$). This aims to reduce the fictitious oscillations of the mass-spring system that represents the lumped nodal mass and the interface stiffness.

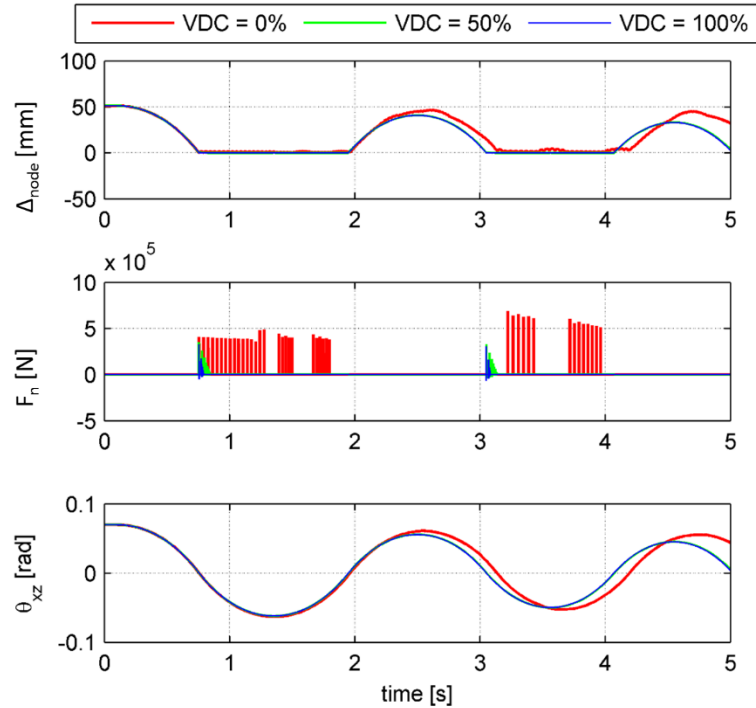


Figure 6.17 Nodal penetration, contact force, and rigid body rocking of a tower with consistent interface stiffness and variable levels of contact damping over two cycles of rotational response.

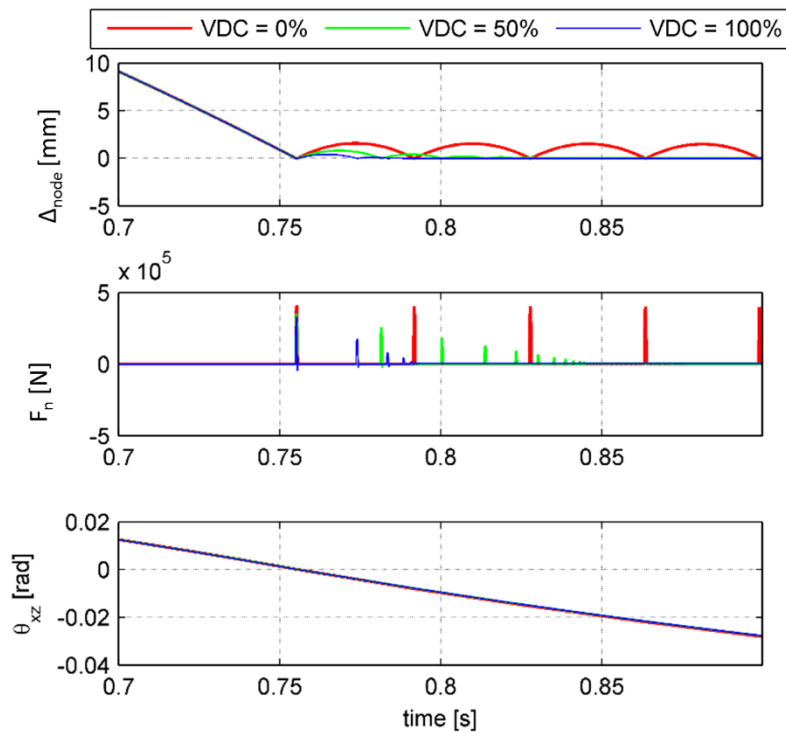


Figure 6.18 Nodal penetration, contact force, and rigid body rocking of a tower with consistent interface stiffness and variable levels of contact damping for a detail view of a single impact event.

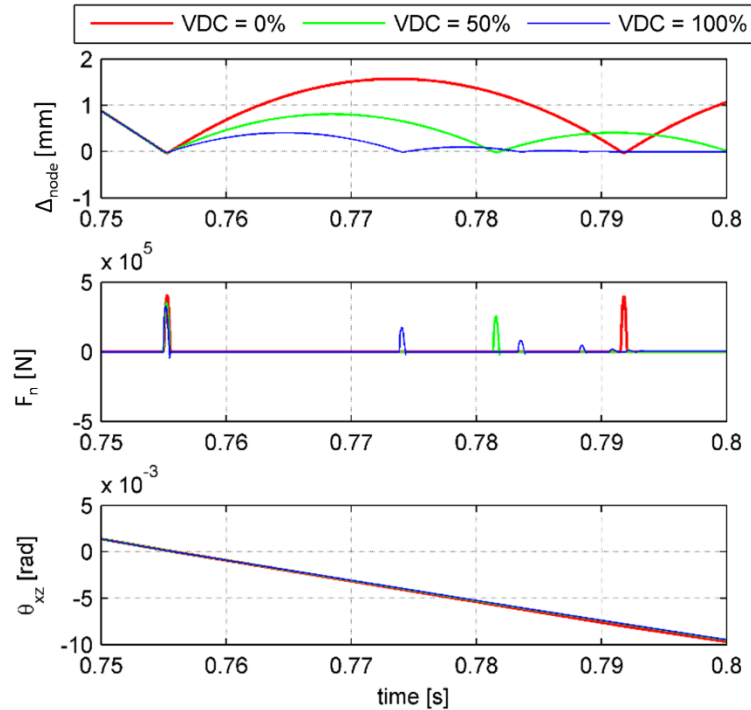


Figure 6.19 Nodal penetration, contact force, and rigid body rocking of a tower with consistent interface stiffness and variable levels of contact damping for a detail view of two nodal penetration events.

6.4.2 Interface Stiffness

The contact-impact algorithm as implemented within LS-DYNA generates spring and dashpot elements at all nodes that are detected to be in contact with another body. These spring elements are linear and generate a force proportional to the nodal penetration of the slave node into the master segment. The proportionality constant, or the spring stiffness, is defined in Equation (6.23) and is a function of the bulk modulus and volume of the penetrated element as well as the area of the penetrated segment. While the exact calculation or input of the spring, or interface, stiffness varies in each implementation (e.g. UDEC), the effect of this implementation in LS-DYNA is explored in this section. Specifically, the general rigid tower structure with variable interface discretization that was used in the previous parametric study is further employed in the current parametric study. As the interface stiffness is a function of multiple properties of element

geometry, the bulk modulus of the material model is the truly varied parameter, while the ratio of segment area to element volume is kept constant as defined in Equation (6.23).

The results of simulations incorporating various levels of the interface stiffness are included in Figure 6.20 and Figure 6.21 for two cycles of rocking response as well as a more detailed view of an impact event. The parametric study varied the interface stiffness at three levels: $K = 1.5 \text{ GPa/m}$; 150 GPa/m ; and $15,000 \text{ GPa/m}$. It is further noted that the median interface value tested (i.e. $K = 150 \text{ GPa/m}$) corresponds to typical material properties for marble, as incorporated in the previous parametric study on contact damping. The representative results in Figure 6.20 and Figure 6.21 are given with respect to the vertical displacement of the extreme corner node (i.e. nodal penetration), the normal contact force, and the rigid body rocking of the representative tower structure. It should be noted that each of these simulations incorporated a consistent value of the viscous contact damping, namely $VDC = 100\%$. However, it is further noted that the damping is a percentage of critical; and, as such, the damping fluctuates with the level of interface stiffness (refer to Equations (6.24) – (6.25) . Nonetheless, a much less significant variation in terms of the nodal penetration is observed over the multi-cycle response in Figure 6.20 for the multiple levels of interface stiffness. The only discernable difference appears after the second rocking cycle, or after many impacts after the effect of small variations has propagated. However, the more detailed view for an individual impact event is provided in Figure 6.21. The differences between the models of various interface stiffnesses is still not observable in terms of the contact force and the rocking. The stiffness, however, shows a significant impact on the nodal penetration. Specifically, the nodal penetration is not sufficiently resisted over a period of nearly 0.025 s , with mild oscillation for the next 0.05 s .

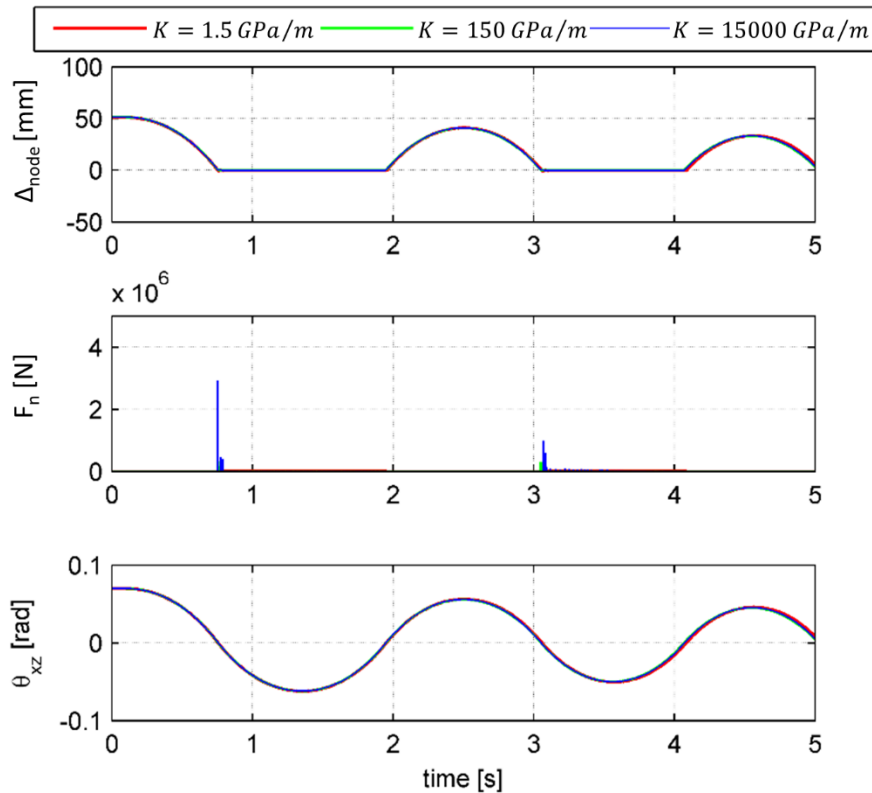


Figure 6.20 Nodal penetration, contact force, and rigid body rocking of a tower with consistent contact damping and variable levels of interface stiffness for two rocking cycles.

As a result of this parametric study, the negative effects of very low interface stiffness values were observed. Models with insufficiently stiff interfaces result in inappropriate levels of nodal penetration, where nearly 1-2 mm of penetration were observed in the study. However, differences in terms of the penetration, bounce, and overall rocking response were not observed for higher levels of interface stiffness. Therefore, interface stiffness values that result from the incorporation of typical material properties are likely to be sufficient for the simulations described in this dissertation.

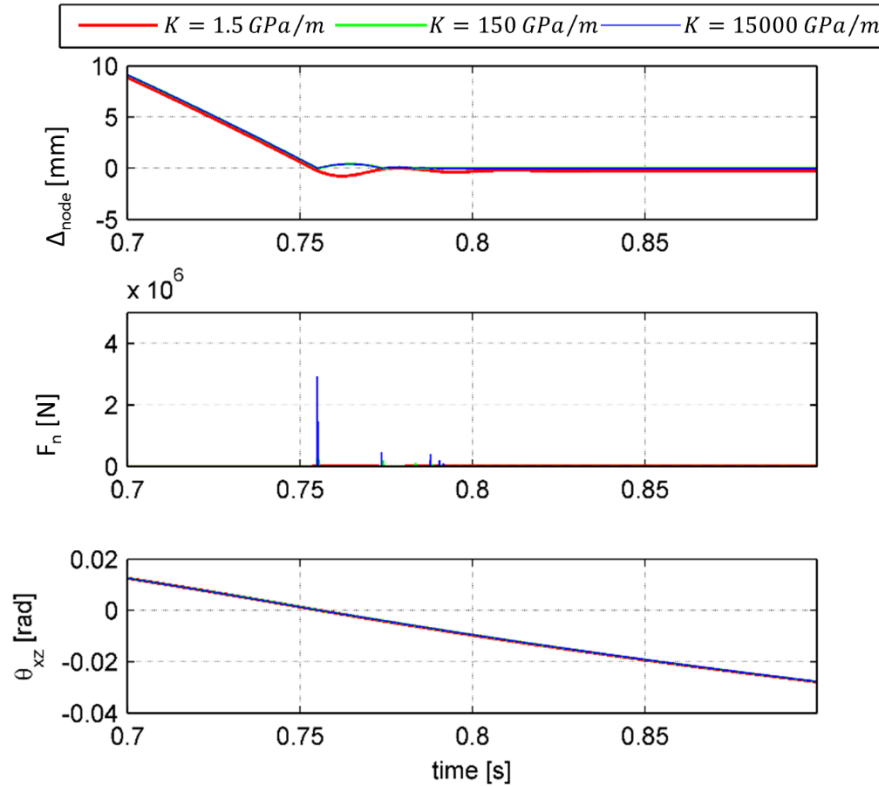


Figure 6.21 Nodal penetration, contact force, and rigid body rocking of a tower with consistent contact damping and variable levels of interface stiffness for a detail view of a single impact event.

6.4.3 Interface Discretization

The implemented contact-impact algorithm generates forces of springs and dashpots at all nodes that are penetrating or in contact with another part in the simulation. As a result, the distribution of contact forces greatly varies as the interface discretization varies. In an effort to study how the interface discretization effects the results of the simulation, a parametric study was devised and is presented in this section. The representative tower structure utilized in the two previous sections is further incorporated in this study along with the ultimately selected damping and interface stiffness parameters. The contact stiffness, as defined in Equation (6.23), is a function not only of the penetrated element's material model, but also of the element's area and volume. As

such, the variation of the interface discretization in the current parametric study enforces that the ratio of the squared area to volume of the element is constant.

The parametric study presented in this section varies the interface discretization from two nodes (similar to the classical model assumption) up to fifty nodes. This discretization is given with respect to a single direction; however, the discretization is identical in the perpendicular direction. Therefore, a simulation denoted as two-node implies a total of four nodes with two nodes in the x -direction and two nodes in the y -direction. The preliminary results of this study are included in Figure 6.22 in terms of the overall rocking response of the tower, the normal contact force, the nodal penetration, and the sum of the nodal masses in contact. This is plotted for the duration of two complete rocking cycles, whereas a more detailed view of an individual impact event is included in Figure 6.23. In contrast to the variation due to the interface stiffness, the impact of the interface discretization on the overall rocking response is quite significant, with deviations observed after the initial impact event. Specifically, the tower attains higher peak rotations with more finely discretized interfaces. However, it is reiterated that the overall rocking response tends to propagate small variations over the duration of rocking. While the effect of the highly discretized interface appears significant after multiple cycles of rocking, the difference of the post-impact peak is within 4%. Therefore, the interface discretization is not necessarily a critical parameter in terms of the overall rocking behavior.

While the discretization is shown to have a mild effect on the post-impact rocking amplitudes, a deeper study of the effects of the interface discretization is included in Figure 6.23, which serves to further explain the observed increase in terms of the rocking response. It is apparent from the plot of nodal penetration and the contact mass that each model initiates impact at the same instant. At this instant, the interface is in full or nearly full contact with the foundation. The difference between the models becomes apparent with respect to the duration of this contact.

Models with coarser interface discretization remain in contact for much longer durations, whereas the finer discretization models smoothly and rapidly initiate rotation about the opposite rocking point, which more closely models the anticipated response. The differences in contact duration are further observed in Figure 6.24, which plots the nodal penetration for multiple nodes along the interface including both extreme edge points. It is clear in these plots that models with finer discretization are able to initiate rocking about the opposite rocking point much quicker than those with coarser discretization. This specifically relates to the increased penetration at impact, which requires additional time to repel prior to the uplift of the opposite corner.

This section presents a parametric study focused on the discretization of the interfaces and the subsequent distribution of contact forces. Models with finer discretization are shown to more closely mimic theory in that a smooth transition between rocking points is observed. However, the variation in terms of the post-impact rocking amplitude was less than 4% between models of two nodes and fifty nodes horizontally at the interface. In addition, the models with very fine discretization take considerably longer to process, as the bulk of the computation expense is associated with the generation of the contact forces at individual nodes. Therefore, the minimum number of interface nodes to sufficiently represent the interface geometry is implemented in the models presented in this dissertation.

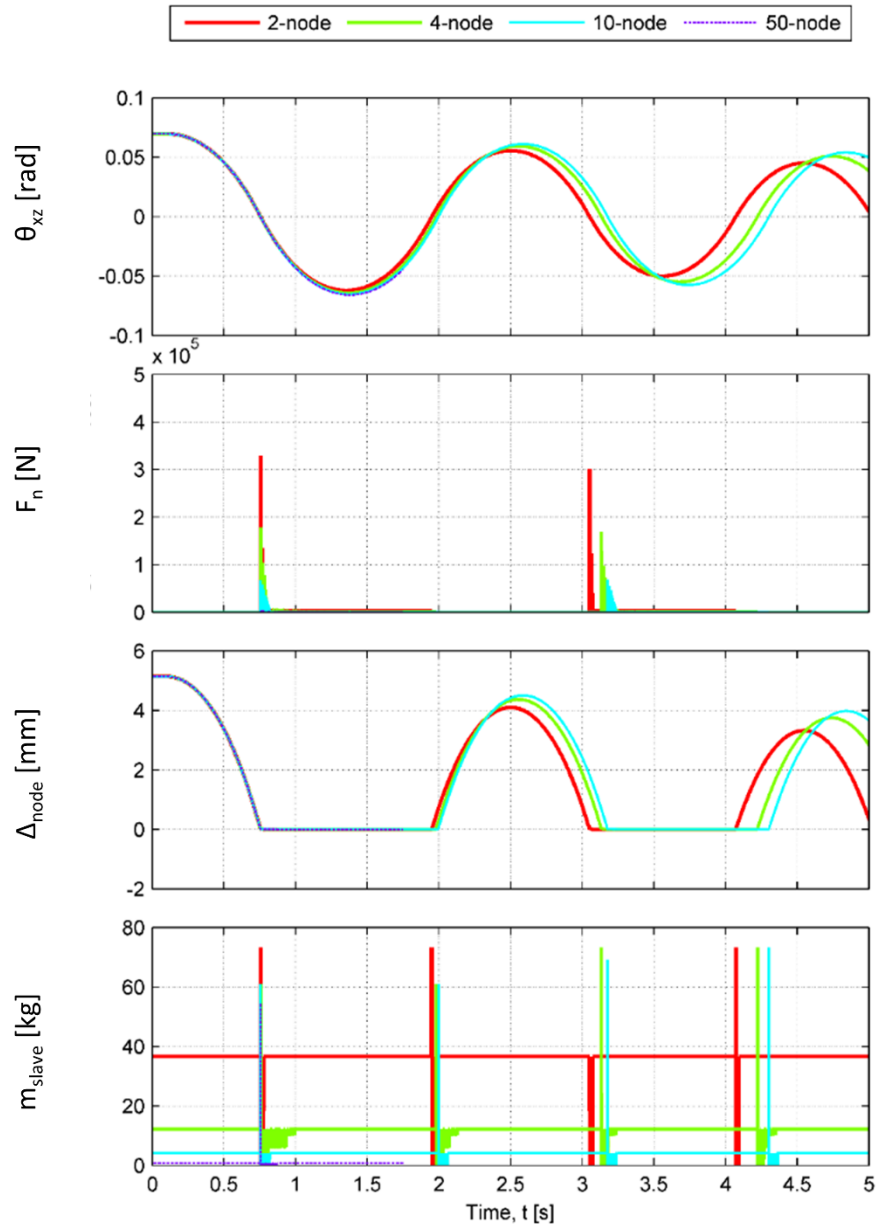


Figure 6.22 Rigid body rocking, contact force at the edge, nodal penetration, and the total slave mass in contact for various levels of discretization, where the discretization is listed with respect to the x-direction but is identical in the y-direction.

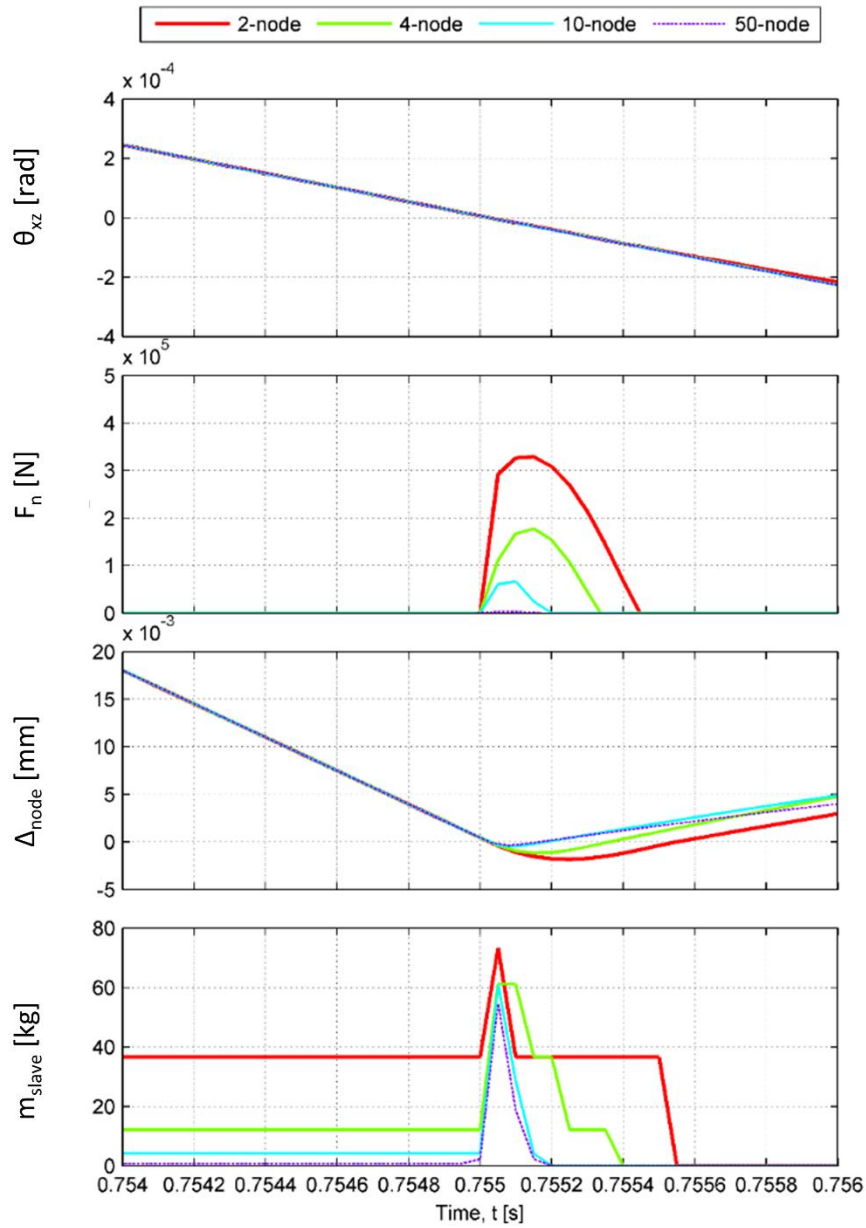


Figure 6.23 Rigid body rocking for a single impact event, contact force at the edge, nodal penetration, and the total slave mass in contact for various levels of discretization, where the discretization is listed with respect to the x-direction but is identical in the y-direction.

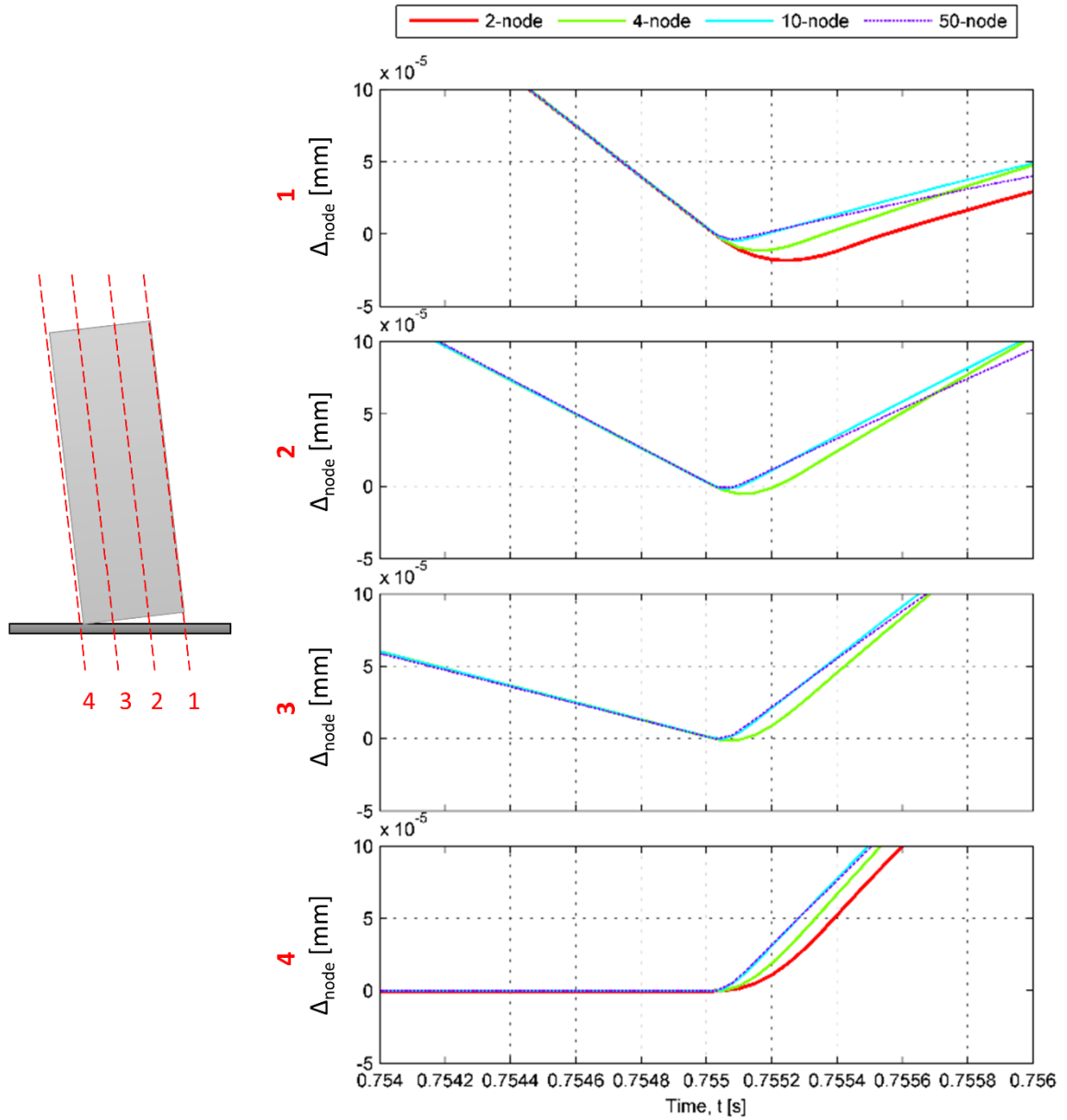


Figure 6.24 Nodal penetration for a single impact event of rocking at four discrete locations along the base of the rocking tower for variable levels of interface discretization.

6.4.4 Calibration

Previous sub-sections outlined the sensitivity of the numerical model to variations in the contact damping, contact stiffness, and interface discretization. Models with little or no damping exhibit significant oscillation of the nodal penetration and contact force, which results in noticeable variation of the rigid body motion (e.g. rocking). To reduce these fictitious oscillations, the proposed model utilizes critical damping (e.g. $VDC = 100\%$) to repel the nodal penetration with little to no oscillation of the contact force. While contact stiffness is shown to have negligible impact on the rotation of the modeled body, models with low stiffness (e.g. $K = 1.5 \text{ GPa/m}$) exhibit excessive nodal penetration; and, as such, the proposed model incorporates contact stiffness values derived from typical material properties (e.g. $K = 150 \text{ GPa/m}$). In addition, the study of interface discretization resulted in a maximum variation of 4% in the rocking response of the body with relatively minimal impacts on the nodal penetration. Therefore, the proposed models incorporate a minimum number of interface nodes to sufficiently describe the geometry.

Numerical predictions of the shake table tests utilize the aforementioned contact parameters within the described model. The center of mass and inertia tensor components are calculated for each geometric configuration of the experimental specimens, while the total mass was measured in the laboratory. These parameters are incorporated within the tower or pedestal part definition to override those values calculated from the finite element mesh, where the part-definition varied for each unique geometric configuration. Due to a noticeable warp in the marble bases of the tower and pedestals, three nodes discretize the interface in the horizontal direction, where this interface geometry was consistent for each specimen. The specified interface geometries for the base of the tower as well as the top and base of the pedestals are included in Figure 6.25 – Figure 6.28. The geometries of the bottom interfaces were approximated based upon visual inspection and manual measurements. However, the tops of the two pedestals were able to be more

closely inspected using a digital level. For all subsequent studies and validation exercises, the numerical models are characterized by these interface geometries as well as the manually overridden geometric and mass properties for the individual configurations, as described in Chapters 4 and 5.

While the geometric, mass, damping, and stiffness parameters describe a significant portion of the numerical model, the final parameter in the model definition relates to the Coulomb friction within the contact-impact algorithm. As previously mentioned, variable velocity sliding tests were conducted as part of the experimental campaign, which yielded measured values for the coefficient of friction throughout testing of each of the interfaces. The marble-marble interfaces below the tower and pedestal yielded average coefficients of friction of 0.4 and 0.6, respectively, with scatter on the order of 0.04. This variation can largely be attributed to differences in construction time and material source between the tower and the pedestals, as well as the potentially worn base of the tower, which was tested prior to the dual-body campaign. In addition, the creation and the smoothing of asperities at the interfaces as well as the subsequent generation of marble dust resulted in a continually evolving interface condition, which further contributes to the variation of the measured coefficients. The alternate interface consisted of low-friction steel plates, which were placed beneath the squatter pedestal for comparison and yielded values that ranged from 0.15 – 0.21, depending upon degradation of the polymer interface. Additional studies of the frictional interfaces indicated that the dynamic coefficient can be taken as 90% that of the static coefficient, as presented by Grossi (2014) as well as Wittich and Hutchinson (2015).

Provided measured values of the friction coefficient, preliminary numerical models were developed for each experimental configuration and can be compared to the experimental response. For each configuration, numerous simulations were conducted, which vary the frictional parameters in an attempt to find a best-fit coefficient. However, using single values for the coefficients does

not produce reasonable agreement. This is demonstrated in Figure 6.29 for the L11 configuration, in which the two trials fail to match the experimental results in both magnitude and shape. Given that the experimental specimen's interface was warped, as shown in Figure 6.25, the two 'halves' of the base could reasonably have different roughness and ultimately different values for the coefficients of friction. Successful agreement of the numerical model incorporating two levels of friction at the base of the tower is attained, as shown in Figure 6.29. Through this procedure, the best fit friction parameters for the L11 configuration are: $\mu_{s1} = 0.25$; $\mu_{s2} = 1.5 * \mu_{s1}$; $\mu_{d1} = 0.9 * \mu_{s1}$; and, $\mu_{d2} = 0.9 * \mu_{s2}$.

Another representative comparison, yet for a dual-body system, is provided in Figure 6.30 for a squat, symmetric tower atop the squatter pedestal with low-friction sliding plates (i.e. L11ss in Chapter 5). While noticeable response is observed in each mode for both the experimental specimens and the corresponding numerical predictions, precise agreement with respect to magnitude is not achieved using the measured value of the coefficient of friction. However, mild adjustment of the friction parameters significantly enhances agreement of the numerical prediction in each response mode for both bodies in the simulation, as seen on the right in Figure 6.30. This type of fitting emphasizes the broad applicability of this type of numerical model to replicate the complex motion of freestanding structural systems. However, fitting friction parameters to each of nearly 500 tests in the campaign is not practical. As a result, this calibration exercise is conducted for each unique geometric configuration for a single test, where this test is either a sliding-dominated response or the response to a simplistic motion such as a pulse. The final fitted values for the friction are included for the single-body tests and the dual-body tests in Table 6.3 and Table 6.4, respectively. It should be noted that in the dual-body tests incorporating the low-friction steel plates, a range of friction values is provided as the plates degrade with accumulated slip, as detailed in Chapter 5. It is further reiterated that the interfaces continually evolved during testing; and, actual friction values are anticipated to deviate from these configuration-based fitted parameters. The

performance of these configuration-specific models is evaluated in the following section with respect to multi-modal behavior, multi-body interactions, and classical rocking dynamics.

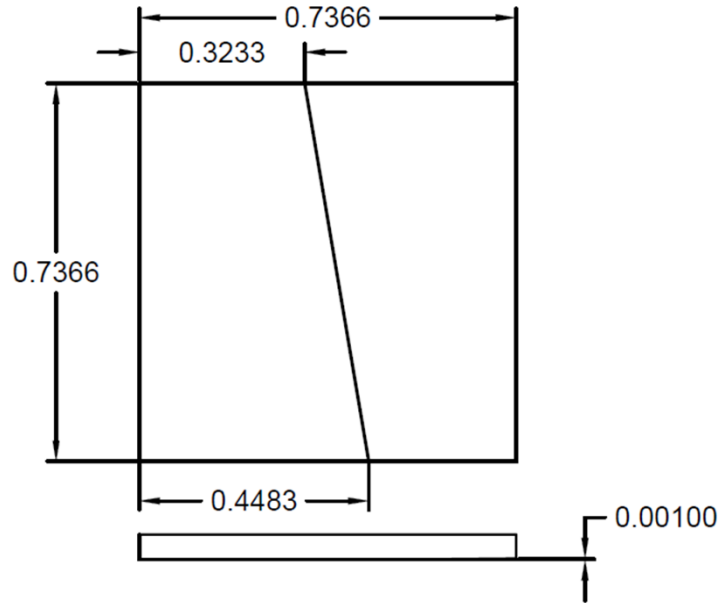


Figure 6.25 Detail drawing of the modeled interface of the tower during experimental model calibration.

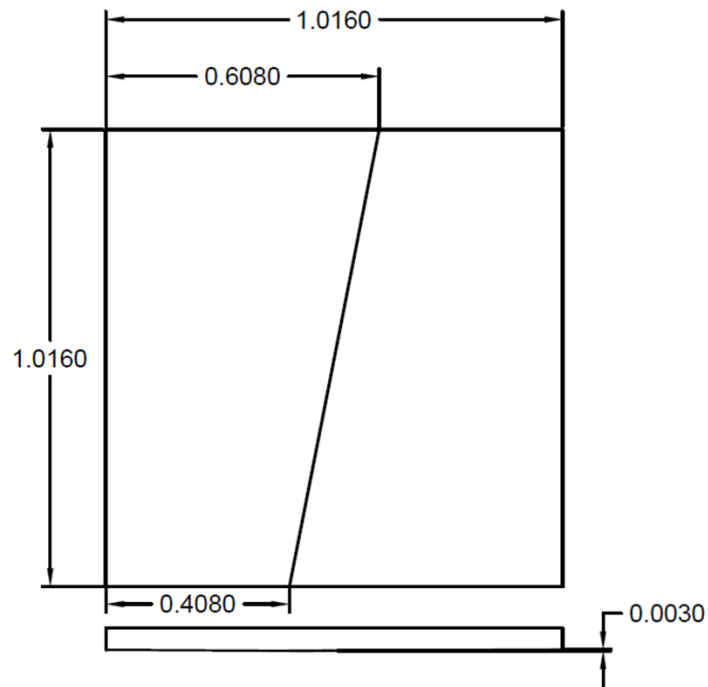


Figure 6.26 Detail drawing of the base of the TM and SM pedestals as modeled during experimental model calibration.

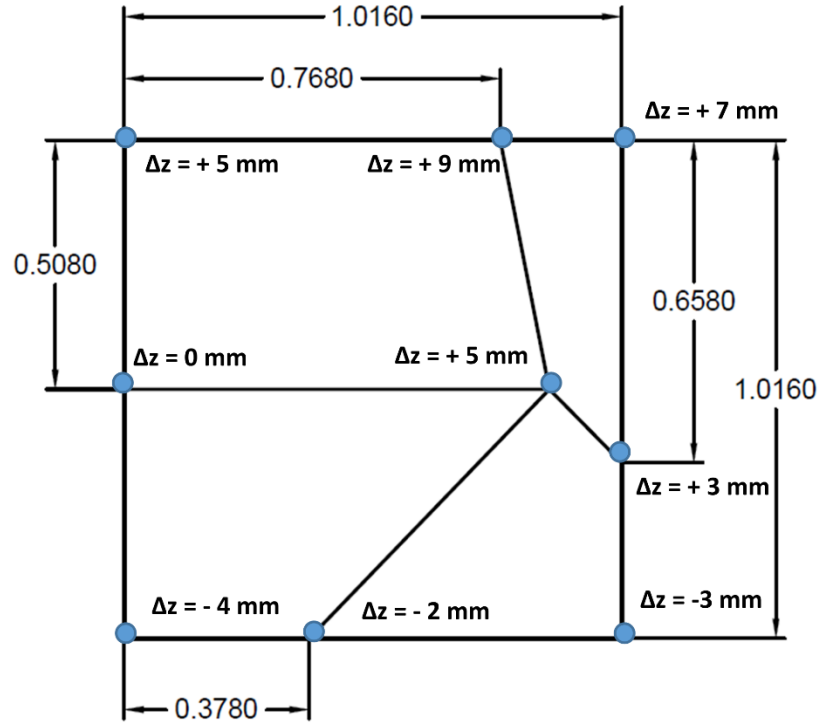


Figure 6.27 Detail drawing of the top of the SM pedestal as modeled during experimental model calibration.

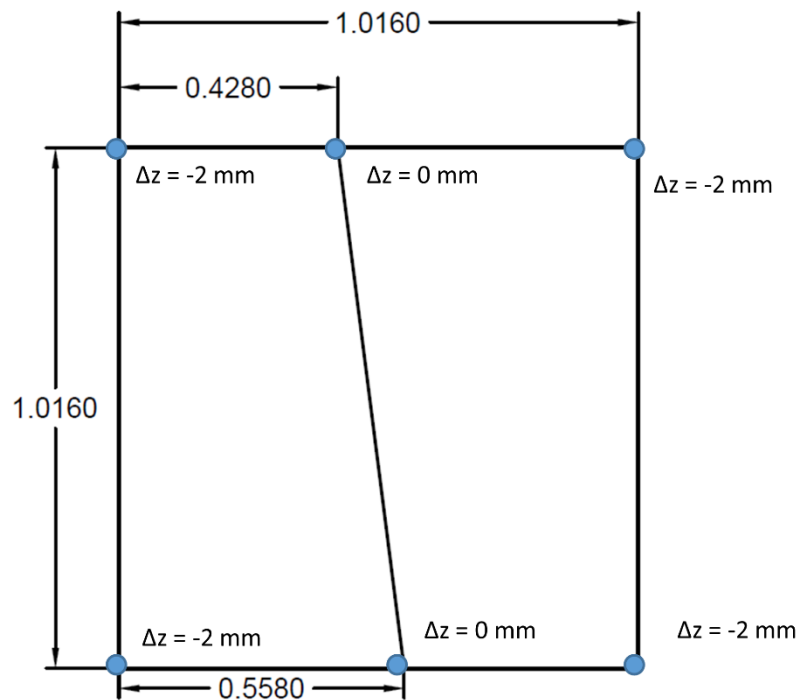


Figure 6.28 Detail drawing of the top of the TM pedestal as modeled during experimental model calibration.

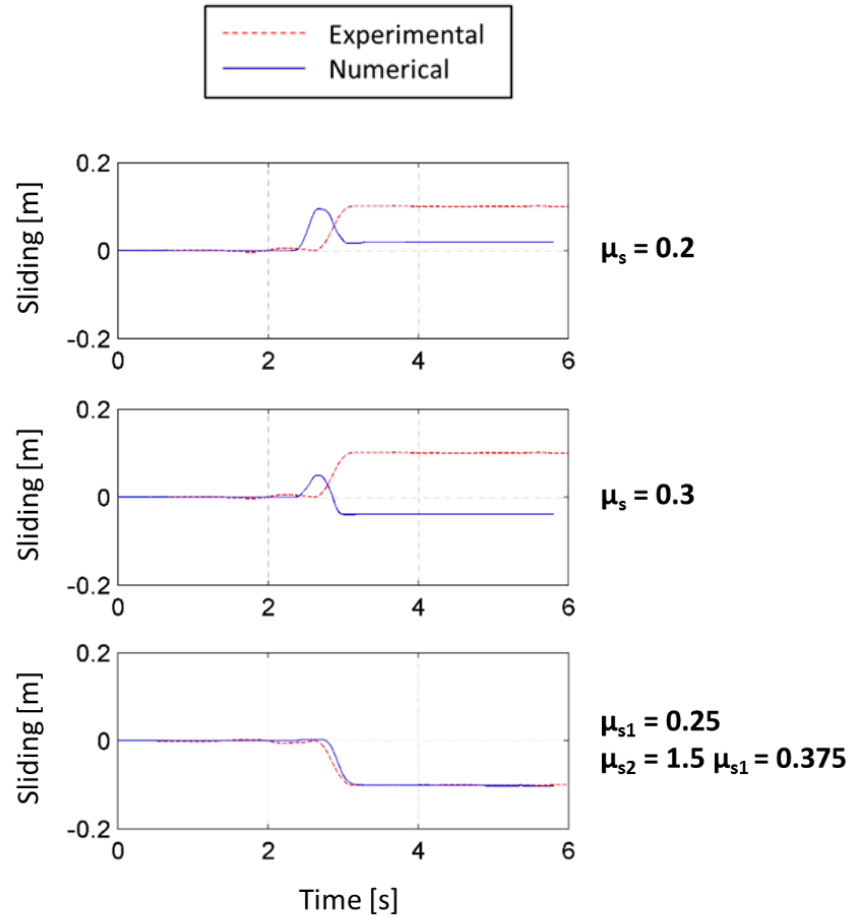


Figure 6.29 Fitting of the friction parameter for the L11 configuration.

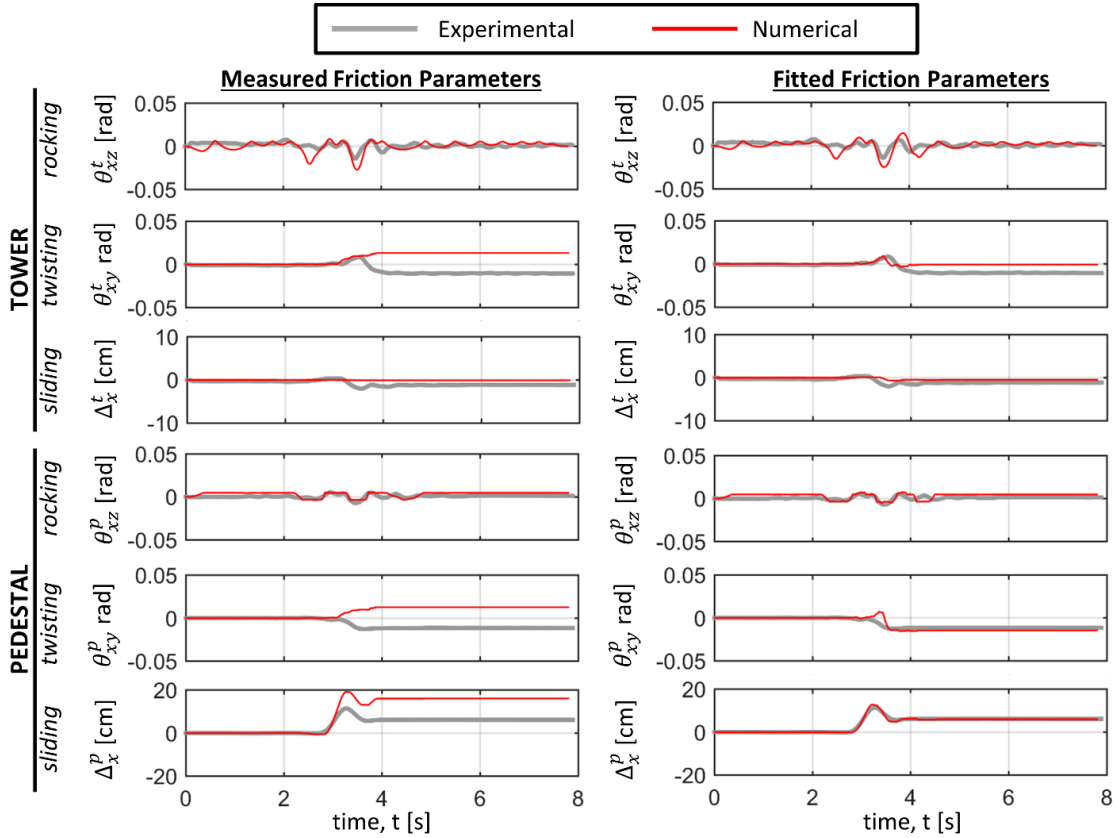


Figure 6.30 Comparison of experimental response of L11ss configuration (refer to Chapter 5) with numerical predictions utilizing the measured ($\mu_p = 0.15$, $\mu_t = 0.40$) and fitted ($\mu_p = 0.20$, $\mu_t = 0.35$) friction parameters.

Table 6.3 Selected coefficients of static friction for single-body configurations

Configuration	Calibrated μ_{s1}
U11	0.25
U21	0.25
U31	0.225
U12	0.225
U13	0.225
L11	0.25
L21	0.25
L31	0.325
L12	0.325
L13	0.3
M11	0.3
M21	0.3
M31	0.325
M12	0.3
M13	0.3

Table 6.4 Selected coefficients of static friction for dual-body configurations

Configuration	Calibrated μ_{s1}^p	Calibrated μ_{s1}^t
L11tm	0.35	0.35
L31tm	0.35	0.35
U11tm	0.35	0.35
U31tm	0.35	0.30
L11sm	0.40	0.25
L31sm	0.35	0.30
U11sm	0.45	0.25
U31sm	0.45	0.25
L11ss	0.15	0.25
L31ss	0.15 \rightarrow 0.20 [†]	0.25
U11ss	0.20 [‡]	0.30
U31ss	0.15	0.25

[†]Higher coefficient of friction yielded better match for later motions (this configuration incorporated additional repeatability tests).

[‡]This configuration included a used steel plate system which was already worn.

6.5 Numerical Model Validation

The ultimate goal of this chapter and of this dissertation is the development and validation of a numerical model that can sufficiently represent the seismic response of freestanding structures. Previous sections of this chapter outline the experimental and analytical implications on the modelling strategy, the development of the numerical model, and the calibration and sensitivity of the model. Two primary experimental observations indicate the complex multi-modal and multi-body response. As such, the model is validated with respect to these observations in this section. A third and final validation is presented with respect to the fundamental rocking dynamics, which are approximated through the implemented contact-impact algorithm. Specifically, the numerical model is compared to the prediction of the extended analytical model, as derived and studied in §6.1, and to the experimental free rocking response.

6.5.1 Multi-Modal Response

Three primary modes of response were observed during both phases of shake table testing, namely, rocking, sliding, and twisting. However, these modes often occurred simultaneously and transitioned from one to another during the same test. This behavior is termed modal interaction and modal transition, respectively. This observation informed the development of the numerical model in that the horizontal and vertical motion of the individual bodies is not restricted through the implementation of a discontinuum approach. Therefore, this multi-modal behavior is validated through comparisons of experimental response data and corresponding numerical predictions, using the configuration-specific models as described in the previous section.

The three interactive modes include slide-rocking, slide-twisting, and rock-twisting, which are the combination of two of the primary response modes. The ability of the numerical models to produce these interactive modes is presented in Figure 6.31 for three sample tests cases overlaid with their corresponding numerical predictions. The results of the numerical simulations with

respect to these interactive modes are not exact matches to the experimental results, which is anticipated due the use of the configuration-specific friction parameters. However, the general shape and response modes agree quite well. Furthermore, both modal interaction and modal transitioning are captured within the simulations. Specifically, for the slide-rocking example in Figure 6.31a, simultaneous sliding and rocking is exhibited in both the experimental data and corresponding numerical prediction for a half cycle of rocking, as well as multiple transitions between rocking, sliding, and slide-rocking. Therefore, the proposed numerical modeling strategy can sufficiently represent the complex multi-modal behavior observed throughout shake table testing.

While the interactive and primary modes are shown to be sufficiently reproduced by the numerical model, additional scatter plots present the ability of the numerical model to adequately capture the magnitude of the response in each of the primary modes in Figure 6.32. This set of scatter plots presents the peak experimental rocking, sliding, and twisting for a given configuration-motion pair against its numerical prediction along with the corresponding linear regression. The model is able to predict the peak rocking quite well, with coefficients of determination in excess of 0.86 for a nearly one-to-one relationship. However, the agreement is reduced with respect to the sliding and twisting modes. Considerable scatter is present for the sliding mode, with a coefficient of determination of 0.35. However, significant variations in the interface friction were observed during shake table testing due to the creation and degradation of asperities and the generation of marble dust. Taking this into consideration, five data points were manually identified as outliers, which increases the coefficient of determination to 0.71. Therefore, provided accurate friction coefficients, the model can sufficiently capture the critical rocking and sliding modes. On the contrary, there is no correlation between the experimental and numerical twisting, which can be attributed to the interface geometry as it was simplified in the discretization.

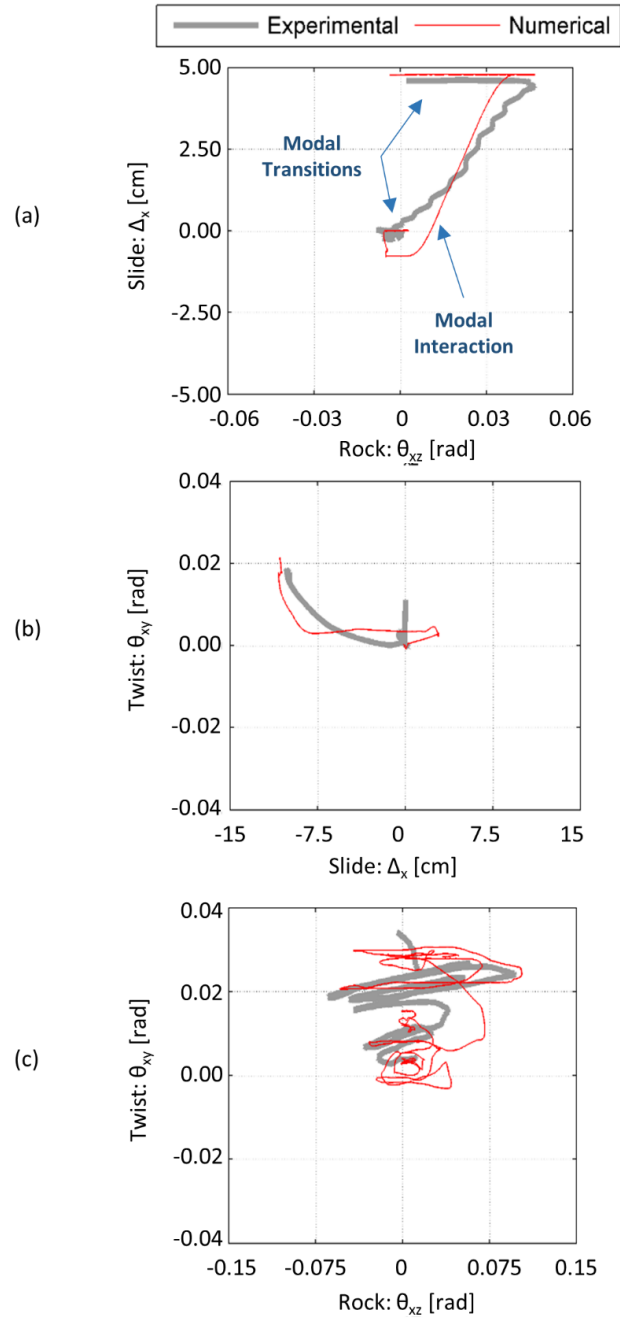


Figure 6.31 Modal interaction diagrams for sample test cases overlaid with numerical predictions for all interactive modes: (a) slide-rock, (b) slide-twist, and (c) rock-twist.

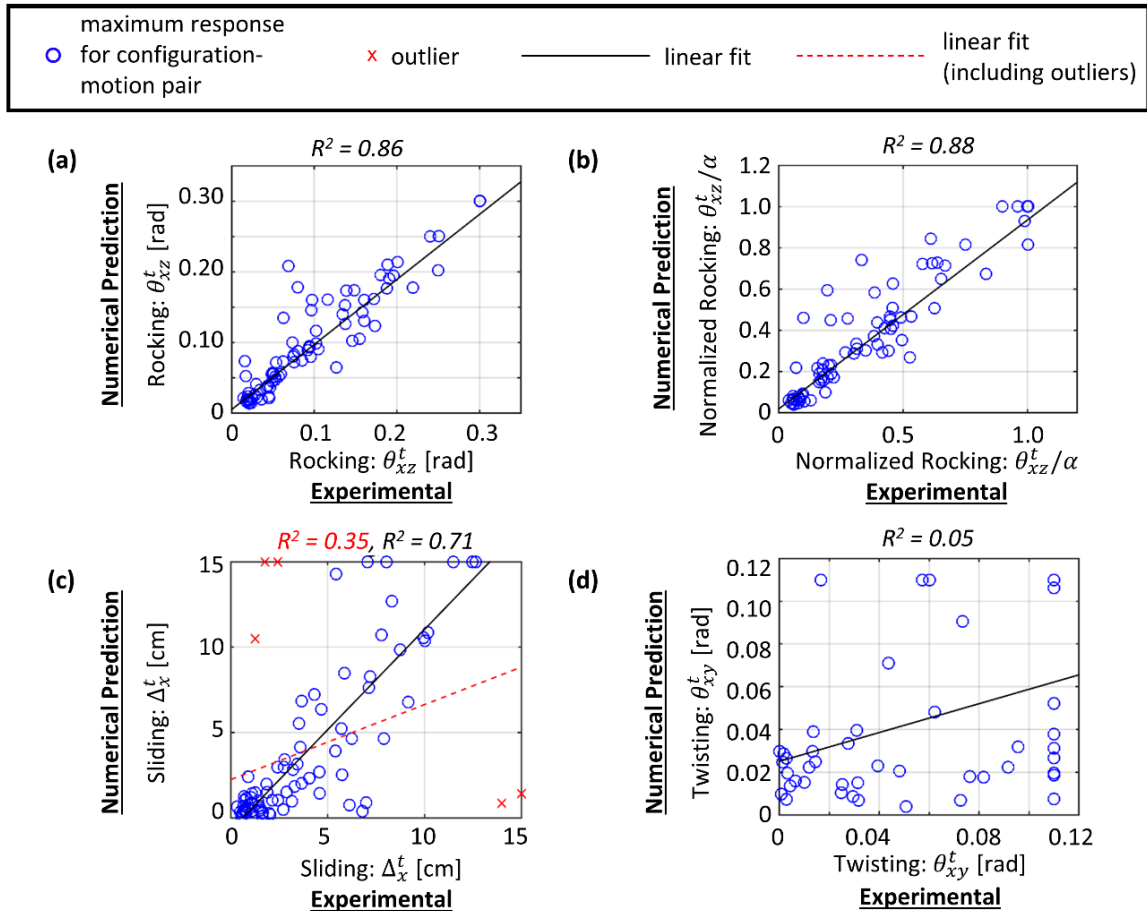


Figure 6.32 Experimental results versus numerical predictions utilizing average model for (a) peak rocking, (b) peak normalized rocking, (c) peak sliding, and (d) peak twisting.

6.5.2 Multi-Body Interaction

As emphasized in Table 6.1, significantly different responses were observed for single-body systems and dual-body systems that incorporated the same tower configuration. The difference in response was attributed to the complex interaction between the individual bodies. For certain configurations, this resulted in system-wide modes with rotation at the base of the pedestal, which was typical of squatter towers atop taller pedestals. In other instances, seemingly negligible motion of the pedestal resulted in a considerably different tower response, which was more typical of taller towers atop either the squat or tall pedestals. These particular situations of interest are

studied in the comparative time histories shown in Figure 6.33 for the situation of the low-motion pedestal and in Figure 6.34 for the system-wide motion situation.

Dual-body systems exhibited noticeably different dynamic responses compared to single-body systems, even in cases of negligible motion of the pedestal. Figure 6.33 presents the experimental rocking and sliding of a tall, symmetric tower in both single- and dual-body configurations along with overlaid numerical predictions. The experimental single-body response is characterized by many cycles of a rocking-dominated response, which is closely replicated by the numerical model. In the dual-body response, the pedestal does not exhibit any significant rocking or sliding, rather only a mild wobble mode is present. However, the tower's response is quite different atop this pedestal than its response as a single-body. While precise agreement is not attained for the multiple bodies, the model is able to sufficiently capture the complex interaction between these two bodies, as the prediction of the tower atop the pedestal is significantly different from the prediction of the single-body tower.

In addition to the general interaction of the two bodies, significantly different behavior was observed at impacts between the experimental single- and dual-body tests. This is exemplified in Figure 6.34, which presents a set of time histories for rocking and sliding of a squat, eccentric tower as a single-body and atop the taller pedestal in a dual-body configuration. In the experiment, the tower atop the pedestal exhibited increased energy dissipation and motion decay compared to the single-body configuration. This is attributed to the impact occurring between two moving bodies, rather than one moving body impacting a stationary foundation. The set of time history comparisons in Figure 6.34 attempts to validate the numerical model with respect to this observation. While the experimental single-body specimen eventually overturns and the numerical model does not, both the experimental data and the numerical prediction evidence multiple cycles of significant rocking. However, the dual-body tower is subject to only a single large-amplitude

rocking cycle, with much of the energy being dissipated after the first impact. This complex interaction between the rocking pedestal and tower is captured, with quite good agreement, in the numerical predictions, which emphasizes the model's ability to capture the interactions and impacts of the multi-body system.

6.5.3 Fundamental Rocking Dynamics

The numerical model proposed and described in this chapter is an approximate model for rigid body dynamics, based upon estimates of contact forces and lumped flexibility. This is in contrast to classically derived equations of motion for rigid bodies, as initially described by Housner for the two-dimensional rocking block (1963). Given the approximate formulation proposed in this dissertation, a brief comparison of the approximate model with the results of fundamental dynamics is warranted and presented in this sub-section.

The free rocking behavior of the experimental L11 configuration is presented in Figure 6.35. This experimental response data is overlaid with the prediction of the classical model (Housner 1963). Marked discrepancies are observed in this comparison, with failure of the model to match the post-impact amplitude (approximately 0.75 s) and the subsequent decay of rocking motion. Recall from §6.1, the extended analytical model with an arbitrary-geometry interface produces significantly different results in terms of the energy dissipation. For this reason, Figure 6.35 also includes the overlaid prediction of the extended analytical model assuming a 1 mm warp at the interface. This extended analytical model is able to capture the post-impact amplitude and the reduction in terms of the decay of rocking motion. Therefore, the experimental specimen is able to be modeled under classical assumptions; and, the numerical model must be able to account for these variations at the interface.

The primary implication of the analytical investigation, presented earlier in this chapter, is the necessity of the numerical model to explicitly model interface geometries, which is fully

incorporated in the proposed LS-DYNA model. However, the consequences of the interface geometry and discretization must be compared to the predictions of analytical models with similar interfaces. As such, the free rocking behavior of the experimental L11 configuration overlaid with the numerical predictions with and without a 1 mm warp at the interface is included in Figure 6.36. The numerical model with a flat interface mimics the predictions of the classical model, which is characterized by an underestimation of the post-impact amplitude as well as a rapid decay of rocking motion. However, the numerical model with an explicitly modeled interface warp is able to match the experimental free rocking behavior quite well in terms of both the post-impact amplitude as well as the reduced decay of rocking motion. Therefore, the approximate model proposed in this dissertation is able to sufficiently capture the fundamental rocking dynamics of freestanding structural systems.

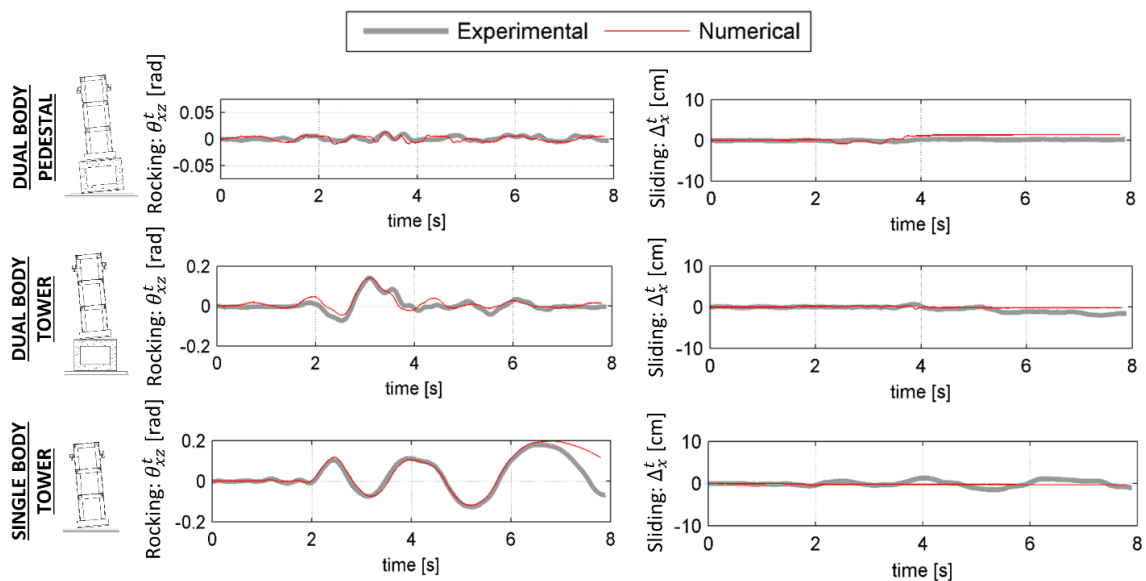


Figure 6.33 Experimental response versus numerical prediction for rocking and sliding time histories of the pedestal and tower of the U11tm configuration as well as the tower of the U11 configuration.

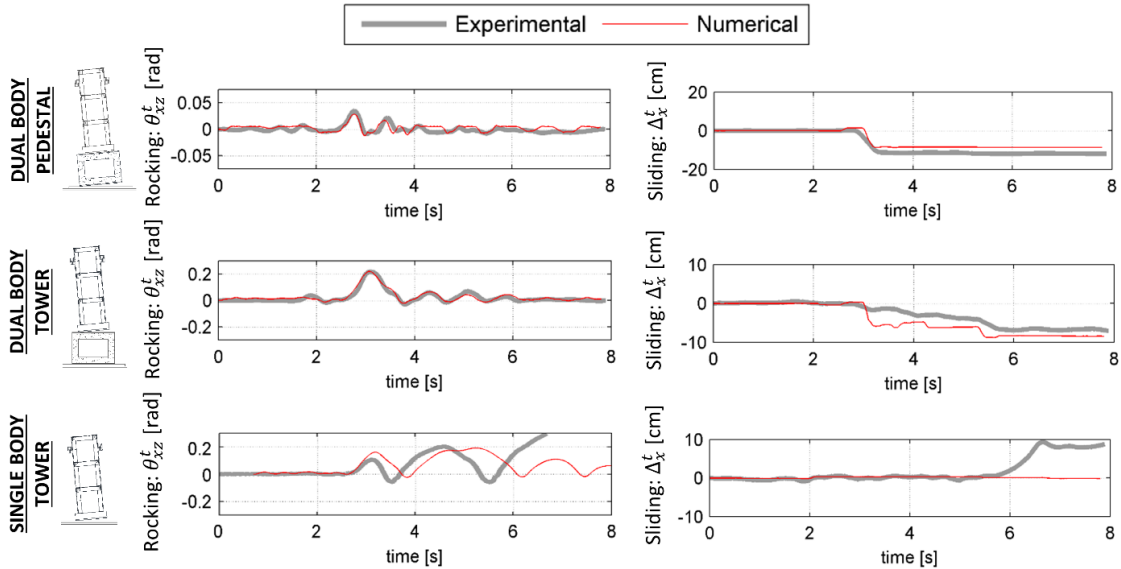


Figure 6.34 Experimental response versus numerical prediction for rocking and sliding time histories of the pedestal and tower of the L31tm configuration as well as the tower of the L31 configuration.

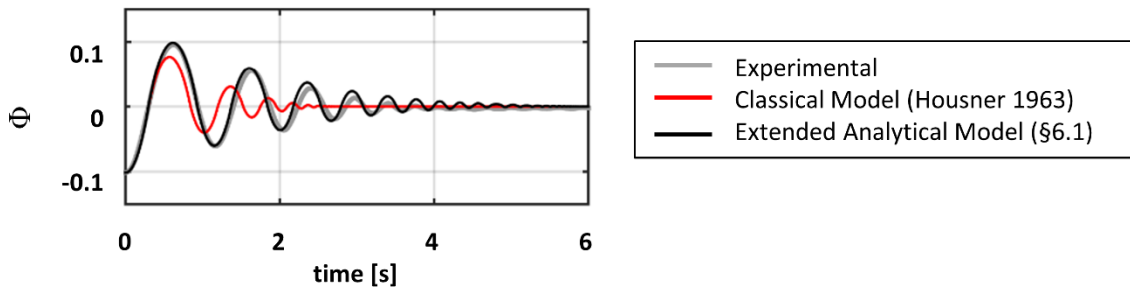


Figure 6.35 Experimental free rocking of the L11 configuration overlaid with that of the classical model and the extended analytical model assuming a 1 mm warp.

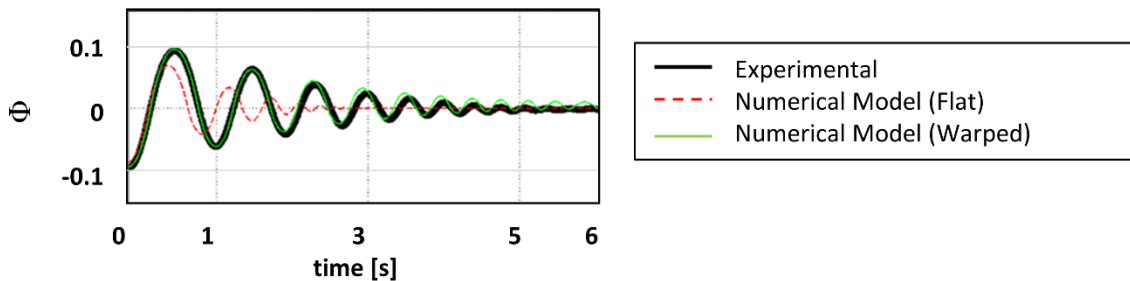


Figure 6.36 Experimental free rocking of the L11 configuration overlaid with the results of the numerical model incorporating a flat interface as well as a warped interface of 1 mm.

6.6 Summary Remarks

Freestanding structural systems represent a very wide variety of everyday, unique, and critical structures including nuclear radiation shields, unreinforced masonry, statue-pedestal systems, classical multi-drum columns, as well as mechanical and electrical equipment. These systems may be unique and irreplaceable or have a significant effect on the post-earthquake functionality of a critical facility. Analytical models have been derived and studied in this context since the landmark study of Housner (1963). This classical model has been extended to include three-dimensional response (e.g. Zulli et al 2012), multiple bodies (e.g. Psycharis 1990), multiple modes (e.g. Shenton and Jones 1991), as well as flexibility of the foundation (e.g. Chatzis and Smyth 2012) and of the body (e.g. Acikgoz and DeJong 2012). These extensions are limited to the individual variable of interest, with significant understanding regarding this variable generated by the narrow focus. However, an analytical formulation accounting for each of these critical variables is not feasible; and, as a result, numerical methods must be developed and validated. In this effort, recent applications of the discrete element method have shown promise for freestanding structural systems (e.g. Papantonopoulos et al. 2002, Peña et al. 2007). However, these applications have been limited to specific structures of interest and biased to systems of squatter blocks. Therefore, the primary goal of this chapter is the development of a numerical model that is applicable across a broad range of geometry. To this end, this chapter is divided into two main sections and studies. The first of which is an analytical investigation into the effects of arbitrary geometries at the interface of the two-dimensional rocking block, as this type of defect was present in the experimental specimens described in Chapters 4 and 5. The second and final section of this chapter is the development and validation of a numerical model, based on approximate contact forces and rigid body dynamics.

The primary conclusions of these analytical and numerical studies include:

- Energy dissipation, which is classically modeled through a coefficient of restitution, is significantly affected by additional rocking points at an interface of a rocking block. Specifically, the reduction in the angular velocity at impacts of a warped foundation can be much less than that of the classical model with two rocking points. Additional conclusions regarding this analytical study can be found in §6.1.9.
- Experimental investigations, presented in Chapters 4 and 5, emphasized the need for numerical models to account for: 1) asymmetric and arbitrary geometries, 2) distinct motion of individual bodies in a multi-body simulation, and 3) three-dimensional responses. Therefore, numerical modeling approaches for freestanding structural systems should be conducted in a discontinuum approach, where the geometry of individual bodies can be accurately represented. This was accomplished in this dissertation through the combination of penalty-based contact algorithms and rigid body dynamics in LS-DYNA.
- Parametric studies on a freestanding body, modeled in LS-DYNA, were conducted with respect to: 1) interface discretization, 2) contact damping, and 3) interface stiffness. While finer discretization at the interface more accurately represents the distribution of contact forces, the effect on the rocking response was less than 4% and the computational time for high numbers of nodes in contact becomes excessive. Therefore, it is recommended to utilize the minimum number of interface nodes to sufficiently represent the interface geometry. The parametric study on contact damping revealed the presence of high-frequency oscillations of the contact force and nodal penetration in the absence of contact damping. Therefore, sufficiently high values of contact damping should be incorporated to eliminate these penetration oscillations. The parametric study on interface stiffness revealed little impact on the rocking response of the blocks; however, nodal penetrations can become excessive for low values of stiffness. Therefore, it is

recommended to utilize realistic material properties for the rigid bodies in the simulations.

- The proposed numerical model was calibrated for individual experimental configurations based upon friction coefficients, which are incorporated in a Coulomb formulation within the penalty-based contact algorithm. This calibration was conducted across the broad range of geometries tested and presented in Chapters 4 and 5, including heights to the center of mass ranging from 0.75 m – 1.6 m and mass eccentricities as low as 60%. The proposed numerical model is able to capture the general response of freestanding structural systems, however exact matches of the numerical predictions to experimental response data is not able to be achieved due to the high sensitivity of the response to small changes in geometry and/or base excitation. Nonetheless, the proposed numerical model is able to sufficiently represent the salient features of freestanding structural dynamics, including multi-modal and multi-body interactions as well as fundamental rocking dynamics.

6.7 Acknowledgements

This chapter, in part, is a reprint of two manuscripts. The first of which has been submitted for publication to the journal *Earthquake Engineering and Structural Dynamics*. Wittich, C.E. and Hutchinson, T.C. (201X). “Rocking blocks with geometric interface defects: analytical development and experimental verification.” *Earthquake Eng. Struct. Dyn.* The second manuscript is currently being prepared for submission for publication of the material. Wittich, C.E. and Hutchinson, T.C. (201X). “Multi-physics model for the seismic response of rigid, freestanding structural systems.” The dissertation author is the primary investigator and first author of both of these manuscripts.

Chapter 7 Conclusions and Recommendations

7.1 Motivation and Scope

Freestanding structural systems are defined as any component or structure that is unattached or unanchored with respect to a foundation or another structure. This general class of structures encompasses a wide variety of everyday, critical, and unique components. Structures of cultural importance are often of this category, the most common including classical multi-drum columns and stone statue-pedestal systems. These culturally, nationally, or religiously significant artifacts have an impact on people and fields of study around the world; and, in many cases, are irreplaceable. Another subset of freestanding structures includes building contents and other components that support a facility's operations, including mechanical and electrical equipment, stacked computer systems, laboratory and office equipment, nuclear radiation shields, and switchboard cabinets. The importance of these structures increases with the criticality of the facility, most notably for schools, hospitals, nuclear power plants, and nuclear storage facilities. A similarly critical subset of freestanding structures includes historic stone buildings and unreinforced masonry walls, which are common throughout the world and typical of residential construction. However, freestanding structural systems have been observed to behave quite poorly during post-earthquake reconnaissance, with evidence of collapsed unreinforced masonry walls, overturned statue-pedestal systems, and damaged electrical transformers reported following recent events (e.g. 2014 South Napa Earthquake, refer to Wittich et al. 2014).

To predict the response of freestanding structural systems, analytical studies have been presented in the literature, stemming from the landmark effort of Housner (1963). In this study, the equations of motion were derived for a two-dimensional, rigid, symmetric, rectangular block resting atop a rigid foundation. This study emphasized the nonlinearity of the dynamic response to

the geometry of the block. Many extensions to Housner's model have been presented in an effort to understand the effects of certain variables, such as three-dimensional geometries and response, multiple modes of response, multiple bodies in a system, flexibility in the body, and flexibility in the foundation (e.g. Zulli et al. 2012, Shenton and Jones 1991, Psycharis 1990, Acikgoz and DeJong 2012, and Chatzis and Smyth 2012, respectively). While the studies have isolated the effects of individual variables, the combination of the aforementioned extensions in an analytical formulation is not feasible. As a result, numerical models have recently been explored, with the discrete element method and its variations showing promise in the ability to capture the seismic response of freestanding structural systems (e.g. Papantonopoulos et al. 2002, Peña et al. 2007). However, numerical models require experimental response data for calibration and validation; and, shake table tests of freestanding structural systems are quite limited in the literature, with the handful of studies being largely biased toward systems of squat, symmetric blocks (e.g. Mouzakis et al. 2002, Drosos and Anastasopoulos 2014). Therefore, the ultimate objective of this dissertation is to develop and experimentally validate a numerical model that can represent the dynamics of freestanding structural systems with high fidelity.

In the pursuit of a general numerical model for freestanding structures, this dissertation addresses three distinct research tasks. The first of which is to define the limits and quantify the extreme geometry that can be anticipated for realistic freestanding structures, as the response is known to be nonlinear with respect to geometry. This task is addressed in Chapter 3 through a field survey of statue-pedestal systems, which are a freestanding structure of extremely complex geometry. The second task is to generate a comprehensive database of experimental response data of freestanding structural systems, accounting for the wide range of anticipated geometries, to realistic earthquake motions. This is addressed in Chapters 4 and 5 for single-body and dual-body systems, respectively. The third task is the development and validation of a numerical model capable of representing the salient features of freestanding structures across a broad range of

geometry. This final objective is addressed in Chapter 6, with an initial analytical study on the impact of warped interfaces followed by the development of a numerical modeling scheme in the widely-utilized LS-DYNA platform. This numerical model is further validated with respect to key observations from the experimental campaigns, namely the multi-modal and multi-body behavior, as well as with respect to the classical dynamics of freestanding systems through the extended analytical model, presented earlier in Chapter 6.

This chapter aims to offer a concise summary of this dissertation. The key results and conclusions of the field survey, experimental campaigns, as well as analytical and numerical modeling are presented in the following section and sub-sections. These key results are followed by a summary of the impact of this research on the study of freestanding structural systems, as well as on the fields of earthquake and structural engineering. The chapter is concluded by a list of recommended areas for further study that build upon the research presented in this dissertation.

7.2 Key Results

7.2.1 Field Survey of Culturally Significant Statues

In this research phase, a field survey of culturally significant statues is presented, which was conducted in Florence, Italy. Field geometric data acquisition in this study involved use of Structure-from-Motion (SfM) and Light Detection and Ranging (LiDAR). While both are powerful strategies currently available to support geometric characterization, SfM and the use of envelope dimensions of the statue are simpler alternatives to LiDAR and the degree of accuracy is critical to characterize its seismic response. These methods can calculate aspect ratio and the distance to the center of mass within 40%; however, differences greater than 100% may arise for the mass moment of inertia if computed using envelope dimensions. Furthermore, inappropriate geometric acquisition such as envelope shape rather than “ground truth” LiDAR can have a significant effect

on analytical predictions of the rocking response, with variations in the rotation up to 50% observed for the surveyed statues.

This field survey attempts to address the first primary research objective of this dissertation, which is to quantify a range of anticipated geometry and generate statistics on extreme geometric configurations of freestanding structural systems. The results of which are to guide an extensive shake table testing campaign, in the pursuit of the second primary objective. Through this survey and subsequent analyses, the following conclusions and implications on shake table testing can be drawn:

- A very broad range of geometric configurations comprise the statue-pedestal systems surveyed. Aspect ratios (height-to-width) ranged from approximately 1.0 to values approaching 10.0. The statues tended to incorporate varying degrees of mass eccentricity, with the majority of statues exhibiting mild eccentricity of the center of mass. However, certain statues were calculated to have eccentricity ratios (ratio of planar widths to the center of mass) approaching 30%, which is severely asymmetric.
- Nearly all of the surveyed statues were mounted freestanding atop a stone pedestal (i.e. unanchored). The footprint of this pedestal is always greater than that of the statue, and a study of the eccentricity shows that the pedestals are consistently symmetric. However, the aspect ratio of the pedestal varies from squat to tall, although this is to a much less degree than the variation of the statues.
- The statue-pedestal systems incorporated stone-stone interfaces for all those surveyed. These interfaces are not polished, and have been subjected to years of degradation and dust accumulation. Furthermore, the statue-pedestal systems are located in buildings as well as outdoors, and subject to a variety of free-field and filtered floor-level motions.

7.2.2 Shake Table Tests of Single-Body Systems

In this research phase, the dynamics of freestanding single-body systems is studied experimentally. The range of geometries tested in this program incorporates heights of the center of mass (h) from 0.75 m through 1.45 m, frequency parameters (p) from 2.13 through 2.56, and slenderness ratios ($\theta_{c1} / \theta_{c2}$) from 0.5 through 1.0, as guided by the previously discussed field survey. In this campaign, fifteen unique geometric configurations were tested using a number of both recorded and simulated earthquake motions. The large-displacement rigid body motion of each configuration was continuously recorded and analyzed in an effort to correlate the geometry and motion characteristics with response mode, magnitude, and direction. The key results of these single-body tests are summarized as follows:

- Multi-modal and three-dimensional responses were observed in nearly all tests including symmetric configurations in which the loading was along an axis of symmetry. The multi-modal response can be observed as either simultaneous modal interaction or as unique modes per direction of the response. Symmetric configurations were the least likely to observe this type of response; however, it was still evident.
- Horizontal mass eccentricity perpendicular to the direction of shaking has little effect on the magnitude of rocking response; however, the three-dimensional effects and twisting are significantly increased with this increased eccentricity.
- In this experimental phase, taller, larger structures ($h \approx 1.45$ m; $p \approx 2.13$; $\theta_c < 15^\circ$) and squatter, smaller structures ($h \approx 0.75$ m; $p \approx 2.56$; $\theta_c > 20^\circ$) respond very differently when mass eccentricity is present. The taller, larger configurations have only a slightly increased rocking response, yet also a significantly increased sliding response due to modal interaction on the larger, squatter side of the structure. The squatter, smaller configurations have significantly increased rocking response and risk of overturning

with a much reduced sliding risk. The squatter, smaller structures with eccentricity were observed to be the most susceptible to overturning.

- The classical rocking model significantly overestimates the free rocking response of both taller symmetric and eccentric configurations, up to 90% in this study. The overestimation is likely related to the additional sources other than geometry which affect the rate of decay such as material effects, base imperfections, and/or mild bouncing. A reduced value for the coefficient of restitution to account for these additional factors greatly improves the performance of the simple rocking model and the agreement with this specific set of experimental results.

The shake table campaign of single-body systems partially addresses the second primary objective of this dissertation, which is to generate a comprehensive database of the experimental response of freestanding structural systems. These tests are intended to inform the development and validation of a numerical model for the seismic response of freestanding structures. As such, key implications of the experimental campaign on numerical modeling are summarized as follows:

- The response of symmetric and asymmetric configurations varied greatly – not only in magnitude of response, but also in the mode of response. As such, the numerical model must be able to adequately represent asymmetric and arbitrary geometries.
- Three-dimensional responses (e.g. twisting) were observed in many cases, even for configurations with apparently planar symmetry. As such, the numerical model must be conducted in a three-dimensional framework.
- Multi-modal responses were observed often for many configurations. These responses included both simultaneous response in two or more modes, as well as transitioning from one mode to another in the same response. As such, the numerical model must allow rotation and translation at all times and in all directions throughout the simulation.

- The classical model was not able to adequately represent the free rocking response of the experimental specimen. This can be attributed to a difference in the energy dissipation of the classical model with the actual specimen. Therefore, a numerical model should allow for some degree of flexibility at the interface.

7.2.3 Shake Table Tests of Dual-Body Systems

Shake table tests of dual-body systems build upon the results of the previously discussed single-body systems, which jointly address the second research objective of this dissertation to generate a comprehensive database of freestanding systems. These tests utilize the same test specimen and test protocol as that of the single-body tests, with the additional incorporation of a bottom-body or pedestal. The range of geometries for the top-body in the dual-body configuration is identical to that of the single-body tests. The range of geometries for the symmetric bottom-body ranged from 0.38 m through 0.76 m for the height of the center of mass, from 2.21 through 3.07 for the frequency parameter, and from 0.59 through 0.93 for the slenderness. The tower and pedestal specimens were combined into sixteen unique combinations and tested on a uni-axial shake table. The three-dimensional displacement response of each specimen was continuously recorded in time and analyzed in an effort to correlate the geometry, friction, and motion characteristics with the dynamic response. The key findings presented in this chapter are summarized as follows:

- Repeatability of the dynamic response of the dual-body system is attainable provided there is a smooth interface with relatively constant frictional resistance. The potential repeatability of specimen response is less achievable when large varying asperities are present, such as that of the incorporated marble-marble interfaces.
- In general, observations of collapse and rocking demands on the tower increase with the presence of a pedestal. This is further increased as the pedestal increases in height (reduced slenderness angle, increased size). However, certain configurations of the

tower were observed to be more stable in the stacked configuration than in the single-body configuration. This is likely related to the increased sliding on an inclined surface and the complex interactions at impact associated with two rotating bodies.

- The results of these experiments reveal the dependence of the response of the pedestal (bottom-body) on the geometry of the tower (top-body). Certain configurations of the dual-body system initiate into a system-wide mode, whereas others initiate into a single-body mode due to the height of the center of mass of the system compared to the tower only.

This dual-body shake table testing campaign, together with the results of the single-body campaign, address the second primary objective of this dissertation, which is to generate of a comprehensive experimental database across a broad range of geometric configurations. This database is intended to inform the development and validation of a numerical model for freestanding structures. While many of the key results of the single-body tests were similarly realized in the dual-body tests, the additional implications of the dual-body tests on numerical modeling are summarized as follows:

- Geometry of upper bodies in a multi-body system distinctly impacts the response of lower bodies. As such, the dynamic response may not be solved in a cascade analysis fashion. Rather, the response of each block must be solved simultaneously.
- The response of a given freestanding structure as a single-body is oftentimes more stable than when the same structure is placed at the top of a multi-body system. However, many geometric configurations evidence an opposite trend. This is attributed to the complex interactions and dynamics between two moving bodies. As such, the motion of each discrete body in the multi-body system must be solved as a discontinuum, rather than an equivalent continuum system.

7.2.4 Numerical Modeling

Numerical models are necessary to represent realistic freestanding structural systems and the many deviations from the classical model that result. As the experimental specimens tested in this dissertation were characterized by mild warps at the interface, it is critical to understand the effect of these geometric variations on the dynamics of the system in an analytical framework. Therefore, an analytical investigation is initially presented prior to the development of the numerical model. In this study, the equations of motion and energy dissipation are presented for a two-dimensional rocking block of arbitrary geometry with arbitrary number of rocking points. The key results and implications of this analytical derivation and subsequent parametric study are included as follows:

- Whereas the classical model is unable to match the rocking response during free rocking tests, the presented model with three rocking points agrees quite well. This agreement is possible without arbitrary modification of the velocity adjustment factor (i.e. coefficient of restitution), rather by considering three rocking points at the interface, as an approximation to base defects. Therefore, numerical modeling must allow for explicitly modeled interface geometry.
- The velocity adjustment factor, which represents energy dissipation, is the instantaneous result of point impacts and can have a value greater than 1 in the presented model, resulting in a finite increase in the angular velocity of the block due to the instantaneous reduction in rocking radius. This is in stark contrast to the classical model, in which this factor is referred to as a coefficient of restitution and always less than 1. In the proposed model, the velocity adjustment factor may be up to 25% larger than that specified in the classical model for squatter blocks ($H/B < 4$). As a result, the classical model may be unconservative and underestimate the rocking response of blocks with interface defects.

- Despite little variation in the velocity adjustment factor for taller blocks, the rotational response of the block with a defect is quite different than that predicted by the classical model. Specifically, the first peak after impact can be nearly 200% greater; however, the decay of the motion is much more rapid. Overturning spectra for a single sinusoidal pulse input further emphasize the significantly increased rate of overturning for both squat and tall blocks, with overturning possible for blocks of three rocking points at amplitudes less than the threshold to initiate rocking motion in the classical model with two rocking points. However, a sinusoidal pulse that overturns a block modeled with two rocking points may not necessarily overturn a block modeled with three rocking points due to its asymmetry.

The proposed numerical model of this dissertation utilized the key results of the field survey, two phases of experimental shake table testing, as well as the aforementioned analytical model in its development and validation. A summary of this numerical model and the key results of the parametric studies include:

- The proposed numerical model follows a discontinuum modeling scheme, as originally proposed by studies focused on the discrete element method. However, the proposed model is developed within the commercially-available and widely-utilized LS-DYNA multi-physics platform. Each body in the simulation is modeled with a rigid material model utilizing solid eight-node brick elements. The mass properties, including centroid and inertia tensor, can be manually overridden and not reliant upon the discretization of the model. The interaction between the individual bodies is modeled through a penalty-based contact algorithm, which generates springs and dashpots at all nodes in contact as well as enforcing Coulomb friction.

- Parametric studies on the numerical model were conducted with respect to: 1) interface discretization, 2) contact damping, and 3) interface stiffness. While finer discretization at the interface more accurately represents the distribution of contact forces, the effect on the rocking response was less than 4% and the computational time for high numbers of nodes in contact becomes excessive. Therefore, it is recommended to utilize the minimum number of interface nodes to sufficiently represent the interface geometry. The parametric study on contact damping revealed the presence of high-frequency oscillations of the contact force and nodal penetration in the absence of contact damping. Therefore, sufficiently high values of contact damping should be incorporated to eliminate these fictitious penetration oscillations. The parametric study on interface stiffness revealed little impact on the rocking response of the blocks; however, nodal penetrations can become excessive for very low values of stiffness. Therefore, it is recommended to utilize realistic material properties for the rigid bodies in the simulations.
- The proposed numerical model was calibrated for individual experimental configurations based upon friction coefficients, which are incorporated in a Coulomb formulation within the penalty-based contact algorithm. This calibration was conducted across the broad range of geometries tested and presented in Chapters 4 and 5, including heights to the center of mass ranging from 0.75 m – 1.6 m and mass eccentricities as low as 60%. The proposed numerical model is able to capture the general response of freestanding structural systems, however exact matches of the numerical predictions to experimental response data is not able to be achieved due to the effect of small changes in geometry and/or base excitation. Nonetheless, the proposed numerical model is able to sufficiently represent the salient features of freestanding structural dynamics, including multi-modal and multi-body interactions as well as fundamental rocking dynamics.

7.3 Research Impact

This dissertation generated three primary products, namely: 1) a unique database of complex geometry of critical freestanding structures, 2) a large database of experimental response data for freestanding structural systems, including single-body and dual-body systems, and ultimately 3) the experimental validation of a numerical model for freestanding systems. The database of geometrically-accurate three-dimensional models of statue-pedestal systems can be utilized for statue-specific predictive studies and interventions. The experimental response data can be utilized by other researchers for the calibration and validation of alternate numerical models, as well as for comparisons with analytical developments. The ultimate outcome of this dissertation, a high-fidelity numerical model, can be incorporated by researchers with confidence for the study of a variety of freestanding structural systems, including mechanical and electrical equipment, unreinforced masonry structures, and given statue-pedestal systems. Furthermore, this model has been developed in a widely-utilized and commercially available platform for ease of implementation by engineers and researchers.

7.4 Recommendations for Future Work

Recommendations for future work in this area include:

- Shake table tests of freestanding bodies that are flexible, which may be useful for future designs of rocking columns and structural elements. In addition, the results of shake table tests of flexible bodies should be used for the validation of an extension to the currently proposed numerical model.
- In this dissertation, the analytical derivation and subsequent parametric studies of rocking blocks with arbitrary interface geometry were described. Experimental verification of the key findings regarding energy dissipation should be conducted

through free rocking tests and dynamic shake table tests of rocking blocks with systematically varied interface geometry.

- The response of freestanding structures is highly sensitive to small changes in geometry, friction, and base excitation, which has been known since early analytical studies of the two-dimensional rocking block. As such, the proposed numerical model should be cast in a probabilistic framework for the development of fragility curves.

References

- Acikgoz, S. and DeJong, M.J. (2012). "The interaction of elasticity and rocking in flexible structures allowed to uplift." *Earthquake Eng. Struct. Dyn.*, 41(15), 2177-2194.
- Agbabian, M.S., Ginell, W.S., Masri, S.F., and Nigbor, R.L. (1991). "Evaluation of earthquake damage mitigation methods for museum objects." *Stud. Conserv.*, 36(2), 111-120.
- Allen, R.H., Oppenheim, I.J., Parker, A.R., and Bielak, J. (1986). "On the dynamic response of rigid body assemblies." *Earthquake Eng. Struct. Dyn.*, 14(6), 861-876.
- Ambraseys, N. and Psycharis I, N. (2011). "Earthquake stability of columns and statues." *J. Earthq. Eng.*, 15(5), 685-710.
- Applied Technology Council (ATC). (2009). *Quantification of building seismic performance factors*. Report No. FEMA p695, ATC, Redwood City, CA.
- Aslam, M., Scalise, D.T., and Godden, W.G. "Earthquake rocking response of rigid bodies." *J. Struct. Div.*, 106(2), 377-392.
- Avery, C. (1970). *Florentine Renaissance Sculpture*, J. Murray, London, U.K.
- Baker, J.W. (2007). "Quantitative classifications of near-fault ground motions using wavelet analysis." *Bull. Seismol. Soc. Am.*, 97(5), 1486-1501.
- Benedetti, D., Carydis, P., and Pezzoli, P. (1998). "Shake table tests on 24 simple masonry buildings." *Earthquake Eng. Struct. Dyn.*, 27(1): 67-90.
- Benson, D.J. and Hallquist, J.O. (1986). "A simple rigid body algorithm for structural dynamics program." *Int. J. Numer. Meth. Eng.*, 22(3), 723-749.
- Berto, L., Favaretto, T., Saetta, A., Antonelli, F., and Lazzarini, L. (2012). "Assessment of seismic vulnerability of art objects: The 'Galleria dei Prigioni' sculptures at the Accademia Gallery in Florence." *J. Cult. Herit.*, 13(1), 7-21.
- Bouguet, J.Y. (2004). "Camera calibration toolbox for MATLAB." <http://www.vision.caltech.edu/bouguetj/calib_doc>
- Chatzis, M.N. and Smyth, A.W. (2011). "Robust modeling of the rocking problem." *J. Eng. Mech.*, 138(3), 247-262.
- Chatzis, M.N. and Smyth, A.W. (2012). "Modeling of the 3D rocking problem." *Int. J. Nonlin. Mech.*, 47(4), 85-98.
- Chiou, B., Darragh, R., Gregor, N., and Silva, W. (2008). "NGA project strong-motion database." *Earthq. Spectra*, 24(1), 23-44.
- Cignoni, P., Corsini, M., and Ranzuglia, G. (2008). "Meshlab: an open-source 3d mesh processing system." *ERCIM News*, 73, 45-46.
- Consortium of Organizations for Strong Motion Observations Systems (COSMOS). (2014). "COSMOS Virtual Data Center". <<http://www.strongmotioncenter.org/vdc/>>. University of California, Berkeley. (January 2014).
- Costa, A.A., Arede, A., Costa, A.C., Penna, A., and Costa, A. (2013). "Out-of-plane behavior of a full scale stone masonry façade. Part 2: shaking table tests." *Earthquake Eng. Struct. Dyn.*, 42(13), 2097-2111.

- Cundall, P.A. (1971). "A computer model for simulating progressive, large-scale movements in blocky rock systems." *Proc., Int. Symp. on Rock Fracture*, Nancy, France, 2-8.
- Cundall, P.A. and Strack, O.D.L. (1979). "A discrete numerical model for granular assemblies." *Geotechnique*, 29(1), 47-65.
- DeJong, M.J. and Vibert, C. (2012). "Seismic response of stone masonry spires: Computational and experimental modeling." *Eng. Struct.*, 40(1), 566-574.
- Di Egidio, A., and Contento, A. (2009). "Base isolation of slide-rocking non-symmetric rigid blocks under impulsive and seismic excitations." *Eng. Struct.*, 31(11), 2723-2734.
- Drosos, V. and Anastasopoulos, I. (2014). "Shake table testing of multidrum columns and portals." *Earthquake Eng. Struct. Dyn.*, 43(11), 1703-1723.
- Earthquake Engineering Research Institute (EERI). (2015). "Earthquake photo galleries." <<https://www.eeri.org/cohost/member-resources/earthquake-photo-galleries>> (Nov. 6, 2015).
- Eberly, D.H. (2010). *Game Physics*, Elsevier, Boston, MA.
- ElGawady, M.A., Ma, Q., Butterworth, J.W., and Ingham, J. (2011). "Effects of interface material on the performance of free rocking blocks." *Earthquake Eng. Struct. Dyn.*, 40(4), 375-392.
- Ericksen, G.E., Concha, J.F., and Silgado, E. (1954). "The Cuzco, Peru earthquake of May 21, 1950." *Bull. Seismol. Soc. Am.*, 44(2A), 97-112.
- Espinosa, A.F., Husid, R., Algermissen, S.T., and De Las Cases, J. (1977). "The Lima earthquake of October 3, 1974: intensity distribution." *Bull. Seismol. Soc. Am.*, 67(5), 1429-1439.
- FARO. (2011). *FARO Laser Scanner Focus 3D: Features, Benefits, & Technical Specifications*, FARO Technologies Inc., Lake Mary, FL.
- Furukawa, Y., and Ponce, J. (2010). "Accurate, dense, and robust multi-view stereopsis." *IEEE T. Pattern Anal.*, 32 (8), 1362-1376.
- Grossi, S. (2014). "Characterization of marble interfaces and dynamic sliding behavior of statues and pedestals for use in seismic response prediction." M.S. Thesis, University of Bologna.
- Han, S., Cho, H., Kim, S., Jung, J., and Heo, J. (2013). "Automated and efficient method for extraction of tunnel cross sections using terrestrial laser scanned data." *J. Comput. Civ. Eng.*, 27(3), 274-281.
- Heikkila, J. and Silven, O. (1997). "A four-step camera calibration procedure with implicit image correction." *Proc., IEEE Computer Vision and Pattern Recognition*, San Juan, PR, 1106-1112.
- Housner, G.W. (1963). "The behavior of inverted pendulum structures during earthquakes." *Bull. Seismol. Soc. Am.*, 53(2), 403-417.
- International Code Council (ICC). (2007). *Acceptance Criteria for Seismic Qualification by Shake Table Testing of Nonstructural Components and Systems*. Report AC156, ICC, Whittier, CA.
- Ishiyama, Y. (1982). "Motion of rigid bodies and criteria for overturning by earthquake excitations." *Earthquake Eng. Struct. Dyn.*, 10(5), 635-650.
- Itasca Consulting Group. (2003). *3DEC Version 3.0: User's Guide*, Itasca, Minneapolis, MN.

- Junior, J. S., Bellon, O., Silva, L., and Vrubel, A. (2011). "Improving 3D reconstruction for digital art preservation." *Proc., 16th Int. Conf. on Image Analysis and Processing*, Springer-Verlag, Berlin, Germany, 374-383.
- Karavasilis, T.L., Seo, C.Y., and Makris, N. (2010). "Dimensional response analysis of bilinear systems subjected to non-pulselike earthquake ground motions." *J. Struct. Eng.*, 137(5), 600-606.
- Kazhdan, M., Bolitho, M., and Hoppe, H. (2006). "Poisson surface reconstruction." *Proc., 4th Eurographics Symp.on Geometry Processing*, Eurographics Association, Aire-la-Ville, Switzerland, 61-70.
- Kim, H., Haas, C.T., Rauch, A.F., and Browne, C. (2002). "Dimensional ratios for stone aggregates from three-dimensional laser scans." *J. Comput. Civ. Eng.*, 16(3), 175-183.
- Kirkpatrick, P. (1927). "Seismic measurements by the overthrow of columns." *Bull. Seismol. Soc. Am.*, 17(1), 95-109.
- Koch, C., Jog, G.M., and Brilakis, I. (2013). "Automated pothole distress assessment using asphalt pavement video data." *J. Comput. Civ. Eng.*, 27(4), 370-378.
- Konstantinidis, D. and Makris, N. (2005). "Seismic response analysis of multidrum classical columns." *Earthquake Eng. Struct. Dyn.*, 34(10), 1243-1270.
- Konstantinidis, D. and Makris, N. (2007). "The dynamics of a rocking block in three dimensions." *Proc., 8th Hellenic Society for Theoretical and Applied Mechanics International Congress on Mechanics*, Patras, Greece, 1-10.
- Konstantinidis, D. and Makris, N. (2009). "Experimental and analytical studies on the response of freestanding laboratory equipment to earthquake shaking." *Earthquake Eng. Struct. Dyn.*, 38(6), 827-848.
- Konstantinidis, D. and Makris, N. (2010). "Experimental and analytical studies on the response of 1/4-scale models of freestanding laboratory equipment subjected to strong earthquake shaking." *B. Earthq. Eng.*, 8(6), 1457-1477.
- Lemos, J.V. (2007). "Discrete element modeling of masonry structures." *Int. J. Archit. Herit.*, 1(2), 190-213.
- Levoy, M., Pulli, K., Curless, B., Rusinkiewicz, S., Koller, D., Pereira, L., Ginzton, M., Anderson, S., Davis, J., Ginsberg, J., Shade, J., and Fulk, D. (2000). "The Digital Michelangelo Project: 3D scanning of large statues." *Proc., SIGGRAPH '00*, Wesley, New York, NY, 131-144.
- Lipscombe, P.R. and Pellegrino, S. (1993). "Free rocking of prismatic blocks." *J. Eng. Mech.*, 119(7), 1387-1410.
- Livermore Software Technology Corporation (LSTC). (2006). *LS-DYNA Theory Manual*. J.O Hallquist (Ed.), LSTC, Livermore, CA.
- Livermore Software Technology Corporation (LSTC). (2013). *LS-DYNA*. LSTC, Version LS-DYNA_971 Revision 78769, Livermore, CA.
- Makris, N. and Black, C.J. (2004). "Dimensional analysis of rigid-plastic and elastoplastic structures under pulse-type excitations." *J. Eng. Mech.*, 130(9), 1006-1018.
- Makris, N. and Roussos, Y.S. "Rocking response of rigid blocks under near-source ground motions." *Geotechnique*, 50(3), 243-262.

- MATLAB Version 8.0.0. (2012). *The Language of Technical Computing*. The MathWorks, Inc., Natick, MA.
- Mirtich, B. (1996). "Fast and accurate computation of polyhedral mass properties." *J. Graph. T.*, 1(2), 31-50.
- Monaco, M., Guadagnuolo, M., and Gesualdo, A. (2014). "The role of friction in the seismic risk mitigation of freestanding art objects." *Nat. Hazards*, 73(2), 389-402.
- Mouzakis, H.P., Psycharis, I.N., Papastamatiou, D.Y., Carydis, P.G., Papantonopoulos, C., and Zambas, C. (2002). "Experimental investigation of the earthquake response of a model of a marble classical column." *Earthquake Eng. Struct. Dyn.*, 31(9), 1681-1698.
- Nigbor, R.L. (1989). "Analytical/experimental evaluation of seismic mitigation measures for art objects." Ph.D. dissertation, Department of Civil Engineering, University of Southern California, Los Angeles, CA.
- Olsen, M.J. (2013). "In-situ change analysis and monitoring through terrestrial laser scanning." *J. Comput. Civ. Eng.*, in press.
- Papantonopoulos, C., Psycharis, I.N., Papastamatiou, D.Y., Lemos, J.V., and Mouzakis, H.P. (2002). "Numerical prediction of the earthquake response of classical columns using the distinct element method." *Earthquake Eng. Struct. Dyn.*, 31(9), 1699-1717.
- Papantonopoulos, C.L. (1997). "The earthquake resistance of ancient columns: a numerical perspective developed at the classical Temple of Apollo Epikourios." *Proc., STREMAH V*, San Sebastian, Spain, 437-446.
- Papastamatiou, D. and Psycharis, I. (1993). "Seismic response of classical monuments – a numerical perspective developed at the Temple of Apollo in Bassae, Greece." *Terra Nova*, 5(6), 591-601.
- Peña, F., Lourenço, P.B., and Campos Costa, A. (2008). "Experimental dynamic behavior of freestanding multi-block structures under seismic loading." *J. Earthq. Eng.*, 12(6), 953-979.
- Peña, F., Prieto, F., Lourenço, P.B., Campos Costa, A., and Lemos, J.V. (2007). "On the dynamics of rocking motion of single rigid-block structures." *Earthquake Eng. Struct. Dyn.*, 36(15), 2383-2399.
- Perry, J. (1881). "Note on the rocking of a column." *Trans. Seismol. Soc. Japan*, 3(1), 103-106.
- Podany, J. (2008). *Advanced in the Protection of Museum Collections from Earthquake Damage: Papers from a Symposium Held at the J. Paul Getty Museum at the Villa on May 3-4, 2006*. Getty Publications, Los Angeles, CA.
- Psycharis, I.N. (1990). "Dynamic behavior of rocking two-block assemblies." *Earthquake Eng. Struct. Dyn.*, 19(4), 555-575.
- Purvance, M.D., Anooshehpour, A., and Brune, J.N. (2008). "Freestanding block overturning fragilities: Numerical simulation and experimental validation." *Earthquake Eng. Struct. Dyn.*, 37(5), 791-808.
- Rosetto, T., Alexander, D., Verucci, E., Ioannou, I., Borg, R.C., Melo, J., Cahill, B., and Kongar, I. (2012). *The 20th May 2012 Emilia Romagna Earthquake*. EPICentre Field Observation Report No. EPI-FO-200512, UCL EPICentre, London, UK.

- Shenton III, H. W. (1996). "Criteria for initiation of slide, rock, and slide-rock rigid-body modes." *J. Eng. Mech.*, 122(7), 690-693.
- Shenton, H.W. and Jones, N.P. (1991). "Base excitation of rigid bodies I: Formulation." *J. Eng. Mech.*, 117(10), 2286-2306.
- Sinopoli, A. (1997). "Unilaterality and dry friction: a geometric formulation for two-dimensional rigid body dynamics." *Nonlinear Dyn.*, 12(4), 343-366.
- Spanos, P.D., Roussis, P.C., and Politis, N.P. (2001). "Dynamic analysis of stacked rigid blocks." *Soil Dyn. Earthq. Eng.*, 21(7), 559-578.
- Tang, P., Huber, D., and Akinci, B. (2011). "Characterization of laser scanners and algorithms for detecting flatness defects on concrete surfaces." *J. Comput. Civ. Eng.*, 25(1), 31-42.
- Thomas, H., Bowes, W., Nelson, B.S., and Pierre, S-A. (1963). "Geologic report on the effects of the earthquake of 22 May 1960 in the city of Puerto Varas." *Bull. Seismol. Soc. Am.*, 53(6), 1347-1352.
- Truong-Hong, L., Laefer, D.F., Hinks, T., and Carr, H. (2012). "Flying voxel method with Delaunay triangulation criterion for façade/feature detection for computation." *J. Comput. Civ. Eng.*, 26(6), 691-707.
- Vassiliou, M.F., Truniger, R., and Stojadinovic, B. "An analytical model of a deformable cantilever structure rocking on a rigid surface: development and verification." *Earthquake Eng. Struct. Dyn.*, 44(15), 2775-2794.
- Winkler, T., Meguro, K., and Yamazaki, F. (1995). "Response of rigid body assemblies to dynamic excitation." *Earthquake Eng. Struct. Dyn.*, 24(10), 1389-1408.
- Wittich, C.E. and Hutchinson, T.C. (2014a). "Development of a rocking-period centered protocol for shake table testing of unattached stiff components." *Proc., 10th National Conference in Earthquake Engineering*, Anchorage, AK, 1-10.
- Wittich, C.E. and Hutchinson, T.C. (2014b). *Shake table tests of unattached, stiff, asymmetric structures – phase 1: floor-mounted*. Structural Systems Research Project Report Series, SSRP-2013/18, Department of Structural Engineering, University of California, San Diego, La Jolla, CA.
- Wittich, C.E. and Hutchinson, T.C. (2015). *Shake table tests of unattached, stiff, asymmetric structures – phase 2: pedestal-mounted*. Structural Systems Research Project Report Series, SSRP-2015/05, Department of Structural Engineering, University of California, San Diego, La Jolla, CA.
- Wittich, C.E., Hutchinson, T.C., Lo, E., Meyer, D., and Kuester, F. (2014). *The South Napa Earthquake of August 24, 2014: Drone-based Aerial and Ground-based LiDAR Imaging Survey*. Structural Systems Research Project Report Series, SSRP-2014/09, Department of Structural Engineering, University of California, San Diego, La Jolla, CA.
- Wittich, C.E., Hutchinson, T.C., Wood, R.L., Kuester, F., and Seracini, M. (2012). *Survey and Characterization of Culturally Important Statues in Florence, Italy*. Structural Systems Research Project Report, SSRP-2012/10, University of California San Diego, Department of Structural Engineering, La Jolla, CA.
- Wu, C. (2011). *VisualSFM: A visual structure from motion system* (computer software), <<http://homes.cs.washington.edu/~ccwu/vsfm>> (1 Oct, 2011).

- Yadav, D., Girdhar, P., Kumar, V., and Kumar, R. P. (2010). "Earthquake vulnerability of free standing monolithic statues." *Eur. J. Sci. Res.*, 44(2), 355-373.
- Yim, C.-S., Chopra, A.K., and Penzien, J. (1980). "Rocking response of rigid blocks to earthquakes." *Earthquake Eng. Struct. Dyn.*, 8(6), 565-587.
- Zhang, J., and Makris, N. (2001). "Rocking response of free-standing blocks under cycloidal pulses." *J. Eng. Mech.*, 127(5), 473-483.
- Zulli, D., Contento, A., Di Egidio, A. (2012). "3D model of a rigid block with a rectangular base subject to pulse-type excitation." *Int. J. Nonlin. Mech.*, 47(6), 679-687.

Appendix A

This appendix summarizes the geometric and mass properties of the surveyed statues, as detailed in Chapter 3. The table includes two images of each surveyed statue along with the following information:

- Name and artist
- Current location
- Mass
- Footprint dimensions
- Center of mass location with respect to the center of the footprint
- Mass moment of inertia
- Method of geometric data acquisition (i.e. LiDAR, SfM, or Envelope Shape)
- Notes on boundary conditions (e.g. freestanding, pedestal, mounted, etc.)

Table A.1 Details on surveyed statues.











Name (Artist)	Location ²	Mass [kg]	Footprint [m]		Height [m]	Center of Mass [m]			Moment of Inertia [kg·m ²]			Method ³	Notes on Boundary Conditions	Photograph	
			x	y		z	x	y	z	I _{xx}	I _{yy}			I _{zz}	yz
<i>Genius of Victory</i> (Michelangelo)	<i>Palazzo Vecchio</i>	2201	0.89	1.00	2.63	0.36	0.48	1.64	1584	1639	234	LiDAR	Free-standing Pedestal-supported		
<i>Hercules and Centaur</i> (de Rossi)	<i>Palazzo Vecchio</i>	--	0.90	1.40	2.25	--	--	--	--	--	--	Env ⁵	Free-standing Pedestal-supported		
<i>Hercules and Diomedes</i> (de Rossi)	<i>Palazzo Vecchio</i>	2361	0.93	0.64	2.78	0.42	0.28	1.53	1182	1211	230	SfM	Free-standing Pedestal-supported		
<i>Florentine Pieta</i> (Michelangelo)	<i>Il Museo dell'Opera del Duomo</i>	2604	0.97	1.32	2.23	0.46	0.58	0.81	842	940	293	LiDAR	Cementitious materials restrains statue to pedestal Pedestal-supported		
<i>Zuccone</i> (Donatello)	<i>Il Museo dell'Opera del Duomo</i>	576	0.55	0.41	1.99	0.27	0.19	0.91	146	149	14	LiDAR	Free-standing		

Table A.1 Details on surveyed statues, Continued.











Name (Artist)	Location ²	Mass [kg]	Footprint [m]			Height [m]			Center of Mass [m]			Moment of Inertia [kg-m ²]				Method ³	Notes on Boundary Conditions	Photograph	
			x	y	z	x	y	z	x	y	z	I _{xx}	I _{yy}	I _{zz}	yz			xz	
<i>Medici Lion</i> (Vacca)	<i>Loggia dei Lanzi</i>	25	0.13	0.28	0.24	0.05	0.13	0.14	0	0	0	SfM	Free-standing Pedestal-supported						
<i>Rape of the Sabine Women</i> (Giambologna)	<i>Loggia dei Lanzi</i>	6998	1.20	1.22	4.27	0.55	0.57	1.76	1016 2	1007 6	1158	SfM	Free-standing Pedestal-supported						
<i>Hercules Beating Nessus</i> (Giambologna/Franc ovilla)	<i>Loggia dei Lanzi</i>	--	0.90	0.70	3.10	--	--	--	--	--	--	Env ⁵	Free-standing Pedestal-supported						
<i>Menelaus and Petrochus</i> (Unknown)	<i>Loggia dei Lanzi</i>	7959	1.67	1.26	3.25	0.71	0.57	0.93	6230	5710	2531	SfM	Free-standing Pedestal-supported						
<i>Rape of Polyxena</i> (Pio Fedi)	<i>Loggia dei Lanzi</i>	5213	1.37	1.35	3.15	0.54	0.62	0.91	3216	3627	1276	SfM	Free-standing Pedestal-supported						

Table A.1 Details on surveyed statues, Continued.





















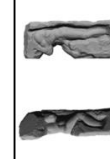
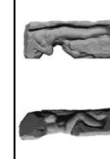
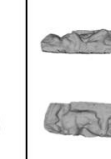
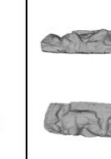
Name (Artist)	Location ²	Mass [kg]	Footprint [m]			Height [m]	Center of Mass [m]			Moment of Inertia [kg·m ²]			Method ³	Notes on Boundary Conditions	Photograph	
			x	y	z		x	y	z	I _{xx}	I _{yy}	I _{zz}			yz	xz
<i>Profeta</i> (di Bartolo)	<i>Il Museo dell'Opera del Duomo</i>	484	0.41	0.64	2.06	0.20	0.31	1.03	146	151	12	LIDAR	Free-standing Pedestal-supported			
																
<i>Re Salomone</i> (Pisano)	<i>Il Museo dell'Opera del Duomo</i>	471	0.60	0.38	1.80	0.30	0.13	0.76	103	107	11	SfM	Free-standing Pedestal-supported			
																
<i>Profeta</i> (Pisano)	<i>Il Museo dell'Opera del Duomo</i>	598	0.56	0.29	1.82	0.27	0.11	0.81	125	134	17	SfM	Free-standing Pedestal-supported			
																
<i>Sibila Tiburtina</i> (Pisano)	<i>Il Museo dell'Opera del Duomo</i>	416	0.52	0.21	1.75	0.24	0.10	0.95	84	91	11	SfM	Free-standing Pedestal-supported			
<i>Profeta</i> (Donatello)	<i>Il Museo dell'Opera del Duomo</i>	1463	0.73	0.94	2.63	0.36	0.43	1.21	686	726	75	LIDAR	Free-standing Pedestal-supported			

Table A.1 Details on surveyed statues, Continued.

Name (Artist)	Location ²	Mass [kg]	Footprint [m]			Height [m]	Center of Mass [m]			Moment of Inertia [kg-m ²]			Method ³	Notes on Boundary Conditions	Photograph		
			x	y	z		x	y	z	I _{xx}	I _{yy}	I _{zz}			yz	xz	
<i>Profeta</i> (di Banco)	<i>Il Museo dell'Opera del Duomo</i>	601	0.51	0.32	1.84	0.26	0.13	0.82	123	130	16	LiDAR	Free-standing Pedestal-supported				
<i>David</i> (Michelangelo)	<i>Galleria dell'Accademia</i>	5569	1.51	1.10	5.09	0.64	0.49	2.46	12617	13268	1154	LiDAR ⁴	Free-standing Pedestal-supported				
<i>St. Matthew</i> (Michelangelo)	<i>Galleria dell'Accademia</i>	3283	0.75	0.63	2.75	0.35	0.19	1.40	2068	2062	374	LiDAR ⁴	Free-standing Pedestal-supported				
<i>Atlas</i> (Michelangelo)	<i>Galleria dell'Accademia</i>	4734	1.32	0.88	2.83	0.64	0.43	1.35	3380	3627	631	LiDAR ⁴	Free-standing Pedestal-supported				
<i>Awakening</i> (Michelangelo)	<i>Galleria dell'Accademia</i>	4192	1.16	1.07	2.77	0.55	0.51	1.54	2611	2837	557	LiDAR ⁴	Free-standing Pedestal-supported				

Notes: ¹To the authors' knowledge, all statues are constructed of marble.

²All locations are in Florence, Italy.

³Method for geometric data acquisition: LiDAR (light detection and ranging), SfM (structure-from-motion), or Env (envelope shape or manual dimensions).

⁴LiDAR point clouds obtained from Stanford University (Levoy et al. 2000).

⁵Additional geometric and mass properties are not calculated for statues characterized solely by Envelope Shape due to its poor estimation.